Aerodynamic Performance of Endwall Contoured Turbine Blades Considering Leakage Flow Interaction

Aerodynamische Effizienz von seitenwandkonturierten Turbinenschaufeln unter Berücksichtigung von Leckageströmungsinteraktion

Von der Fakultät für Maschinenwesen der
Rheinisch-Westfälischen Technischen Hochschule Aachen
zur Erlangung des akademischen Grades eines
Doktors der Ingenieurwissenschaften genehmigte Dissertation

vorgelegt von
Tobias Winfried Zimmermann

Berichter: Univ.-Prof. Dr.-Ing. habil. Manfred Christian Wirsum
Prof. Tekn. Dr. Damian Vogt

Tag der mündlichen Prüfung: 24.07.2017

Diese Dissertation ist auf den Internetseiten der Universitätsbibliothek online verfügbar.

Acknowledgements

This thesis was developed within the framework of my research and working time at the Institute of Power Plant Technology, Steam and Gas Turbines. I would like to acknowledge the joint research program COORETEC-Turbo in AG Turbo. The work has been supported by the Bundesministerium für Wirtschaft und Technologie (BMWi) (file number 03ET2013) on the basis of an adjudication of the German Parliament. Furthermore, I'd like to thank General Electric Company (ALSTOM Power) for their financial and technical support during this research project. The greatest credit for this thesis, however, is due to my doctoral supervisor Univ.-Prof. Dr.-Ing. habil. Manfred Wirsum, who supported my work in any conceivable manner and who initiated the collaboration to conduct this research project. Additionally I'd like to thank Prof. Tekn. Dr. Damian Vogt for supporting me by examination of this thesis.

No project is carried out in isolation and this section allows the author to say thank you to the many people that have helped to write this thesis. First, I would like to thank all of my colleagues for several inspiring discussions and the pleasant working atmosphere. Also I'd like to express my gratitude to the workshop staff who manufactured all required parts for the test rig. Especially the commitment of Hans-Peter Nießen, Markus Riemschoß, Hans-Josef Scheeren and Thomas Lillot and of my students Johannes Pohl, Tobias Ebus, Alexander Gronwald and Talu Ünal has to be mentioned as the tests could not have been run successfully without their support. Many thanks to Germar Heibges for his help with electrical components. Furthermore, I'd like to say thank you to the colleagues at GE, Cristos Georgakis, Peter Millington, Andrew Fowler, Sten Kramer, Kush Patel and Sanjay Mata for their constructive technical support. Many thanks are also dedicated to several students who acquired important components to this work within the framework of their theses.

Besides the technical aspects I wish to say thank you to my fiancée Jana for the strong backing during all measuring campaigns and stressful situations. Then, I want to thank my parents Winfried and Christiane and my grandparents Siegfried and Brigitte for their patience, devotion and their support during my period of education that finally set the basis of this dissertation. Also I'd like to thank Jana's family who admitted me, warmly.

Last but not least I would like to thank all of my long-standing and close friends and their partners who were always by my side: Christian Bauer, Christian Dölle, Florian Feuer, Andreas Fuhr, Arne Modersohn, Carsten Reese, Julian Schmitz, Thomas Schumacher, Jan Wiese and Mathias Wilhelm. Here, special thanks are dedicated to Mathias Diefenthal, Marius Schumacher and Philipp Vinnemeier, who did the proof reading of the present thesis.

Aachen, July 2017, Tobias W. Zimmermann

Abstract

Tangential endwall contouring is intended to improve the blading efficiency in turbomachinery. The present thesis focusses on the influence of leakage flows on the performance of non-axisymmetric endwall contouring in combination with a compound lean turbine blading.

All tests were conducted on a 2 stage axial turbine test rig at the Institute of Power Plant Technology, Steam and Gas Turbines (IKDG) of RWTH Aachen University. The test rig is driven with air. Two sealing set-ups are applied to create two different leakage mass flows. Four operating points are investigated that represent the design point as well as overload and partload conditions.

The endwall contouring is applied on both hub and tip sides. Three configurations are compared. A baseline design without endwall contouring, contoured stator vanes and non-contoured rotor blades as well as contoured vanes and blades.

At first, all configurations are investigated with a negligible leakage flow rate at the casing side. The results show that the vane contoured configuration performs best in stage 1 while the fully contoured set-up loses in efficiency for the design point and in partload compared to the baseline configuration. This trend is flipped in stage 2 as the fully contoured version performs best and the vane contoured configuration loses significantly. This finding suggests that endwall contouring has the potential to increase the efficiency of multi stage turbines.

The second focus is put on the interaction of endwall contouring and leakage flow. These investigations show that neither the vane contoured nor the fully contoured set-up show an increased efficiency at any operating point. The trends within the first stage are similar to the measurements with the low amount of leakage flow. In the second stage both contouring designs perform worse than the baseline, leading to the assumption that the change in efficiency is mainly caused by the re-entering leakage mass flow upstream the contouring and not by the flow that enters the cavities in front of the rotor contouring.

Kurzzusammenfassung

Nicht-achssymmetrische Seitenwandkonturierung soll eingesetzt werden, um den Schaufelwirkungsgrad in Turbomaschinen zu erhöhen. In der vorliegenden Arbeit wird der Einfluss von Leckageströmung auf die Wirkungsweise der Seitenwandkonturierung in Verbindung mit einer "Compound Lean" Turbinenbeschaufelung untersucht.

Alle experimentellen Versuche wurden mit dem 2-stufigen Axialturbinen-Prüfstand des Instituts für Kraftwerkstechnik, Dampf- und Gasturbinen (IKDG) der RWTH Aachen University durchgeführt. Die Versuchsturbine wird mit Luft betrieben. Zwei Dichtungskonfigurationen werden eingesetzt, um zwei unterschiedliche Leckage-Raten zu generieren. Außerdem werden vier Betriebspunkte untersucht, die den Auslegungspunkt sowie Überlast- und Teillast-Zustände repräsentieren.

Die Seitenwandkonturierung ist sowohl an der Nabe, als auch gehäuseseitig appliziert und es werden drei Beschaufelungs-Konfigurationen verglichen. Ein Basis-Design ohne Seitenwandkonturierung, konturierte Statorschaufeln und nicht konturierte Rotorschaufeln, sowie eine Variante in der sowohl Stator- als auch Rotorschaufeln konturiert sind. In einem ersten Schritt werden alle Konfigurationen mit einer vernachlässigbaren gehäuseseitigen Leckage-Rate untersucht. Die Messergebnisse zeigen, dass die Konfiguration mit konturierten Statorschaufeln den höchsten Wirkungsgrad in Stufe 1 hat, wohingegen die voll-konturierte Variante im Vergleich zum Basis-Design einen schlechteren Wirkungsgrad im Auslegungspunkt und in Teillast aufweist. Dieser Trend kehrt sich in Stufe 2 um, in der die voll-konturierte Konfiguration die höchste Effizienz hat und deutliche Verluste bei der Statorkonturierten Variante zu verzeichnen sind. Hieraus lässt sich ableiten, dass diese Form der Seitenwandkonturierung das Potenzial bietet den Wirkungsgrad von mehrstufigen Turbinen zu erhöhen.

Aufbauend auf den zuvor beschriebenen Untersuchungen wird der weitere Fokus dieser Arbeit auf die Interaktion von Seitenwandkonturierung und Leckageströmung gelegt. Diese Untersuchungen zeigen, dass weder die am Stator konturierte, noch die voll-konturierte Konfiguration zu einem Wirkungsgradanstieg in allen untersuchten Betriebspunkten führt. Das Verhalten in Stufe 1 ist vergleichbar zu den Ergebnissen mit geringen Leckage-Raten. Dahingegen sind die Wirkungsgrade der beiden konturierten Varianten in Stufe 2 schlechter als der Wirkungsgrad der Basis-Konfiguration. Dies führt zu der Annahme, dass die Änderung des Wirkungsgrades primär durch den einströmenden Leckage-Massenstrom stromauf der Seitenwandkonturierung verursacht wird und nicht durch die Strömung, welche vor den Rotorschaufeln in die Kavitäten fließt.

Contents

Nomenclature

Symbol	Description	Unit
a	Specific Work	$\frac{J}{kg}$
A	Area	m^2
$\vec{A}$	Vector perpendicular to surface area	m^2
c	Absolute velocity	$\frac{m}{s}$
$\vec{c}$	Vector of velocity	$\frac{m}{s}$
c_{B}	Gap between labyrinth tip and rotor	m
c_{p}	Specific heat constant	$\frac{J}{kg\,K}$
cl	Clearance	m
D	Diameter	m
$\dot{\vec{D}}$	Angular momentum flow	Nm
f	Field variable within the flow section	$-$
f	Volume force	$\frac{N}{m^3}$
F	Force	N
h	Enthalpy	$\frac{kJ}{kg}$
h	Height	m
$\dot{H}$	Enthalpy flow	W
I	Specific, intensive state variable	$-$
k	Straddle factor	$-$
l	Length	m
m	Mass	kg
$\dot{m}$	Mass flow	$\frac{kg}{s}$
M	Radial position of probe measurement	m
Ma	Mach number	$-$
n	Rotational speed	$\frac{1}{min}$
p	Pressure	Pa
P	Power	Pa
Pr	Prandtl number	$-$
r	Radius	Pa
$\vec{r}$	Vectorial field coordinate	m

Symbol	Description	Unit
$\bar{r}_{\mathrm{p}}$	Parameter of dyname	m
R	Specific gas constant	$\frac{J}{kg\,K}$
Re	Reynolds number	$-$
s	Specific entropy	$\frac{kJ}{kg\,K}$
S	Free control surface	$\frac{kJ}{kg\,K}$
$\dot{S}$	Entropy flow	W
t	Time	s
t_0	Time interval of measurement	s
T	Temperature	$^{\circ}C$
u	Specific intrinsic energy	$\frac{J}{kg}$
V	Volume	m^3
x	Load	$-$
x	Pitchwise circumferential position	$-$
x	Relative blade length	m
z	Number of labyrinth tips	m
Δ	Difference	$-$
Δ_{B}	Deviation, remaining flux	$-$
ε_{B}	Specific outflow number	$-$
η	Efficiency	$-$
κ	Isentropic coefficient	$-$
λ	Thermal conductivity	$\frac{W}{m\,K}$
μ	Passage coefficient	$-$
υ	Specific volume	$\frac{m^3}{kg}$
φ	Flow coefficient	$-$
Φ	Volume related dissipation energy	$\frac{W}{m^3}$
ψ_{h}	Load coefficient	$-$
ρ	Density	$\frac{kg}{m^3}$
$\vec{\vec{\sigma}}$	Stress tensor	$\frac{N}{m^2}$
ζ	Loss	$-$

Abbreviations

Symbol	Description
2D	Constant section airfoils
3D	Airfoils with application of lean and bow
3HP	3-hole probe
5HP	5-hole probe
AR	Aspect ratio
BASE	Baseline configuration without endwall contouring
BS	Brush seal
CBF	Cross blade flow
CFD	Computational fluid dynamics
CPF	Cross passage flow
CV	Corner vortex
CP	Clocking position
DP	Design point
FLS	Full labyrinth seal
GRLS	Groove ridge labyrinth seal
HP	High pressure
HV	Horse shoe vortex
IBL	Inlet boundary layer
IP	Intermediate pressure
KM	Kreitmeier
LF	Leakage flow
LI	Leakage flow interaction
LP	Low pressure
LS	Labyrinth seal
MEWC	Meridional endwall contouring
MF	Main flow
MP	Measurement plane
MP10	Measurement plane upstream of the first stage
MP12	Measurement plane between the both stages (interstage)

Symbol	Description
MP22	Measurement plane downstream of the second stage
OP	Operating point
PAD	Probe adjusting device
PS	Pressure side
PV	Passage vortex
RF	Recovery factor
RPM	Revolutions per minute
SPBL	Separated profile boundary layer
SS	Suction sided
SR	Slenderness ratio
STLS	straight through labyrinth seal
TEWC	Tangential endwall contouring
TEWC-V	TEWC only applied on the stator vanes
TFV	Trailing filament vortex
TP	Temperature probe
TR	Traupel
TSV	Trailing shed vortex

Subscripts

Symbol	Description
ax	Axial
b	Blade
b	Mean momentum
BL	Bearing losses
c	Absolute velocity
e	Mean energy
in	Inlet
is	Isentropic
k	Mean value of continuity
LF	Leakage flow
m	Mean
Max	Maximal
MF	Main flow
MP10	Measurement plane upstream of the first stage
MP12	Measurement plane between the both stages (interstage)
MP22	Measurement plane downstream of the second stage
out	Outlet
pol	Polytropic
Prof	Profile losses
PS	Pressure side
r	Rotor
rad	Radial
Sec	Secondary losses
ss	Static - static
SS	Suction sidet
T	Turbine
Th	Theoretical
t	Total
tt	Total - total

Symbol	Description
WB	Water brake
x	Coordinate
y	Coordinate
z	Coordinate
λ	Related thermal conductivity

1 Motivation and primordial objective

The employment of fossil fired power plants will be necessary in future decades to secure a stable energy supply. The global energy demand will rise up by additional 70% until 2030 according to a forecast by the European Commission [40]. The great majority of this demand (88%) will be covered by energy from fossil fuels in 2030. Furthermore, the increased involvement of renewable energies requires a flexible operation of conventional power equipment, while keeping the maximum efficiency over a wide operating range. Almost one third of the total European energy consumption is caused by losses of the energy conversion processes [41].

Therefore, the optimization of efficiency is a major development focus for turbo machinery to reduce the effective fuel consumption as well as environmental pollution of the power plant. Primarily the efficiency of power plants can be enhanced by increasing the inlet temperature as well as the inlet pressure of the turbine. However, this method is limited by the mechanical integrity of the material. Due to the high research costs and long development time frame of alloys, the aerodynamic optimization of airfoils possesses a high potential to improve the efficiency by keeping the thermodynamic boundary conditions.

Leakage losses cause inner losses of turbo machines as well as profile or secondary losses. In general, their amount is proportional to the gap above the blade shroud. Leakage losses are caused by the pressure difference along the sealed section. Büscher [20] showed that this pressure difference has a substantial influence on the leakage across a stage. Thus, stator vanes of impulse blading show higher leakage rates than rotor blades. The leakage flow impacts the main flow in different ways. On the one hand, less fluid participates in energy conversion, on the other hand it modifies the incident flow to the next stage. These effects cause losses due to flow interaction and mixing losses, and finally lead to a decrease of efficiency. Figure 1.1 a) illustrates a shrouded airfoil that is sealed by means of a labyrinth seal. A portion of the main flow splits up upstream the airfoil and passes across the shroud through the labyrinth fins. This leakage flow re-enters the main channel and mixes with the main flow downstream of the last cavity.

Tangential Endwall Contouring (TEWC) is a passive method to reduce secondary losses in the main flow. The contouring is used to expand or constrict the flow area selectively to influence the local static pressure, the resulting pressure gradient and finally the velocity profile. It is applied at the tip side (casing) or hub side along the flow passage and has to be designed under consideration of the airfoil shape to achieve an optimal efficiency. As one can see in Figure 1.1 b) the contouring is applied between two airfoils along the complete flow path in the axial direction.

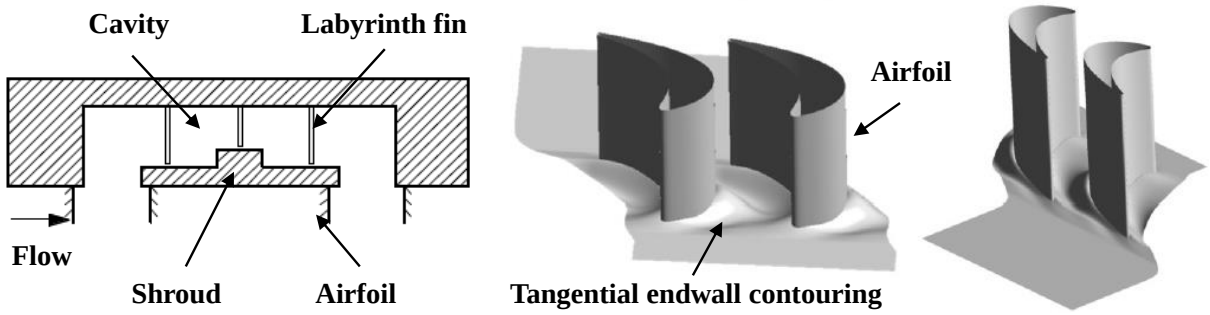

a) Shroud sealed with labyrinth seals **b)** Tangential endwall contouring

Figure 1.1: a) Schematic of a shroud sealed with labyrinth seals [108] b) Illustration of tangential endwall contouring [2]

At the Institute of Power Plant Technology, Steam and Gas Turbines (IKDG), experimental investigations on TEWC were conducted by Schwab [125] on a 2-stage axial turbine. Shrouded "constant section airfoils" (2D) were investigated in a baseline configuration (BASE) without TEWC and a contoured design in which the TEWC is applied on rotor and stator on the hub and tip side. The contoured design investigated is unique as it does not have any bump or constriction of the main channel. This is caused due to the requirement that it must be applicable as a retrofit option to the turbine.

The shrouds are sealed by means of labyrinth seals (LS) which reduce the leakage flow down to approximately 10‰ compared to the main flow. The performance of the turbine has been measured in four operating points (OP). These operating points represent the design point (OP3), two overload points (OP1 and OP2) and one part load point (OP4). Figure 1.2 shows the polytropic efficiencies of all OPs normalized to the efficiency at design point OP3. The efficiencies were derived in two ways (represented by the marker style). Schwab [125] calculated the efficiency using Equation 5.9, only based on measured probe data (temperature and pressure). Bearing losses and frictional losses are also considered in Equation 5.10. It can be seen that the efficiency is increased globally by TEWC for a wide range of load coefficients up to a load coefficient of about +2.0.

Motivated by these findings, a research project has been conducted to improve the understanding of this kind of endwall contouring. The investigations that are presented in this thesis are the result of findings that were made during this project. All publications, which are shown subsequently in this chapter, have been prepared within the framework of this research. They explain why the focus of the present thesis is on the comparison of 3D airfoils and the impact of leakage flow interaction to endwall contouring (see Chapter 5 and Chapter 6).

In a first step, Zimmermann et al. [161] investigated the same blading type as Schwab [125] (2D TEWC) with brush seals on the casing side to minimize the interaction of leakage flow and

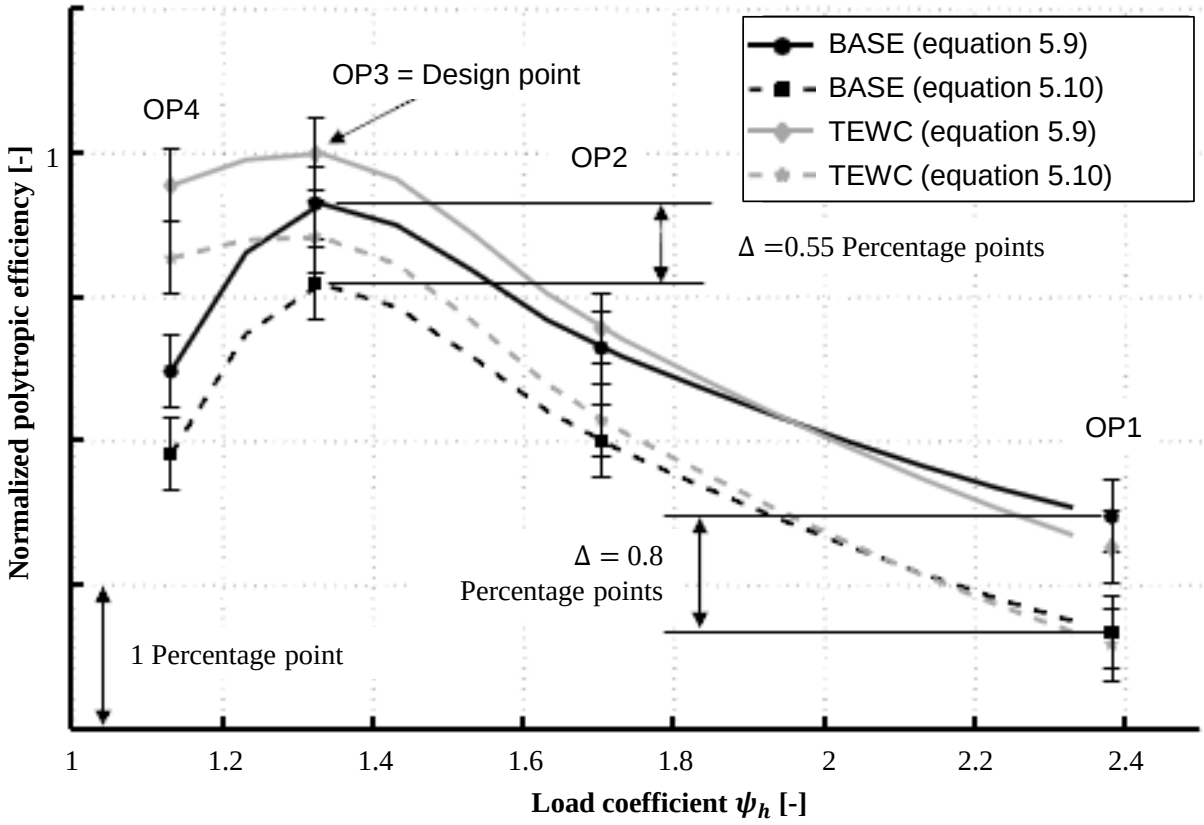

Figure 1.2: Normalized efficiencies of 2D BASE LS and 2D TEWC LS configuration (Schwab [125])

endwall contouring. Additionally, the measurement equipment and procedure was upgraded to detect smaller deviations that are expected to occur within the flow field when implementing TEWC. Further details according to this topic are presented by Zimmermann et al. [162]. The investigations of Schwab [125] were extended with the goal to suppress the mixing effects of leakage flow and main flow. The impact of rotor - stator interaction is considered. For these investigations, the leakage flow of the groove ridge labyrinth seal consisting of three sealing tips (10‰ $\dot{m}_{mainflow}$) was reduced down to approximately 1‰ by means of a combined labyrinth and brush seal (BS). For this configuration all dimensions of shroud and cavities were kept constant and the centred seal tip was replaced by a brush seal that overlaps the shroud. This ensures a bristle contact for all OP, respectively for different centrifugal forces.

As shown in Figure 1.3, the efficiency of the configuration with brush seal (BS) at design point (OP3) could be improved by 1.9% points compared to the LS configuration. An even higher increase in efficiency of 3.9% points was observed for the overload condition (OP1). These findings indicate that the performance of the TEWC is influenced by the leakage flow. In other words, it is not fully moistened due to the leakage flow that mixes with the main flow upstream the TEWC location. A detailed flow analysis has shown that the flow field downstream of the first rotor is homogenized by means of TEWC. Therefore, especially the second stage performs better due to the proper inflow from

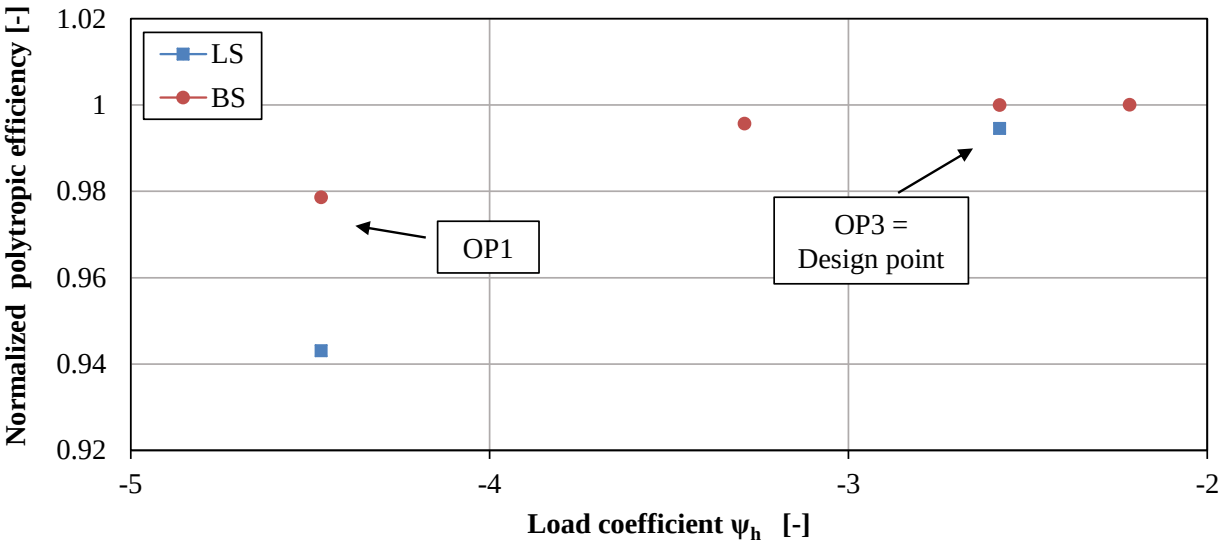

Figure 1.3: Normalized efficiencies of 2D TEWC LS and 2D TEWC BS configuration (Zimmermann [161])

the first stage, and the reduced mixing effects of leakage flow and main flow. In both stages the flow is more uniform than before.

Measurements of the surface pressure distribution along the span of one vane at two radial heights have shown that the incidence was improved, especially at the off design point OP1. For this operating point one can see that the flow field of the LS configuration is influenced across the whole span by a zone of inhomogeneity that nearly disappeared by reducing the leakage flow. It has to be mentioned that the load coefficient is twice as large as shown by Schwab [125] due to a different definition.

The investigations of Zimmermann et al. [163] focus on 2D as well as 3D airfoils in baseline and endwall contoured configuration. All airfoil configurations are investigated in combination with BS on the casing side. A low leakage mass flow of approximately 1‰ could be realized for all configurations. The prior findings of a more uniform inflow to the second stage (see Zimmermann [161]) could be validated for the 2D configuration and are also seen for the 3D airfoils. However, the beneficial effect could not be observed in the same scale as for the 2D airfoils. This is because the 3D airfoils are more efficient as in comparison to the 2D airfoils. A detailed analysis of the polytropic efficiency of each stage showed that the efficiency of the first stage suffers from TEWC for both airfoil types, while the efficiency increases in the second stage. Figure 1.4 summarizes these findings for all OP and the four airfoil configurations. In stage one, the efficiency is nearly the same for OP1 and OP2 for both airfoil types. In OP3 it is decreased by a similar amount however, OP4 suffers most for the 3D configuration. Stage two shows a constant positive offset for the TEWC configurations that is higher for the 2D airfoils. Having a look at the global efficiency of the 3D airfoils, the benefit of the second stage can not compensate the losses of the first stage. Table 1.1 shows how the present thesis extends the previous investigations.

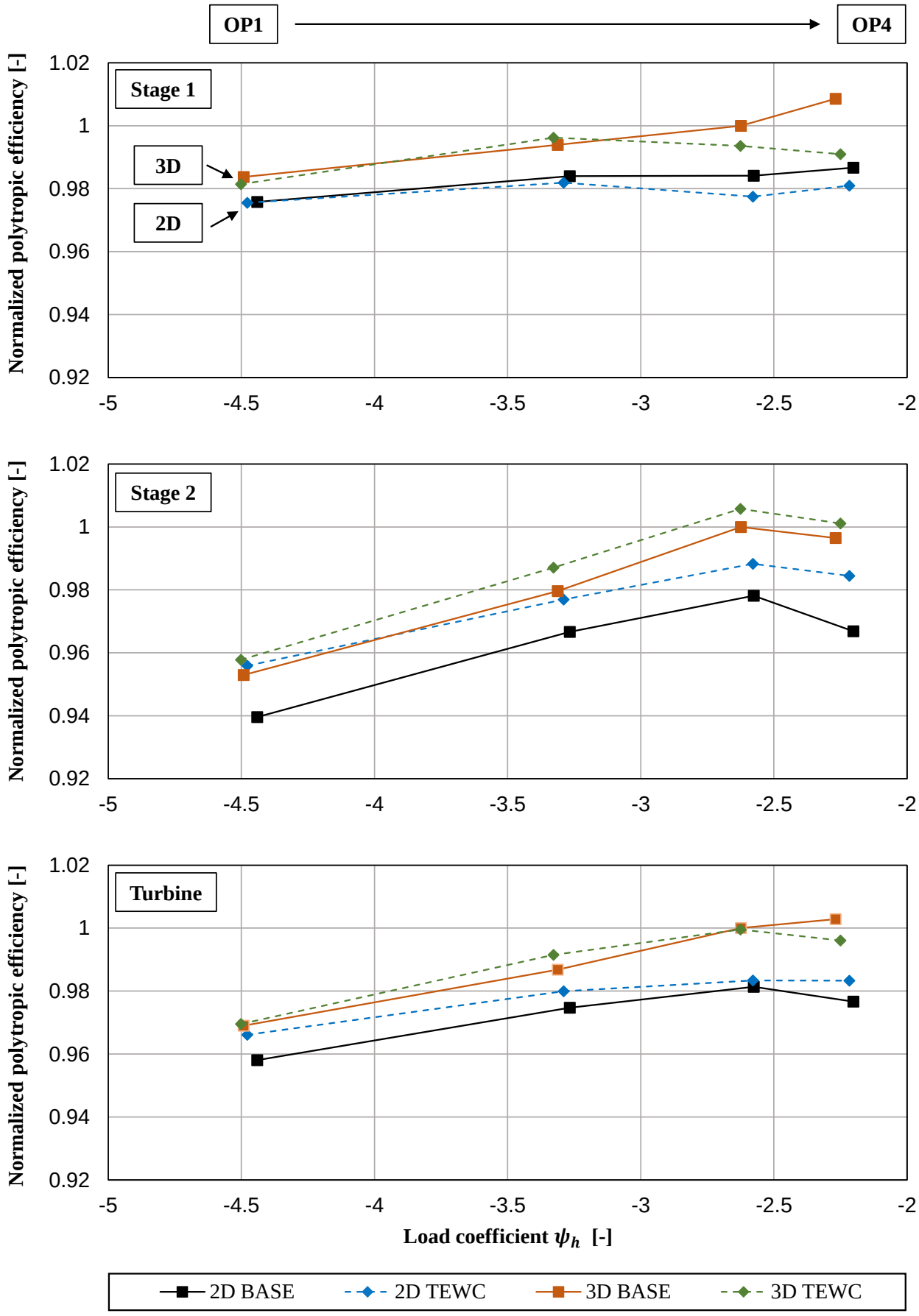

Figure 1.4: Normalized efficiencies of 2D BASE BS, 2D TEWC BS, 3D BASE BS and 3D TEWC BS configuration [163]

Table 1.1: Overview of the investigations by Schwab [125] and Zimmermann [161] [163])

	2D LS	2D BS	3D BS	3D LS
BASE	Schwab [125]	Zimmermann [161]	Zimmermann [163]	Present thesis
TEWC				
TEWC-V				

1.1 Structure of the thesis

In Chapter 2, the physical fundamentals of secondary flow are outlined. Furthermore, the state of the art of manipulation of the secondary flow is shown. For this purpose, advanced 3D airfoil design features, tangential endwall contouring, leakage flow interaction and sealing technologies are explained in detail on the basis of a literature review.

The experimental facility including its measurement technology is described in Chapter 3. There, the test conditions of the turbine as well as its constructive design are shown. The measurement equipment such as a pressure distribution vane, pressure probes and temperature probes are introduced.

The methodology to post process the measured data is explained in Chapter 4 with focus on the derivation of leakage flow, mechanical power measurement and the calculation of efficiency. Two "averaging methods" according to Traupel [142] and Kreitmeier [83] were applied and compared for the present test case. The results were analysed by uncertainty analysis that also contains a theoretical approach according to GUM [73] and an analysis of two redundant measurements conducted before and after all measurement campaigns.

Finally, the performance of the turbine including its operating point stability is outlined in Chapter 5. These findings will then be analyzed more deeply by means of a detailed flow analysis in Chapter 6.

2 Physical fundamentals and state of the art

This chapter is intended to give an overview of relevant research conducted over the past decades. The focus lies on the investigation of TEWC as well as the flow phenomena that are caused by secondary flow. In general, the physical effects of secondary flow in turbo machinery is well understood. However, the definition of secondary flow or vortex phenomena is not standardized. Section 2.1 serves to define the basic terminology of secondary flow briefly, because the discussion of the present investigation is highly related to these effects. Section 2.2 shortly describes the technical methods that are utilized to manipulate the secondary flow. Additionally, the effects of leakage flow interaction and sealing methods are shown in Section 2.3 and 2.4 respectively, to put the present research in the latest context of state of the art.

2.1 Secondary flow

In general, all kinds of flow phenomena that deviate from the main flow are referred to as "secondary flow". Secondary flow is characterized by low kinetic energy and a more complex, three dimensional fluid motion that participates in the energy conversion only to a limited extend. An almost "two dimensional" secondary flow characteristic can be observed for the main flow of a turbine. However, the flow is dominated by more complex flow structures in the peripheral zones. Such additional complexity in flow structure is caused by the interaction of several effects. For example the radius of the leading edge has a major impact on the flow [62]. According to Denton, secondary flow losses contribute up to 30% of the total losses of a profile [25].

Optimization of the flow behaviour is a current goal of turbine development. It is pursued to minimize the amount of secondary flow, which has a negative impact on the efficiency of turbo machines. Several opinions concerning the fraction of secondary losses compared to the overall loss can be found in literature (e.g. [52], [60] or [151]). Gregory-Smith et al. [52] stated, that up to 40% of total losses are caused by secondary flow. It is therefore, of paramount importance to understand the physical characteristics of secondary flows to realize a targeted exertion of influences by applying new technical features in turbo machinery. The most important "secondary flow effects" are shown in Figure 2.1, where several vortex distributions are shown that are briefly explained.

A closer look on the main flow reveals that the centrifugal forces are caused by flow deflection in the passage and that they are equalized by the pressure gradient that is present between suction side (SS) and pressure side (PS) of the airfoils and across the span between hub to the shroud. The fluid is decelerated close to the wall or airfoil due to "no slip conditions" at the very surface. In turbo machines, the flow velocity is constantly increased in the radial direction until it reaches the velocity of the main flow. This area of flow is known as boundary layer flow [135]. Here, flow angles and

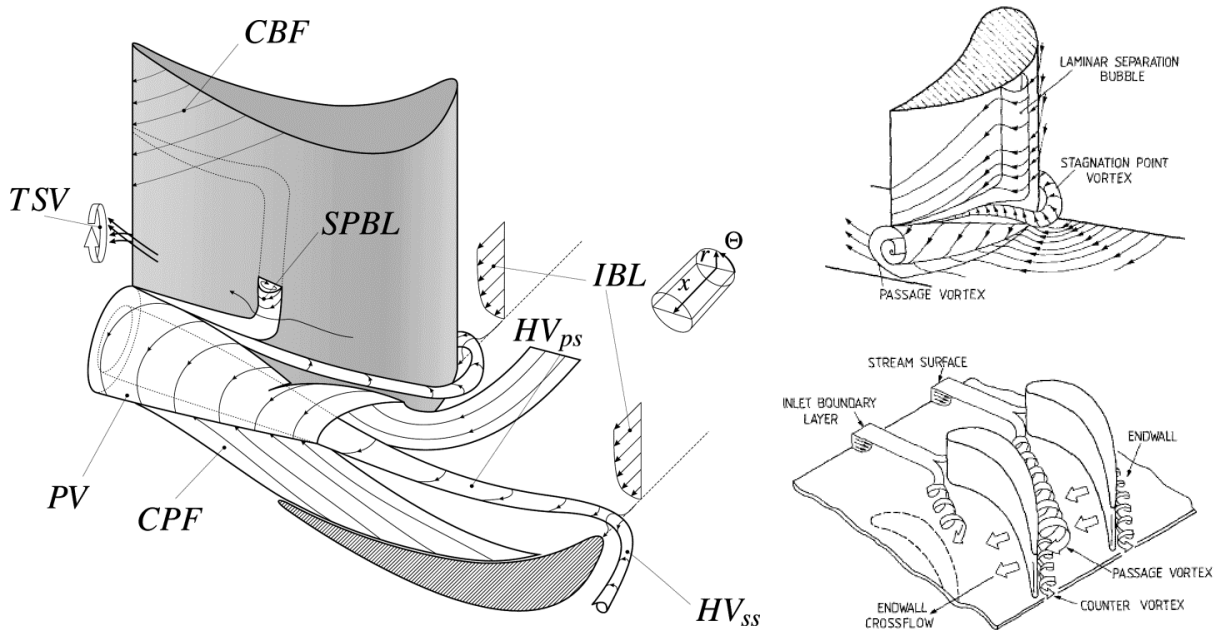

Figure 2.1: Secondary flow models of a stator vane [79], [86] and [111]

velocities are invariant to radial position. This causes warping of the inlet boundary layer (IBL) at the endwall and airfoil surface that induce the cross-passage flow (CPF) and the cross-blade flow (CBF). The constant pressure force within main flow and boundary layer, and the demand of continuity cause the cross-blade flow (CBF) to twist [141]. As a result, a closed vortex is propagating further downstream that deflects the flow to the pressure side (PS) close to the wall. The flow that passes the return flow area of this vortex is deflected towards the suction side (SS). This passage vortex (PV) starts within the blade passage between the leading edge and the first third of the axial chord length [99] and remains downstream the blade row [86].

The leading edge of the airfoil separates the flow to pressure side (PS) and suction side (SS) due to accumulation of the inflow boundary layer at the stagnation point [131]. The so called horse-shoe vortex (HV) develops also because of the lower kinetic energy of the boundary layer and the surrounding pressure field that is embossed by the main flow [32]. It consists of two branches which propagate along the suction side (SS) (HV_{SS}) and the pressure side (HV_{PS}). The HV_{PS} has a greater influence on the channel flow because it is shifted towards the channel center due to the pressure gradient between suction side (SS) and pressure side (PS) [87]. The direction of rotation is identical for the pressure sided horse shoe vortex (HV_{PS}) and the passage vortex (PV). Thus, both vortices merge further downstream in many cases [132]. Typically a new boundary layer is formed downwards of a separation line located on the wall [100]. The HV_{SS} propagates close to the SS and is lifted by the counter rotating passage vortex (PV) towards the channel centre [78]. The intensity of the horse shoe vortex (HV) is mainly influenced by the radial pressure gradient along the trailing edge and the pressure distribution upstream the airfoil [16]. Sauer et al.[120] have shown that the HV can be influ-

enced by modifications of the leading edge. The HV_{SS} has been intensified leading to a reduction of approximately 50% of the endwall losses.

The corner vortex (CV) (or counter vortex as named by Langston [86] in Figure 2.1) is induced by the passage vortex (PV) and emerges due to local separation that results from the sharp geometry between endwall and airfoil e.g. at the root [74]. Flow is accumulated in the corner and set in motion by the passage vortex (PV) with a contrary sense of rotation, while propagating downstream [49]. In theory the corner vortex (CV) appears on pressure side (PS) and suction side (SS). However, its presence is more likely on the suction side (SS) because of the passage vortex (PV) that moves towards the suction side (SS) on its way through the blade passage [1]. According to Wang et al. [151] this kind of vortex may not be seen for airfoils with fillet radii on the hub and tip side. Therefore, it can be expected that its influence is negligible for the present investigation, as all airfoils are manufactured with a certain rounded corner at their roots.

Another kind of vortex, which is induced at the trailing edge of an airfoil, was described by Hawthorne et al. [61]. At the trailing edge, the fluid transport towards the suction side (SS) induced by the passage vortex (PV) causes a back flow due to mass continuity from the channel centre towards hub and tip respectively. This flow interacts with the PV and generates a shear layer close to the trailing edge [65]. Then, a pair trailing shed vortices (TSV) emerge on hub and tip side, that are counter rotating to the passage vortex (PV) and that can be identified in the area of the wake close to the boundary layer [114].

Schlienger et al. [121] made investigations with a 2-stage axial turbine test rig and stated, that transient secondary flows in the "inter-stage" are mainly controlled by the hub passage vortex and the shed secondary flow field that occur due to the upstream stator vane row. These findings are supported by the investigations here shown (see Section 6).

More detailed explanations of the physical formation mechanism of these flow effects, especially for subsonic axial turbines, are given e.g. by Zebner [159] or Restemeier [116].

2.2 Targeted manipulation of the secondary flow

According to Havakechian et al. [60], the secondary loss generation in a turbine is primarily influenced by several design parameters of an airfoil. The aspect ratio (AR) that describes the ratio of blade height to blade length influences the secondary flow massively. An increase in aspect ratio (AR) also leads to an increase in profile losses due to the lager airfoil surface. However, the impact of secondary losses and endwall losses are reduced. Also, the pitch-chord ratio is of high relevance as the kinetic energy of the secondary flow varies quadratically with a change of the blade pitch while the

blade length is constant. Furthermore, the relative flow turning, the ratio of relative velocities, the blade loading parameter, the inlet boundary layer (IBL), the boundary layer at the trailing edge, the Reynolds number, the Mach number or the leakage flow interaction (LI) have an influence on the secondary flow. Figure 2.2 summarizes the aerodynamic losses of a turbine as a fraction of leakage losses (ζ_{Leak}), caused by secondary flow (ζ_{Sec}), and profile losses (ζ_{Prof}). A distinction between low pressure (LP), intermediate pressure (IP) and high pressure (HP) turbines is made depending on the aspect ratio (AR).

In addition, advanced 3D design features can be applied to the airfoil. Both, an inclined design (*lean*) and a curved design (bow) showed the potential to improve the flow near the endwalls. It is also advantageous to sweep the airfoil shape in axial direction [50].

Furthermore, meridional (MEWC) and tangential endwall contouring (TEWC) can be applied to the hub and / or tip regions of the blade to influence the aerodynamic performance. For MEWC the flow channel is e.g. constrained in axial direction and several design approaches have been investigated by Dejc et al. [24], Morris et al. [97], Boletis et al. [15], Kopper et al. [81] or Haas et al. [55]. All investigations showed a reduction of the overall losses.

Due to the beneficial potential, the MEWC has been evolved into a TEWC. Here, the contouring

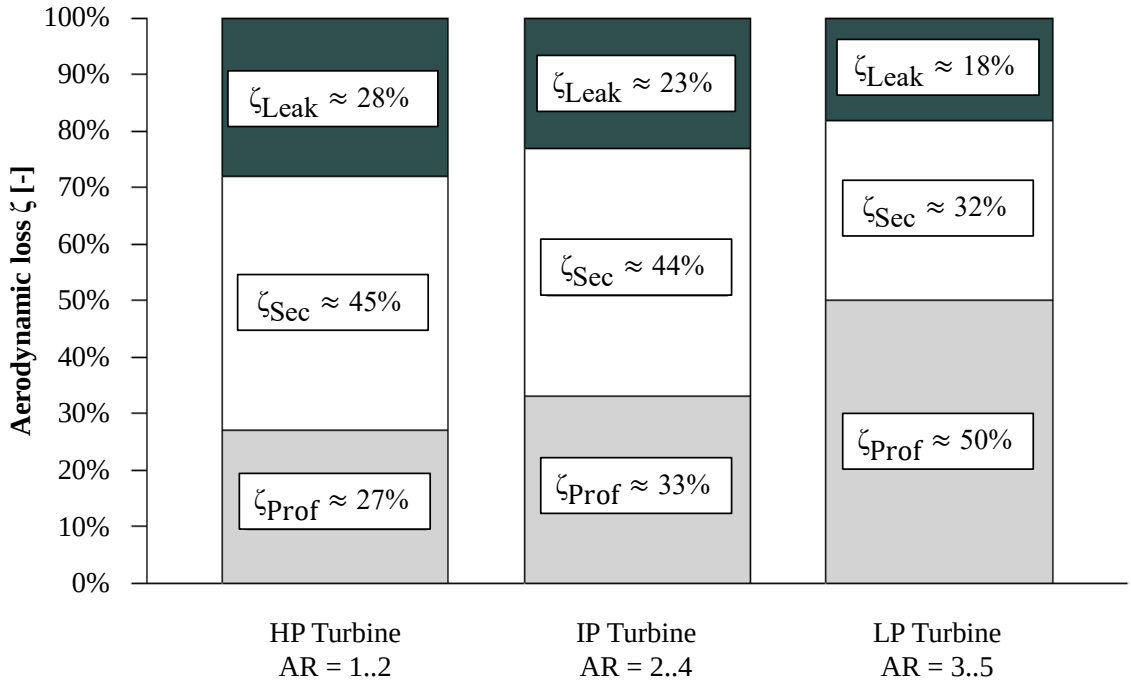

Figure 2.2: Origin and importance of aerodynamic losses in reaction stages by Havakechian et al. [60] from Beer [9].

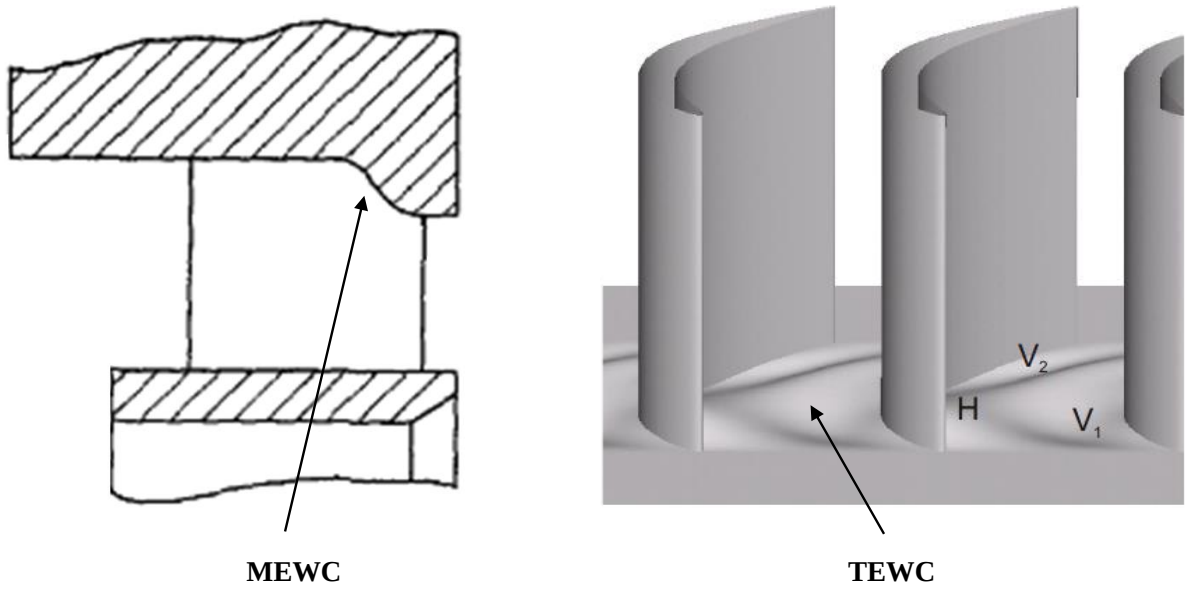

Figure 2.3: Schematic of MEWC and TEWC according to Povinelli [112] and Knezevici et al. [80]

.

follows the curvature of the airfoils so the contouring is additionally applied in circumferential direction [97]. A detailed description of earlier investigations is given in Section 2.2.2. Figure 2.3 shows an example of both types of contouring.

The investigations presented in this thesis are dedicated to only a limited number of the design features explained above. 3D airfoils with *bow* design are investigated in BASE, TEWC and also a combined TEWC-V configuration. By changing the sealing configuration from a groove ridge labyrinth seal (LS) to a combined labyrinth - brush seal (BS) it is evaluated how the leakage flow effects the TEWC performance. Here, the first case represents an influenced flow field with a leakage flow (LF) of 10‰ of the main mass flow (MF), while a nearly undisturbed MF is realized with the brush seals (BS), which had leakages of only 1‰ during the tests.

In the following sections the scientific development of advanced 3D design features, TEWC and a brief explanation of leakage flow interaction and counteracting sealing technologies will be discussed.

2.2.1 Advanced 3D airfoil design features

As described in the introduction of this section, a three dimensional airfoil design has the potential to improve the flow pattern. A distinction is made between *lean* and *bow* (the letter is also known as *compound-lean*) airfoils that can be designed as a positive or a negative type (Figure 2.4). Positive *lean* is inclined towards the pressure side (PS) and negative *lean* inclined in direction of the suction side (SS), respectively. This design was introduced by Dejc et al. in 1962 [24]. In case of *bow* airfoils a convex pressure side (PS) represents the positive type and vice versa.

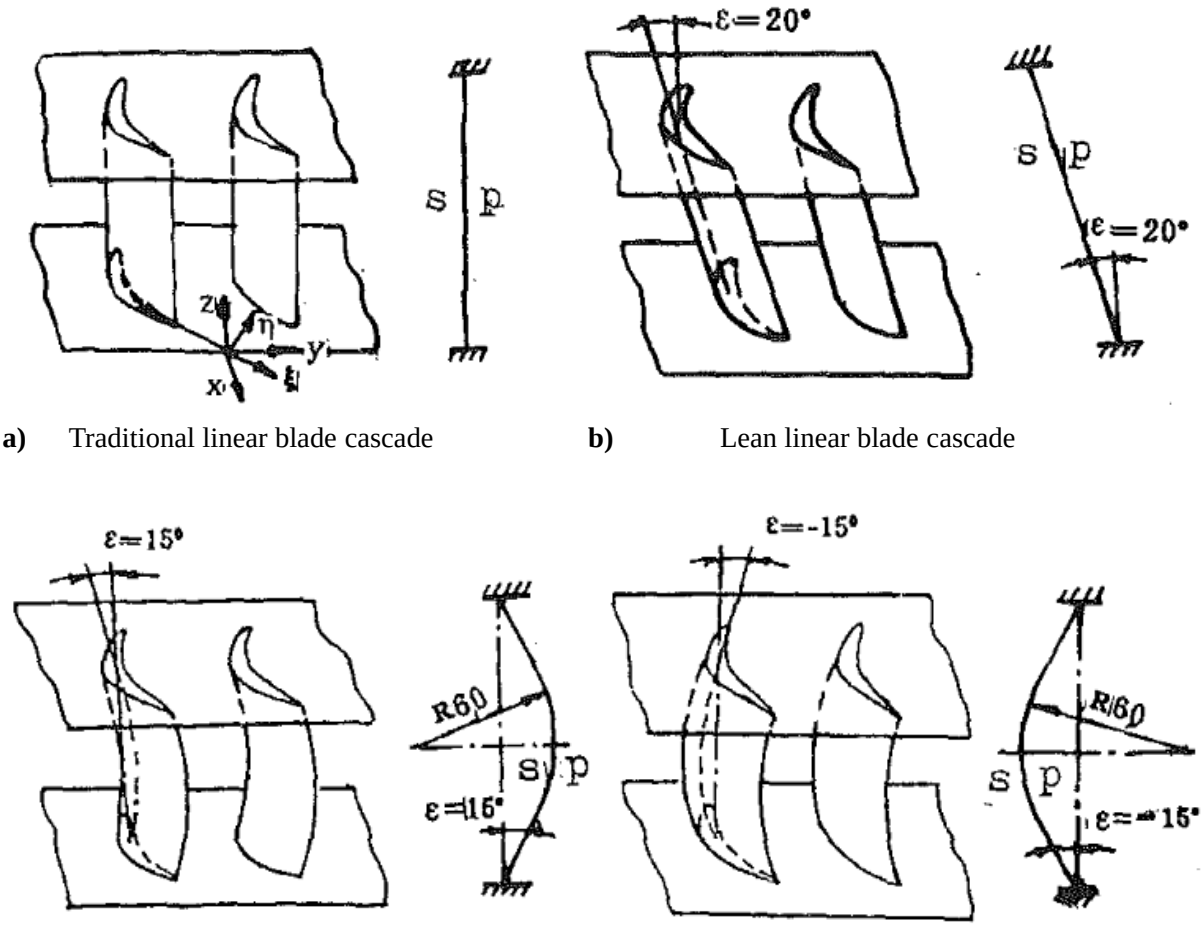

a) Traditional linear blade cascade **b)** Lean linear blade cascade

c) Positively curved blade cascade **d)** Negatively curved blade cascade

Figure 2.4: Schematic of 3D shaped airfoils according to Wanjin et al. [153]

Hormouziadis et al. [67] categorized the influence of *lean* to the flow. They stated that *lean* is a probate method to control the following features:

- Level of reaction
- Radial loading distribution
- Secondary flow
- Related effects of secondary flow downstream the blade row

Denton and Xu [27] give an explanation how changes of the pressure field influence the streamline curvature within the flow channel in the axial direction for a non twisted blade (see Figure 2.5).

Investigations by Harrison [56] conducted in a turbine cascade with un-leaned, straight-leaned and compound-leaned airfoil configurations led to the identifcation of five potential influences on the loss generation in a turbine cascade due to *lean* or *bow*:

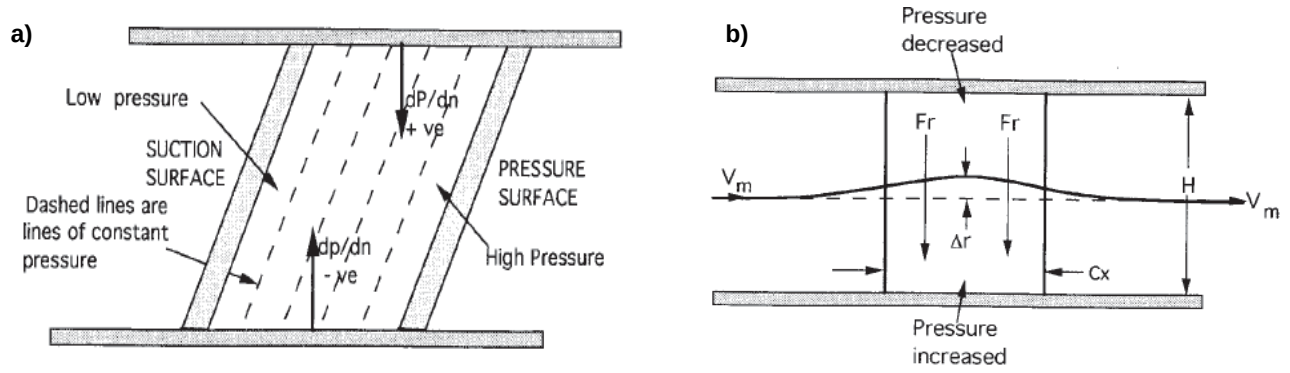

Figure 2.5: a) Pressure distribution in a hypothetical leaned blade row with no spanwise variation in flow b) Effect of blade *lean* on streamline curvature [27]

- Flow velocities
- Blade surface boundary layer transition
- Endwall boundary layer transition
- Mixing losses
- Other effects

A significant change of the static pressure especially in the mid chord area, was demonstrated for a positive *lean* configuration by Denton and Xu [27]. This effect mainly influences the pattern and size of the inlet boundary layer (IBL) that is accelerated and becomes thinner at the low pressure endwall. On the contrary the inlet boundary layer (IBL) is thickened on the high pressure endwall while it is decelerated. This leads to the positive effect of loss reduction on one endwall side due to lower velocities. However, the performance is decreased at the opposite endwall. The investigations displayed that *lean* design can increase the loss coefficient slightly. No overall effects were observed by application of *compound-lean*. However, the flow turning is increased, and downstream mixing losses as well as spanwise variation of the mean flow angle are reduced. This can enhance the efficiency of a turbine in a multi row environment.

Further investigations of *lean* and *bow* airfoils by Walker et al. [148], Grant et al.[51], Wanjin et al. [153], Wang et al. [152], Pioske et al. [110], Jansen et al. [75] or Duden et al. [34] support the findings explained above and are summarized in detail e.g. by Beer [9]

2.2.2 Tangential endwall contouring

TEWC is applied to influence the local static pressure and with that the oblige pressure gradient and velocity field within the blade passage. This is realized by a intentional constriction or expansion of the local flow area. Also the driving forces of the secondary flow phenomena are effected with the

purpose to change the load distribution and hence the efficiency. In the past decades, several design proposals for TEWC have been investigated and published.

Bischoff [13] showed the first non-axisymmetric contour design in 1983. Later investigations by Atkins et al. [5], Hartland et al. [57] and Harvey et al. [59] could confirm the assumption that TEWC has the potential to increase the efficiency of turbo machines. Those investigations were conducted in a linear cascade rig. The TEWC, studied in [5], [57] and [59], has a ridge in the area near the trailing edge close to the suction side (SS). On the contrary, the flow channel is contracted on the pressure side (PS). Gregory-Smith et al. [52] proceeded the investigations ([5], [57] and [59]) by omitting the ridge close to suction side (SS) and by constraining the TEWC to the area within the blade passage. Further investigations by Ingram et al. [71] with equivalent TEWC designs and improved measuring technology showed higher loss reduction for TEWC design P2 by limiting TEWC to grid width in contrast to the investigations of Gregory-Smith et al. Finally Ingram et al. [72] endeavored to develop a design to show the limits of loss reduction by means of TEWC (P3). Despite a massive reduction of secondary kinetic energy (SKE-43%) the authors found an increase of secondary losses downstream the blade row. This contradicts previous findings that the reduction of secondary losses is associated with lower SKE. The authors suspect that fluid separation caused by the frim shape of the TEWC is responsible for this effect. Praisner [113] and Knezevici [80] studied different airfoil and TEWC designs in an experimental cascade and could confirm that TEWC is an effective method to decrease secondary losses.

On the basis of investigations performed in linear cascades (references [5], [52], [57], [58], [71] and [72]), Brennan et al. [16] investigated TEWC on rotor and casing in a one stage aircraft engine rig. They found an increase in efficiency of about 0.24% points. Rose et al. [118] studied another TEWC design on the same test rig at different load coefficients and measured an increase in efficiency of $0.59\% \pm 0.25\%$ points. All further investigations support this tendency of superior performance of TEWC airfoil designs as compared to conventional airfoils [10], [35], [36], [46] and [134]. However, it is stated that TEWC shows more benefit on vanes than on blades.

Improved 3D airfoils combined with TEWC were studied by Bagshaw et al. [6], [7], [8] and by Gregory-Smith et al. [53] in a linear cascade rig. The authors found reduced losses across a large portion of the span and a reduction of total pressure loss by 16% (relative). Pöhler et al. [111] and Niewöhner et al. [101] researched different blading and TEWC designs on a 1.5 stage test turbine. They showed an overall efficiency increase of the turbine with TEWC. This investigation emphasizes that losses are increased within the stator row while the losses in the rotor passage are lower compared to a design without the TEWC. A detailed summary of the investigations published before 2008 is summarized by Schwab [125]. The following Table 2.1 is intended to continue the classification of research with focus on TEWC till 2016, however, it does not claim to be complete.

Table 2.1: Summary of experimental investigations on TEWC (based on Schwab [125] and updated till 2016)

Classification of the test rigs	Comments	Airfoil type	Publication
Linear Cascade	No leakage flow interaction No impact of blade division No rotor - stator interaction	2D	[2], [5], [24], [52], [57], [58], [59], [70], [71], [72], [80], [81], [97], [99], [113], [131], [138]
		3D	[6], [7], [8], [53], [54], [110]
Annular Cascade	No leakage flow interaction No rotor - stator interaction	2D	[15], [154]
		3D	[109]
Turbine	All effects are covered	2D	[42], [46], [55], [76], [96], [123], [124], [125], [126], [163]
		3D	[10], [16], [36], [35], [101], [111], [118], [133], [134], [163]

2.3 Leakage flow interaction

Another important field of research is dedicated to the impact on the efficiency caused by the leakage flow that enters the main annulus on casing or tip side. On the one hand, leakages across shrouded airfoils re-enter the flow channel downstream as shown in Figure 2.6 a). On the other hand, purge flows that are used to cool hot materials in gas turbines, are guided into the main flow, which is depicted in Figure 2.6 b).

Early investigations by Denton et al. [26] in 1976 provided two dimensional experimental data gathered in a shrouded steam turbine. On this basis further investigations were performed to expand the knowledge of the connection between the cavity leakage flow and the main flow in turbines. The investigations by Pfau et al. [105] that were conducted in an annular cascade turned out that leakage flow (LF) has an influence on the main mass flow (MF) exit angle.

The same effect was surveyed by Peters et al. [104] and Anker et al. [4] in a 1.5-stage low speed axial turbine. They stated that the small turning of the flow within the cavity causes a lack of velocity of the re-entering leakage flow (LF) compared to the main mass flow (MF). This leads to a suction sided incidence of the stator downstream. The measured amount of additional losses was in good agreement to the correlation shown by Korschunov et al. [82] that was derived by experiments in a linear cascade, however, there were differences in the increase of losses with a growing clearance. A numerical study in 2011 by Biester et al. [12] utilizing RANS simulations supported these experiments.

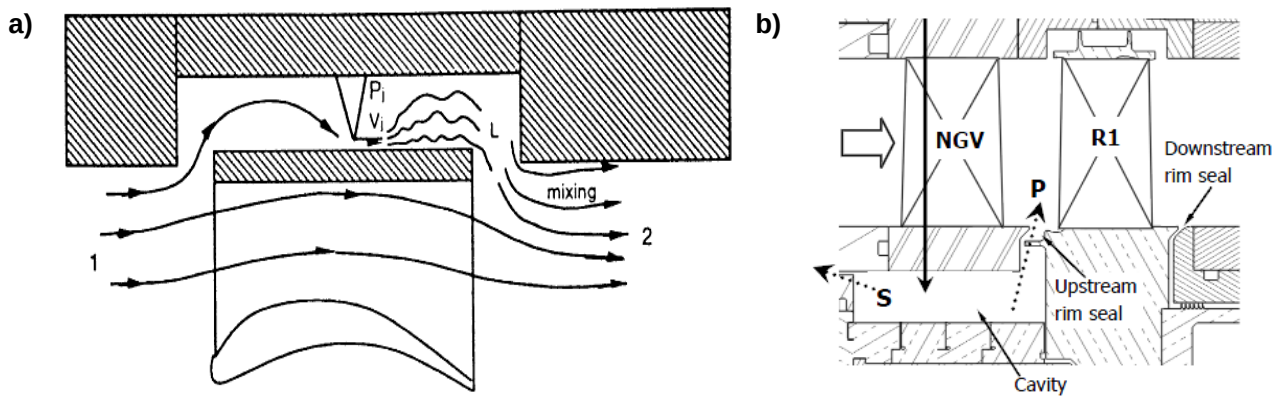

Figure 2.6: a) Flow across a shrouded rotor tip seal [108] b) Purge flow (P) on hub side entering the main channel through the rim seal [76]

Experimental and accompanying numerical investigations by Hunter et al. [68], [69] were conducted on a 2-stage turbine rig. They showed that the low momentum fluid generated in stator one on the hub side emerges downstream with the secondary flow of rotor 1 to 7.5% span at the rotor 1 trailing edge. The associated total pressure deficit and radial variation in circumferential flow angle causes the formation of two additional vortices in the stator 2 passage. The two extra vortices are of sufficient strength to confine the classical secondary flow vortex to the suction side corner in stator 2. Later, Pfau et al. [106], [107] substantiated similar effects on a different 2-stage turbine test rig.

A more detailed distinction of the losses connected with the cavity flow is proposed by Wallis et al. [150]. They identified the cavity entry, the clearance gap, the mixing with the main mass flow (MF) and the incidence on the following row as individual contributors to cavity flow induced loss. The authors attempted to decrease the losses caused by the mixing losses by means of different turning device designs. Their purpose is to increase the deflection of the leakage flow (LF) before it re-enters the main flow channel. Wallis et al. [150] succeeded to manipulate the tangential velocity of the leakage flow (LF). However, the overall performance decreased compared to the reference configuration without turning devices. Gier et al. [47] confirmed the findings of Wallis et al. [150] and estimated the amount of losses due to leakage flow (LF) re-entry to 60% of the overall leakage flow (LF) losses. Mahle et al. [92] developed a device that is located at the exit of the cavity. It is used to turn and accelerate the leakage flow (LF) before re-entering the main flow channel. By this means the authors showed a reduction of mixing losses of about 63% resulting in an overall efficiency enhancement of 0.1% for the 3-stage low pressure turbine investigated.

Even if purge flow is not a relevant topic for the discussion of leakage flow interaction (LI) in steam turbines, a brief summary of the current state is given below as investigations were carried out that consider TEWC downstream the rim seal. Therefore, these findings may support the discussion in Chapter 5.

McLean et al. [94], [95] and Girgis et al. [48] investigated the effects of cooling flows on the main flow ($LF = 1\%MF$) in high pressure gas turbines. They stated that the injected flow causes losses in efficiency of up to 2%. They also found a significant change in pressure coefficient, wake width, three-dimensional velocity field, and exit angles, and therefore suggested to consider LF-effects during the blading design process. The investigations of Lynch et al. [91] revealed that TEWC with a platform gap shows a 12% higher "mixed out loss" compared to a configuration without gap.

Schübpach et al. [124] performed experimental and numerical investigations that were dedicated to the leakage flow (LF) impact on the TEWC performance. Two TEWC and one baseline design were compared. The authors found a decreased efficiency of 0.6% for the baseline case and down to 1.2% for the TEWC design due to changes of the pressure distribution in front of the blade row. Jenny et al. [76] used the same 1.5-staged axial turbine to investigate one TEWC design. They focussed on different injection levels (0.4%, 0.8% and 1.2% of main mass flow (MF)) and made the statement that the static pressure increases by 1% per percent of injection flow in the hub region of the rotor inlet. For the highest injection rate of 1.2%, an incidence change of up to $-9°$, was measured that lead to separation as shown by Yamamoto et al. [158] or Hodson et al. [63].

2.4 Sealing technology

The amount of leakage flow (LF) and the resulting leakage flow interaction (LI) in turbines is mainly caused by the sealing of the rotating parts against the rigid counterpart. For steam turbines, shrouded airfoils sealed by means of LS are state of the art. (In addition, the rotor is sealed against the ambient pressure with brush seals that are capable to realize high pressure drops across a smaller axial distance compared to LS.)

It is the goal of the present investigation to analyse the impact of tip leakage flows to the TEWC performance. By implementation of a BS above the shroud the leakage flow (LF) could be reduced by 89% down to 1‰ main mass flow (MF) compared to the LS configuration. Therefore, this section gives an overview of these two sealing technologies. Detailed information about the mass flow calculation through both kinds of sealing approaches is given in Section 4.1 in connection with the leakage flow (LF) determination for the present test case.

2.4.1 Labyrinth seals

Labyrinth seals (LS) are commonly used if gaps between moving and fixed parts have to be sealed without contact. They are well suited to meet applications with high rotational speed and temperature due to their robust design. In addition, a constant sealing performance can be guaranteed for a long operation period. The reduction of the leakage flow is realized by increasing the flow resistance. A labyrinth seal (LS) consists of several seal tips, which are only located at the casing or tip side

(straight through labyrinth seal (STLS)), or on both sides (full labyrinth seal (FLS)). Another type, the so called groove ridge labyrinth seal (GRLS), is used in the present test rig and is shown on the right hand side of Figure 2.7. The mountability of STLS is simple, however, the sealing performance is about 40% lower compared to FLS with similar axial length. 50 - 70% of the sealing effectivity of the FLS can be achieved with GRLS [23].

A minimal gap of 1-2% of hub diameter has to be realized to avoid contact during start up or while passing the critical bending speed of the rotor. Concurrently, the gap has to be minimized to optimize the sealing performance. Matthias [93] discussed the vortex phenomena within the cavities extensively. The more tips that are connected in series, the better the sealing [140].

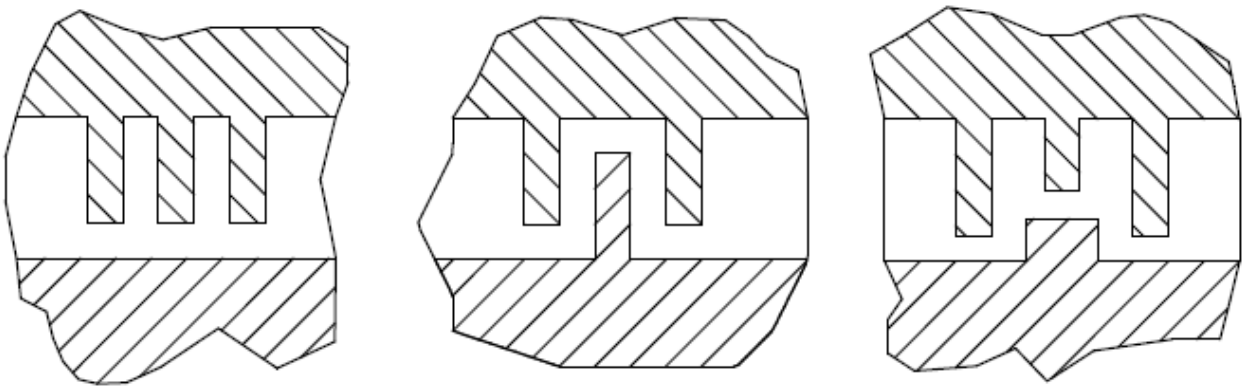

Figure 2.7: a) Straight through labyrinth seal b) Full labyrinth seal c) Groove ridge labyrinth seal [20]

2.4.2 Brush seals

Brush seals (BS) were initially developed for the aviation industry, improved and implemented in stationary steam turbines in 2000 for the first time (see Pastrana et al. [103]). During the last few years several labyrinth seals (LS) in power plants have been replaced by brush seals (BS) as part of retrofit measures. According to Schwarz [128], combinations of labyrinth seals (LS) and brush seals (BS) are the most effective design and are installed in new plants. Sealing of the rotor against the environment is the main application area of brush seals (BS), however, shrouded blades are sealed with this technology too. Figure 2.8 illustrates the main components of a common BS design in lateral and plane view.

In general brush seals (BS) can be characterized by two different designs. One design contains a backing plate the brush and a front plate; all components are tightened together with a surrounding weld seam. The second design consists of a brush package that is clamped between a back and front

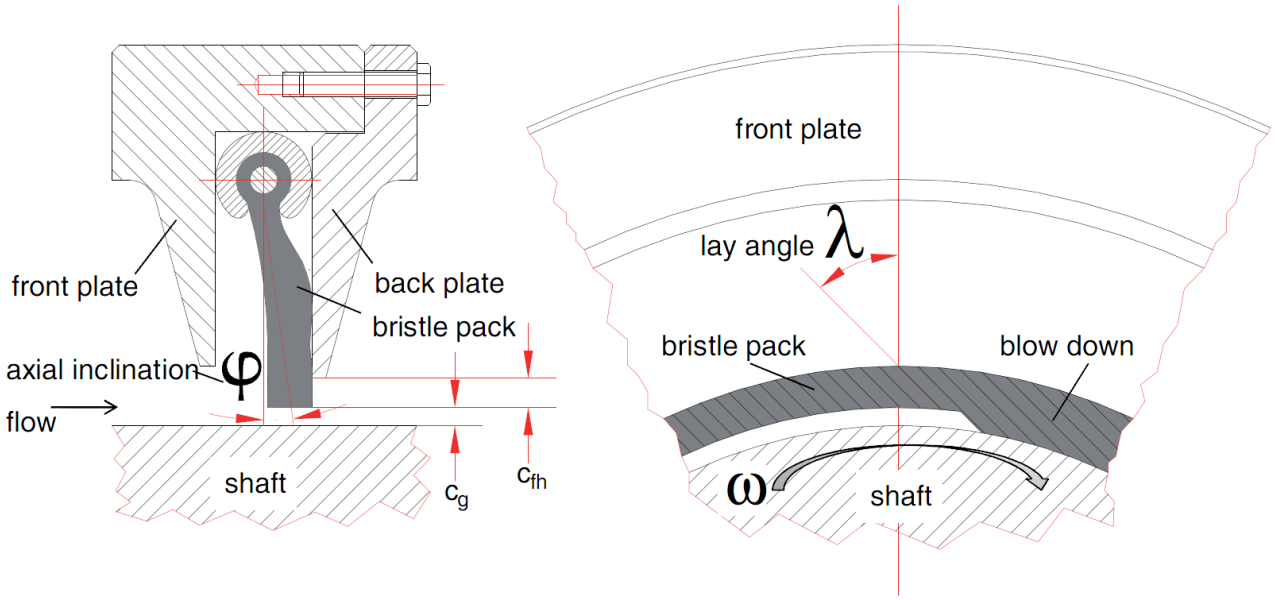

Figure 2.8: Illustration of brush seal parameters and geometries (Schwarz [128])

plate (as shown in Figure 2.8). A 25% reduction in installation height, a reduced weight and simplified mounting compared to the design with backing plate distinguishes this design. In addition, non metallic materials can be used as bristles (see Gail et al. [45]). Brush seals (BS) can be mounted with a gap or overlapping to the rotor. However, wear has to be taken into account in this case.

The flow within the brush seals (BS) is quite complex and several design parameters such as axial inclination, lay angle, bristle diameter or the thickness of the bristle pack have to be taken into account to implement an appropriate seal. A detailed discussion is provided by Schwarz et al. [127],[128]. The brush seal (BS) technology is not further elaborated on in this thesis because the brush seals (BS) are used as a method to reduce leakage flow interaction (LI) rather than being a part of the current investigation.

2.5 Scope of the present work

Various fields of research in turbo machinery have been introduced in this chapter. It has been shown that losses can be reduced by several design approaches such as the airfoil design, endwall contoured hub or tip areas, or reduced leakage flows. All of these methods showed a positive impact if they were applied separately. In addition it has been shown that 3D airfoils in combination with TEWC has the potential to enhance the efficiency in turbo machines. Furthermore, all three aspects have been investigated for aircraft engines by taking hub sided purge flows into consideration. Here, it has been stated that the efficiency of a formerly superior TEWC configuration drops below the performance of a baseline design when leakage flow comes into play.

The investigations of the airfoils and TEWC designs subject of this thesis also support the above outlined findings that TEWC has the potential to increase the efficiency in turbo machinery. Especially the positive impact on the second stage is highly promising, assuming that it also occurs on all subsequent stages in turbines with a higher number of blade rows.

On basis of these insights, the present thesis is dedicated to transmit the previous findings to the effect of a casing sided leakage flow (LF) in combination with 3D endwall contoured airfoils. It will be shown that the positive impact of TEWC vanishes for 3D airfoils if a certain ratio of leakage flow to main flow is exceeded. These new insights are used to answer the question of if a retrofit measure of an existing turbine by means of TEWC is potentially beneficial.

Furthermore, it is investigated in detail how the endwall contouring influences the flow within each airfoil row. By combining contoured vanes with baseline blades (TEWC-V) in both stages it is shown where the effects of the TEWC take place.

3 Experimental facility

A detailed overview of the test rig is presented in this chapter. The details of the supply infrastructure and the turbine with its measurement properties are explained in Section 3.1 and Section 3.2. Also, the probe measurement technology is described in more detail in Section 3.3 as it is of high importance for the flow field analysis. Furthermore, due to changes compared to the previous investigations by Schwab [126], the measurement procedure as it was conducted for the present test cases is briefly explained.

3.1 Test bed

All experiments were conducted on a 2-stage air driven turbine that is equipped with shrouded high pressure steam turbine airfoils. A piping plan of the test rig and all auxilary devices is shown in Figure 3.1. The turbine is driven by air, which is supplied by two radial compressors. These compressors are operated in parallel to deliver the required mass flow. The system is designed as a closed loop to minimize environmental impact on the measurement. Three additional compressors pressurize the purge air system that is needed to avoid leakages through the rotor sealing. This ensures a constant and well known mass flow through the turbine which is of high importance for the determination of the turbine efficiency.

The design turbine inlet temperature of $90°C$ can be adjusted within a tolerance range of $\pm 0.5K$ by means of the aftercooler and a cooling bypass. A maximum air mass flow rate of 13.9kg/s enters the test turbine at an static inlet pressure of $3.2 \cdot 10^5$Pa that is adjustable with a tolerance of about 3‰. The turbine's static outlet pressure is about $2.31 \cdot 10^5$Pa, which is equivalent to a pressure ratio of 1.4 across the two stages. These conditions result in a Mach number of about 0.15 and a Reynolds number (Re_c) of approximately $2.5 \cdot 10^5$. The pressure ratio as well as the mass flow are adjusted with the bypass and the turbine outlet valve.

The metering orifice that is needed to determine the mass flow rate has been calibrated externally as described by Schwab [126]. The additional calibration was required because the run-in and run-out distance upstream, respectively downstream the orifice does not meet the requirements of standard DIN - EN ISO 5167 [30][31].

To ensure homogeneous inflow conditions of the turbine, a divergent duct with a length of 3m ($\widehat{=} 5D$) forms the connection between turbine inlet valve and the inlet of the rig. Here, the measurement of total pressure by means of a pitot tube serves as reference value for the flow field. A honeycomb structure is installed in front of the first stator row to ensure uniform flow conditions.

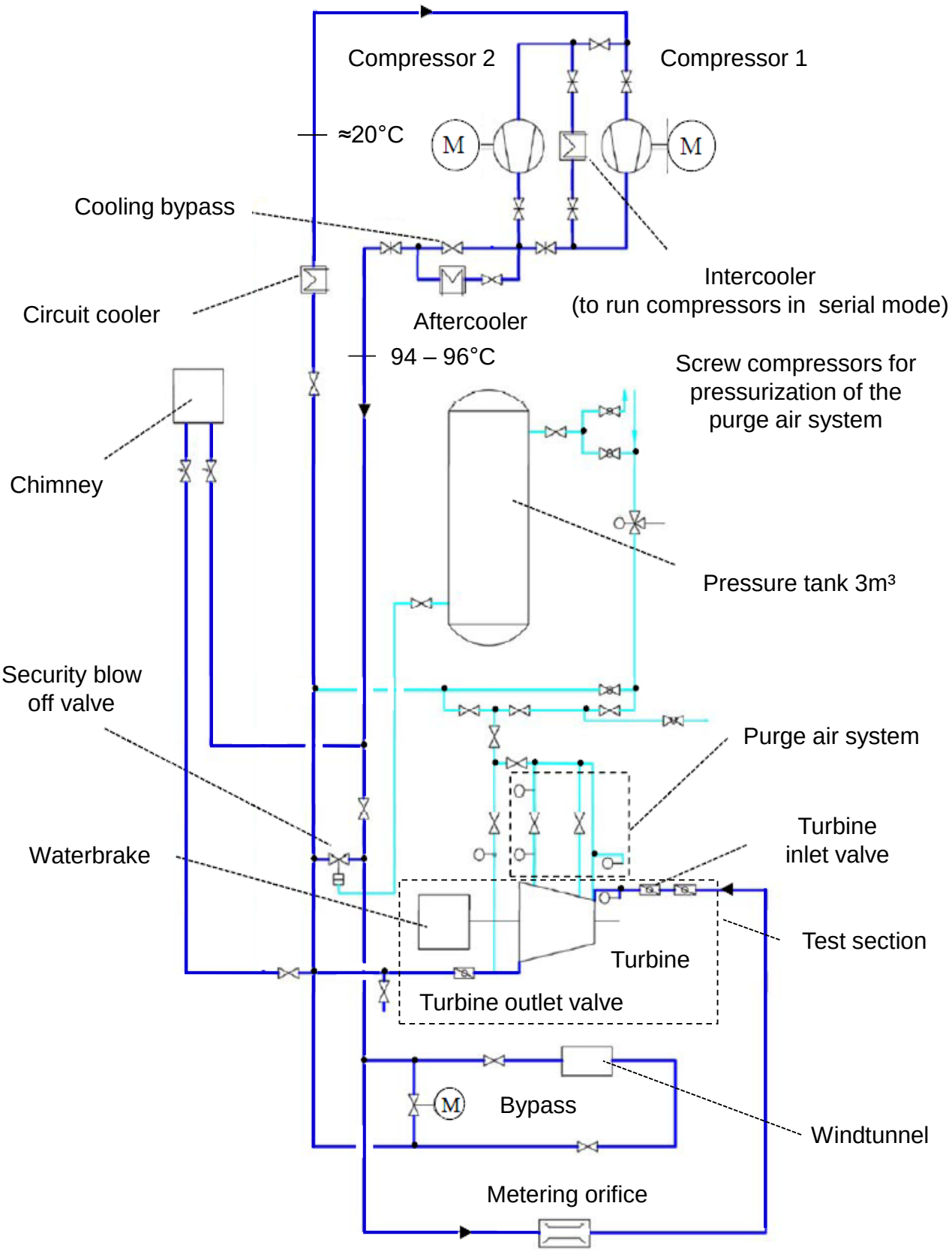

Figure 3.1: Piping diagram of the experimental facility to the standard DIN2481 [29][126]

Table 3.1 summarizes the specification of the turbine at its design point for the 3D baseline (without TEWC) configuration with brush seals (BS). The thermodynamic boundary conditions (T_{in}, p_{in} and p_{out}) are kept constant for all other operating points. Only rotational speed and therewith the load coefficient ψ_{h} is varied by means of the water brake and calculated with Equation 3.1.

$$\psi_{\mathrm{h}} = \frac{2 \cdot \Delta h}{u_{\mathrm{in}}^2 + u_{\mathrm{out}}^2} \tag{3.1}$$

The water break is mounted on a swing frame with hydrostatic bearings, which allows accurate measurement of the torque with a load cell that is connected to a lever. In OP1 the engine runs at the lowest speed ($\approx$ 3500RPM) while the highest speed is adjusted for OP4 ($\approx$ 5200RPM).

At the outlet of the turbine, the air stream has to be bent by $90°$ because of the presence of the water brake. This causes a non-symmetric flow in the circumferential direction. Swirl barriers are installed downstream of the last rotor to minimize the influence on the measurement behind the second stage. A more detailed description of the apparatus can be found in Schwab [125].

The equipped turbine is shown in Figure 3.2a. The two casing parts are screwed at the two split joints to allow a simplified accessibility to the internal parts that are designed as a modular structure. As one can see in Figure 3.2b, Sealing Ring 2 is located at a fixed position of the turbine casing. The vane carriers and Sealing Ring 1 are precisely braced against this component. This design approach ensures the same axial positioning of the airfoils after a reconstruction of the test rig and for all configurations respectively.

For the present test cases an axial distance of 0.73 axial blade length (l_{ax}) has been set between each blade row. The casing sided shroud is sealed by means of combined labyrinth seal and brush seal as well as with a pure GRLS as depicted in Figure 3.3. The hub side is sealed with GRLS, only, because BS cannot be mounted on rotating parts and the radial thickness of the stator shroud is not appropriate for the required groove.

Table 3.1: Specifications of the turbine design point of the 3D baseline configuration with BS

Parameter	Unit	Value
Inlet pressure	[Pa]	$3.2 \cdot 10^5$
Pressure ratio	[-]	1.4
Inlet temperature	[$°C$]	90
Ma number	[-]	0.15
Speed	[RPM]	4775
Mass flow	[kg/s]	12.82
Flow coefficient φ	[-]	0.5
Load coefficient ψ_{h}	[-]	2.62

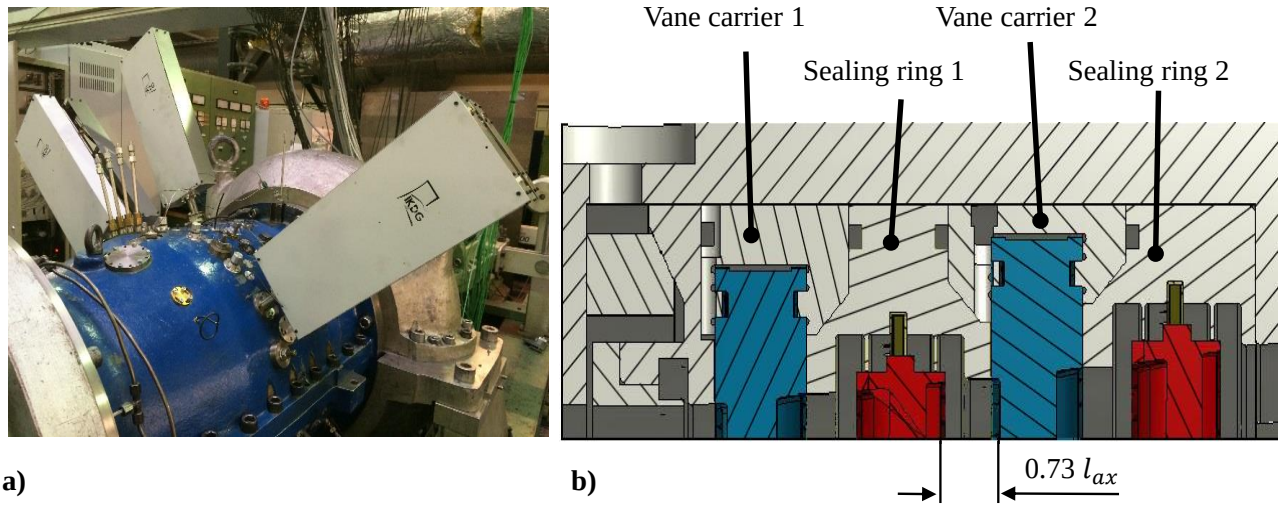

Figure 3.2: a) Test turbine equipped with probe adjusting devices b) Detailed view of the constructive assembly of vane carriers and sealing rings in example for the BS configuration

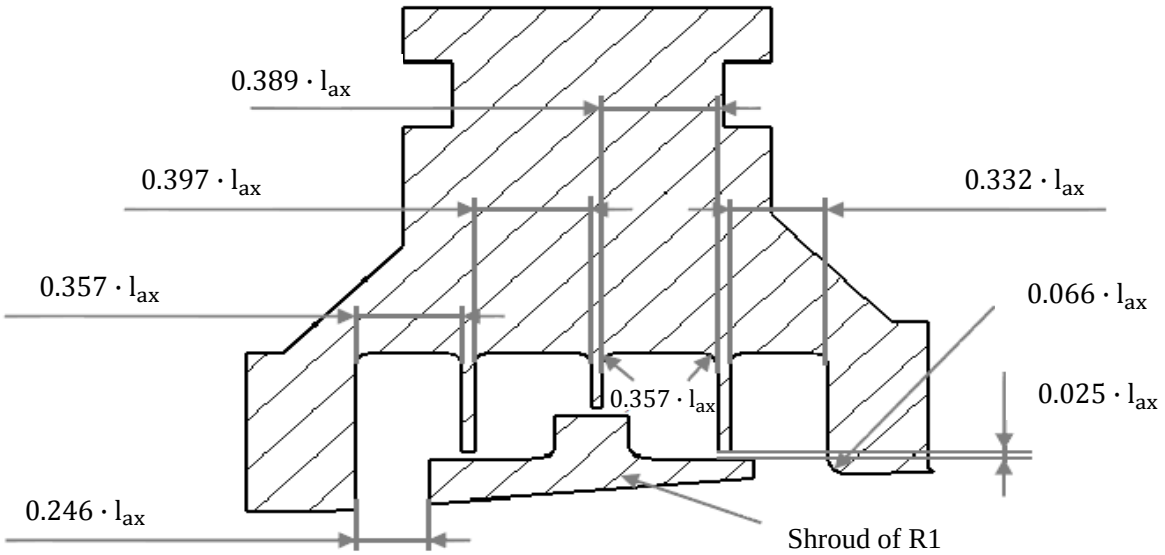

Figure 3.3: Geometry of the shroud cavity above the first rotor

The second set of investigations was conducted after replacement of the centred labyrinth tip with a brush seal (BS), as it is shown in Section 4.1. The bristles touch the rotor from the very beginning to ensure a closed clearance for all OP. Friction losses have to be accepted, however, it will be shown that the sealing benefit compensates for these losses. A special brush seal (BS) design of MTU is implemented due to the small building space within the sealing rings. In contrast to the described common designs, the bristle package is wrapped with a thin metal sheet that also builds the backing plate. The bristles are made of Haynes25® with a diameter of 0.07mm and a laying angle $\lambda = 45°$.

To change the sealing design from labyrinth seal (LS) to brush seal (BS), only the sealing rings have to be replaced. For both sealing designs, the dimensions within the cavities as well as the radial

clearance between the labyrinth fins is kept constant to ensure equivalent test conditions for the different airfoil types.

Furthermore, both vane carriers can be rotated in parallel by means of a lever mechanism to realize a pitch-wise stepless measurement of the flow field. Each airfoil type is mounted in its dedicated carrier to ensure that the circumferential position of the vanes does not change between two measurement campaigns. Therefore, only the carriers are changed if another airfoil configuration has to be investigated.

The airfoils and the TEWC were designed by Alstom Power (now General Electric). The depth of the TEWC varies in the axial direction and a 'sudden jump' has to be overcome by the flow that moves from pressure side (PS) to suction side (SS). Due to limited space within the shroud of the stator, the depth of the groove is smaller on the hub side compared to casing side. Here, the TEWC is applied on the airfoil root. The contouring design is limited to a groove design as it is required to be applied to an existing airfoil set during retrofit of a turbine. Figure 3.4 shows the characteristics of the TEWC that is investigated and illustrates its shape and position within the blade passage.

A compound lean design (3D) has been chosen as it was found to be the most efficient, as mentioned previously in Section 2.2.1. Table 3.2 shows the aspect ratio (AR) and the slenderness ratio (SR) of the airfoils in each row and stage. The aspect ratio (AR) is defined as blade height (h_b) referred to blade length (l_b) while the slenderness ratio (SR) represents the ratio of h_b and the mean diameter D_m of the airfoil row. Furthermore, the ratio of axial clearance (cl_ax) between shroud and sealing and radial clearance (cl_rad) between shroud and fin referred to the h_b are given.

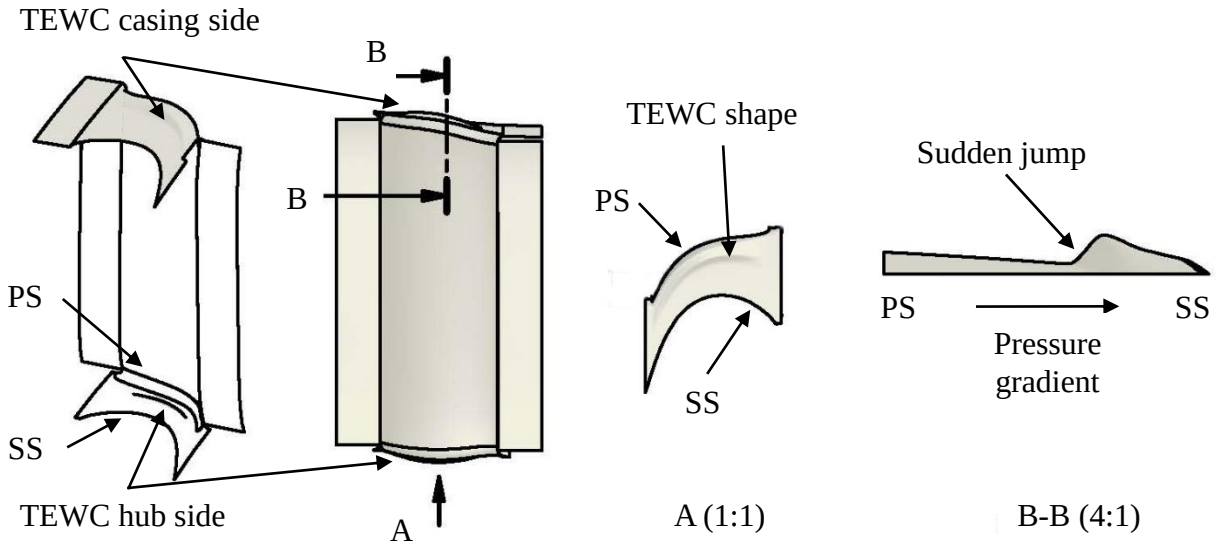

Figure 3.4: Shape of the TEWC and illustration of the sudden jump

Table 3.2: Geometry parameters of the airfoils for stator and rotor in stage 1 und 2

	# Airfoils	$\frac{h_\mathrm{b}}{l_\mathrm{b}}$	$\frac{h_\mathrm{b}}{D_\mathrm{m}}$	$\frac{cl_\mathrm{ax}}{h_\mathrm{b}} \cdot 100\%$	$\frac{cl_\mathrm{rad}}{h_\mathrm{b}} \cdot 100\%$
Stator 1 (S1)	55	2.2268	0.1612	9.5	0.95
Rotor 1 (R1)		2.2903	0.1682	9.1	0.91
Stator 2 (S2)		2.4565	0.1764	8.6	0.86
Rotor 2 (R2)		2.5550	0.1858	8.1	0.81

3.2 Measurement technology

To determine the turbine's flow conditions and thermal efficiency, temperature and pressure sensors were applied at different radial and circumferential positions and at several measurement planes (MP) along the machine axis. In order to set and record the thermodynamic boundary conditions, four wall pressures were recorded on casing and the rotor side at the inlet downstream the honeycomb and at the outlet of the turbine.

Additionally, one vane of the second stage is equipped with pressure holes on two discrete span positions. As shown in Figure 3.5, 13 measuring positions are placed at 90% span that have been determined in advance by numerical simulations. This allows analysis the pressure distribution of pressure side (PS) and suction side (SS) close to the TEWC at 90% span by taking the occurring flow characteristics in consideration. An axial limitation of the measurements is caused by the thin trailing edge at $85\% \, \frac{x}{l}$.

Each measurement hole has a diameter of about 1mm with a 0.8mm connector drilling that is required to attach the pressure sensors to the outside of the turbine. By this means, any influence on the airfoil surface and its respective roughness can be avoided, however the manufacturing effort is in-

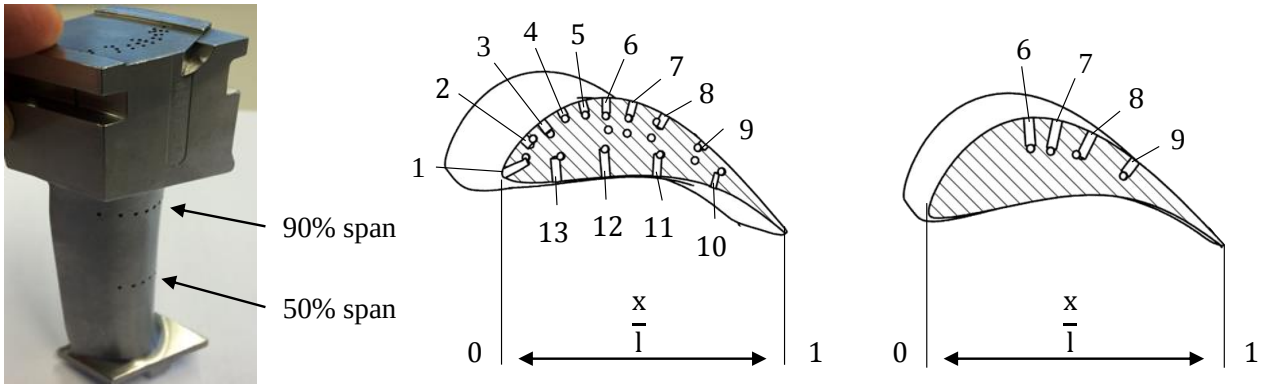

a) Pressure distribution vane **b)** 90% span **c)** 50% span

Figure 3.5: a) Pressure distribution vane and measuring positions on SS and PS located at b) 90% span and c) 50% span

creased. All measurement holes are milled perpendicularly to the airfoil surface. This ensures proper measurements and avoids errors as they were found by Shaw [129] or Wüst [157]. The number of measuring positions on the suction side (SS) is higher compared to the pressure side (PS) because the accelerated flow undergoes a larger pressure gradient and a bigger turning and therefore, the measuring resolution has to be increased to capture the present phenomena.

As one can see in Figure 3.5, only 4 measurements are conducted on the suction side (SS) at 50% span. This is caused by the limited airfoil thickness and the compound lean design, which additionally constricts the build space for the connector drilling. The aim here was to capture the transition point.

Because one focus of the present investigations is dedicated to the influence of leakage flow interaction on TEWC performance, the estimation of the amount of leakage flow (LF) through the casing sided sealing is essential. Therefore, static pressure is measured at six positions in axial direction along the flow path through the cavities to determine the pressure drop of each sealing tip and the brush seal (BS), respectively. These measurements are conducted redundantly with an circumferential offset to take inhomogeneous flow distributions into consideration. As shown in Figure 3.3, the radial clearance between the shroud and labyrinth fin is set to $0.025 \cdot l_{\mathrm{ax}}$. However, variations in this gap due to different speeds means that centrifugal forces have to be considered. Therefore, the clearance is measured by means of an eddy current probe while the test is running. A sampling frequency of about 500kHz meets the Shannon-Theorem $f_{\mathrm{sampling}} \geq 2 \cdot f_{\mathrm{max}}$ for all OP. A schematic of both sealing designs including the locations of the measurement locations are depicted in Figure 3.6

At the outlet measuring plane, four total pressure Kiel-head rakes - each with 5 radial measuring points - are used to detect the circumferential distribution of the flow downstream the second stage. Figure 3.7 illustrates the setup described.

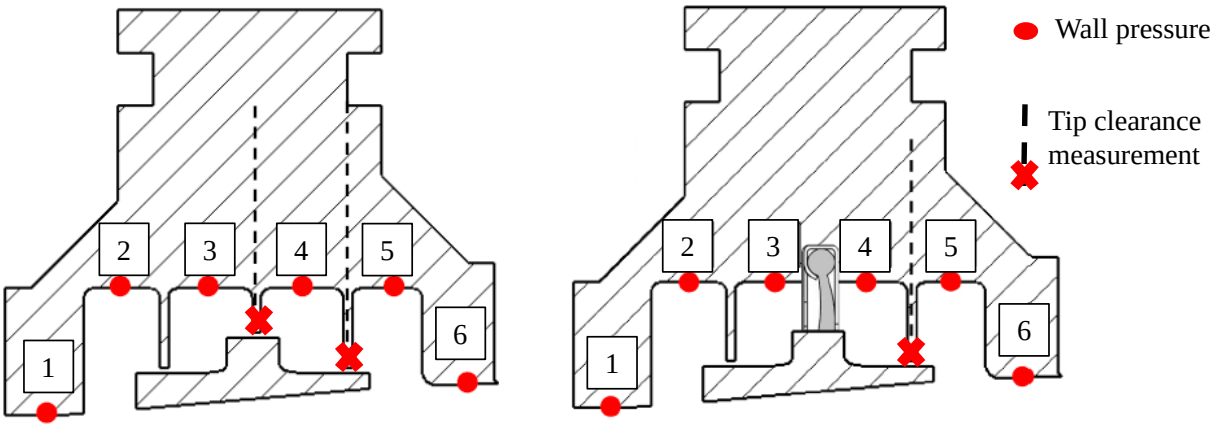

Figure 3.6: Investigated sealing configurations and respective measurement locations a) LS b) BS

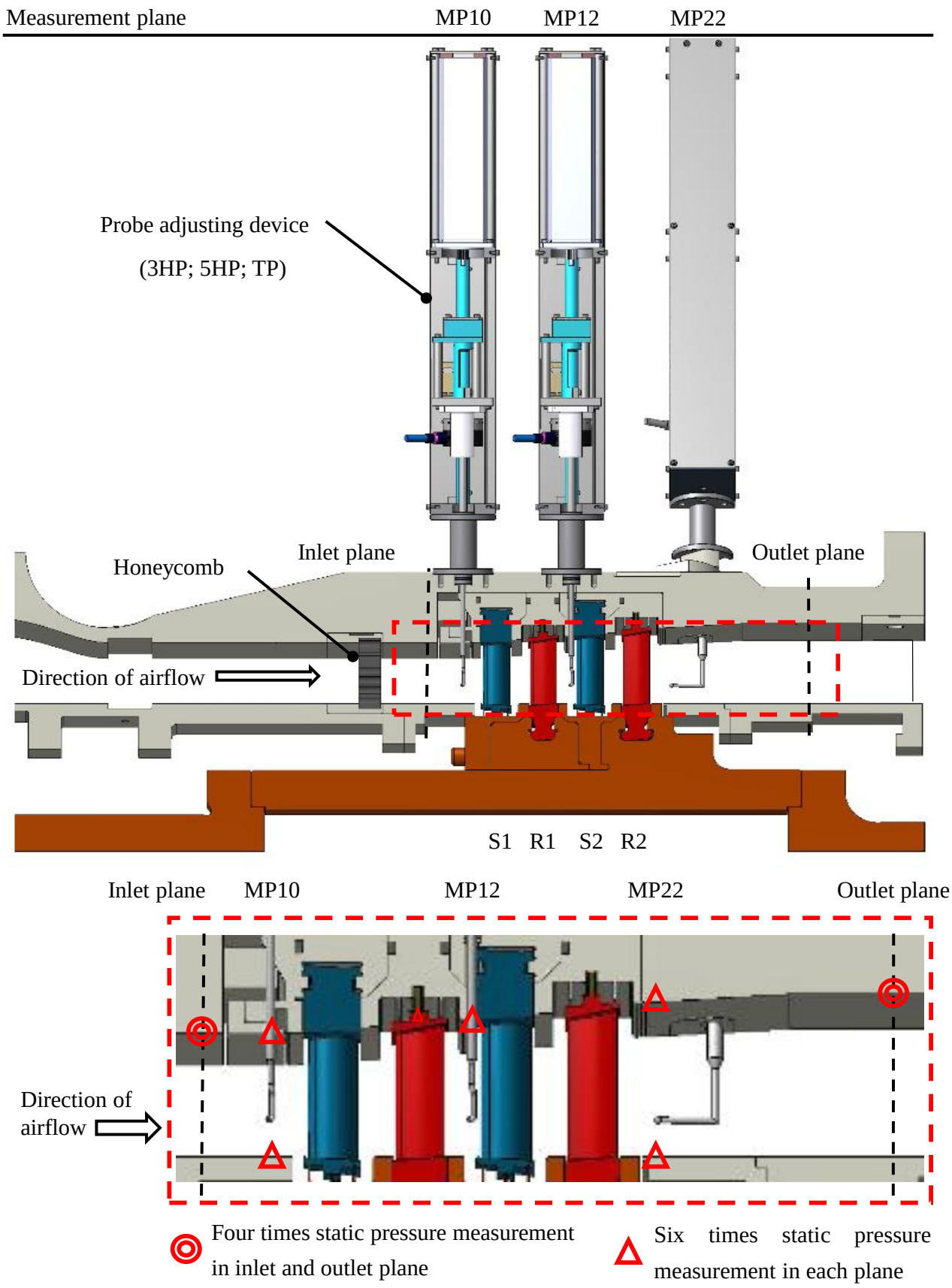

Figure 3.7: Cross section of the 2-stage axial turbine

3.3 Sensors

Figure 3.8 shows the 3-hole probes (3HP) and 5-hole probes (5HP) which were used to determine the flow field at three measurement planes (MP). MP10 is located in front of the first stage, MP12 is located between stage 1 and stage 2 and MP22 gives information about the flow characteristics behind the second rotor. In addition, wall pressures that serve as reference pressures, are measured in these three planes as well. Therefore, more accurate differential sensors can be used to measure the pressure difference at the probe head. The absolute pressure is measured separately and summed up during the post processing process.

All probes are movable in the radial direction through the flow channel by means of a high precision probe adjusting device (PAD). The radial movement is achieved in incremental steps of $3.9\mu m$, while the probe can be rotated in increments as small as $0.09°$. This high positioning accuracy is necessary as it impacts the measurement result immediately (see Restemeier [116]). Temperature probes and pressure probes are mounted with a circumferential displacement illustrated in Figure 3.2. This allows measurements of both temperature and pressure information simultaneously with separate probes. This approach avoids possible errors due to modified flow conditions that could occur if the TP is applied beneath the 5HP head on the same stem.

The measurement process is automated and all probes are adjusted simultaneously to their respective target position. This ensures that deviations in inlet temperature over time only have a negligible influence on the calculation of the thermal efficiency. Thermal efficiency is derived from the temper-

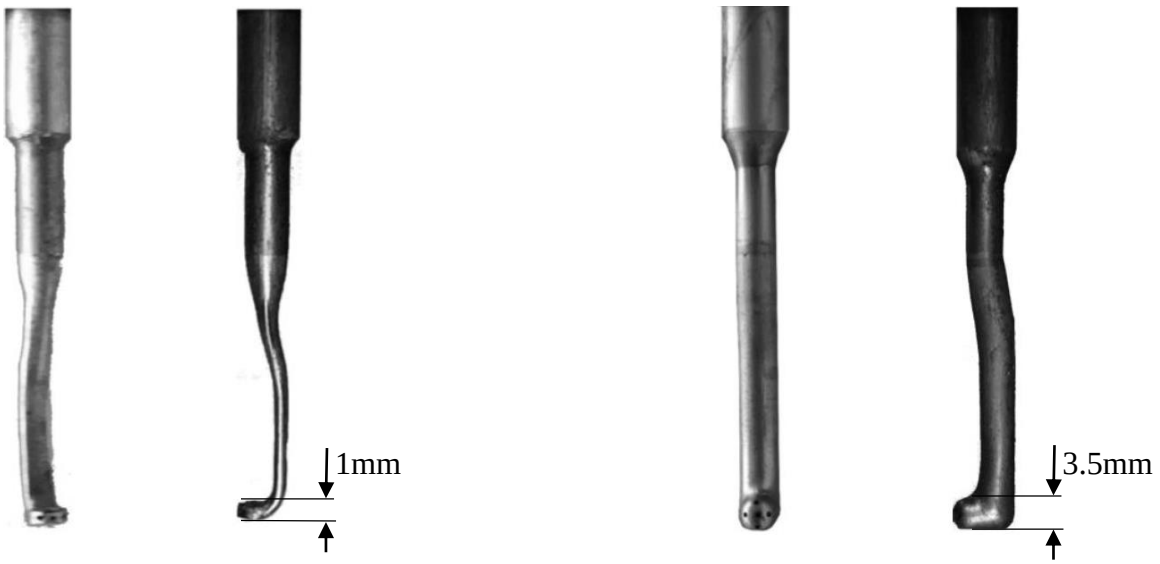

Figure 3.8: Deployed pressure probes in MP10 and MP12: a) 3-hole probe b) 5-hole probe

ature difference between MP10 and MP22. Both stator rows can be rotated by 1.2 pitches (about $8°$) to 'simulate' a circumferential displacement of the probes. By this technique a two dimensional flow field can be determined for a certain cross section of the flow channel. The resulting grid of 392 measuring points (see Figure 3.9) is composed of 56 radial probe measurements conducted on seven 'clocking' positions (CP) of the stator rows. A safety distance of $3‰$ channel height is set on hub and casing endwall to avoid a crash of the probe and to ensure a proper measurement. Further information about the accuracy of the PAD, a grid study and an analysis of the thermal impact on the probe position is given by Zimmermann et al. [162].

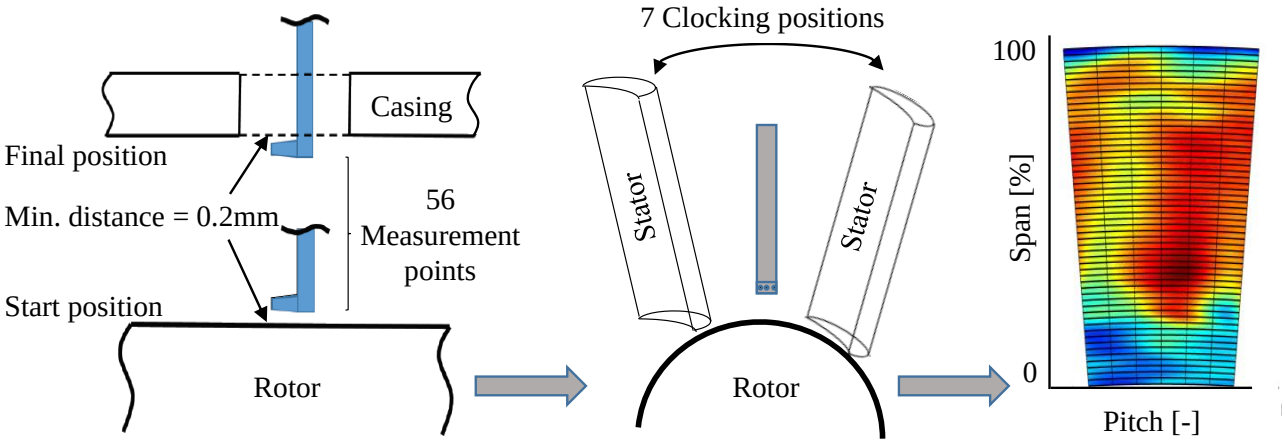

Figure 3.9: Clocking procedure and two dimensional pressure field composed of measured probe data

3.3.1 Pressure probes

The probes were calibrated in a wind tunnel for Mach numbers between 0.1 and 0.25 relating to the Mach number values within the duct. An angle range of $\pm 20°$ is calibrated in increments of $4°$ for yaw and pitch angle. The calibration is performed according to Bohn et al. [14] and can be treated as known [147], thus the calibration methodology is not descriped in this section. The equations and explanation to this topic are briefly presented in Appendix A.

The probe head geometry is designed to be small to minimize the effect on the flow and to meet the requirement of small distances between each pressure hole. According to Wallén [149] and Bubeck [17], this is an appropriate method to avoid measurement errors caused by gradients within the flow field. Nevertheless, intrusive probe measurement causes changes of the flow field, which effects the recorded value. The probe head impacts the boundary layer and the flow close to the walls and the transient vortices in this area according to Bubolz et al. [18]. Furthermore, the Reynolds number has to be taken into account as it is presented by Dominy et al [33] or Willinger [155]. They found that separation at the probe head occurs for Reynolds numbers below $15 \cdot 10^3$, which is much

smaller than the Reynolds number of the present probes ($Re_c = 2.52 \cdot 10^4$). Kauke et al. [77] calibrated several probes at a certain Reynolds number and applied the so gained calibration coefficients to measurements of flows with higher Reynolds numbers. They found that multi hole probes showed deviations in total pressure caused by change of the Reynolds number and for Mach numbers higher than 0.3. For the present test case, both the critical Reynolds number as well as the critical Mach number are not exceeded. Therefore, the error caused by the Reynolds number is not further elaborated.

Furthermore, the test procedure has been optimized as shown in Figure 3.10. Several approaches were implemented to increase the accuracy and the reproducibility of the probe measurements. Changing the probe design from 3HP to 5HP requires an additional test day and thus each OP is investigated redundantly. By altering the measuring sequence (3HP: OP1 $\rightarrow$ OP4, 5HP: OP4 $\rightarrow$ OP1) as well as by inverting the clocking direction (3HP: CP1 $\rightarrow$ CP7, 5HP: CP7 $\rightarrow$ CP1), the chances of the measurements of being influenced by systematic errors are reduced. Furthermore, the probes of the first tests (3HP + TP) face the flow with different angles than the probes of the second tests (5HP + TP) as depicted in the bottom right corner of Figure 3.10. However, the probe is rotated almost perpendicular to the flow to guarantee that the measurement is conducted for the calibrated angle range.

3.3.2 Temperature probes

The temperature probe (TP) is designed with the goal to have a small measuring sensitivity with respect to flow angle for an angle range of $\pm 20°$ according to the design proposals of Saravana-

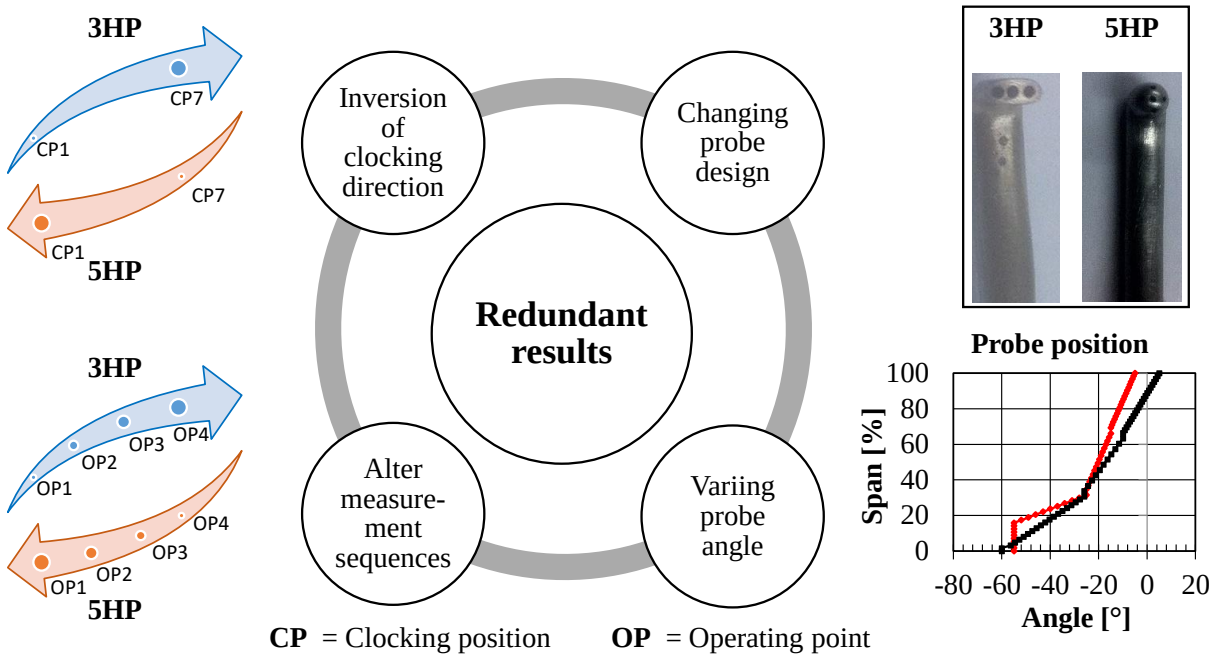

Figure 3.10: Measures to prevent errors and to increase quality of the measurement

muttoo [119]. The measuring tip of a 0.2mm Type K thermocouple captures the temperature at the stagnation point of the ball shaped probe head (Figure 3.11). This thermocouple Type K has been chosen because of its linear behaviour up to temperatures of 1200K (see Nitsche et al. [102]). The thermocouple is insulated to the stem and the probe head with plastic to minimize measurement errors caused by heat conduction. Radiation can be neglected due to the low temperatures on turbine (see Zeisberger [160]).

However, the assumption of an adiabatic stagnation can not be made for practical measurements in turbo machinery. In case that the probe would not represent a flow resistance, the measured value would be the local static temperature. As this is not the case, the measured temperature lies between the total temperature and the static temperature. Therefore, the so called recovery factor (RF) has to be determined for each probe by means of calibration [11]. A recovery factor (RF of 1 represents the total temperature) thus a high recovery factor (RF) is desired to be [66]. For the present probes, values of 0.8, 0.83 and 0.88 (see Appendix A) were derived for the RF that lie in good accordance to the findings of Saravanamuttoo [119] where probes facing the flow show a recovery factor (RF) of 0.8 ± 0.09.

The static and dynamic calibration has been performed for the whole measuring chain consisting of an acquisition system, cable and a temperature probe (TP) to reduce errors as they could occur by altering the respective combination [38]. In addition, each probe cannot be manufactured identically, thus deviations of the Reynolds number can not be avoided that influence the measured results [130]. Also the Prandtl number and Mach number have an impact on the measurement result and therefore require a separate calibration for each probe with appropriate flow conditions [37].

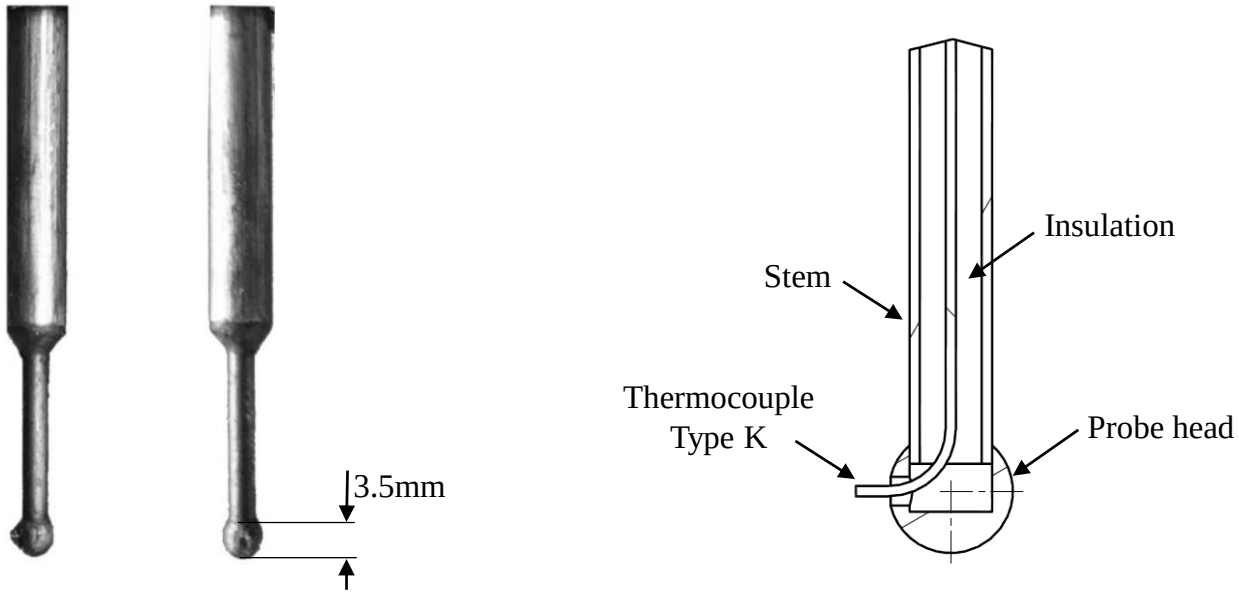

Figure 3.11: Deployed temperature probe in MP10 and MP12

Additional information about the rig and the measurement equipment including a description of the measurement acquisition system is given by Schwab [125]. Furthermore an error analysis for the pressure and temperature measurement is presented in Section 4.5.

3.3.3 Angle definition and velocity triangles

To derive the incidence of a blade located downstream of each measurement plane, the flow angle has to be specified. For the present turbine, the flow angle is 0 when the flow runs in parallel to the machine's axis. A deflection to the right hand side is defined positively while the yaw angle of flow that is directed to the left shows a negative sign. Figure 3.12 illustrates this definition and also shows the velocity vectors $\vec{c}$ of the rigid reference system and of the rotating system $\vec{w}$. Assuming that the incidence of the design point OP3 serves as reference, a further negative angle is respective to positive incidence and vice versa.

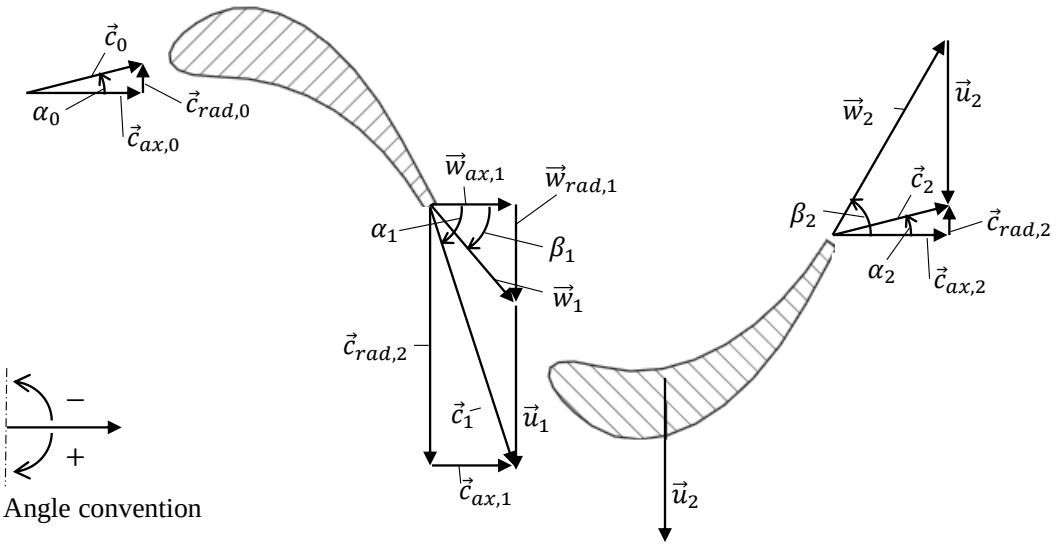

Figure 3.12: Angle convention and velocity triangles for one stage of the test turbine

4 Methodology

This chapter summarizes the approaches of data preparation and introduces the mathematical standards that are utilized to evaluate the performance of the different configurations investigated.

It is shown in section 4.1 how the leakage flow is calculated for both sealing technologies. The determination of the power and the equations to derive the turbine efficiency are introduced in Section 4.2 and in Section 4.3. Furthermore, the results of two averaging methods according to Traupel [142] and Kreitmeier [83] are discussed in Section 4.4. These two averaging methods are applied to all measurements to ensure comparability of the different airfoil configurations and to support the discussion of the phenomena, which result due to changes of the sealing configuration or by applying TEWC to the endwalls. Finally, the probe measurement accuracy is analyzed again and assessed in the framework of an error analysis in Section 4.5. A constant section airfoil configuration with TEWC and brush seal (BS) (2D TEWC BS) is used as a reference and serves as basis of these investigations.

4.1 Derivation of leakage flow

The presence of leakage flow is an inevitable consequence of the gaps between rotating and fixed parts. The introduced labyrinth seal (LS) and brush seal (BS) are utilized to reduce this leakage flow (LF). Two analytical approaches are introduced to calculate the leakage flow (LF) through both types of sealings.

4.1.1 Leakage through labyrinth seals

The leakage flow (LF) through the present GRLS is calculated according to Stodola [137]. This method has been proven to be appropriate by Deckner [23]. The labyrinth seal (LS) is modelled as an idealised sequence of isentropic accelerations with isobaric heat recovery. A portion of the static pressure is transformed to dynamic pressure in the narrowest clearance of the flow passage. This causes a pressure drop for two consecutive cavities according to Equation 4.1 in the case of little pressure difference across the labyrinth tip. The speed c is defined as given by Equation 4.2 [23].

$$\Delta p = \rho \cdot \frac{c^2}{2} \tag{4.1}$$

$$c = \sqrt{2 \cdot \Delta h} \tag{4.2}$$

The reduced pressure implies a reduction of the flow density. Therefore, the velocity is increased at each clearance that has to be passed, to meet the requirement of continuity. The maximum speed is reached at the outlet fin of the sealing (see Thomas [139]). This characteristic "Fanno-curve" is shown

in Figure 4.1 for the subsonic range that is applicable for the present case, as only three labyrinth fins exist and the flow does not reach sonic speed in any case.

The cross section between the fin and shroud that is passed by the leakage flow (LF) can be calculated with Equation 4.3. This approximation is allowed for the present case, as the radial clearance cl_{rad} is significantly smaller than the shroud diameter D ($cl_{\mathrm{rad}} \ll D = 2 \cdot r_{\mathrm{r}}$).

$$A = cl_{\mathrm{rad}} \cdot \pi \cdot D \tag{4.3}$$

By taking the number of the measurements within the cavities into consideration (Figure 3.3), the theoretical leakage flow (LF) through the labyrinth seal (LS) ($\dot{m}_{\mathrm{Lf,Th}}$) can be calculated with Equation 4.4 where z is equivalent to the number labyrinth tips and υ represents the specific volume.

$$\dot{m}_{\mathrm{LF,Th}} = A \cdot \sqrt{\frac{p_2^2 - p_5^2}{z \cdot p_1 \cdot \upsilon_1}} \tag{4.4}$$

This theoretical LF has to be modified because the labyrinth seal (LS) design has a significant impact on the sealing performance. Total turbulence can only be generated in FLS, thus kinetic energy is not fully dissipated to frictional heat due to streamlines passing the gap between tip and shroud. According to Egli [39] Equation 4.4 is extended by a factor k that allows consideration of the ratio of clearance to labyrinth split s/t and the number of tips. As GRLS are applied in the present test case, this factor has not to be taken into consideration and is set to a value of 1 (see Egli [39]).

Another effect to consider is the constriction of streamlines close to bottlenecks and the sealing tips. The resulting effective cross section depends on the shape of tip edge, tip inclination and ratio

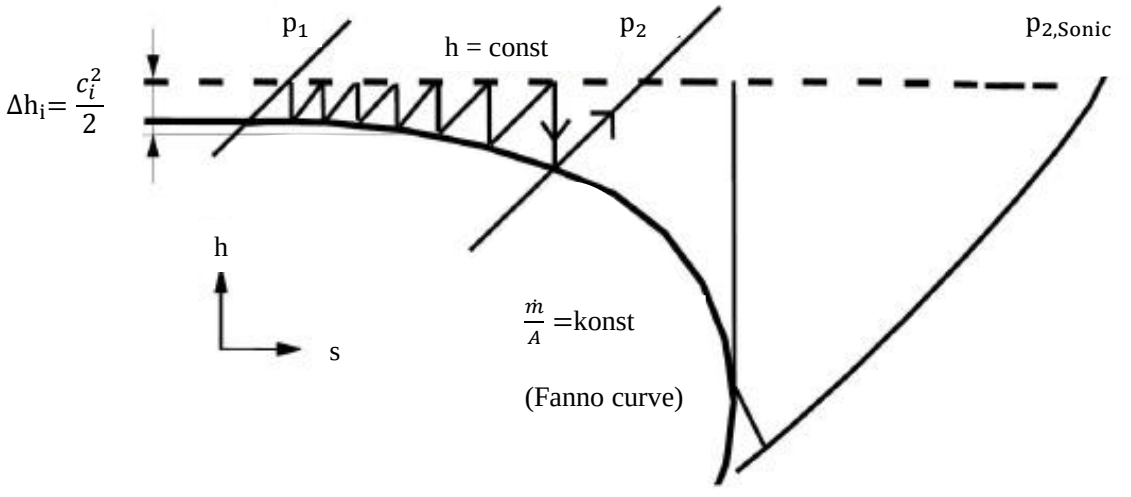

Figure 4.1: Idealized throttling process through a LS (translated from Deckner [23])

of clearance to cavity height. These effects are captured by the factor μ that was found to be a value of 0.7 by Trutnovski [144]. Equation 4.5 shows the extended formula that is used to determine the leakage flow (LF) through the labyrinth seal (LS).

$$\dot{m}_{\mathrm{LF,LS}} = k \cdot \mu \cdot cl_{\mathrm{rad}} \cdot \pi \cdot 2r_{\mathrm{r}} \cdot \sqrt{\frac{p_2^2 - p_5^2}{z \cdot p_1 \cdot \upsilon_1}} \tag{4.5}$$

It will be shown in Section 5.1 that the pressure drops linearly across the three labyrinth tips. All OP show similar pressure levels at inlet and outlet of the cavity Accordingly, the pressure can be assumed to drop over only the sealing tips. The pressure within the first cavity (point (2)) and last cavity (point (5)) is used to calculate the pressure drop, while the thermodynamic condition at the inlet of the first cavity provides the required values for the denominator of Equation 4.4 and Equation 4.5. Here, the values are measured at point (1) because the temperature within the cavity is unknown (p_1 and p_2 are nearly equal thus this assumption is allowable).

4.1.2 Leakage through brush seals

The calculation of leakage flow (LF) through brush seals (BS) is a special case of the determination of leakage flows (LF) through labyrinth seal (LS) as described in Section 4.1.1. The clearance between the shroud and bristle tip varies depending on the surrounding pressure difference and cannot assumed to be constant due to periodic and local unsteadiness. Therefore, the brush seal (BS) has been designed overlapping to the shroud to ensure equivalent conditions for all operating points.

The present design is a combination of brush seal (BS) and labyrinth seal (LS) and is modelled likewise. Tip leakages are calculated as shown above, while the leakage through the brush seals (BS) is calculated according to Müller [98] using the following Equation 4.6. A combined calculation as presented by Stodola is not possible. Thus, the leakage of tip and brush seal (BS) are calculated separately. It was decided not to use the calculation methods used by Chupp [21] and Holle [64] because some values are required that cannot be provided for the present turbine test rig.

$$\dot{m}_{\mathrm{LF,BS}} = 2\pi \cdot r_{\mathrm{r}} \cdot c_{\mathrm{B}} \cdot \varepsilon_{\mathrm{B}} \cdot \frac{p_1}{R \cdot T_1} \tag{4.6}$$

The leakage flow (LF) through the brush seal (BS) is influenced by the shroud radius r_{r}, the gap between backing plate and rotor c_{B}, specific outflow number ε_{B} and the thermodynamic condition at the inlet of the cavity. It will be shown in Section 5.1 that the pressure almost exclusively drops over the brush seal (BS) (point (3) to (4)). For this reason, the overall leakage flow is calculated with Equation 4.6. The specific outflow number ε_{B} is calculated via the pressure drop across the brush seal (BS) and the correlation by Egli [39] depicted in Figure 4.2.

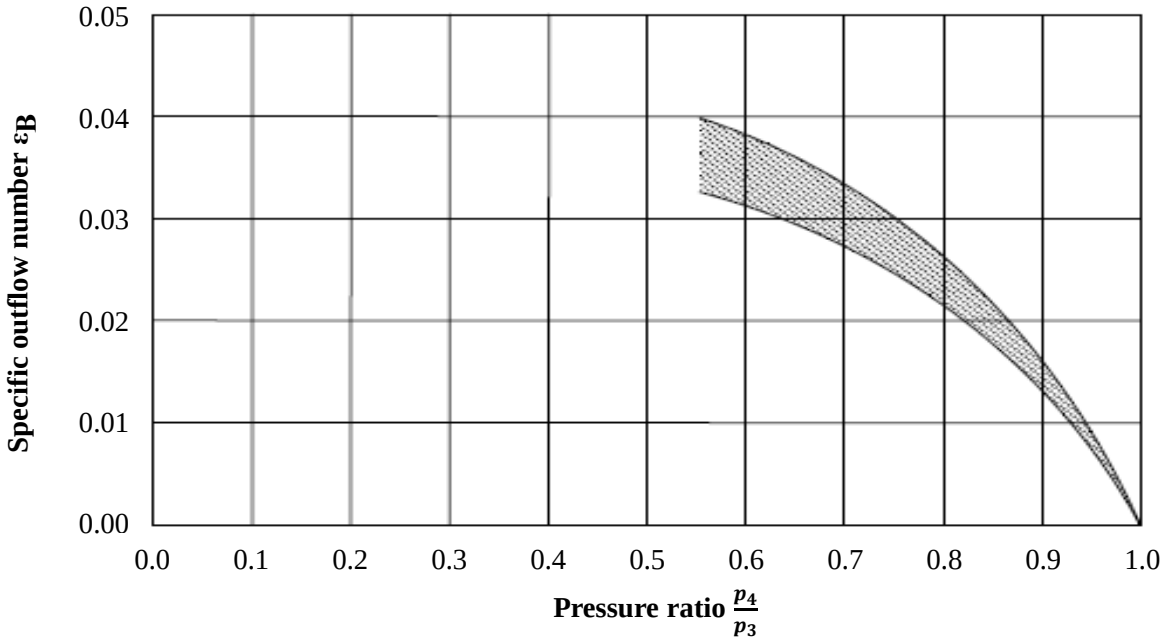

Figure 4.2: Specific outflow coefficient of a BS (according to Egli [39] translated from Müller [98])

A detailed analysis of the impact on the flow caused by changing the sealing configuration from a labyrinth seal (LS) to a brush seal (BS) has been performed for two OP and the reference airfoil configuration 2D TEWC by Zimmermann et al. [161] experimentally. Curkovic et al. [22] investigated the local phaenomena by means of CFD for the same setup.

4.2 Mechanic power measurement

The power of the turbine can be derived in two different ways. An enthalpy change from MP10 to MP22 can be calculated directly from the probe data according to Equation 4.7. Herein the MF and the heat capacity are considered, both of which are averaged arithmetically. The turbine is assumed to be adiabatic to the environment.

$$P = \dot{m} \cdot \bar{c}_{\mathrm{p}} \cdot (T_{\mathrm{t,MP22}} - T_{\mathrm{t,MP10}}) \tag{4.7}$$

Furthermore, the power available at the waterbrake (P_{WB}) is specified as a function of momentum M and rotational speed n. The momentum M results from the force F that is measured by means of a force cell, which is connected to a lever at the water brake. The rotational speed is measured with an incremental rotary encoder that is attached to the shaft. This procedure is beneficial compared to the power determination via probe data, as it also covers frictional losses caused by the brush seal (BS) that cannot be avoided. A dedicated determination of the bearing losses (P_{BL}) can be achieved due to the swing frame construction of the water brake. This is an important feature, as the bearing

losses are different for all OP. Friction losses between air and rotor within the side cavities as well as heat conduction at the casing side are not further taken into consideration as they are of the same order of magnitude for all investigated configurations (see Schwab [125]). The final formulation of the turbine's power is given in Equation 4.8.

$$P_{\mathrm{T}} = P_{\mathrm{WB}} + P_{\mathrm{BL}} \tag{4.8}$$

$$P_{\mathrm{WB}} = 2\pi \cdot n \cdot l_{\mathrm{Lever}} \cdot F \tag{4.9}$$

4.3 Calculation of the efficiency

The assessment of the efficiency of the energy conversion processes is a common way to answer the question of if the application of a novel feature is useful. Therefore, the equations defined by Traupel are utilized to calculate the efficiency of the turbine [142].

The isentropic efficiency describes the quality of the flow in turbo machines, however they should not be interpreted as energetic efficiencies in the narrow sense. Instead of setting the energetic advantage related the expenditure, this kind of efficiency describes an idealized process with an isentropic pressure drop between the outlet and the inlet condition. Here, the lower enthalpy difference in comparison to the real process is referred to the enthalpy difference of the idealized one. It is assumed that the constitutional change is adiabatic and the influence of potential energy can be neglected. However, the consideration of the kinetic energy is useful. Hence, the total-to-total isentropic efficiency for the present turbine ($\eta_{\mathrm{is,tt}}$) is calculated according to Equation 4.10.

$$\eta_{\mathrm{is,tt}} = \frac{h_{\mathrm{MP22}} - h_{\mathrm{MP10}} + 0.5 \cdot (c^2_{\mathrm{MP22}} - c^2_{\mathrm{MP10}})}{h_{\mathrm{MP22,is}} - h_{\mathrm{MP10}} + 0.5 \cdot (c^2_{\mathrm{MP22}} - c^2_{\mathrm{MP10}})} \tag{4.10}$$

A substance database is used to calculate the enthalpy values (h) as well as the entropy values (s) that are required to determine the isentropic enthalpy (h_{is}). This software has been developed by the University Zittau Görlitz [85] and combines measured data and theoretical fundamentals according to Lemmon et al. [88] [89]. The water load of the air that runs through the turbine has been set to a value of zero (see Schwab [125]) as it is pumped in a closed loop that includes moisture separators.

The kinetic energy is not considered to calculate the static-to-static isentropic efficiency ($\eta_{\mathrm{is,ss}}$) that is given in Equation 4.11.

$$\eta_{\mathrm{is,ss}} = \frac{h_{\mathrm{MP22}} - h_{\mathrm{MP10}}}{h_{\mathrm{MP22,is}} - h_{\mathrm{MP10}}} \tag{4.11}$$

It is also a feasible option to derive the related static-to-static polytropic efficiency ($\eta_{\mathrm{pol,ss}}$) as a func-

tion of $\eta_{\mathrm{is,ss}}$ due to the assumption of ideal gas. The isentropic coefficient κ is derived by averaging of κ_{MP10} and κ_{MP22}, logarithmically.

$$\eta_{\mathrm{pol,ss}} = \frac{\kappa}{\kappa - 1} \cdot \frac{ln\left[\eta_{\mathrm{is,ss}} \cdot \left(\left(\frac{p_{\mathrm{MP22}}}{p_{\mathrm{MP10}}}\right)^{\frac{\kappa-1}{\kappa}} - 1\right) + 1\right]}{ln\left(\frac{p_{\mathrm{MP22}}}{p_{\mathrm{MP10}}}\right)} \tag{4.12}$$

Instead of exclusively using the probe measurement, the polytropic efficiency can also be calculated referring to the power (P_{T}) and the main mass flow ($\dot{m}_{\mathrm{MF}}$), while taking friction and further losses into consideration. The resulting formulation for $\eta^{*}_{\mathrm{pol,ss}}$ is given in equation 4.13.

$$\eta^{*}_{\mathrm{pol,ss}} = \frac{\frac{P_{\mathrm{T}}}{\dot{m}_{\mathrm{MF}}} - \frac{c^2_{\mathrm{MP22}} - c^2_{\mathrm{MP10}}}{2}}{\frac{P_{\mathrm{T}}}{\dot{m}_{\mathrm{MF}}} - \frac{c^2_{\mathrm{MP22}} - c^2_{\mathrm{MP10}}}{2} - \frac{\tilde{T}_{\mathrm{MP22}} - \tilde{T}_{\mathrm{MP10}}}{ln\left(\frac{\tilde{T}_{\mathrm{MP22}}}{\tilde{T}_{\mathrm{MP10}}}\right)} \cdot (s^2_{\mathrm{MP22}} - s^2_{\mathrm{MP10}})} \tag{4.13}$$

4.4 Data averaging

Averaging the measured data is a key factor to determine the efficiency. Several standard procedures can be found in literature. The standard guideline VDI-4675 [145] has been utilized to select established methods to average the measurement data of the inhomogeneous flow fields.

An investigation has shown that the averaging methods according to Reynolds [117], Favre [43] [44], and Adamczyk [3] are not suitable to post process the present data. This is due to the fact that required information cannot be recorded by the measurement setup. Turbulence models have to be compared in detail to imply an exact determination of flow fluctuation that has not been realized in the last years despite of an increased computing capacity. The methods of Truckenbrodt [143], Livesey and Hugh [90] only consider velocity components that are directed in parallel to the machine axis. The requirement to also interpret radial and tangential velocity components of the flow field disqualifies these methods, because important information is not considered. The methodology of Stewart [136] and Scholz [122] does not fulfil the balance of total momentum and total temperature for conservative fluxes. Therefore, this approach is not further elaborated as larger deviations arise if the interaction of blade rows downstream the measurement probe are taken into consideration.

Traupel [142] introduced a method that applies a mass averaging on an extensive number values. Also velocity vectors, that are not parallel to the machine axis, are included. Additionally, the equations of continuity as well as the equations of energy are satisfied. For that, Traupel implements form factors that have to be observed in detail as it is not guaranteed that aero- and thermodynamic

processes are described precisely if the form factors become too large. However, this approach is common standard to average data gathered in turbo machines, and is therefore further elaborated in this thesis.

The methodology of Kreitmeier [84] also includes the conservation of momentum and swirl in addition to the non conservative equations. Furthermore, form factors, transient fluctuation values and related uncertainties are avoided. Kreitmeier expresses the averaging instructions in terms of reversible and irreversible equilibration processes. The reversible calculations are based on the determination of mechanical and thermal energy losses and of entropy. The irreversible process is used to solve energy, mass, momentum and swirl balances. Kreitmeier reduces a three dimensional problem to a one dimensional problem by means of both types of processes. On the one hand, uncertainties are reduced, on the other hand, inhomogeneities of the flow field are captured more detailed.

For this reason, the following sections are dedicated to apply and compare the methods of Traupel and Kreitmeier regarding to the present case. A detailed analysis of the resulting efficiencies and deviations between both formulations is presented for data of the reference blading.

4.4.1 Averaging methodology according to Traupel

Traupel [142] postulates that the extensive state variables have to be mass averaged. Therefore, an extensive state value L and the related specific value I are calculated as shown in Equation 4.14.

$$I(t_0) = \frac{L(t_0)}{m(t_0)} \tag{4.14}$$

Here, $m(t_0)$ describes the mass that flows through an arbitrary pipe cross section at a discrete time instance t_0. Furthermore, the steady-state mean value of the specific value I is determined by means of limit value generation for transient flows:

$$\bar{I} \equiv \lim_{t_0 \to \infty} |I(t_0)| \tag{4.15}$$

If I is subject to transient fluctuations, t_0 has to be chosen to be large compared to the time interval of individual transient flow phenomena. It should be that multiple of the smallest periodic fluctuation to allow the simplification of Equation 4.15 with sufficient accuracy.

$$\bar{I} = I(t_0) \tag{4.16}$$

Using the above mentioned assumption for the time interval t_0, an exact averaging of any state variable can be performed using Equation 4.14.

$$\bar{I} = \frac{1}{m(t_0)} \cdot \int \rho \, c_\mathrm{z} \, I \, dA \, dt \tag{4.17}$$

By applying Equation 4.17 on the relevant data, the averaged values of the specific volume, enthalpy, entropy and velocities can be defined in Cartesian coordinates as follows:

$$\bar{v} = \frac{1}{m(t_0)} \cdot \int \rho \, c_\mathrm{z} \, v \, dA \, dt = \frac{1}{m(t_0)} \cdot \int c_\mathrm{z} \, dA \, dt \tag{4.18}$$

$$\bar{h} = \frac{1}{m(t_0)} \cdot \int \rho \, c_\mathrm{z} \, h \, dA \, dt \tag{4.19}$$

$$\bar{s} = \frac{1}{m(t_0)} \cdot \int \rho \, c_\mathrm{z} \, s \, dA \, dt \tag{4.20}$$

$$\bar{c}_\mathrm{bz} = \frac{1}{m(t_0)} \cdot \int \rho \, c_\mathrm{z}^2 \, dA \, dt \tag{4.21}$$

$$\bar{c}_\mathrm{bx} = \frac{1}{m(t_0)} \cdot \int \rho \, c_\mathrm{x} \, c_\mathrm{z} \, dA \, dt \tag{4.22}$$

$$\bar{c}_\mathrm{by} = \frac{1}{m(t_0)} \cdot \int \rho \, c_\mathrm{y} \, c_\mathrm{z} \, dA \, dt \tag{4.23}$$

On this occasion, the index b represents a momentum mean value for the calculation of the velocities. Following this, the index k is chosen for mean values of continuity and the index e describes an energy based averaging. Velocity components that do not have an index describe the actual velocity at a certain location within the flow. These values are not averaged by any mathematical operation.

Along with the calculation of the velocity utilizing the momentum mean value, velocity may be also calculated with the equation of continuity (Equation 4.24). Here, the velocity is expressed by the cross sectional area A, the mass flow and the mass averaged specific volume. Furthermore, it can be determined with an energy base method according to Equation 4.25.

$$\bar{c}_\mathrm{kz} = \frac{\dot{m} \, \bar{v}}{A} \tag{4.24}$$

$$\bar{c}_\mathrm{e}^2 = \frac{1}{m(t_0)} \cdot \int \rho \, c_\mathrm{z} \, \left(c_\mathrm{x}^2 + c_\mathrm{y}^2 + c_\mathrm{z}^2 \right) \, dA \, dt \tag{4.25}$$

Traupel introduced form factors that can be used to convert the various averaged velocities into each other to cause a connection for further calculations.

$$\bar{c}_\mathrm{b}^2 = \bar{c}_\mathrm{bx}^2 + \bar{c}_\mathrm{by}^2 + \bar{c}_\mathrm{bz}^2 \tag{4.26}$$

$$\bar{c}_\mathrm{kz} = (1 + \epsilon_\mathrm{k}) \tag{4.27}$$

$$\bar{c}_\mathrm{e} = (1 + \epsilon_\mathrm{e}) \tag{4.28}$$

The total enthalpy can be determined via energy equation combined with the formerly introduced form factors:

$$\bar{h}_{\mathrm{t}} = \bar{h}_{\mathrm{s}} + \frac{1}{2} \cdot (1 + \epsilon_{\mathrm{e}})^2 \cdot \bar{c}_{\mathrm{b}}^2 = \bar{h}_{\mathrm{s}} + \frac{\bar{c}_{\mathrm{e}}^2}{2} = \frac{1}{m(t_0)} \cdot \int \rho \, c_{\mathrm{z}} \left(h_{\mathrm{s}} + \frac{\bar{c}^2}{2} \right) dA \, dt \tag{4.29}$$

Hence, static values can be inserted in Equation 4.19 to determine the static enthalpy or total values for the calculation of the total enthalpy respectively. Subsequently, the static enthalpy is indexed with "s" and total values are indexed with "t". In the case that an enthalpy equation is suitable for both conditions, the index is left out.

The static as well as the total pressures are calculated with an area averaged method in contrary to the mass averaged extensive variables. This is due to the fact that the standard force of an infinite element i can be calculated by multiplication of its cross sectional area A_{i} and the predominant pressure p_{i}. Furthermore, the resulting force on an element is defined as the sum of all external forces:

$$\vec{F}_{\mathrm{i}} = p_{\mathrm{i}} \cdot A_{\mathrm{i}} \tag{4.30}$$

$$\vec{F}_{\mathrm{sum}} = \sum \vec{F}_{\mathrm{i}} = \sum p_{\mathrm{i}} \, A_{\mathrm{i}} \stackrel{!}{=} \bar{p} \, A \tag{4.31}$$

Consequentially, the mean value of the pressure is defined according to Equation 4.32 for transient calculations.

$$\bar{p} = \frac{1}{A \, t_0} \cdot \int \rho \, dA \, dt \tag{4.32}$$

Hereafter, the thermal and caloric state equations are considered in addition to the averaging methods described above. It is not possible to satisfy all equations of the averaging method and state equations concurrently. Therefore Traupel differentiated three strategies:

a) $\bar{p}$ is calculated with Equation 4.32 and $\bar{h}$ is calculated with Equation 4.19. The averaged specific volume and the mean entropy follow as a function of the mean values and calculation of the state equations.

   $\bar{v} = f\left(\bar{h}, \bar{p}\right) \quad and \quad \bar{s} = f\left(\bar{h}, \bar{p}\right)$

b) Equation 4.19 is used to determine $\bar{h}$ and $\bar{s}$ is calculated with equation 4.20. The averaged specific volume and the mean pressure result from a function of the averaged values and calculation of the state equations.

   $\bar{v} = f\left(\bar{h}, \bar{s}\right) \quad and \quad \bar{p} = f\left(\bar{h}, \bar{s}\right)$

c) $\bar{v}$ is derived with Equation 4.18 and $\bar{h}$ is calculated with Equation 4.19. The mean entropy and mean pressure are determined by calculation of the state equations and can be described as a

function of the averaged values.

$$\bar{s} = f\left(\bar{h}, \bar{v}\right) \quad and \quad \bar{p} = f\left(\bar{h}, \bar{v}\right)$$

Following this, the calculation method is explained for case a). The pressure and enthalpy are averaged in a first step using Equation 4.19 and 4.32. In the case that the entropy and the specific volume are calculated by means of the mean values, Equation 4.18 and 4.20 are violated. The same issue occurs for the respective state values of case b) or c).

Traupel described the problem with an idealised example. One may consider two equivalent mass flows running through the same cross section, which differ only by their respective temperature. Thus the enthalpy of one mass flow is higher at the same pressure level as it is shown in Figure 4.3.

The state A results from averaging pressure and enthalpy for case a). This point differs compared to point B that results from averaging enthalpy and entropy. The difference is substantiated due to the fact that the mixing of two different mass flows is an irreversible process. Only case a) considers an increase of entropy that is produced during the mixing process.

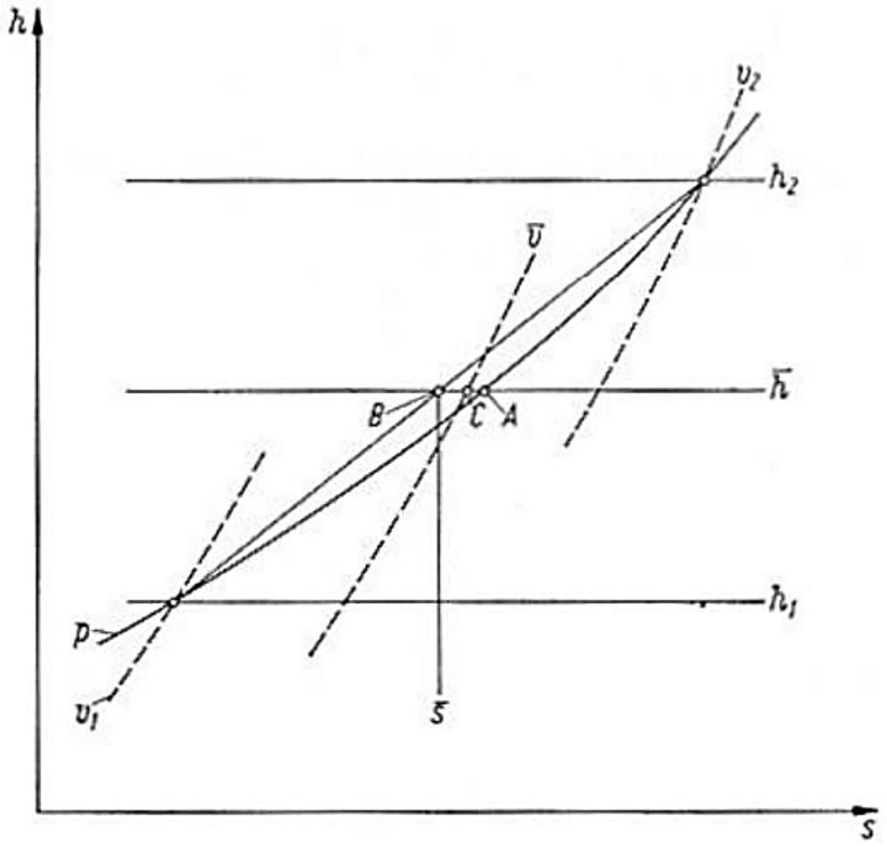

Figure 4.3: H-s-diagram showing the comparison of different averaging approaches according to Traupel [142]

The point C (calculated in case c)) is located between the two points A and B. Traupel explains this as the mixing may be assumed as a reversible process if energy would be gained due to the temperature difference. If this energy was used to compress the fluid, the resulting pressure level would be higher at a lower entropy value.

The h-s-diagram in Figure 4.3 clearly shows that it is not possible to fulfil all thermodynamic requirements concurrently and to describe a fluid state completely by means of an averaging method. Nevertheless, Traupel stated that the differences of the introduced averaging methods are much smaller than measurement uncertainties, thus the results are equivalent. Finally, Traupel stated that Method a) is most suitable for turbo machinery. Therefore it is applied within the present investigation.

4.4.2 Averaging methodology according to Kreitmeier

The variety of averaging methods leads inevitably to problems with the comparability of investigations from several sources. Particular problems include the form factors to calibrate the balance equations that are partly defined differently and the time averaging of flux terms. The averaging method according to Kreitmeier [84] is performed without using these kinds of simplifications. For this, Kreitmeier defines a hypothetical reversible and irreversible equilibration processes by means of the thermodynamic and aerodynamic balance equations. Below, the corresponding set of equations is presented and explained.

General balance equations

The following general balance equations built the basis of the calculations according to Kreitmeier [83].

Mass balance:

$$\frac{\partial}{\partial t}\int\limits_{\mathrm{V}} \rho \, dV + \int\limits_{\mathrm{A}} \rho \, \vec{c} \, d\vec{A} = 0 \tag{4.33}$$

Linear momentum balance:

$$\int\limits_{\mathrm{V}} \frac{\partial \left(\rho \, \vec{c}\right)}{\partial t} dV + \int\limits_{\mathrm{A}} \rho \, \vec{c} \, \left(\vec{c} \, d\vec{A}\right) = \int\limits_{\mathrm{A}} \vec{f} dV + \int\limits_{\mathrm{A}} \vec{\vec{\sigma}} d\vec{A} \tag{4.34}$$

Angular momentum balance:

$$\int\limits_{\mathrm{V}} \frac{\partial \left[\rho \, \left(\vec{r} \times \vec{c}\right)\right]}{\partial t} dV + \int\limits_{\mathrm{A}} \rho \, \left(\vec{r} \times \vec{c}\right) \, \left(\vec{c} \, d\vec{A}\right) = \int\limits_{\mathrm{V}} \left(\vec{r} \times \vec{f}\right) dV + \int\limits_{\mathrm{A}} \vec{r} \times \left(\vec{\vec{\sigma}} d\vec{A}\right) \tag{4.35}$$

Mechanical energy balance:

$$\int_{\mathrm{V}} \frac{\partial \left(\rho \frac{\vec{c}^{\,2}}{2}\right)}{\partial t} dV + \int_{\mathrm{A}} \rho \frac{\vec{c}^{\,2}}{2} \left(\vec{c}\, d\vec{A}\right) = \int_{\mathrm{V}} \vec{c}\, \vec{f}\, dV + \int_{\mathrm{V}} \frac{p}{v} \frac{Dv}{Dt}\, dV + \int_{\mathrm{A}} \vec{c}\, \vec{\vec{\sigma}}\, d\vec{A} - \int_{\mathrm{V}} \Phi\, dV \quad (4.36)$$

Mechanical and thermal energy balance:

$$\int_{\mathrm{V}} \frac{\partial \left[\rho \left(u + \frac{\vec{c}^{\,2}}{2}\right)\right]}{\partial t} dV + \int_{\mathrm{A}} \rho \left(u + \frac{\vec{c}^{\,2}}{2}\right) \left(\vec{c}\, d\vec{A}\right) = \int_{\mathrm{V}} \vec{f}\, \vec{c}\, dV + \int_{\mathrm{A}} \vec{c}\, \vec{\vec{\sigma}}\, d\vec{A} + \int_{\mathrm{A}} \lambda\, \nabla T\; d\vec{A} \quad (4.37)$$

Thermal energy balance expressed with the notion of intrinsic energy:

$$\int_{\mathrm{V}} \frac{\partial (\rho\, u)}{\partial t} dV + \int_{\mathrm{A}} \rho\, u \left(\vec{c}\, d\vec{A}\right) = -\int_{\mathrm{V}} \frac{p}{v} \frac{Dv}{Dt}\, dV + \int_{\mathrm{V}} \Phi\, dV + \int_{\mathrm{A}} \lambda\, \nabla T\; d\vec{A} \quad (4.38)$$

Thermal energy balance expressed with the notion of entropy:

$$0 = -\int_{\mathrm{V}} \rho\, T \frac{Ds}{Dt}\, dV + \int_{\mathrm{V}} \Phi\, dV + \int_{\mathrm{A}} \lambda\, \nabla T\; d\vec{A} \quad (4.39)$$

Entropy balance:

$$\int_{\mathrm{V}} \frac{\partial (\rho\, s)}{\partial t} dV + \int_{\mathrm{A}} \rho\, s \left(\vec{c}\, d\vec{A}\right) = \int_{\mathrm{V}} \frac{\Phi}{T}\, dV + \int_{\mathrm{V}} \lambda \left(\frac{\nabla T}{T}\right)^2 dV + \int_{\mathrm{A}} \lambda \left(\frac{\nabla T}{T}\right) d\vec{A} \quad (4.40)$$

The Equations 4.33 - 4.36 are balance equations of aerodynamics while the Equations 4.38 - 4.40 are fundamentals of thermodynamics. Equation 4.37 is used in both, thermo- as well as aerodynamics [156].

The first term on the left hand side of each equation describes the temporal change of the balanced values within the control volume. The second term represents the flux of the field variables through the control region. All given balances are universally valid for an absolute system.

Simplification of balance equations

To apply the averaging method of Kreitmeier to the test data of the turbine test rig, several assumptions can be made that simplify the above given balance equations.

a) Quasi-steady state conditions

Most flow processes are periodically transient in common praxis. Therefore, the flow conditions

may be assumed as "quasi-steady state" and the balance equations can be derived by means of the mean value theorem for the integral calculus:

$$\lim_{t_0 \to \infty} \frac{1}{t_0} \cdot \int_0^{t_0} \left[\int_V \frac{\partial \rho}{\partial t} \, dV \right] \, dt + \lim_{t_0 \to \infty} \frac{1}{t_0} \cdot \int_0^{t_0} \left[\int_A \rho \, \vec{c} \, d\vec{A} \right] \, dt = 0 \tag{4.41}$$

The first term includes the temporal change of the balanced values becomes negligible leading to a simplified balance equation.

b) Gas as flow medium

As the turbine is driven with air the flow medium is a gas and only gravitational force appears as volume force. Therefore, the terms that include the vector of the volume force can be neglected compared to the transport terms.

c) Tangential stress

The stress tensor $\vec{\vec{\sigma}}$ consists of normal (pressure) and tangential stresses (friction). The tangential stresses can be ignored at the free portion of the control surface as they are much smaller compared to the normal stresses. This assumption leads to Equation 4.42.

$$\vec{\vec{\sigma}} \, d\vec{A} = -p \, d\vec{A} \tag{4.42}$$

d) Heat transfer

The portion of heat conduction is negligible compared to the transport phenomena across the control region and is therefore not considered.

Transformations of balance equations

In addition to the simplifications that are explained above, the following transformations are conducted in the framework of the averaging process:

a) Notion of enthalpy

The enthalpy used for the balance equations is defined according to Equation 4.43.

$$h = u + \frac{p}{\rho} \tag{4.43}$$

b) Pressure change and shift work

The effort that is required to cause a volumetric change is expressed by the pressure change and the shift work of the control volume:

$$\int_{\mathrm{V}} \frac{p}{v} \frac{Dv}{Dt} \, dV = -\int_{\mathrm{V}} \vec{c} \nabla p \, dV + \int_{\mathrm{A}} p \, \vec{c} \, d\vec{A} \tag{4.44}$$

c) System limits of the control volume The surface control volume is separated in two types as depicted in Figure 4.4. The free control surfaces are designated with S_{i} while wall surfaces are labelled with A_{i}.

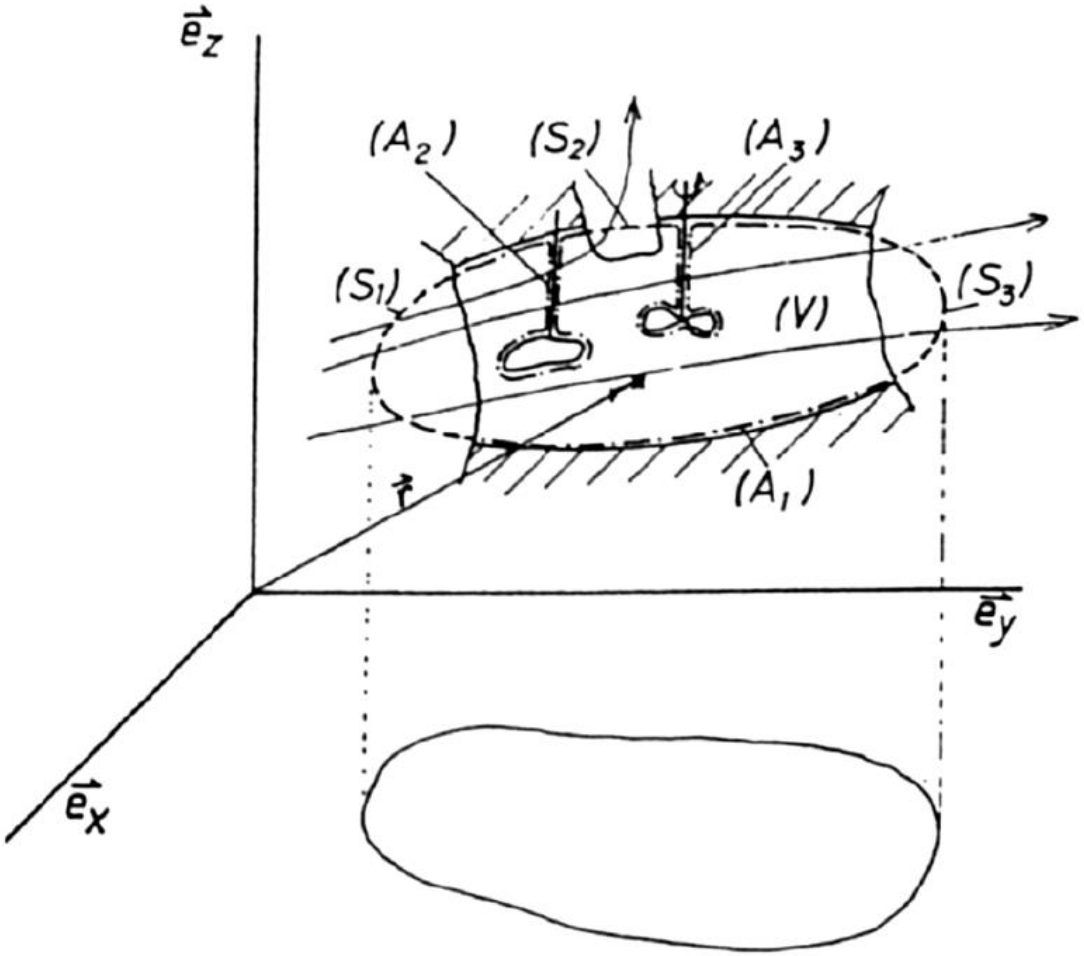

Figure 4.4: Schematic of the control volume and its defined system limits according to Kreitmeier [84]

Resulting simplified balance equations

Simplified mass balance:

$$\frac{1}{t_0} \cdot \int_0^{t_0} \int_S \rho \, \vec{c} \, d\vec{S} \, dt = 0 \tag{4.45}$$

Simplified linear momentum balance:

$$\frac{1}{t_0} \cdot \int_0^{t_0} \int_S \rho \, \vec{c} \, \left(\vec{c} \, d\vec{S} \right) \, dt + \frac{1}{t_0} \cdot \int_0^{t_0} \int_S p \, d\vec{S} \, dt = \frac{1}{t_0} \cdot \int_0^{t_0} \int_A \vec{\vec{\sigma}} d\vec{A} \, dt \tag{4.46}$$

Simplified angular momentum balance:

$$\frac{1}{t_0} \cdot \int_0^{t_0} \int_S \rho \, (\vec{r} \times \vec{c}) \, \left(\vec{c} \, d\vec{S} \right) \, dt + \frac{1}{t_0} \cdot \int_0^{t_0} \int_S p \, \left(\vec{r} \times d\vec{S} \right) \, dt = \frac{1}{t_0} \cdot \int_0^{t_0} \int_A \vec{r} \times \left(\vec{\vec{\sigma}} d\vec{A} \right) \, dt \tag{4.47}$$

Simplified mechanical energy balance:

$$\frac{1}{t_0} \cdot \int_0^{t_0} \int_S \rho \, \frac{\vec{c}^2}{2} \, \left(\vec{c} \, d\vec{S} \right) \, dt = -\frac{1}{t_0} \cdot \int_0^{t_0} \int_V \vec{c} \, \nabla p \, dV \, dt + \frac{1}{t_0} \cdot \int_0^{t_0} \int_A \vec{c} \, \vec{\vec{\sigma}} \, d\vec{A} \, dt + \frac{1}{t_0} \cdot \int_0^{t_0} \int_V \Phi \, dV \, dt \tag{4.48}$$

Simplified mechanical and thermal energy balance:

$$\frac{1}{t_0} \cdot \int_0^{t_0} \int_S \rho \, \left(h + \frac{\vec{c}^2}{2} \right) \, \left(\vec{c} \, d\vec{S} \right) \, dt = \frac{1}{t_0} \cdot \int_0^{t_0} \int_A \vec{c} \, \vec{\vec{\sigma}} \, d\vec{A} \, dt + \frac{1}{t_0} \cdot \int_0^{t_0} \int_A \lambda \, \nabla T \, d\vec{A} \, dt \tag{4.49}$$

Simplified thermal energy balance expressed with the notion of enthalpy:

$$\frac{1}{t_0} \cdot \int_0^{t_0} \int_S \rho \, h \, \left(\vec{c} \, d\vec{S} \right) \, dt = \frac{1}{t_0} \cdot \int_0^{t_0} \int_V \vec{c} \, \nabla p \, dV \, dt + \frac{1}{t_0} \cdot \int_0^{t_0} \int_V \Phi \, dV \, dt + \frac{1}{t_0} \cdot \int_0^{t_0} \int_A \lambda \, \nabla T \, d\vec{A} \, dt \tag{4.50}$$

Simplified thermal energy balance expressed with the notion of entropy:

$$0 = -\frac{1}{t_0} \cdot \int_0^{t_0} \int_V \rho \, T \, \vec{c} \, \nabla s \, dV \, dt + \frac{1}{t_0} \cdot \int_0^{t_0} \int_V \Phi \, dV \, dt + \frac{1}{t_0} \cdot \int_0^{t_0} \int_A \lambda \, \nabla T \, d\vec{A} \, dt \tag{4.51}$$

Simplified entropy balance:

$$\frac{1}{t_0} \cdot \int_0^{t_0} \int_S \rho\, s \left(\vec{c}\, d\vec{S}\right) dt = \frac{1}{t_0} \cdot \int_0^{t_0} \int_V \frac{\Phi}{T}\, dV\, dt + \frac{1}{t_0} \cdot \int_0^{t_0} \int_V \lambda \left(\frac{\nabla T}{T}\right)^2 dV\, dt + \int_A \lambda \left(\frac{\nabla T}{T}\right) d\vec{A}\, dt \tag{4.52}$$

In Equation 4.45 - 4.52, the left hand side shows the terms of fluxes across the free surface S of the control volume. The source productivity and the fluxes passing the control surface are given on the right hand side of these equations [156].

Fluxes of field variables

To simplify matters, the following abbreviations are used to formulate the fluxes of the field variables of the simplified balance equations.

Mass flow $\dot{M}$:

$$\dot{M} = \frac{1}{t_0} \cdot \int_0^{t_0} \int_S \rho\, \vec{c}\, d\vec{S}\, dt \tag{4.53}$$

Total linear momentum flow $\dot{\vec{I}}_\mathrm{t}$:

$$\dot{\vec{I}}_\mathrm{t} = \frac{1}{t_0} \cdot \int_0^{t_0} \int_S \rho\, \vec{c} \left(\vec{c}\, d\vec{S}\right) dt + \frac{1}{t_0} \cdot \int_0^{t_0} \int_S \rho\, d\vec{S}\, dt \tag{4.54}$$

Total angular momentum flow $\dot{\vec{D}}_\mathrm{t}$:

$$\dot{\vec{D}}_\mathrm{t} = \frac{1}{t_0} \cdot \int_0^{t_0} \int_S \rho\, (\vec{r} \times \vec{c}) \left(\vec{c}\, d\vec{S}\right) dt + \frac{1}{t_0} \cdot \int_0^{t_0} \int_S p \left(\vec{r} \times d\vec{S}\right) dt \tag{4.55}$$

Total enthalpy flow $\dot{\vec{H}}_\mathrm{t}$:

$$\dot{H}_\mathrm{t} = \frac{1}{t_0} \cdot \int_0^{t_0} \int_S \rho \left(h + \frac{\vec{c}^2}{2}\right) \left(\vec{c}\, d\vec{S}\right) dt \tag{4.56}$$

Enthalpy flow $\dot{H}$:

$$\dot{H} = \frac{1}{t_0} \cdot \int_0^{t_0} \int_S \rho\, h \left(\vec{c}\, d\vec{S}\right) dt \tag{4.57}$$

Flow of kinetic energy $\dot{K}$:

$$\dot{K} = \frac{1}{t_0} \cdot \int_0^{t_0} \int_S \rho \frac{\vec{c}^2}{2} \left(\vec{c} d\vec{S} \right) dt \tag{4.58}$$

Entropy flow $\dot{S}$:

$$\dot{S} = \frac{1}{t_0} \cdot \int_0^{t_0} \int_S \rho \, s \left(\vec{c} d\vec{S} \right) dt \tag{4.59}$$

Kreitmeier [84] defines Equations 4.53 - 4.56 as "conservation fluxes" while Equation 4.57 - 4.59 are "non conservation fluxes".

Averaged field variables

Kreitmeier [83] established three averaging methodologies utilizing various models. He defined the irreversible, reversible and semi-reversible averaging. In the following section, the methods are introduced and discussed. The assumptions and equations are described in advance to an explanation of the model and its analytical treatment. The variety of requirements in practical applications is the reason why more than one approach has to be considered.

a) Irreversibly averaged field variables

The resulting system of equations is developed by replacing the field variables within the surface integrals (Equation 4.53 - 4.59) by area averaged values. These are constant across the free surface S and over time t_0.

$$\dot{M} = \bar{\rho} \, \bar{\vec{c}} \, \vec{S} \tag{4.60}$$

$$\dot{\vec{I}}_t = \bar{\rho} \, \bar{\vec{c}} \left(\bar{\vec{c}} \, \vec{S} \right) + \bar{p} \, \vec{S} = \bar{\vec{c}} \, \dot{M} + \bar{p} \, \vec{S} \tag{4.61}$$

$$\dot{\vec{D}}_t = \bar{\vec{r}} \times \dot{\vec{I}}_t + \Delta \dot{\vec{D}}_t \tag{4.62}$$

$$\dot{H}_t = \bar{\rho} \left(\bar{h} + \frac{\bar{\vec{c}}^2}{2} \right) \left(\bar{\vec{c}} \, \vec{S} \right) = \left(\bar{h} + \frac{\bar{\vec{c}}^2}{2} \right) \dot{M} \tag{4.63}$$

$$\dot{H} = \bar{\rho} \, \bar{h} \left(\bar{\vec{c}} \, \vec{S} \right) + \Delta \dot{H} = \bar{h} \, \dot{M} + \Delta \dot{H} \tag{4.64}$$

$$\dot{K} = \bar{\rho} \frac{\bar{\vec{c}}^2}{2} \left(\bar{\vec{c}} \, \vec{S} \right) + \Delta \dot{K} = \frac{\bar{\vec{c}}^2}{2} \dot{M} + \Delta \dot{K} \tag{4.65}$$

$$\dot{S} = \bar{\rho} \, \bar{s} \left(\bar{\vec{c}} \, \vec{S} \right) + \Delta \dot{S} = \bar{s} \, \dot{M} + \Delta \dot{S} \tag{4.66}$$

$$\bar{h} = f \, (\bar{\rho} \, , \bar{p}) \tag{4.67}$$

$$\bar{s} = f \, (\bar{\rho} \, , \bar{p}) \tag{4.68}$$

The additional term $\dot{\vec{D}}_t$ appears in Equation 4.62 that is required, due the linear momentum flow. $\dot{\vec{I}}_t$ is not perpendicular to the angular momentum flow $\dot{\vec{D}}_t$ in general. The remaining fluxes $\Delta \dot{H}$,

$\Delta\dot{K}$, $\Delta\dot{S}$ in Equation 4.64 - 4.66 are especially remarkable. This is a special feature of balanced based averaging methods and of fundamental significance for the balancing process according to Kreitmeier. The implementation of these variables is required as the equation system would be overdetermined without them.

The model of irreversible averaging is developed by means of a flow between two control sections that is assumed to be in quasi-steady state conditions. The inlet is indexed with 1 while the cross section that represents the outlet is indexed with 2. The control volume V is limited to its sides by the wall surfaces S as shown in Figure 4.4. The following equations result by inserting the Equations 4.53 - 4.59 (definition of fluxes) into the simplified balance equations 4.45 - 4.52.

$$\dot{M}_1 + \dot{M}_2 = 0 \tag{4.69}$$

$$\dot{\vec{I}}_{\mathrm{t},1} + \dot{\vec{I}}_{\mathrm{t},2} = \frac{1}{t_0} \cdot \int_0^{t_0} \int_{\mathrm{A}} \vec{\vec{\sigma}}\, d\vec{A}\, dt \tag{4.70}$$

$$\dot{\vec{D}}_{\mathrm{t},1} + \dot{\vec{D}}_{\mathrm{t},2} = \frac{1}{t_0} \cdot \int_0^{t_0} \int_{\mathrm{A}} \vec{r} \times \left(\vec{\vec{\sigma}} d\vec{A}\right)\, dt \tag{4.71}$$

$$\dot{H}_{\mathrm{t},1} + \dot{H}_{\mathrm{t},2} = \frac{1}{t_0} \cdot \int_0^{t_0} \int_{\mathrm{A}} \vec{c}\,\vec{\vec{\sigma}}\, d\vec{A}\, dt + \frac{1}{t_0} \cdot \int_0^{t_0} \int_{\mathrm{A}} \lambda \nabla T\, d\vec{A}\, dt \tag{4.72}$$

$$\dot{H}_1 + \dot{H}_2 = \frac{1}{t_0} \cdot \int_0^{t_0} \int_{\mathrm{V}} \vec{c} \nabla p\, dV\, dt + \frac{1}{t_0} \cdot \int_0^{t_0} \int_{\mathrm{V}} \Phi\, dV\, dt + \frac{1}{t_0} \cdot \int_0^{t_0} \int_{\mathrm{A}} \lambda \nabla T\; d\vec{A}\, dt \tag{4.73}$$

$$0 = -\frac{1}{t_0} \cdot \int_0^{t_0} \int_{\mathrm{V}} \rho T\, \vec{c} \nabla s\, dV\, dt + \frac{1}{t_0} \cdot \int_0^{t_0} \int_{\mathrm{V}} \Phi\, dV\, dt + \frac{1}{t_0} \cdot \int_0^{t_0} \int_{\mathrm{A}} \lambda \nabla T\; d\vec{A}\, dt \tag{4.74}$$

$$\dot{K}_1 + \dot{K}_2 = -\frac{1}{t_0} \cdot \int_0^{t_0} \int_{\mathrm{V}} \vec{c} \nabla p\, dV\, dt + \frac{1}{t_0} \cdot \int_0^{t_0} \int_{\mathrm{A}} \vec{c}\,\vec{\vec{\sigma}}\, d\vec{A}\, dt - \frac{1}{t_0} \cdot \int_0^{t_0} \int_{\mathrm{V}} \Phi\, dV\, dt \tag{4.75}$$

$$\begin{aligned} \dot{S}_1 + \dot{S}_2 = {} & \frac{1}{t_0} \cdot \int_0^{t_0} \int_{\mathrm{V}} \frac{\Phi}{T}\, dV\, dt + \frac{1}{t_0} \cdot \int_0^{t_0} \int_{\mathrm{V}} \lambda \left(\frac{\nabla T}{T}\right)^2\, dV\, dt \\ & + \frac{1}{t_0} \cdot \int_0^{t_0} \int_{\mathrm{A}} \lambda \left(\frac{\nabla T}{T}\right)\, d\vec{A}\, dt \end{aligned} \tag{4.76}$$

The terms on the right hand side of the equations shown above represent the resulting effects of the walls to the balance volume or rather the effects that occur inside. The control surfaces are adjacent close to the boundaries at an infinitesimal point of view ($A \to 0$). Therefore, the

surface integrals on the right hand side of the equations disappear and the walls do not effect the volume further. Consequently the fluxes of the control surfaces 1 and 2 have to be identical. The remaining volume integrals of Equation 4.74, 4.75 and 4.76 are defined with $\Delta\dot{H}$, $\Delta\dot{K}$ and $\Delta\dot{S}$ as describe below:

$$\Delta\dot{H} = -\frac{1}{t_0} \cdot \int_0^{t_0} \int_V \vec{c} \nabla p \, dV \, dt - \frac{1}{t_0} \cdot \int_0^{t_0} \int_V \Phi \, dV \, dt \tag{4.77}$$

$$\Delta\dot{K} = \frac{1}{t_0} \cdot \int_0^{t_0} \int_V \vec{c} \nabla p \, dV \, dt + \frac{1}{t_0} \cdot \int_0^{t_0} \int_V \Phi \, dV \, dt \tag{4.78}$$

$$\Delta\dot{S} = -\frac{1}{t_0} \cdot \int_0^{t_0} \int_V \frac{\Phi}{T} \, dV \, dt - \frac{1}{t_0} \cdot \int_0^{t_0} \int_V \lambda \left(\frac{\nabla T}{T} \right)^2 \, dV \, dt \tag{4.79}$$

The averaging process can be interpreted as a equilibration process by implementing the remaining fluxes. Equation 4.80 results by summation of the Equations 4.77 and 4.78.

$$\Delta\dot{H} + \Delta\dot{K} = 0 \tag{4.80}$$

Thus, a portion of the flux of kinetic energy namely $\Delta\dot{K}$ merges into the enthalpy flux $\Delta\dot{H}$.

The remaining entropy flux $\Delta\dot{S}$ may be deemed to be source productivity that is generated during the equilibration process inside of the balance volume. It is composed of two dissipation terms that are related to friction and temperature compensation. Therefore, Kreitmeier defines this method as irreversible averaging because both sources appear at the same time.

In the following context the analytical treatment is explained. The system of the Equations 4.60 - 4.68 can be transferred into three subsystems:

Subsystem I comprises the Equations 4.60, 4.61, 4.63 and 4.67 and the unknown variables $\bar{\rho}$,$\bar{p}$, $\bar{h}$ and $\bar{\vec{c}}$. Two possible solutions are received by means of iteration. Substitution of the velocity component by implementing Equation 4.61 in Equation 4.60 and 4.63 provides the following equations:

$$\frac{1}{\bar{\rho}} = \frac{I_{\mathrm{t,x}} \cdot A_{\mathrm{x}} + I_{\mathrm{t,y}} \cdot A_{\mathrm{y}} + I_{\mathrm{t,z}} \cdot A_{\mathrm{z}} - \bar{\rho} \left(A_{\mathrm{x}}^2 + A_{\mathrm{y}}^2 + A_{\mathrm{z}}^2 \right)}{\dot{M}^2} \tag{4.81}$$

$$\bar{\rho}^{\,2}\,\left(A_{\mathrm{x}}^2+A_{\mathrm{y}}^2+A_{\mathrm{z}}^2\right)-2\bar{\rho}\,\left(I_{\mathrm{t,x}}\cdot A_{\mathrm{x}}+I_{\mathrm{t,y}}\cdot A_{\mathrm{y}}+I_{\mathrm{t,z}}\cdot A_{\mathrm{z}}\right)+\left(I_{\mathrm{t,x}}^2+I_{\mathrm{t,y}}^2+I_{\mathrm{t,z}}^2\right)$$
$$-2\dot{M}^2\left(\frac{\dot{H}_{\mathrm{t}}}{\dot{M}}-\bar{h}\right)=0 \tag{4.82}$$

The above mentioned equations are visualized in Figure 4.5 by means of a h-s-diagram. It is evident that two mathematical solutions a subsonic and a sonic one occur. Kreitmeier suggests to examine the following criteria to choose the physically practical solution.

i) The irreversibly averaged entropy $\bar{s}$ has to be larger than the reversibly averaged one $\tilde{s}$ in Equation 4.89.

ii) In case that condition i) is fulfilled, the solution with the smallest deviation to $\tilde{h}$ has to be chosen. This assumption avoids an alleged existing compression shock during the equilibration process.

The Subsystem II consists of Equation 4.62. The unknown variables, the effective radius $\bar{\bar{r}}$ and the parameter of $\bar{r}_{\mathrm{p}}$ can be calculated directly.

Subsystem III is formed with the Equations 4.64, 4.66 and 4.68 and contains the unknown variables $\Delta\dot{H}$, $\Delta\dot{K}$, $\Delta\dot{S}$ and $\bar{s}$. All four variables can be determined if the subsystem I is solved.

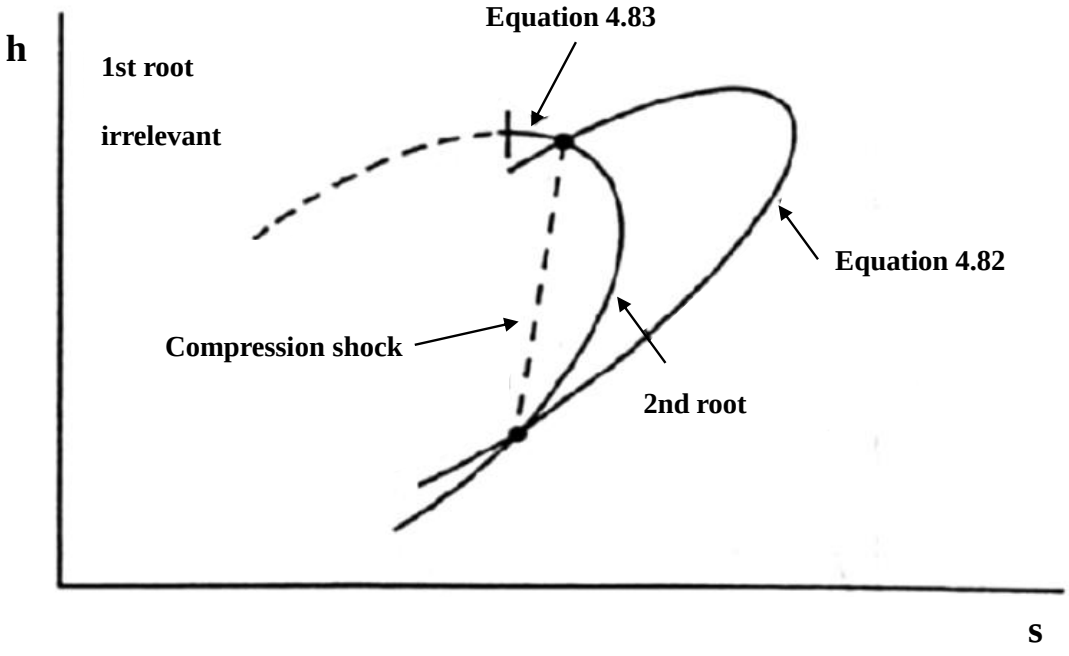

Figure 4.5: Solution curves of Equation 4.81 and 4.82 in an h-s-diagram (Kreitmeier [84])

Therefore, the irreversible averaging methodology according to Kreitmeier enables to formulate the remaining fluxes and all fluxes that are defined by the balance equations by means of irreversibly averaged field variables.

b) Reversibly averaged field variables

The handling of the above introduced remaining fluxes is circumstantial for thermodynamic investigations where the fluxes $\dot{H}$, $\dot{K}$ amd $\dot{S}$ are utilized. Thus, it is desirable to eliminate these terms. This can be achieved by assigning a higher priority to the thermodynamic balance equations (Equations 4.38 - 4.40) than to the aerodynamic balance equations (Equations 4.33 - 4.36). The fluxes $\dot{M}$, $\dot{\vec{I}}_{\mathrm{t}}$ and $\dot{\vec{D}}_{\mathrm{t}}$ are not formulated with mean values. $\dot{H}_{\mathrm{t}}$, $\dot{H}$, $\dot{K}$ and $\dot{S}$ are still expressed by area averaged variables.

$$\dot{M} \equiv \dot{M} \tag{4.83}$$

$$\dot{\vec{I}}_{\mathrm{t}} \equiv \dot{\vec{I}}_{\mathrm{t}} \tag{4.84}$$

$$\dot{\vec{D}}_{\mathrm{t}} \equiv \dot{\vec{D}}_{\mathrm{t}} \tag{4.85}$$

$$\dot{H}_{\mathrm{t}} = \left(\tilde{h} + \tilde{k}\right)\, \dot{M} \tag{4.86}$$

$$\dot{H} = \tilde{h}\, \dot{M} \tag{4.87}$$

$$\dot{K} = \tilde{k}\, \dot{M} \tag{4.88}$$

$$\dot{S} = \tilde{s}\, \dot{M} \tag{4.89}$$

The model of the reversible averaging method is described as a quasi-steady state flow between two control surfaces as it has been also described for the irreversible averaging method.

The walls also do not have an influence on the equilibration process due the assumption that $A \rightarrow 0$ is valid at the boundaries. To eliminate the remaining fluxes $\Delta\dot{H}$, $\Delta\dot{K}$ and $\Delta\dot{S}$, the following requirements have to be met for the Equations 4.77 - 4.79:

i) As both integrands of Equation 4.79 are always positive, each of both terms has to be identical 0. This is realized with the border crossing $\Phi \rightarrow 0$ (no inner friction) and $\lambda \rightarrow 0$ (no inner heat transfer).

ii) The Equations 4.77 and 4.78 imply the following additional requirement after the boundary crossing $\Phi \rightarrow 0$:

$$\frac{1}{t_0} \cdot \int_0^{t_0} \int_{\mathrm{V}} \vec{c}\, \nabla p \, dV \, dt \rightarrow 0 \tag{4.90}$$

This condition cannot be interpreted directly and is therefore transformed as follows:

The convective change of the pressure can be formulated with Equation 4.91 and the implementation of the streamline coordinate x:

$$\vec{c} \nabla p = c \frac{\partial p}{\partial x} \tag{4.91}$$

With:

$$dV = d\vec{A}\, dx \tag{4.92}$$

Equation 4.90 can be written as:

$$\frac{1}{t_0} \cdot \int_0^{t_0} \int_{\mathrm{V}} \vec{c} \frac{\partial p}{\partial x}\, d\vec{A}\, dx\, dt = 0 \tag{4.93}$$

For integration between two points 1 and 2 along the streamline x and extending with $pv = 1$ Equation 4.90 is transformed to Equation 4.94.

$$\frac{1}{t_0} \cdot \int_0^{t_0} \int_{\mathrm{V}} \rho\, \vec{c}\, d\vec{A} \int_1^2 v \frac{\partial p}{\partial x}\, dx\, dt = 0 \tag{4.94}$$

The Equation 4.94 can be interpreted as all the internal work that is required to change the pressure along the streamline has to compensate each other. This means that no type of energy is allowed to merge with another one.

Another interesting connection can be shown with Equation 4.51, which can be transformed to Equation 4.95.

$$\frac{1}{t_0} \cdot \int_0^{t_0} \int_{\mathrm{A}} \rho\, \vec{c}\, d\vec{A} \int_1^2 T \frac{\partial s}{\partial x}\, dx\, dt = 0 \tag{4.95}$$

This equation reveals that the areas beneath the expansion and the respective compression curve in an T-s-diagram have to be identical. As no entropy is generated with this averaging method, it has been named "reversible averaging method" by Kreitmeier [84].

The Equation System 4.83 - 4.89 contains the unknown variables $\tilde{h}$, $\tilde{k}$ and $\tilde{s}$, which can be calculated directly. In contrary to the irreversible averaging, only the Balance Equations 4.49 - 4.52 can be expressed by mean values.

c) Semi-reversibly averaged field variables

As already mentioned, the remaining fluxes $\Delta\dot{H}$, $\Delta\dot{K}$ and $\Delta\dot{S}$ occur in the equations of the irreversible averaging method. Especially the remaining entropy flux has been traced to effects within the equilibration volume that are caused by friction and temperature compensation. These dissipation terms have been avoided for the reversible averaging method to eliminate these remaining fluxes. Additionally, Kreitmeier introduced a third averaging method, that only considers the source term caused by inner thermal conduction.

By applying the same procedure as described for the irreversible averaging method and considering that the remaining fluxes $\Delta\dot{H}$ and $\Delta\dot{K}$ disappear, the following equation system can be derived:

$$\dot{M} \equiv \dot{M} \tag{4.96}$$

$$\dot{\vec{I}}_{\mathrm{t}} \equiv \dot{\vec{I}}_{\mathrm{t}} \tag{4.97}$$

$$\dot{\vec{D}}_{\mathrm{t}} \equiv \dot{\vec{D}}_{\mathrm{t}} \tag{4.98}$$

$$\dot{H}_{\mathrm{t}} = \left(\hat{h} + \hat{k}\right)\, \dot{M} \tag{4.99}$$

$$\dot{H} = \hat{h}\, \dot{M} \tag{4.100}$$

$$\dot{K} = \hat{k}\, \dot{M} \tag{4.101}$$

$$\dot{S} = \hat{s}\, \dot{M} + \Delta\dot{S}_{\lambda} \tag{4.102}$$

Here, only $\dot{H}_{\mathrm{t}}$, $\dot{H}$, $\dot{K}$ and $\dot{S}$ are expressed by mean values, as described for the reversible averaging method. Furthermore, a suitable model is developed for the remaining entropy flux $\dot{S}_{\lambda}$.

Again, this model is described utilizing a quasi-steady state flow between two control surfaces that are limited by the walls A. Then, the assumptions for the semi-reversible equilibration process can be determined by applying the Balance Equations 4.69 - 4.76 on the equilibration volume.

Also, the border crossing $A \rightarrow 0$ is applied to eliminate the influence of the limiting walls. Neglecting the internal friction causes $\Phi \rightarrow 0$. Additionally, Kreitmeier demands that no type of energy is allowed to merge with another one.

The remaining fluxes $\dot{H}$ and $\dot{K}$ are close to 0 in line with these approaches and the entropy flux can be formulated with Equation 4.103. The index λ refers to the entropy production due to inner thermal conduction.

$$\dot{S}_\lambda = -\frac{1}{t_0} \cdot \int_0^{t_0} \int_V \lambda \left(\frac{\nabla T}{T} \right)^2 \, dV \, dt \tag{4.103}$$

Equation 4.95 is still valid, as the simplified balance equation of thermal energy (4.51) has to be satisfied. Hence, the area beneath the compression curves shown in Figure 4.5 has to be of the same size as beneath the compression curves. As the integrand in Equation 4.103 is still larger than zero, it can be stated that:

$$\hat{s} > \tilde{s} \tag{4.104}$$

The Equation System 4.96 - 4.102 contains the unknown variables $\hat{h}$, $\hat{k}$, $\hat{s}$ and $\dot{S}_\lambda$. While the first two variables can be determined directly, $\hat{s}$ and $\dot{S}_\lambda$ have to be derived in an iterative process.

Comparison of the averaging methods

The previous paragraphs have shown how the fluxes of field variables within a defined equilibration volume can be formulated or replaced by various balance based mean variables and by the application of the three averaging methodologies according to Kreitmeier [84]. Table 4.1 gives an overview of the differences between the averaged field variables for each averaging method. It can be concluded, that one averaging approach is not sufficient to answer all questions of fluid dynamic problems. It has been decided to choose the correct approach based on which topic of investigation needs to be focused on

Table 4.1: Overview of the averaged field variables [83]

Fluxes of field variables	Averaged field variables		
	irreversible	**reversible**	**semi-reversible**
$\dot{M}$	$\bar{\rho}$, $\bar{\vec{c}}$	Not expressed	
$\dot{\vec{I}}_\mathrm{t}$	$\bar{\vec{c}}$, $\bar{p}$		
$\dot{\vec{D}}_\mathrm{t}$	$\bar{\vec{r}}$, $\bar{r}_\mathrm{p}$		
$\dot{H}_\mathrm{t}$	$\bar{h}$, $\bar{\vec{c}}$	$\tilde{h}$, $\tilde{k}$	$\hat{h}$, $\hat{k}$
$\dot{H}$	$\bar{h}$, $\left(\tilde{h} - \bar{h}\right)$	$\tilde{h}$	$\hat{h}$
$\dot{K}$	$\vec{r}$, $\left(\tilde{k} - \bar{k}\right)$	$\tilde{k}$	$\hat{k}$
$\dot{S}$	$\bar{s}$, $(\tilde{s} - \bar{s})$	$\tilde{s}$	$\bar{s}$, $(\tilde{s} - \bar{s})$

If the emphasis is placed on fluid mechanics, the irreversible approach is best suited. However, if it is placed on thermodynamic investigations, the reversible or semi-reversible method must be chosen. As both topics occur for the present investigation, all three averaging methods according to Kreitmeier have to be considered. A detailed analysis for the present data will be shown in Section 4.5.

4.4.3 Definition of the measurement grid

Each measurement plane (MP) contains 55 airfoil passages called pitches, of these one pitch is surveyed. It is assumed that identical flow phenomena occur in all pitches. To determine the flow field for one pitch, the probe is moved to six discrete circumferential positions called "clocking positions" as described in Section 3.3.1 (the sevenths CP is measured redundantly to the first one and therefore not taken into account to calculate the MF).

The probe measurement is conducted on 56 radial measurement positions between hub and shroud that have various distances to increase the resolution close to hub and tip. By this means, a measurement grid with the shape of a circular area section is created. The probe data has to be allocated to its respective surface element. This is important, as the area on the outer diameters is larger and therefore the data collected at the shroud is weighted differently compared to data collected close to the hub. This weighting factor varies for the averaging methods discussed and is further investigated in Section 4.5.

To calculate the size of each surface element, the following Equation 4.105 has to be utilized:

$$dA = r\, d\phi\, dt \tag{4.105}$$

The surface element $A_{2,2}$ will be examined below. It is assumed that the radii r_1 and r_2 are well known. $A_{2,2}$ results by the integration of Equation 4.105 to:

$$A_{2,2} = \int_{\mathrm{r_1}}^{r_2} \int_{0}^{\phi_1} r\, dr\, d\phi = \int_{\mathrm{r_1}}^{r_2} r\, \phi_{\mathrm{i}}\, dr = \left[\frac{r^2}{2} \cdot \phi_{\mathrm{i}} \right]_{\mathrm{r_1}}^{r_2} = \left(r_2^2 - r_1^2 \right) \frac{\phi_{\mathrm{i}}}{2} \tag{4.106}$$

The angle ϕ_{i} corresponds to the angle between two CP and results by the dimensions of the test rig to $1.09°$. The limiting radii (blue coloured) of each surface are located centred between two measurement points. The radius of the measurement point is called with M in Figure 4.6.

$$r_{2,1} = \frac{M_{1,1} + M_{2,1}}{2} \approx r_{2,2} = \frac{M_{1,2} + M_{2,1}}{2} \tag{4.107}$$

The distance between two radii to the surface limits is not constant. This is because as the probe positions vary for each CP due to the actuation accuracy of the PAD that lie in a magnitude of $\approx 4\mu m$.

Two examples are marked with red circles in Figure 4.6 to illustrate the effect. This discrepancy is handled with an inhouse programmed software tool that allocates an explicit surface element to each measurement point.

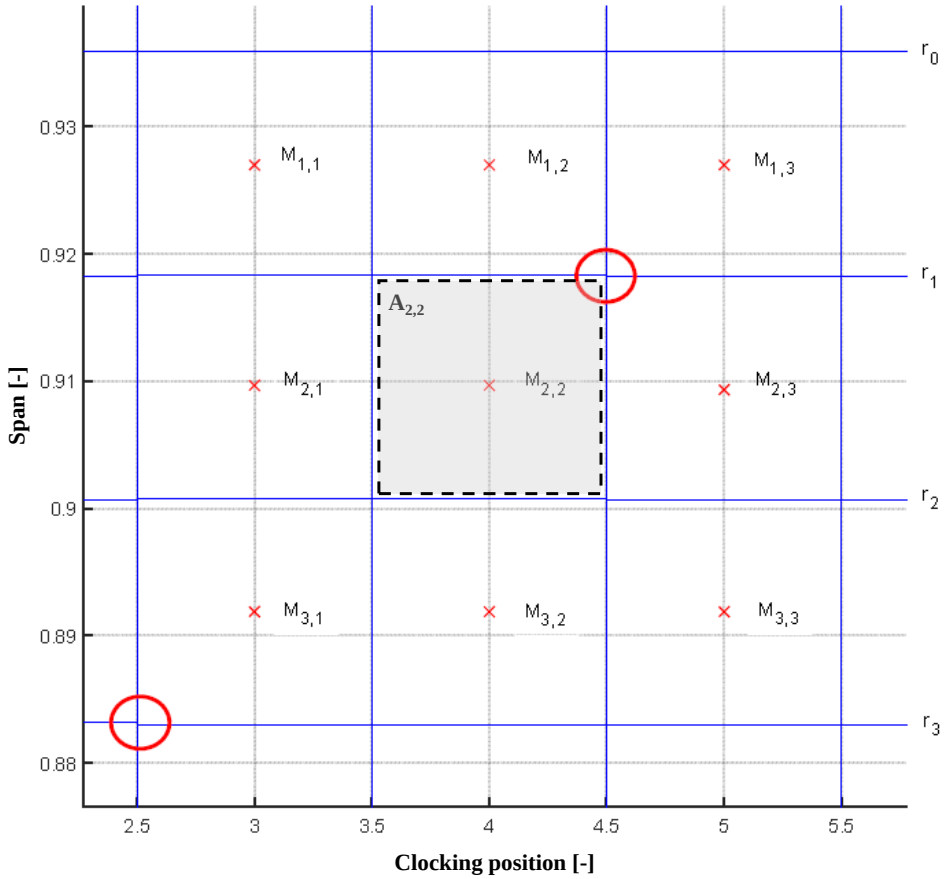

Figure 4.6: Distribution of the measurement grid

4.5 Uncertainty analysis

The knowledge of measurement uncertainties is essential to assess the quality of experimental investigations. Therefore, the uncertainties of the measurement chain, the probe measurement and of the introduced averaging methodologies are quantified.

The measurement chain of pressure and temperature measurement has been reviewed according to the "Guide to the Expression of Uncertainty in Measurements" (GUM) [73] that takes into account the recommendations given in DIN 1319-3 [28]. This guideline has been chosen as it is best suited for turbo machinery and has been used for similar test rigs (see e.g. Regina [115]). The fundamentals of this analysis have been published by Zimmermann et al. [163] and are therefore not further explained in detail. Table 4.2 summarizes the uncertainties for the essential measurement values.

Table 4.2: Combined standard uncertainties of flow parameters measured according to GUM [73]

Flow parameter	Unit	Uncertainty
α	[°]	0.10339
γ	[°]	0.15626
Ma	[-]	0.0008933
p_{t}	[Pa]	312.38
p_{s}	[Pa]	341.08
T	[K]	0.1299
η	[%]	0.39

4.5.1 Uncertainty of probe measurement

With the aim of proving if the present measurements lie within the range set by the theoretically determined uncertainties, the reference blading 2D TEWC BS has been measured before (in 2015) and after (in 2016) all later presented investigations. Hence, the influence of several mechanical assembly processes and the operating time of the brush seal (BS) is taken into consideration. The analysis is shown exemplary for the design point.

Figure 4.7 shows the angle distribution across the flow channel span of all measurement planes (MP) for both tests. Additionally, the deviation is shown in the diagrams below to visualize the deviations. The yaw angle α has been chosen, as the data of all pressure holes within the probe head is required for its determination. One can see that both tests nearly capture an equivalent distribution in all measurement planes (MP). It can also be seen in MP12 and MP22 that the largest deviation occur at 20% span where the channel vortex is located. As it is not exactly at the same radial position in both tests, the deviation in this area is at its maximum due to the fact that the absolute value at a discrete span position is compared. Therefore, the maximal mean deviation of $0.48°$ is larger than the deviation according to GUM.

The analysis of the total pressure distribution in Figure 4.8 also shows good matching of results for all MP. Despite the fact that the operating point stability, which is further discussed in Chapter 5, impacts the pressure level in MP10 directly, the maximal deviation is below 2‰. In MP12, the largest discrepancy of 0.7‰ also occurs at 20% span while the mean deviation of 84Pa is far below the calculated value of 312Pa. The highest mean deviation appears for the outlet pressure in MP22 that is also dependent on the OP stability and refers to the inlet pressure. One can recognize that the overall pressure level deviates by 278Pa while the radial deviations fluctuate by about ± 0.5‰. Nevertheless, the mean deviation is below 1‰ and lies in good agreement with the predetermined value shown in Table 4.2.

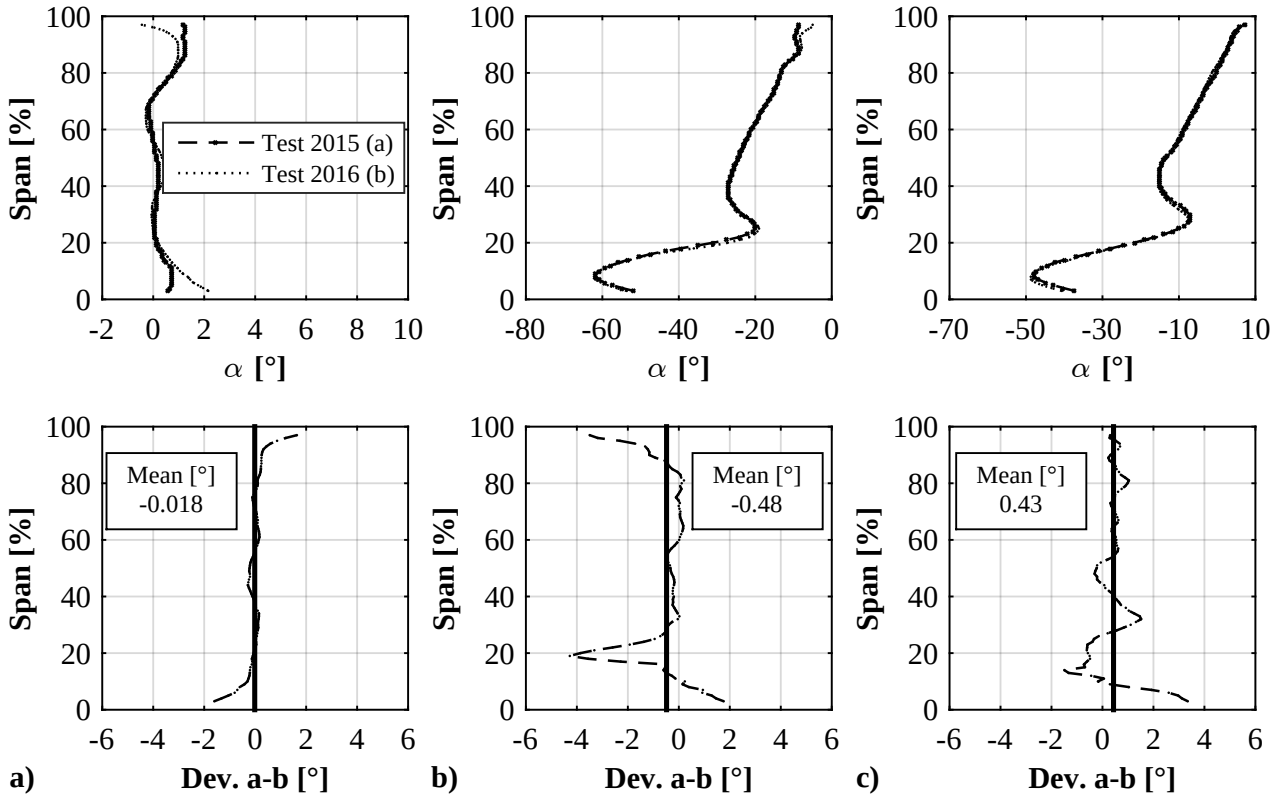

Figure 4.7: Analysis of the measured flow angle distribution in a) MP10, b) MP12 and c) MP22

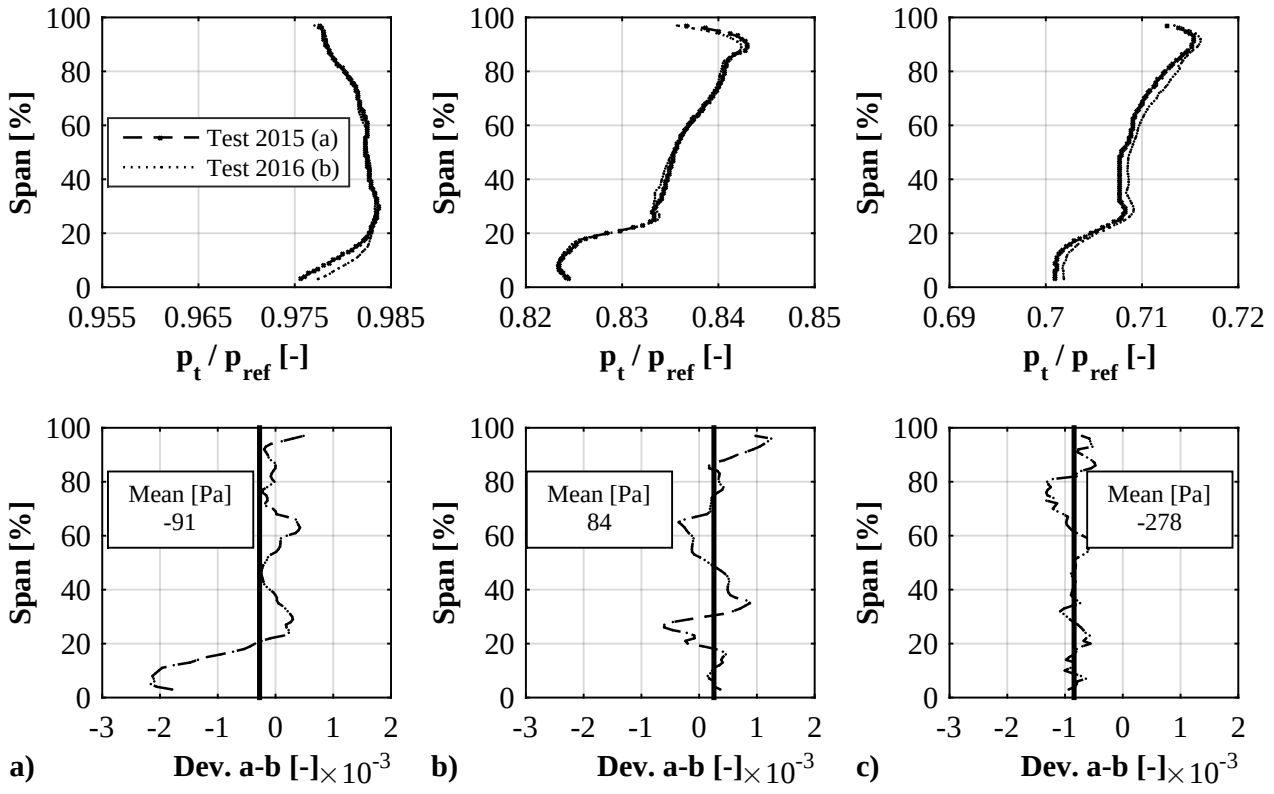

Figure 4.8: Analysis of the measured total pressure distribution in a) MP10, b) MP12 and c) MP22

Finally, the uncertainty of the total temperature measurement is shown in Figure 4.9. Here, it can be seen that the mean values of all measurement planes (MP) are below 0.03K, which is by a factor of four better than the predicted value of 0.1299K according to GUM. The measurement supports the method of the calibration of all temperature probes against the TP that is used in MP10.

However, it is likely that the absolute value of all measurement planes (MP) has an uncertainty according to GUM. It can be stated that the uncertainty of the efficiency is related to the mean deviation shown here, as it is calculated via the temperature differences between all measurement planes (MP). Thus, an absolute shift of e.g. 0.1K in all measurement planes (MP) would not have an influence on the derived efficiency.

It can also be stated that all vortex structures are well captured in size and location. To capture the largest temperature deviation, the here shown values of +0.012K at the inlet and -0.022K at the outlet temperature are assumed. This very uncertainty of 0.034K leads to an uncertainty in efficiency of about 0.108%, which is three times smaller compared to GUM (0.39%).

The data measured in 2015 with 3HP and 5HP is analysed and discussed additionally to also consider the blockage effect and manufacturing tolerances of the probes. For this purpose, MP12 has been chosen for this investigation as the flow field is the most complex and the intrusive impact of

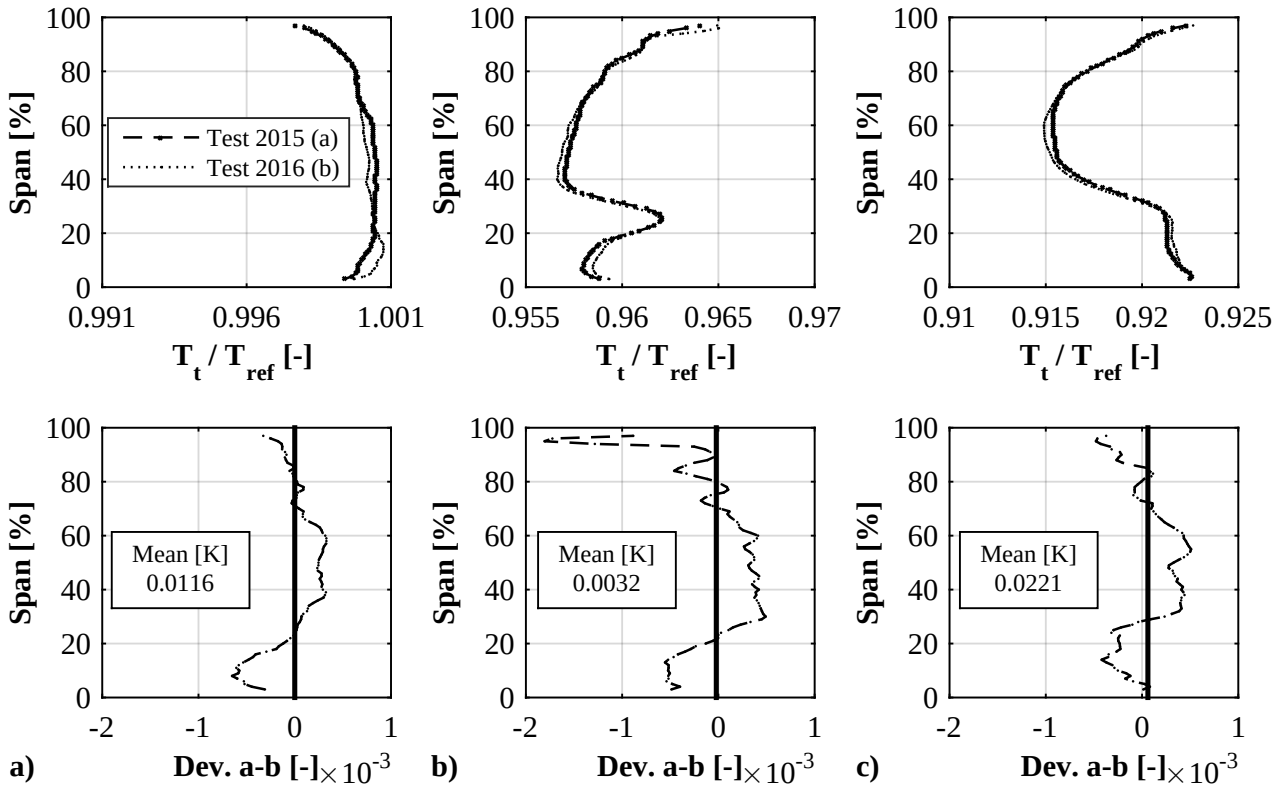

Figure 4.9: Analysis of the measured total temperature distribution in a) MP10, b) MP12 and c) MP22

the probe stem is expected to be higher than in MP10 and MP22. Furthermore the interaction of rotor and stator exists, and therewith an impact of the probe geometry can be identified more clearly.

Figure 4.10 a) shows the comparison of the measured yaw angle in MP12. One can see, that the deviation is of the same as it was shown for the different test days in Figure 4.7. The biggest discrepancy is caused by the channel vortex that has a slightly varying position. Another difference can be recognized close to the casing that could be a result of the different probe head designs. Globally, the mean deviation of $0.41°$ is equivalent to the deviation that was determined before via 5HP ($0.48°$).

For the total pressure distribution, the curve shape of the 3HP seems to be more accurate at 20% span as a turning point of the channel vortex is depicted more in detail than for the 5HP measurement. The resulting local deviation of 3‰ does still meet the required tolerance, however, this example shows that redundant tests with different probe designs are necessary to identify weaknesses of the measurement procedure and to validate numerical simulations correctly. The mean deviation of 240Pa lies in good accordance to the predictions according to GUM [73].

Although, the TP are self contained and are not affected by the pressure probe design directly, the total temperature distribution has to be considered as well to determine the impact of the different

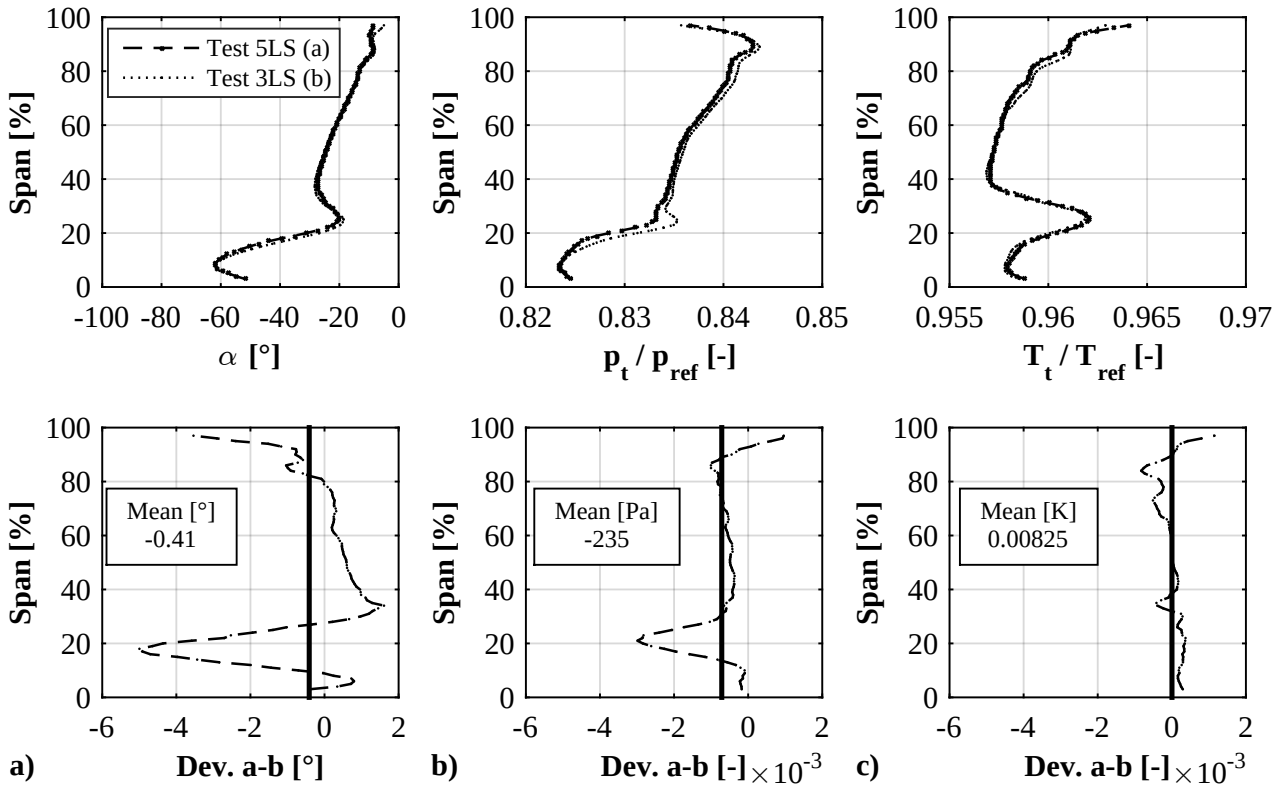

Figure 4.10: Comparison of data measured in MP12 with 3HP and 5HP a) Yaw angle α, b) Total pressure and c) Total temperature

pressure probe designs. This is justified by the fact that the total temperature is a function of the measured probe temperature, the recovery factor and the Ma-number, which is calculated by means of the pressure probe data. Without doubt it can be seen in Figure 4.10 c) that the qualitative distribution of the 3HP and 5HP measurement is identical. Even close to the casing the deviation is slightly above 1‰ and therefore negligible.

4.5.2 Uncertainty caused by averaging methodology

As the previous section focussed on the uncertainties that are caused by the measurement itself, the influence of the post processing is analysed in this section. Therefore, both introduced averaging methods according to Traupel (TR) and Kreitmeier (KM) are applied on the data set of the 5HP measurement in 2015.

Figure 4.11 shows the distribution of the polytropic efficiency across span. It has to be mentioned that this analysis does not claim to depict the exact change of one streamline. Here, the measured data of each measurement plane (MP) is compared for each radial position to what is permitted as all probes measure at the same percentage span position within their respective measurement plane (MP). Furthermore these diagrams should serve to qualitatively visualize how the averaging methods differ.

By looking at the turbine's efficiency, it is observed that both methods show an equivalent distribution across span. However, the deviation plot below states that both methods do not deviate just by a constant offset. Especially in the hub area between 10% and 40% span, local differences of up to 0.4% can be seen. The same tendencies can be found by calculating the efficiencies for stage 1 and stage 2 separately, while the maximal amplitudes are even higher compared to the turbine's efficiency.

The global analysis of the polytropic efficiency of all OP (see Figure 4.12) shows that the trends are captured by both averaging methods equivalently. It can be seen that the largest deviations occur for OP1, which results from the fact that the flow shows larger secondary flow losses and the respective vortex phenomena have a major impact on the efficiency calculation as it was explained before. Regarding all OP a scatter band of 0.157% results for the overall efficiency calculation. For stage 1, a value of 0.227% has been found while stage 2 shows the biggest discrepancy of 0.351%. This value is roughly of the same amount that was calculated utilizing GUM (0.39%).

In summary it can be stated that the uncertainties of the measurements are well known. The analysis of the reference blading before and after the later presented investigations aimed to consider wear of the brush seal (BS), the impact of the assembly processes as well as recalibration of the pressure and temperature transducers during the testing period. Also, the influence of the probe intrusion and

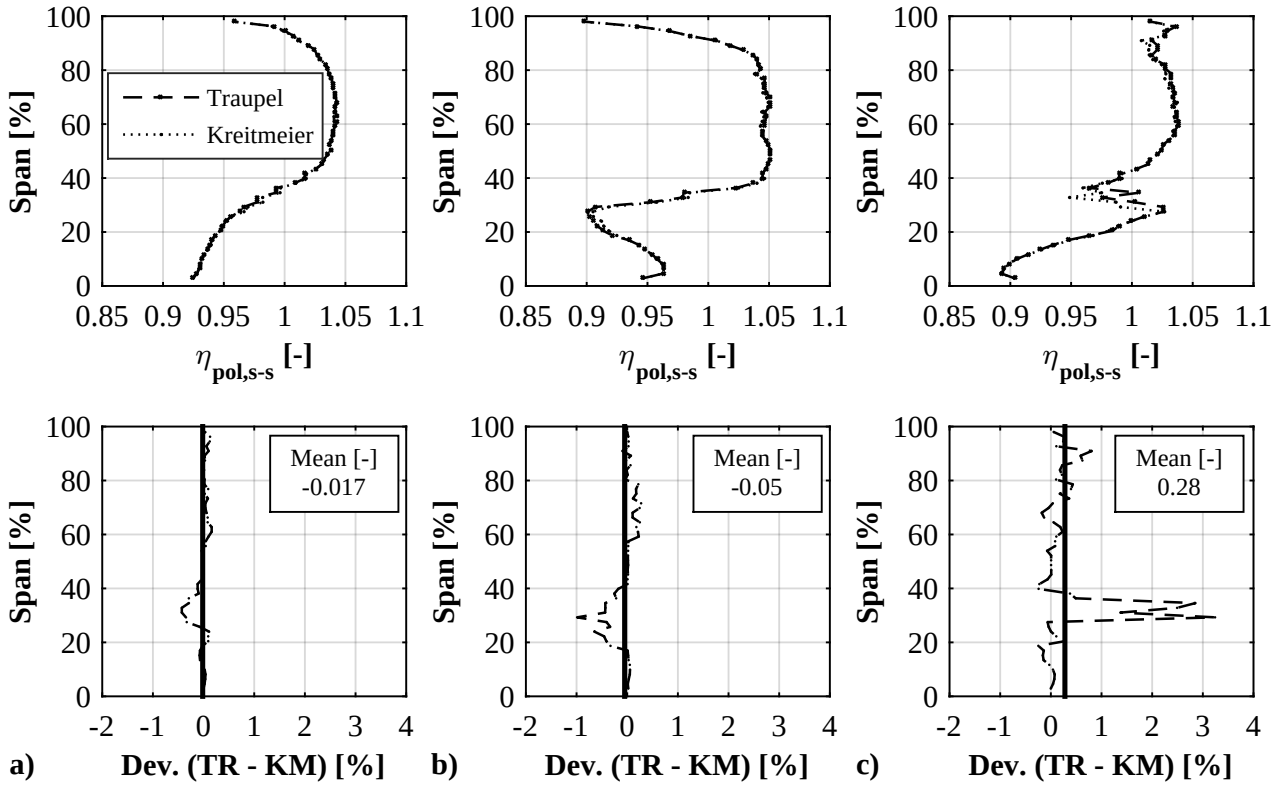

Figure 4.11: Comparison of the polytropic efficiency of OP3 across span calculated with the methods of Traupel (TR) and Kreitmeier (KM) for: a) Turbine, b) Stage 1 and c) Stage 2

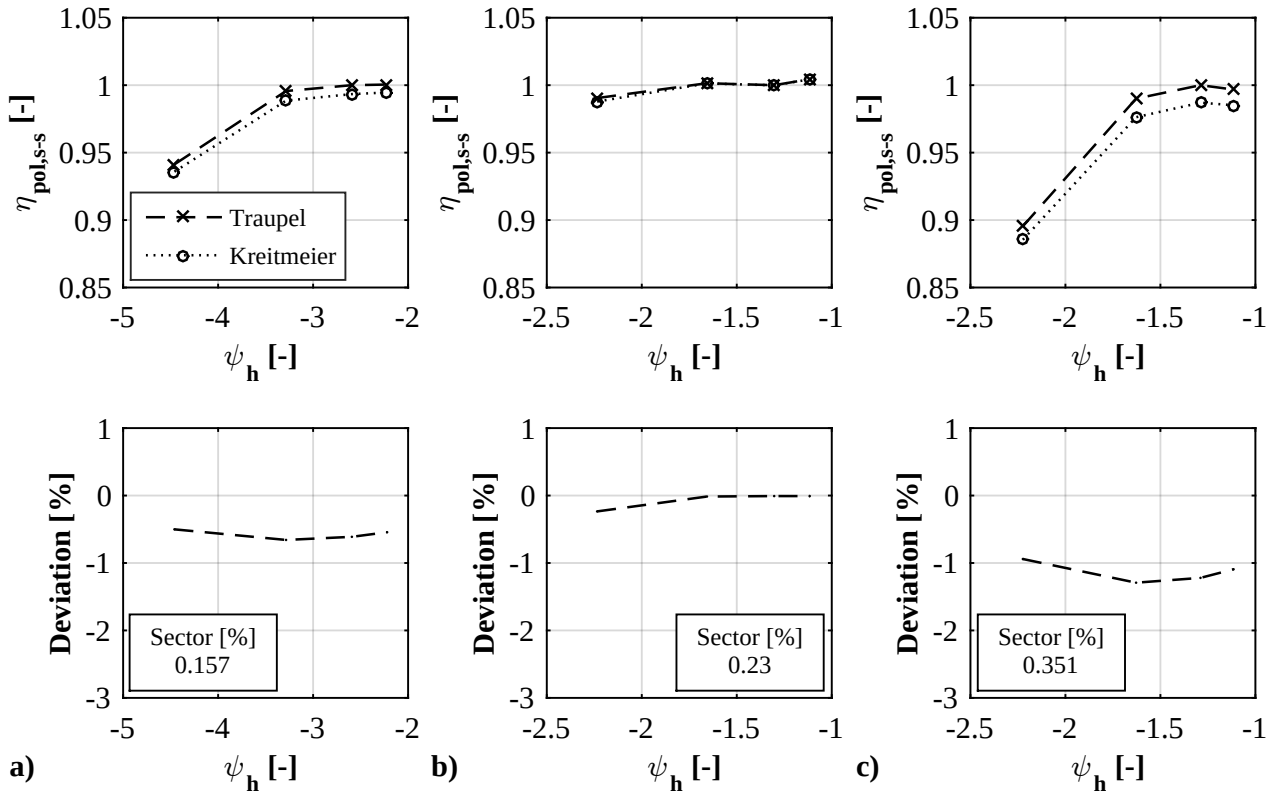

Figure 4.12: Comparison of the global polytropic efficiency of all OP calculated with the methods of Traupel (TR) and Kreitmeier (KM) for: a) Turbine, b) Stage 1 and c) Stage 2

respective blocking effects have been considered by the redundant measurement with 3HP and 5HP. The application of both averaging methods is necessary for the complex phenomena that are investigated as their sensitivity to vortices has been shown. Both methodologies, however, are evaluated on on the results according to Traupel. This will be shown as this method is further established and therefore more suitable to compare the present results to international investigations.

Furthermore, these validation tests have shown that the uncertainties of the rig lie in good accordance to the predictions according to GUM. However, especially the temperature measurement is way more accurate, which is of highest significance to determine the changes in efficiency of the different blading types. Therefore, the following Table 4.3 shows the resulting uncertainties of the test data.

Table 4.3: Uncertainties of flow parameters resulting of reference tests

Flow parameter	Unit	Uncertainty
α	[°]	0.48
γ	[°]	0.51
Ma	[-]	0.0012
p_{t}	[Pa]	280.00
p_{s}	[Pa]	292.12
T	[K]	0.034
η	[%]	0.108

4.6 Summary

In this chapter it was shown, how the measured data is post processed. Two methods were introduced that allow the derivation of leakage flows trough labyrinth seals as well as through brush seals. Additionally the measurement of mechanic power was described.

The efficiency of the turbine is calculated by means of two methods. One method was shown that includes the mechanic power and therewith bearing losses and friction losses. However, this method is not suitable to determine the stage efficiency of both stages separately. Therefore, a second method was introduced that is based on the probe measurements only.

Two data averaging methodologies according to Traupel [142] and Kreitmeier [83] were applied on the present test data and compared to each other. It was shown that the efficiency calculated according to Traupel is higher compared to the one derived with the equations of Kreitmeier. Furthermore, a detailed analysis across the span showed that the efficiency did not just show a constant offset. The occurring vortex phenomena impact both averaging methodologies significantly. Therefore, the methodology of Traupel has been chosen to be used for the following analysis at it is used more often in common literature.

An uncertainty analysis of the flow parameters has been conducted according to GUM [73]. Two redundant tests were carried out before and after all measurement campaigns to evaluate the consistency of each data set. The results of the comparison of both tests were in good agreement with the theoretical approach according to GUM. However, especially the temperature measurement showed better consistency than it was calculated theoretically. The resulting uncertainty of the efficiency that was derived to 0.108 is much smaller than the uncertainty calculated via GUM (0.39). Therefore, it is reasonable to discuss the influence of TEWC on the turbine's efficiency.

5 Performance of the turbine

All methodologies introduced previously are applied to determine the performance of the turbine and therewith, also to analyse the various blading and endwall configurations regarding their influence to the flow.

In this section it will be shown that all investigations were conducted with equal boundary conditions by comparing the operating point stability of each test day. Furthermore, the amount of leakage flow of each labyrinth as well as the brush seal test is analysed to verify an equal impact for the different airfoil investigations.

Then, the efficiency of the turbine is benchmarked. At first, the differences between the BASE, TEWC, and TEWC-V set ups are analysed for labyrinth seal (LS) and brush seal (BS) separately to highlight the characteristics of the endwall contouring feature regarding its sensitivity to leakage flow (LF) interaction. Later, the airfoil configurations are kept and the comparison is conducted for both sealing configurations to put the focus on the leakage flow interaction, exclusively.

5.1 Operating point stability

Due to the small changes in efficiency that are expected by application of TEWC, constant inlet and outlet conditions are of highest importance. Figure 5.1 shows the deviations of all values, which are required for estimation of efficiency, during the measurement time of all operating points (OP) and configurations.

It can be seen, that the inlet temperature of $90°$C varies with a maximal amplitude of about $\pm$0.3K during a test day, which is equivalent to 0.83‰. The spread of the pressure level at the inlet and outlet lies in a range of $\pm$300Pa. This corresponds to a relative deviation of 0.94‰, referred to the inlet pressure level of 3.2bar and 1.3‰ referred to 2.3bar outlet pressure respectively. The resulting pressure ratio of 1.387 deviates by about 2.16‰ from its mean value. The four diagrams in the bottom of Figure 5.1 show the rotational speed of the turbine at each operating point (OP). Here it can be seen that the highest deviation from its mean is about 8RPM, which is 2.25‰ in OP1 and 1.55‰ in OP4. Consequently, the deviations at OP2 and OP3 lie in between these values.

On basis of the data shown here, it can be stated that all tests were conducted under similar operating conditions. Therefore, the differences between the different configurations that are further discussed, can be related to the respective feature that lies in the focus of the present analysis.

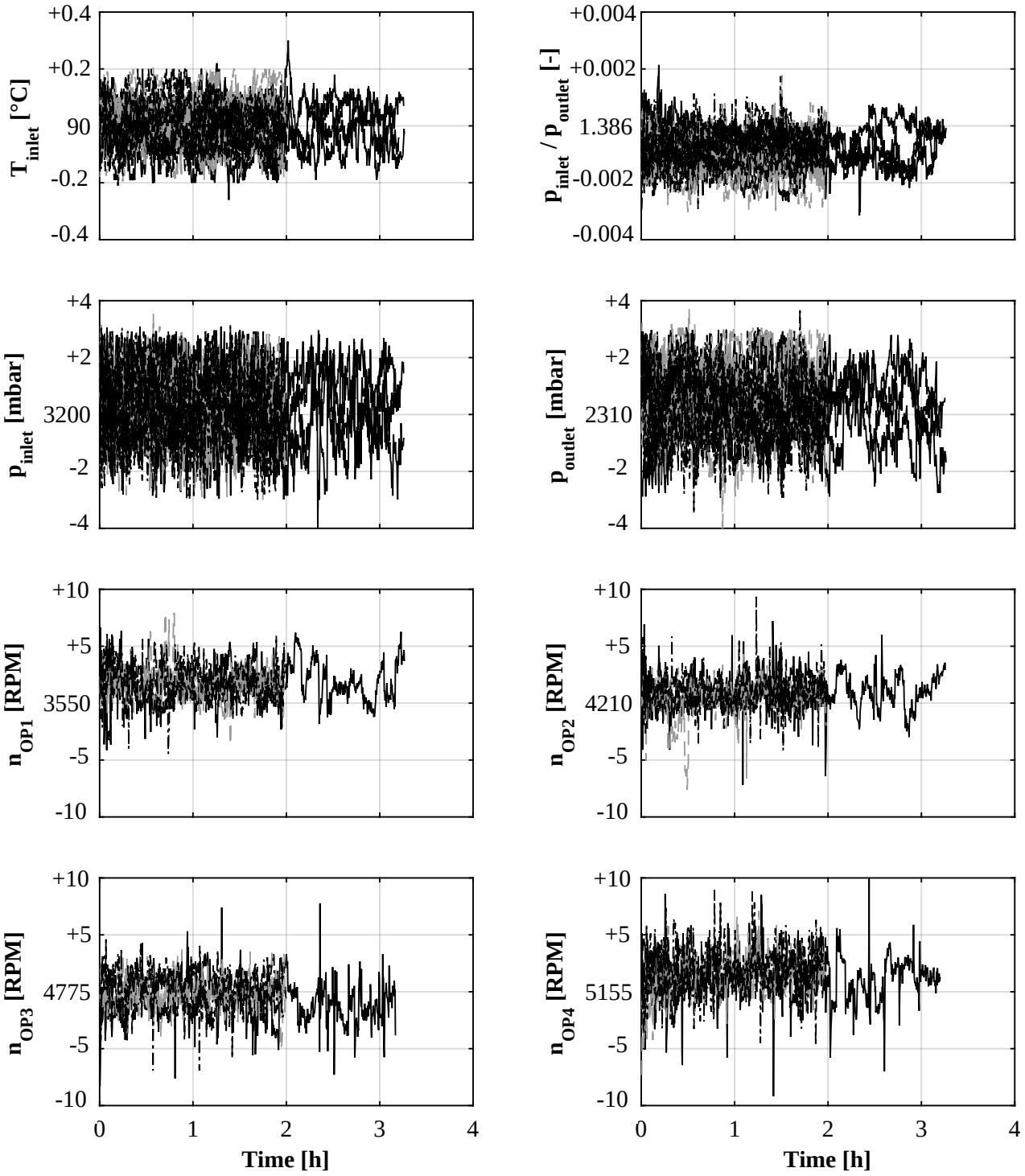

	$\overline{T}_{inlet}$	$\overline{\pi}$	$\overline{p}_{inlet}$	$\overline{p}_{outlet}$	$\overline{n}_{OP1}$	$\overline{n}_{OP2}$	$\overline{n}_{OP3}$	$\overline{n}_{OP4}$
	[°C]	[-]	[mbar]	[mbar]	[RPM]	[RPM]	[RPM]	[RPM]
——— 3D BASE	90.001	1.3852	3200.7	2310.7	3551.8	4211.1	4774.2	5156.3
– – – 3D TEWC	90.024	1.3851	3200.3	2310.4	3551.9	4210.8	4774.6	5156.7
–·–·– 3D TEWC-V	90.037	1.3854	3200.6	2310.2	3551.6	4211	4775.2	5156.7

Figure 5.1: Comparison of the boundary conditions (inlet temperature, pressure ratio, inlet pressure, outlet pressure and speed), set for each OP and all investigated configurations

In addition to the conditions that are set during the test, the resulting LF has to be analysed in advance of the investigations of other features. Figure 5.2 shows for the design point OP3, how the pressure drops within the cavities that are located above the shroud of rotor 1. It can be seen that for the brush seal (BS) configuration, which is shown in the left bottom of this very figure, the pressure drops nearly exclusively between measuring position 3 and 4, where the brush seal (BS) is located. It has to be kept in mind that the pressure level at the inlet and outlet of the sealing is set by the main flow pressure level. Despite these finding, the pressure drops linearly across all cavities for the labyrinth seal (LS) configuration where the brush seal (BS) is replaced by a third fin that is designed equal to the adjacent ones. These effects also occur for the other operating points (OP), similarly.

Applying Equations 4.5 and 4.6 to the measured data provides the resulting leakage flow (LF) for both sealing configurations (depicted in Figure 5.3).

It can be seen that the leakage flow (LF) of all BS tests lies in a range of 0.105% - 0.115% in reference to the respective main flow (MF) of each operating points (OP). Only small variations below 1g/s are a result of the variation of the operating point (OP) and speed respectively. Also a change of the airfoil configuration does not show significant changes in leakage flow (LF) due to the overlapping bristles that ensure equal contact to the shroud surface at any circumferential velocity.

Another picture is drawn by comparison of the labyrinth seal (LS) test. On the one hand, the leakage flow of all configurations is significantly higher and lies between 0.805% to 0.828% at the design point. Moreover, the different operating points (OP) have more significant influence that result in a range of 0.04%. Also the manufacturing tolerances of the airfoils and therewith the shroud diameter impact the resulting leakage flow (LF) as the clearance between the fins changes. That is the reason why the BASE and the TEWC-V configuration that were measured with the same rotor, show an equivalent leakage flow (LF) while the level of the TEWC configuration is slightly lower.

The here shown results justify two statements:

Firstly, it can be stated that the difference in leakage flow (LF) between both sealing configurations is large enough to identify the impact of leakage flow (LF) to the TEWC due to the nearly non existent leakage flow (LF) of the brush seal (BS) configuration.

Secondly it has to be considered, that the deviation of about 5% between all operating points (OP) as well as the different airfoil configurations seems to be large for the labyrinth seal (LS) configuration on a first view. However, it has to be considered that the resulting difference of 0.5% is of the same for the brush seal (BS) configuration if it is referred to the overall leakage flow (LF) level. This is due to the fact that the leakage flow (LF) is $\approx$8 times higher for the labyrinth seal (LS)

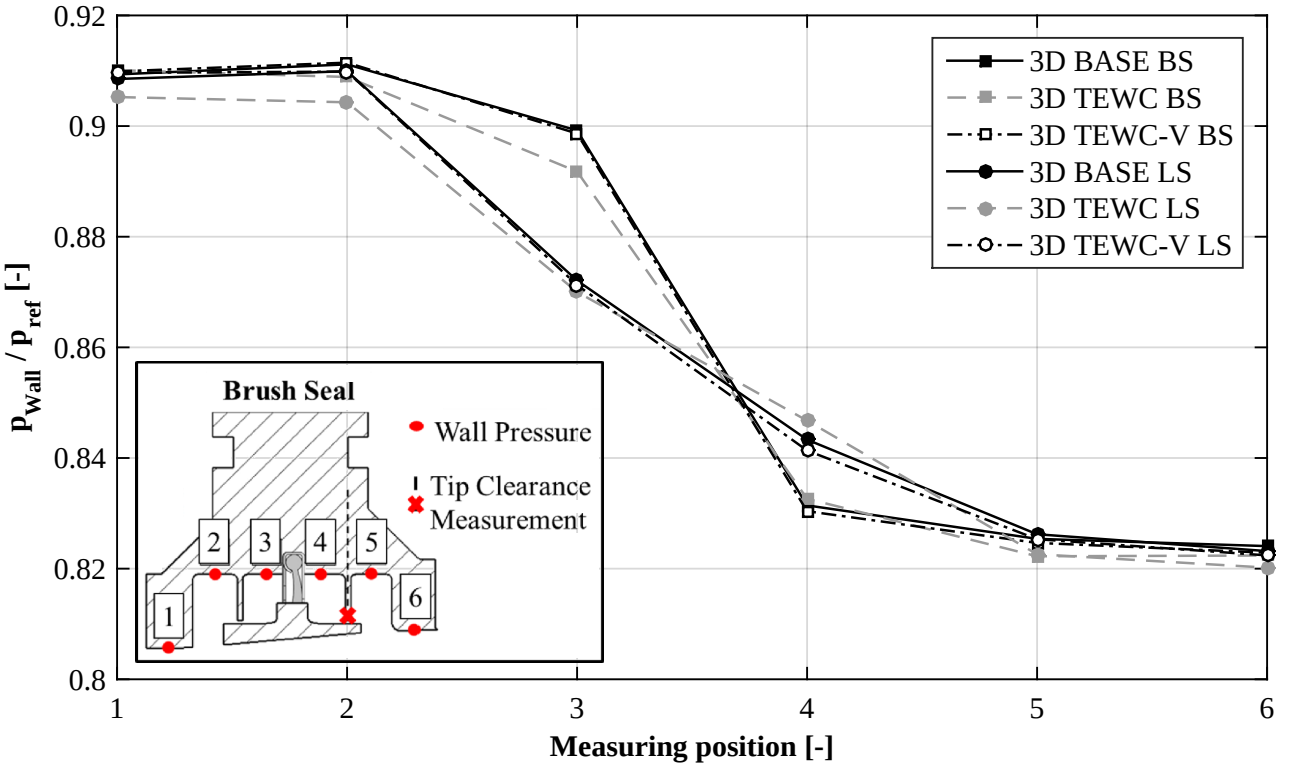

Figure 5.2: Pressure distribution through the cavities of rotor 1 for OP3 and all investigated configurations

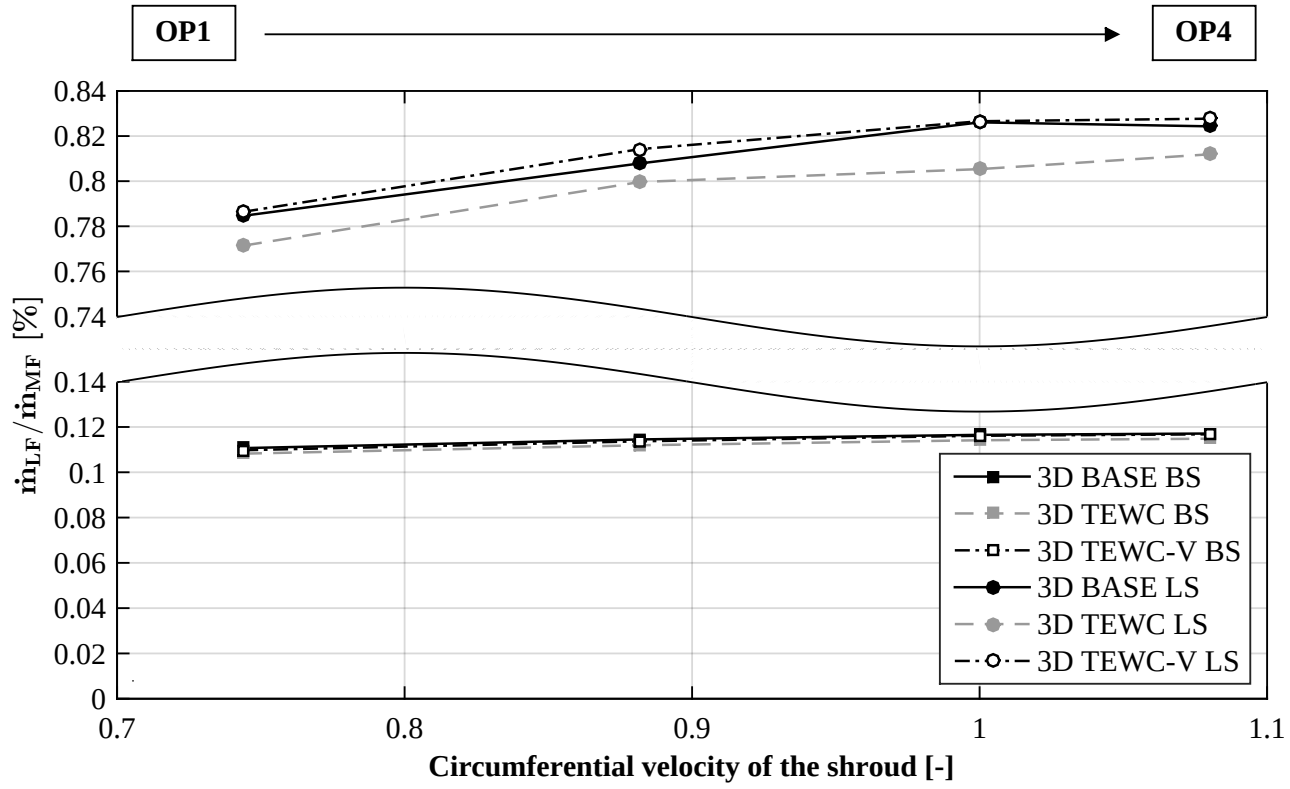

Figure 5.3: Comparison of the resulting leakage flow referred to the corresponding main flow of each OP and all investigated configurations

configurations. Therefore, it is justified to discussed equal leakage flow (LF) conditions for all configurations and the respective operating point (OP).

5.2 Benchmark of efficiencies

It was shown in the previous Section 5.1 that all investigations were conducted with nearly equal boundary conditions. The following subsection is dedicated to answer questions of the TEWC performance as well as to investigate the influence of leakage flow (LF) in combination with endwall contoured blading. The design point OP3 serves as reference for all subsequent discussions in its respective configuration. The left hand side of each figure shows the absolute distribution of the investigated value while a detailed plot of the present deviations is given on the right hand side. To evaluate if the endwall contouring has the potential to increase the aerodynamic efficiency of turbines, the test results of a configuration with hub and tip sided contoured vanes (3D TEWC-V) and contoured vanes as well as contoured blades (3D TEWC) are compared against a reference design of this kind of airfoil (3D BASE) that does not have any contouring. These investigations are carried out separately with a brush seal (BS) and a labyrinth seal (LS). The prefix "3D" is omitted for purpose of a better legibility. Figure 5.4 illustrates the configurations described.

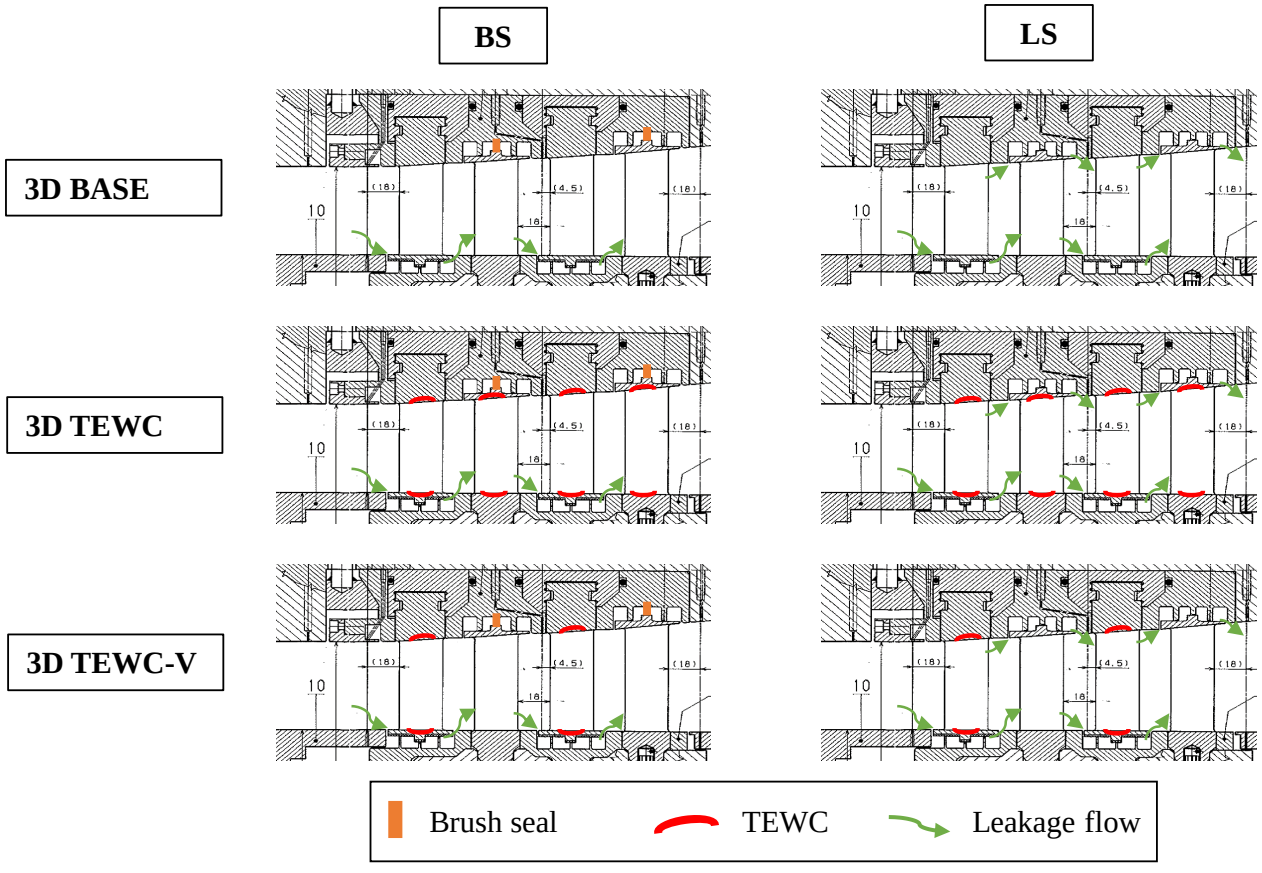

Figure 5.4: Summarizing illustration of all investigated configurations and the occuring leakage flow

5.2.1 Baseline vs. tangential endwall contouring

Comparison of blading configurations with brush seals

At first, the brush seal (BS) configurations are discussed as the occurring differences can be related to the contouring feature, because of the practical absence of leakage flow (LF).

At the top of Figure 5.5 an overview of the resulting power is given. This power is measured via the force cell of the water brake. It can be recognized that the TEWC configuration shows nearly the same power output level compared to the BASE configuration for all operating points (OP). It has a slightly higher output in OP2, while it is lower in OP3. In contrary, the power output of the TEWC-V configuration is higher for all operating points (OP), especially in OP1 and OP2. However, it has to be mentioned, that the amount of maximal 5kW lies within the fluctuation range during the test and could therefore also be caused by measurement uncertainties.

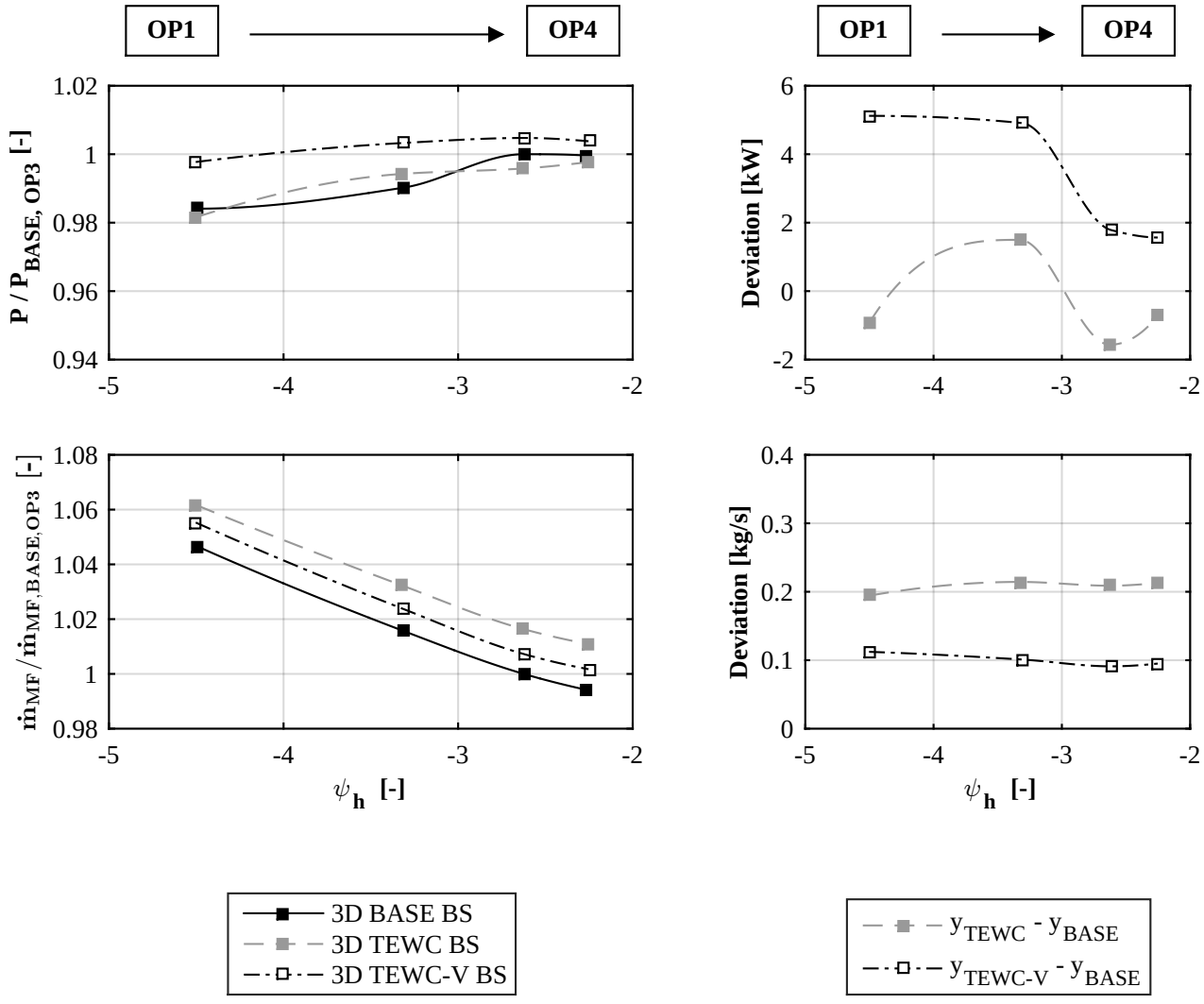

Figure 5.5: Comparison of the resulting power and mass flow for each OP and all investigated configurations with brush seals

Having a look at the main flow (MF) it can clearly be stated that the main flow (MF) level of the TEWC-V configuration is ≈100g/s higher compared to the BASE configuration for all operating points (OP) due to the increased cross-sectional flow area. This lies in good accordance with the measured main flow (MF) of the TEWC configuration that is also contoured at the rotor and has therewith twice the amount of surface extension as compared to the TEWC-V design. Therefore, the resulting main flow (MF) is ≈200g/s larger than BASE for all operating points (OP). It has to be added, that all of the data shown here is gathered with the orifice upstream the turbine and not calculated by means of the probe data.

Both parameters, power and main flow (MF), are utilized to determine the polytropic efficiency according to Equation 4.13. Therefore, all effects such as friction between the shroud and brush seal (BS), bearing losses and so on are taken into consideration. The resulting efficiencies for all operating points (OP) are shown in Figure 5.6 in the first line. One can see, that TEWC-V lies on the same level as the BASE configuration for OP1 and OP2 while the efficiency drops by about ≈0.25% for the DP and in part load. The same tendencies can be seen for the fully contoured blading (TEWC), however, also the efficiency of OP1 suffers and the efficiency in part load (OP4) drops by about ≈0.6%.

In the following section, the efficiencies that are calculated with Equation 4.12, are discussed. Equation 4.13 can only be applied for the whole turbine and a discussion of each stage based on Equation 4.13 is not possible. The efficiencies shown are calculated with the probe data and do not include frictional losses. That is why the curve of the TEWC design in Figure 5.6 is shifted slightly towards higher efficiencies, while the tendencies are the same as in previous diagrams. On a first sight it appears that endwall contouring is not an appropriate method to increase the efficiency of turbines. Having an individual look at both stages it turns out that this statement cannot be made that easily.

In stage 1, the endwall contoured vane (TEWC-V) causes an obvious increase in efficiency for OP1 to OP3 with values of more than 1% and even almost 1% for the design point (OP3). In contrary, the fully contoured blading is on the same level as the reference blading in OP1 and OP2 and then performs worse down to ≈1.8% in part load. That leads to the assumption that the contouring of the vane optimizes the inflow and the performance of the first rotor row, significantly. An additional contouring of the rotor seems to compensate this beneficial upstream condition thus the resulting output of the stage gets worse.

More interesting is the analysis of the efficiency of stage 2 as this stage operates under more realistic inflow conditions than stage 1 (which can be expected to prevail in a multi-stage environment of deployed turbines). Here, the trend is flipped and the TEWC configuration shows the best results. Furthermore, it is worth mentioning that all operating points (OP) shown nearly the same gain in efficiency of about ≈0.7%. The TEWC-V performance lies far below baseline and especially the

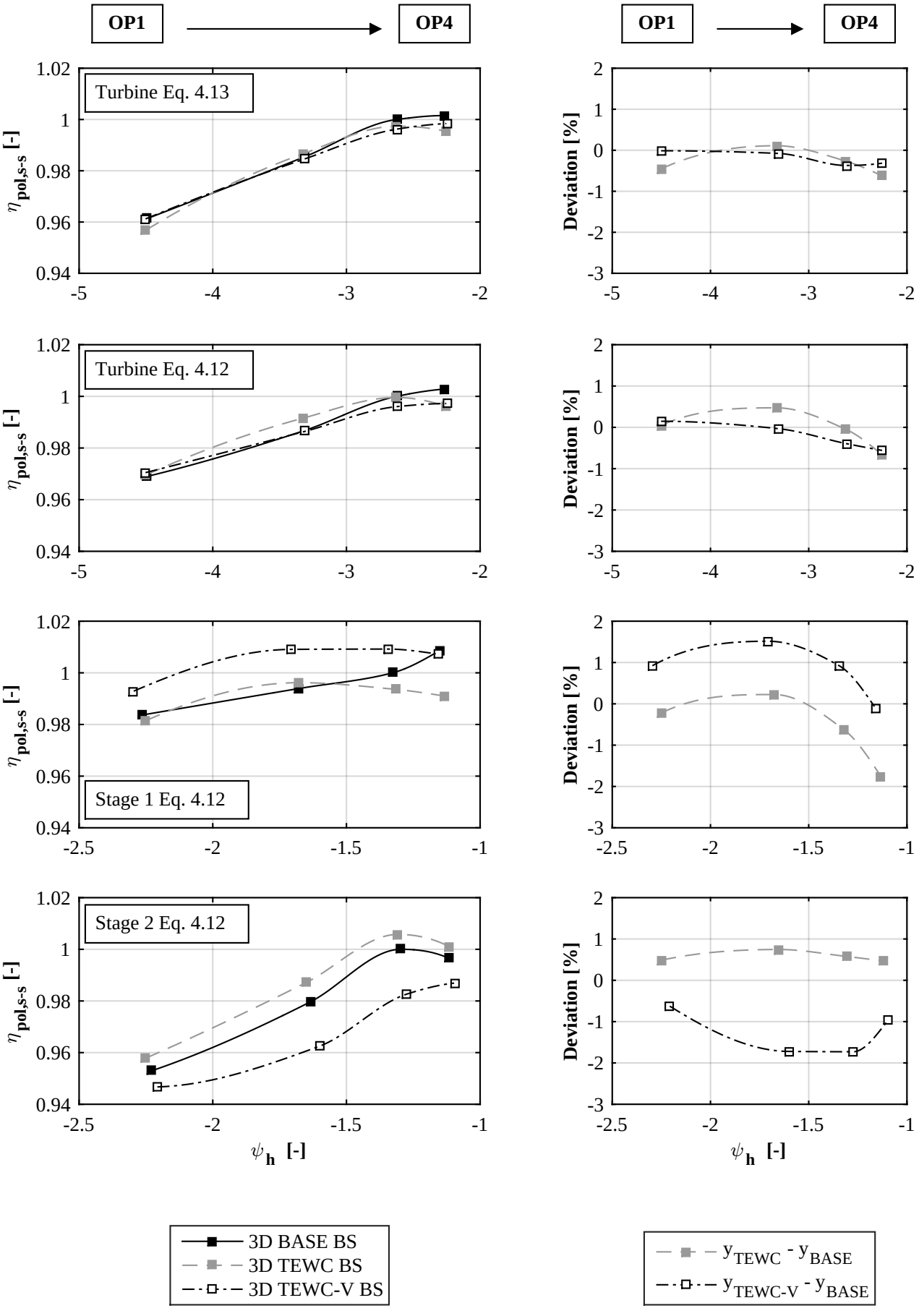

Figure 5.6: Comparison of the resulting polytropic efficiencies for each OP and all configurations with brush seals

design point (OP3) looses nearly 1.8%.

Due to the fact that the behaviour between stage 1 and stage 2 differs so much, a detailed analysis of the efficiency across span is performed to determine where benefits and losses occur within the flow channel to further optimize the endwall contouring. These diagrams do not claim to depict the efficiency of a streamline, as this is not a feasible option for the test. Instead, the reader may interpret these diagrams qualitatively to identify regions across span, that are influenced by the rotor or the casing sided contouring.

Considering both stages by comparing the turbine's efficiency it can seen in Figure 5.7 that for TEWC-V almost no change occurs for OP1 and OP2. For OP3 the overall level is lower and a negative peak can be seen in the hub region at ≈35% span. For OP4 this is also the case, however, no deviation can be seen in the upper channel area. The distribution of the full contoured blading (TEWC) is much more complex. An increased efficiency can be observed for all operating points (OP) close to the casing as well as in the centre area because losses occur at the hub and near the casing at ≈85% span.

An isolated view of stage 1 shows, that the benefit for TEWC-V is mainly caused by changes of flow in the hub region up to ≈40% span for OP1 to OP3. Small losses can be seen close to the casing. The worse overall tendencies of the TEWC configuration result from losses close to the casing as well as between 0 and 30% span where the passage vortex (PV) is located.

In stage 2, TEWC-V losses occur especially for OP2 and OP3 nearly across the whole span with peaks in the PV area at 30% span that also exist in OP1 and OP4. For TEWC, a massive increase in efficiency can be identified close to the casing and also improvements in the centre region, especially in OP4. However, also negative peaks exist close to the PV.

By taking into consideration that the first stage of the turbine is placed downstream a honeycomb structure and therefore, does not have realistic inflow conditions and due to the fact that common turbo machines are running with multiple stages, it can be stated that the TEWC configuration has the potential to increase the efficiency of turbines in case that the effect that is measured in stage 2 can be reproduced within the following stages. The detailed investigation of the reason for these findings are presented later on in Chapter 6.

However, these findings do not consider any influences of leakage flow (LF) that occur in reality. Therefore, the results with labyrinth seal (LS) are discussed in detail.

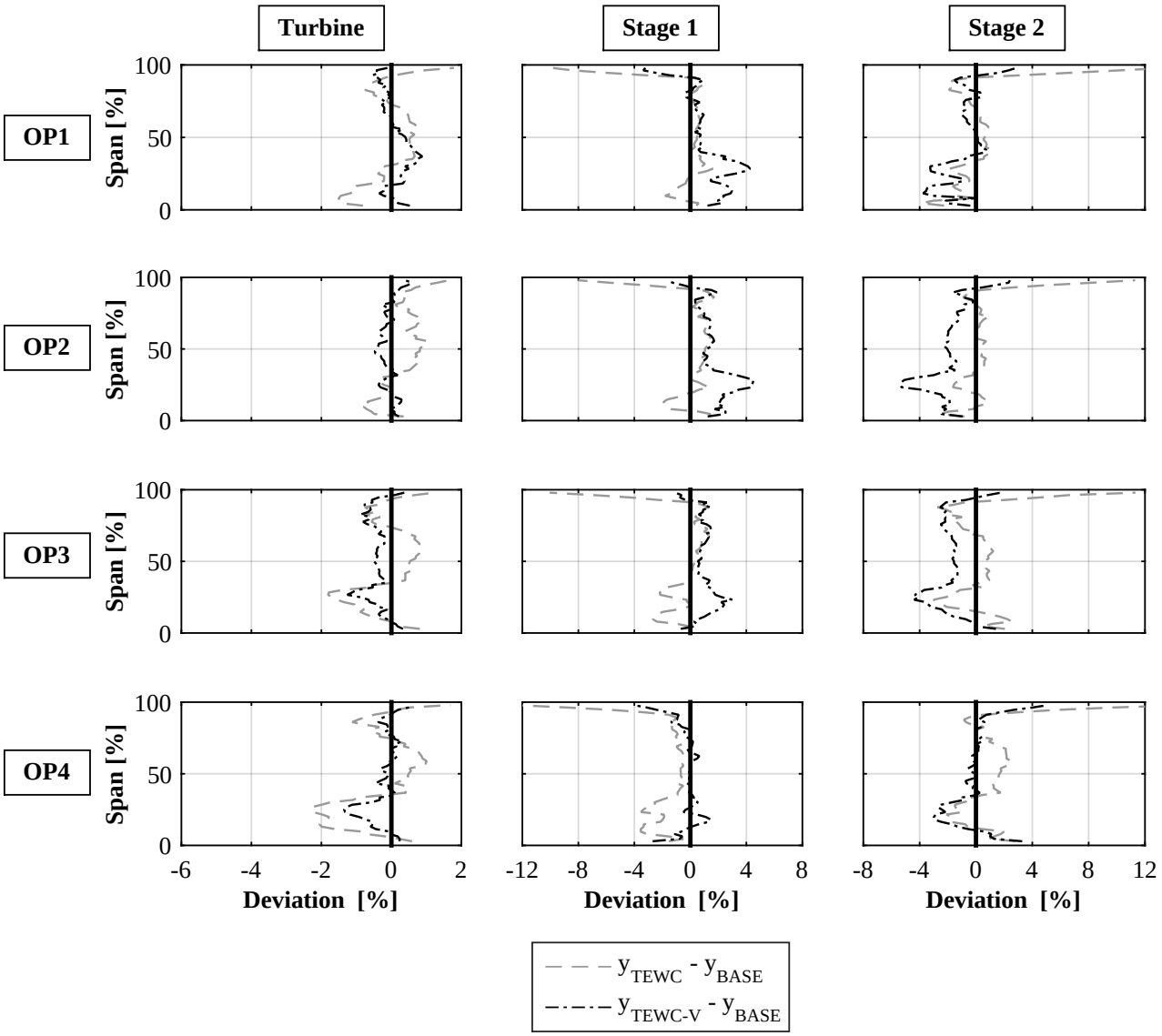

Figure 5.7: Detailed analysis across span of the resulting polytropic efficiencies for each OP and all configurations with brush seals

Comparison of blading configurations with labyrinth seals

In Figure 5.8 it is shown that the power output for the BASE set up is the highest one of all investigated variants. The TEWC-V configuration shows the smallest deviation in OP1 and deviates almost linearly up to 4kW in OP4 while the full contouring shows a nearly constant offset of about 2kW. An equivalent tendency like for the brush seal (BS) discussion can be seen by observing the main flow (MF). The main flow (MF) of the TEWC-V configuration is increased by ≈70g/s while a shift of ≈115g/s occurs for the TEWC design. A lower change compared to the brush seal (BS) investigations was expected as more leakage passes the sealing and fewer fluid participates the energy conversion.

Again, the polytropic efficiencies of the turbine and both stages are summarized in Figure 5.9 in this case for the labyrinth seal (LS) configuration. Globally, including friction according to Equa-

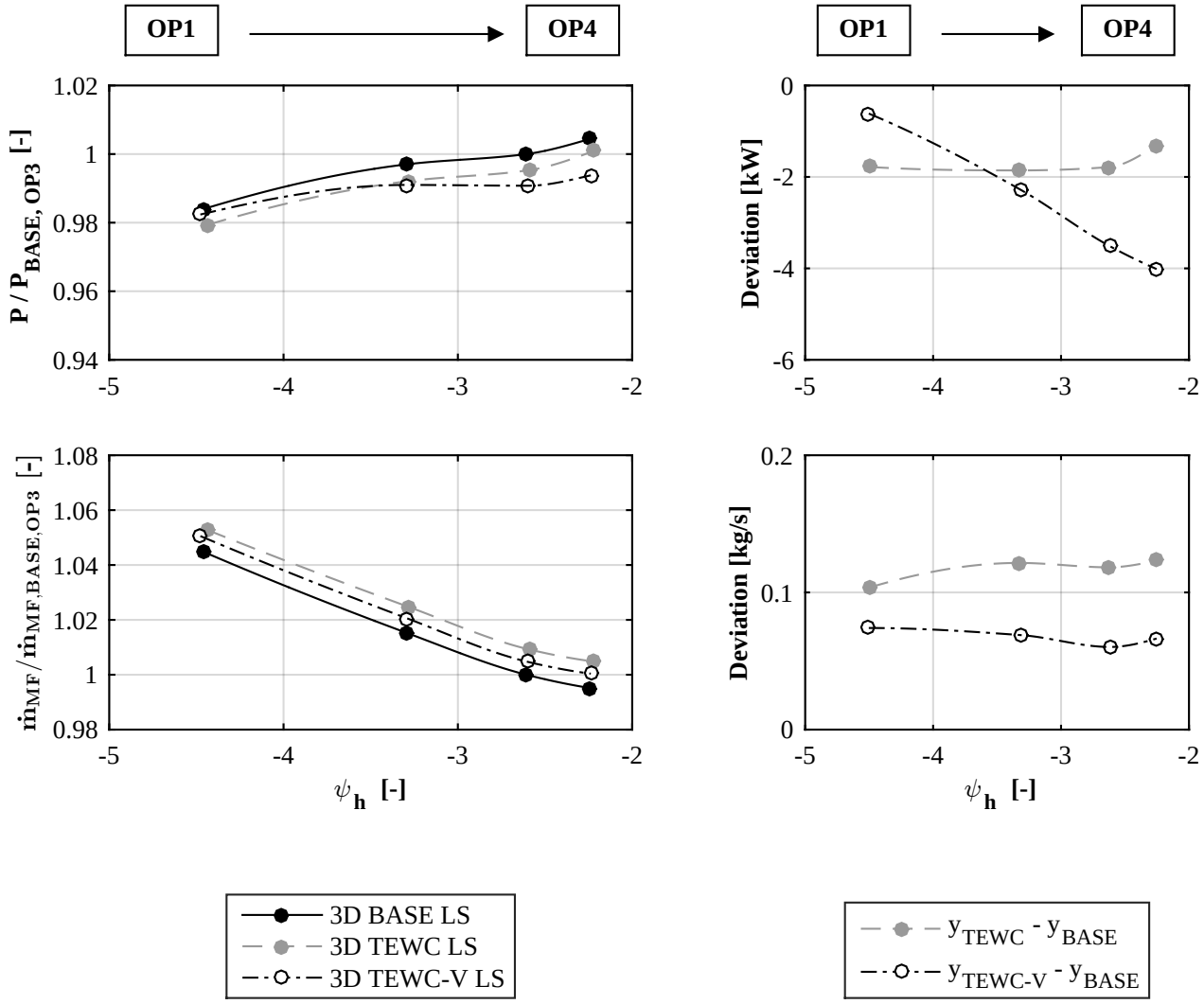

Figure 5.8: Comparison of the resulting power and mass flow for each OP and all investigated configurations with labyrinth seals

tion 4.13, the various airfoil configurations show bigger differences. In parallel to the brush seal (BS) results, the reference design performs best and TEWC-V is on the same level in OP1 and drops down to ≈0.85%. While the full contoured TEWC set up lied in this range with brush seal (BS) as well, now it performs worse of about ≈1% for OP1 to OP3 and even ≈1.8% in OP4. The same effects can be seen for the efficiencies calculated by means of Equation 4.12.

In stage 1 it is remarkable, that all effects and also the curve shapes observed for the brush seal (BS) investigations of all airfoil configurations are repeated, just on another level of efficiency. (This will be illustrated later on in Figure 5.12 where all values are referred to 3D BASE BS in OP3.) The TEWC-V efficiency is higher for OP1 and OP3 by about 0.6%. Up to 1% benefit can be observed in OP2 while OP4 shows the same level in efficiency as shown in the baseline configuration. TEWC is equal in OP1 and OP2 and then performs worse in OP3 and OP4 down to ≈1.8%.

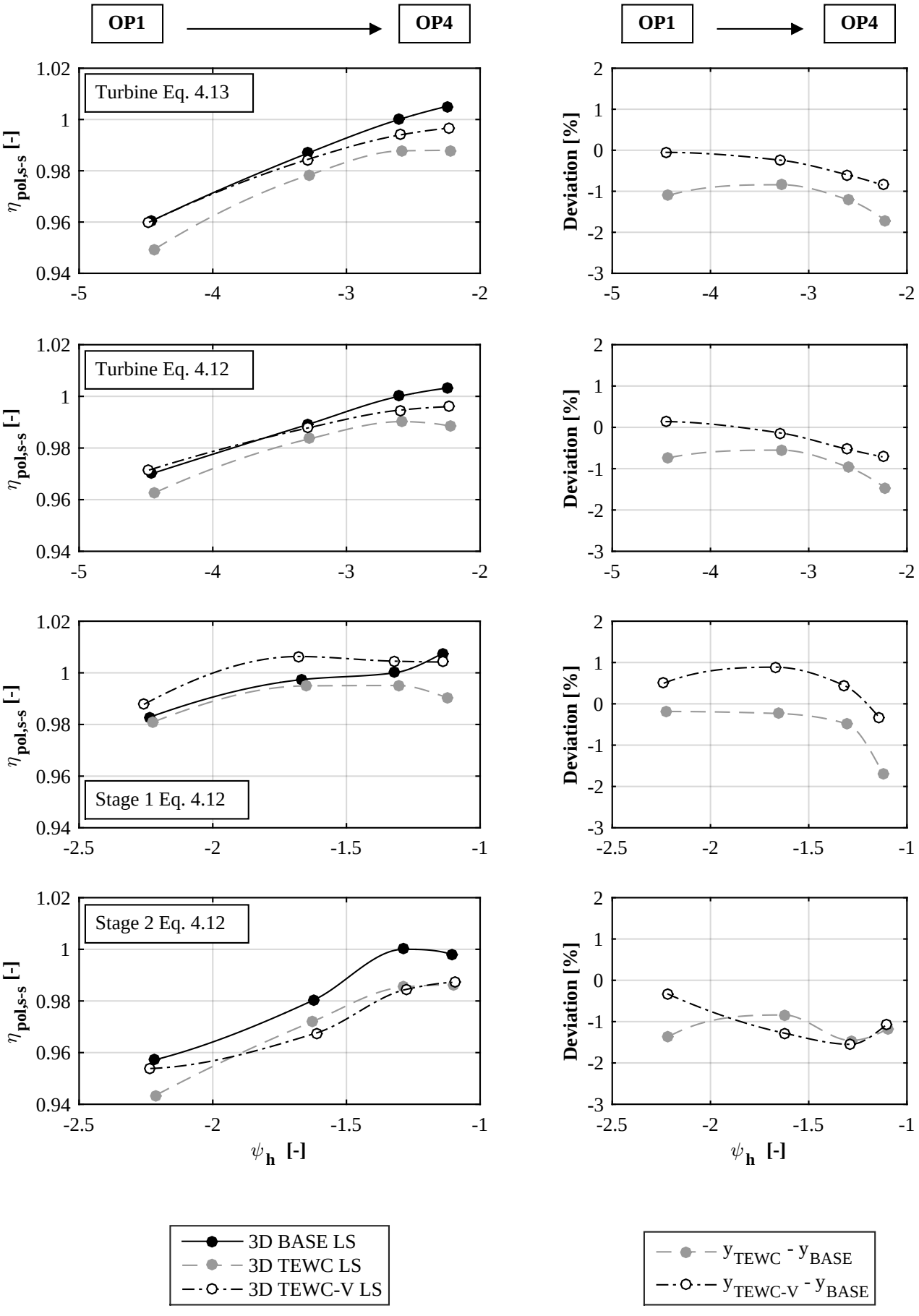

Figure 5.9: Comparison of the resulting polytropic efficiencies for each OP and all configurations with labyrinth seals

Another picture is drawn for stage 2. While TEWC showed an increased efficiency for all OP with brush seal (BS), it is now lower with labyrinth seal (LS) by about ≈1% for all operating points (OP). Also TEWC-V lies in this range, however, it did not show beneficial tendencies for brush seal (BS), as well.

As the change of the casing sided sealing configuration does not have an impact on the trends in stage 1, two assumptions can be made:

On the one hand, the impact of fluid that is sucked out of the main channel into the cavity upstream the TEWC can be neglected. On the other hand the TEWC does not work properly if a certain amount of leakage flow (LF) re-enters the annulus upstream as the boundary layer is thickened up and the TEWC is not fully moistened or passed by the flow correctly. Interestingly, this does not affect the stator performance directly as shown by comparing TEWC-V BS and LS. That implies that the guidance within the stator and the resulting incidence of the downstream located rotor is the key driver of the benefit that can be seen for TEWC BS.

This finding leads to the statement that the amount of leakage flow (LF) in an existing turbine has to be known in advance to decide whether TEWC should be applied in a retrofit measure to increase the turbine's effiency.

The detailed analysis of the efficiency across the span in Figure 5.10 shows that the impact of leakage flow (LF) at the casing impacts the TEWC performance in such a significant way, that also the centre area of the flow channel is influenced. For TEWC-V the effects compared to the brush seal (BS) configuration can be repeated. No significant changes can be identified between casing and the centre of the annulus while losses occur close to the casing. For TEWC the changes are even larger and have to be discussed more in detail.

By comparing the brush seal (BS) and labyrinth seal (LS) one can see that two effects seem to be influencing each other. The benefit close to the casing that can be seen for the brush seal (BS) set up does not occur any more, if a certain amount of leakage flow (LF) is present (LS set up). In addition the overall level is decreased, which leads to a shift to the left hand side and an overall negative efficiency compared to the baseline. Therefore, the distribution between brush seal (BS) and labyrinth seal (LS) looks that different for TEWC that has lost its overall positive impact on the turbine's efficiency. That also implies that the main impact, of course can be seen close to the casing, where the sealing is switched.This leads to the assumption that changes in the hub area are mainly caused by an overall drop in performance. However, also variations of the incidence in this span region that result due to the impact on the PV are responsible for the losses shown here.

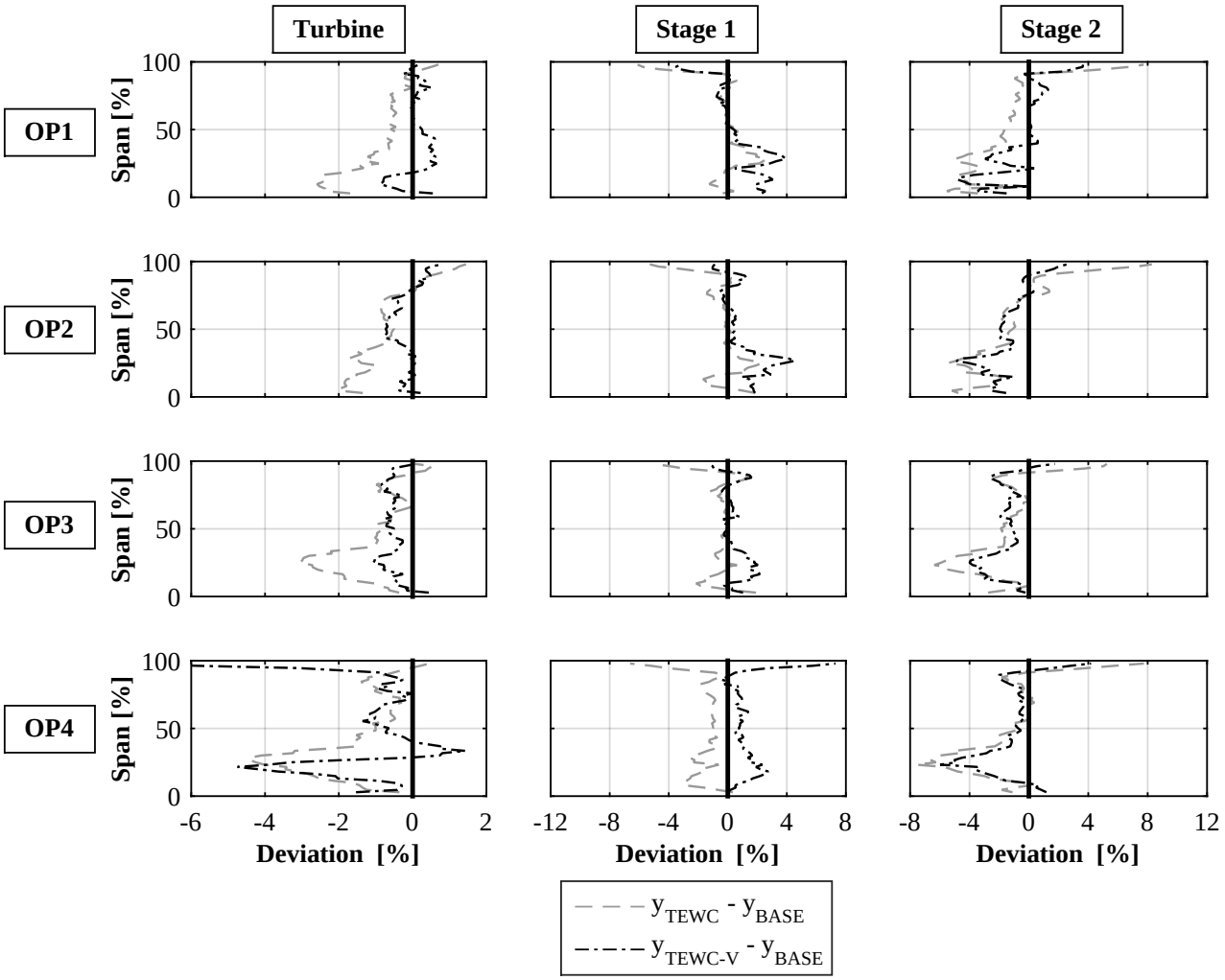

Figure 5.10: Detailed analysis across span of the resulting polytropic efficiencies for each OP and all configurations with labyrinth seals

5.2.2 Labyrinth seal vs. brush seal

The previous discussions were dedicated to identify the impact of endwall contouring in comparison to the baseline configuration. It has been shown that the effects that are caused by endwall contouring are quite complex and that the amount of leakage flow is significant for the performance of the contouring. Therefore, on the one hand, the previously shown variables are now refer to the design point OP3 of the 3D BASE BS configuration to visualize all investigated configurations comparably. Furthermore, the plots on the right hand side of all subsequent figures illustrate the impact of the leakage flow (LF) by comparing the respective airfoil type, only.

Having a look on the power output in Figure 5.11 one can see that the labyrinth seal (LS) configuration for BASE and TEWC lies ≈4-5kW above the brush seal (BS) set up. Especially for TEWC-V the deviation increases from OP1 to OP4, which is caused by the friction of the brush seal (BS) that increases to higher speeds. For the BASE configuration the trend is the same, however, OP2 shows

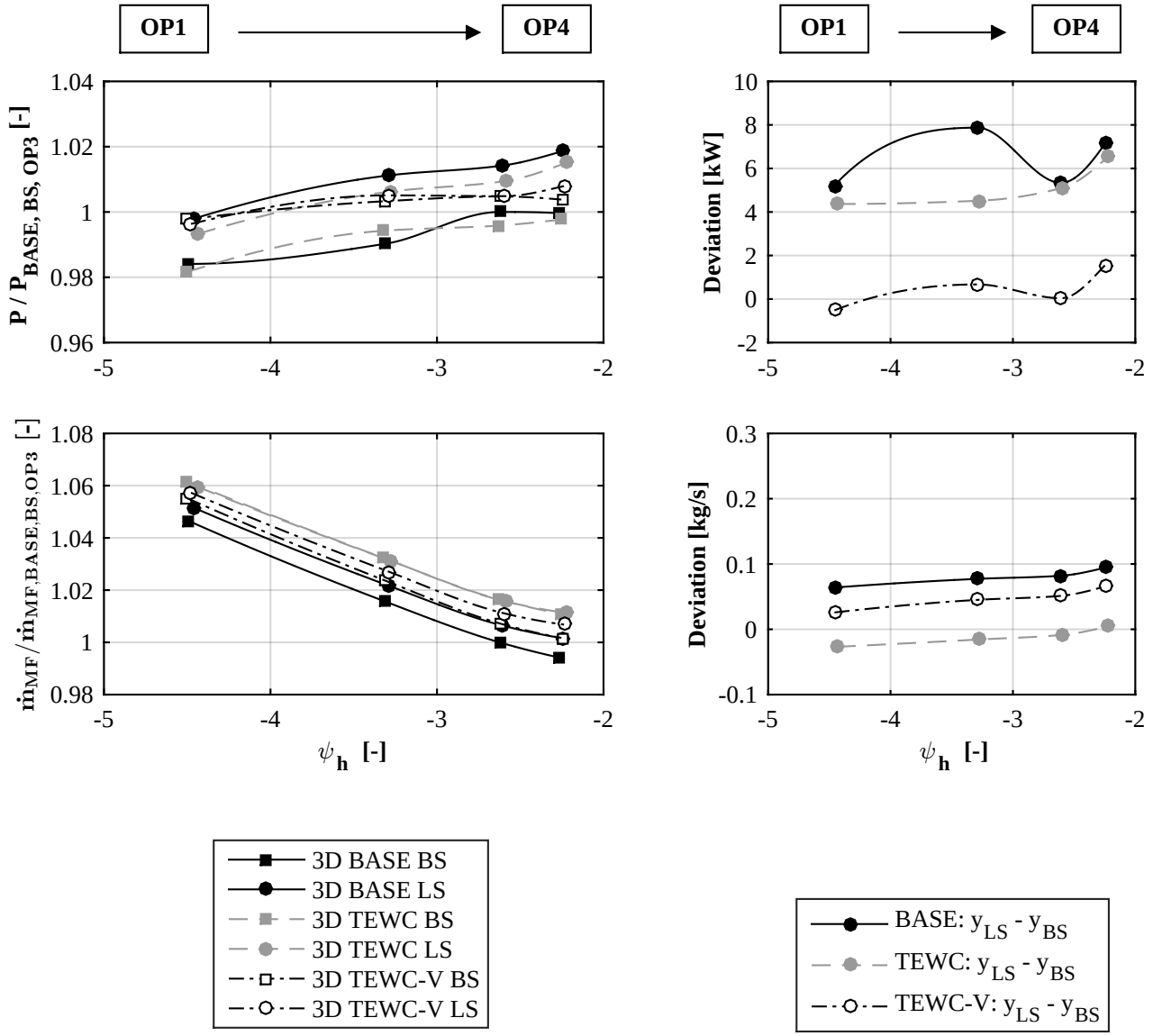

Figure 5.11: Comparison of the resulting power and mass flow for each OP and all investigated configurations with labyrinth seals and brush seals

a peak that should be related to measurement uncertainties. Almost no change can be seen for the TEWC-V configuration. This is mainly caused by the higher output of the brush seal (BS) configuration (compare with Figure 5.5).

The largest change of about ≈95g/s in main flow (MF) can be seen for the BASE airfoils while the full contoured blading (TEWC) hardly shows any change. The TEWC-V configuration lies in between with ≈45g/s. All configurations show a slight increase in deviation of ≈10g/s from lowest to highest speed (OP1 → OP4).

Figure 5.12 summarizes all investigations with both sealing configurations. The efficiency of all set ups is referred to 3D BASE BS in OP3. A global analysis of the turbine's efficiency utilizing

Equation 4.13 and 4.12 indicates that the efficiency of each configuration drops for higher leakage flow (LF) (labyrinth seal (LS) configurations) within the considered range of operation. Hereby the efficiency of BASE and TEWC-V is decreased by ≈0.8% while the fully contoured blading (TEWC) is more sensitive to the re-entering leakage flow (LF) and losses are ≈1.5%.

A detailed look at stage 1 reveals that all airfoil types suffer by about ≈1.5% due to less fluid that participates the energy conversion.

The level of efficiency for the BASE configuration in stage 2 remains constant. Also the TEWC-V set up, which has an efficiency level lying significantly below BASE does not show an inpact for OP3 and OP4, while the efficiency for OP1 and OP2 is increased by about ≈0.5%. The benefit that was generated by applying TEWC in combination with brush seal (BS) shows an opposite trend if leakage flow (LF) is also taken into consideration. Therefore, a loss of 1.5% for OP1, OP2 and OP4 down to 2% for the design point can be seen.

Also the detailed analysis of the turbine's efficiency across span that is shown in Figure 5.13 states that TEWC losses are nearly constant from the hub up to a span of 80% and further close to the casing. The negative impact between 60 - 80% can also be recognized for the BASE and TEWC-V set up, however, the efficiency does not change from the centre passage to the hub.

By analysing both stages independently, it is clearly shown that all configurations mainly show losses close to the casing in stage 1 and then by nearly the same amount across the remaining flow passage.

In stage 2, the gain in efficiency in the centre channel for BASE and TEWC-V is sufficient to cover the upstream losses leading to the previously discussed distribution of the turbine's efficiency. Only the efficiency of the TEWC configuration drops again.

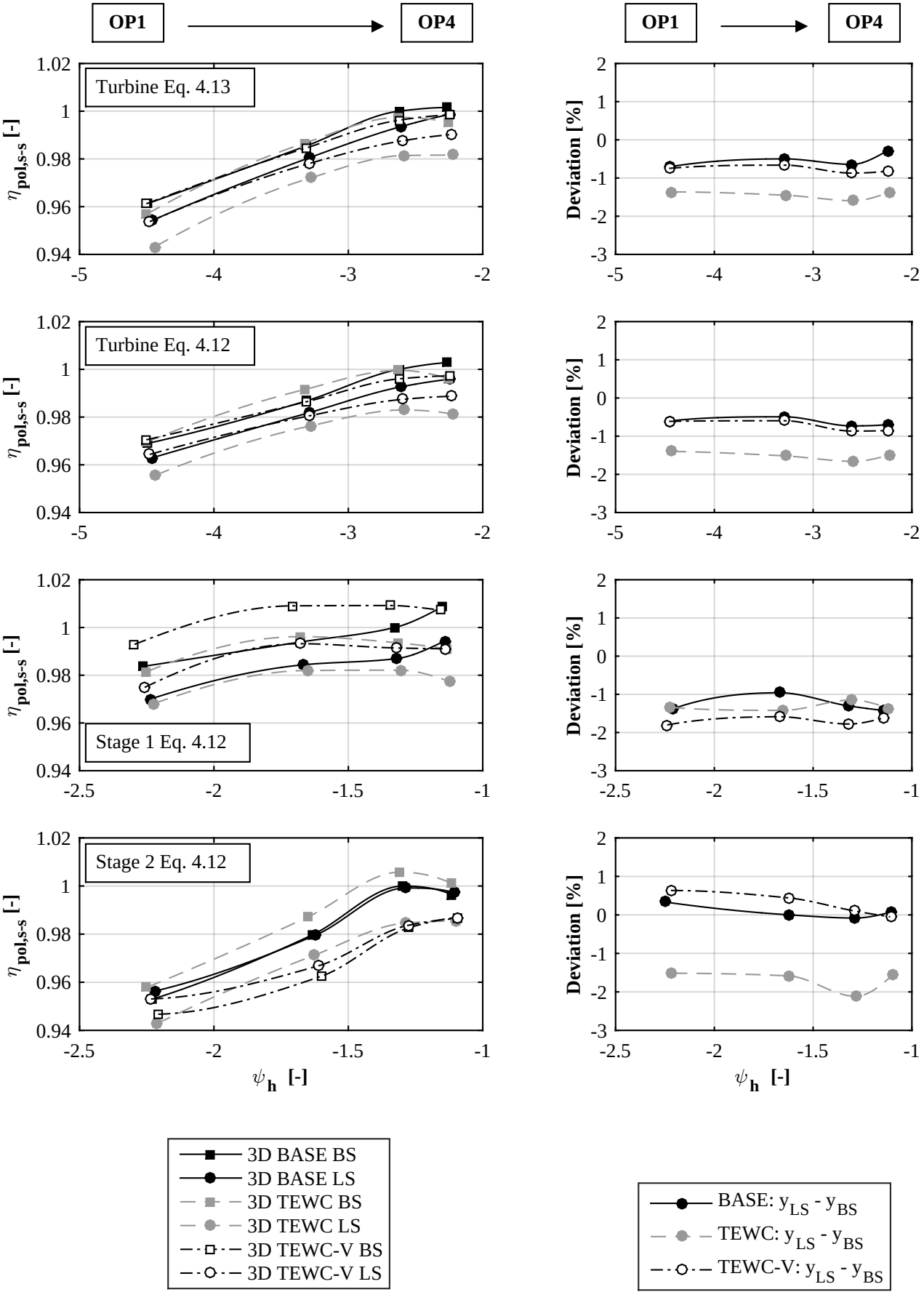

Figure 5.12: Comparison of the resulting polytropic efficiencies for each OP and all configurations with labyrinth seals and brush seals

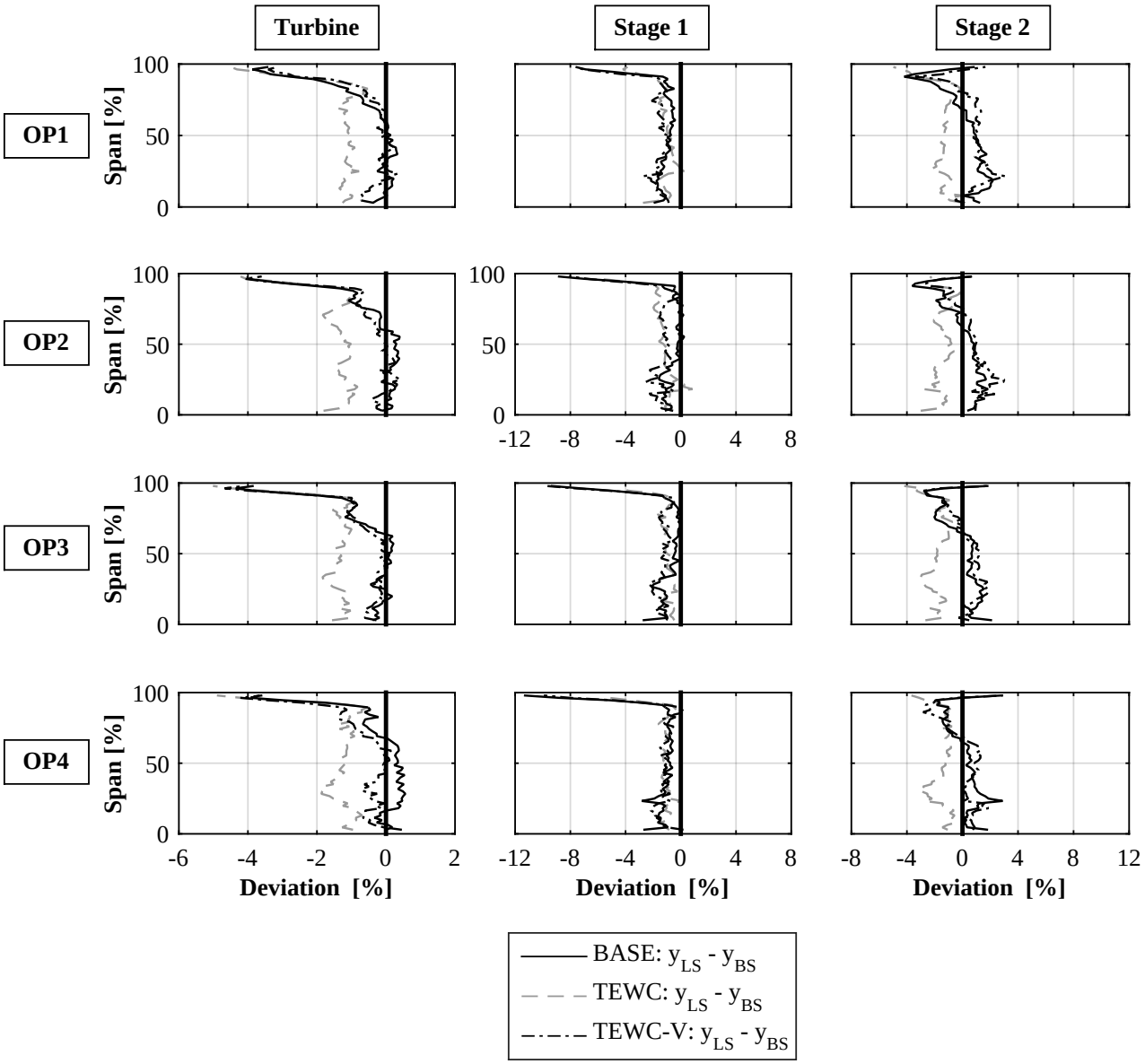

Figure 5.13: Detailed analysis across span of the resulting polytropic efficiencies for each OP and all configurations with labyrinth seals and brush seals

5.3 Summary

The discussions within this sections have shown that all tests were carried out with comparable boundary conditions.

An analysis of the leakage flows showed that hardly any leakage flow interaction can be expected for the brush seal (BS) configuration while the leakage flow (LF) of the labyrinth seal (LS) set up is ≈8 times higher.

Furthermore, it has been shown that endwall contouring has the potential to increase the efficiency of an advanced compound lean blading in the case of the brush seal (BS) configuration. Here, stage 2

has been chosen as a representative case as its inflow is more likely to depict the realistic behaviour of commercial turbo machinery.

This benefit gain changes and the efficiency of TEWC suffers with the presence of a re-entering leakage flow (LF) upstream the second stage. Also the investigation of each airfoil type with both sealing configurations showed that endwall contoured blading (TEWC) is much more sensitive to leakage flow interaction (LI) than a blading with divergent cylindrical walls (BASE). The measurement of the intermediate set up TEWC-V supported these findings. Here it was shown that the application of contouring on the vane exclusively results in a comparable dependency to leakage flow interaction (LI) than was seen for the BASE set up. The sensitivity to LI can be dedicated to endwall contouring that is applied on the rotor. All these findings are summarized in Figure 5.14 and Figure 5.15.

Figure 5.14: Summary of changes in efficiency of TEWC and TEWC-V compared to BASE for all configurations with brush seals

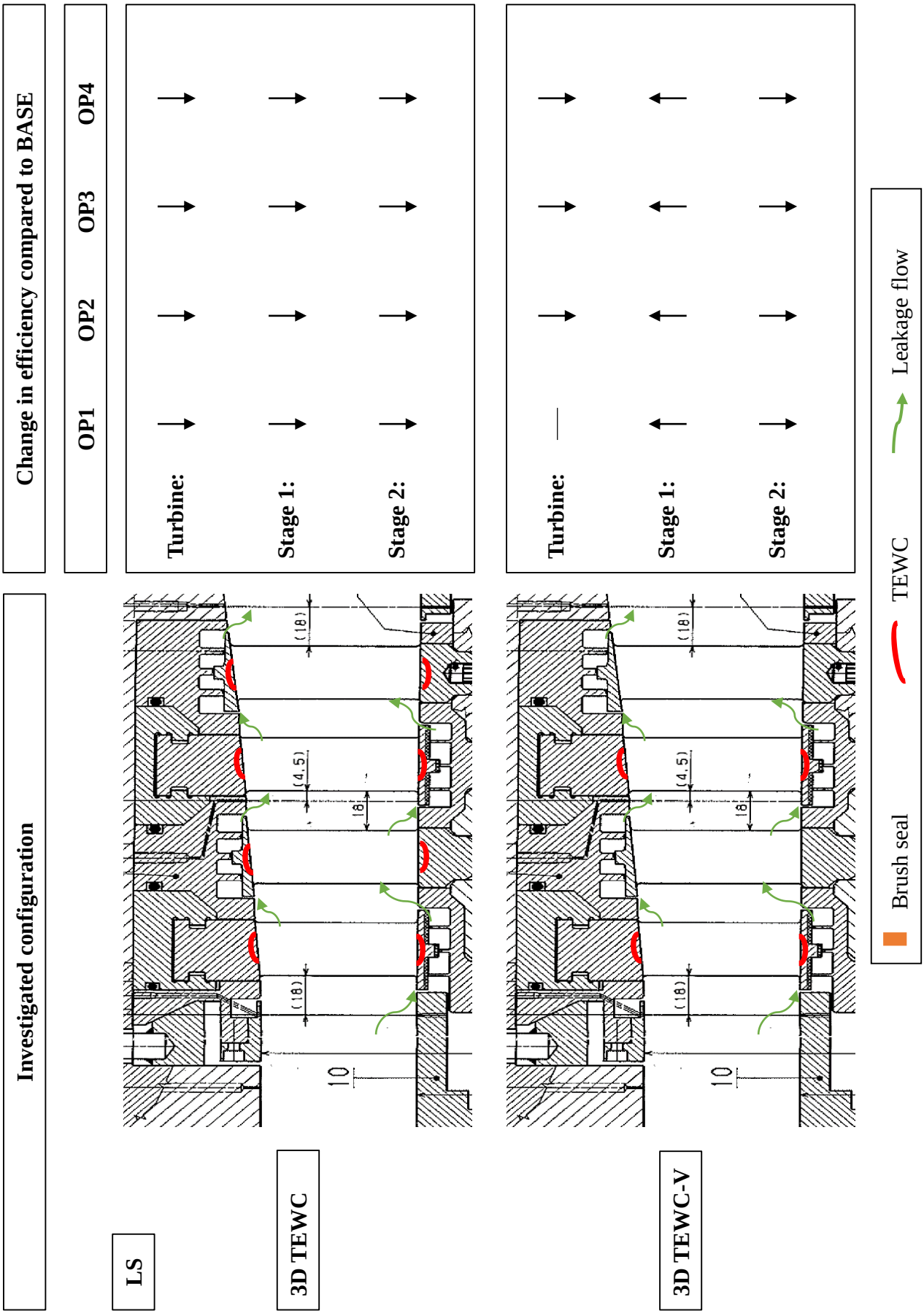

Figure 5.15: Summary of changes in efficiency of TEWC and TEWC-V compared to BASE for all configurations with labyrinth seals

6 Detailed analysis of the flow field

The previous chapter has shown that TEWC and also the influence of leakage flow interaction have a significant impact on the turbine's performance. Therefore, the flow fields of each configuration are investigated in detail across the span to identify potential physical reasons for the global changes. This is done by means of contour plots that show a 2D section of one airfoil passage. Furthermore, this data is averaged circumferentially and plotted against different configurations to visualize deviations at certain span locations. The yaw angle α, total pressure p_{t} and total entropy Δs_{t} (in reference to the environmental conditions) have been chosen for this purpose. Also, the pressure distribution is compared across one vane of stator 2 at two discrete span positions at 90% and 50% of the span.

OP1 has been chosen to show the further described flow phenomena, as the changes here are the highest. Therefore, it is the best example for visualization purposes. The results of all remaining OP are given in Appendix B to compare the respective values for all OP in a single one page figure. For this reason the scaling of some axes does not seem well suited for OP1 within this chapter. Please note that the markers for the TEWC-V configuration have been left out for the circumferentially averaged data plots for purpose of illustration.

The structure of this chapter is related to the previous one, starting with an analysis of the influence of TEWC neglecting leakage flow interaction (brush seal configurations). Then, leakage flow interaction is considered by comparing the resulting flow fields of the labyrinth seal measurements. Finally, the influence of labyrinth and brush seal set ups is analysed for each airfoil type separately.

6.1 Baseline vs. tangential endwall contouring

Figure 6.1 illustrates the contour plots of the yaw angle α in MP12 for the brush seal configurations. Especially for OP1 it can be seen that the yaw angle changes across the whole span for the BASE configuration and therewith the incidence of stator two that is located downstream of MP12. For TEWC-V this variation gets thinner in circumferential direction, however, vortices at 20 and 80% span seem to be strengthened. For TEWC the downsizing of this area can also be recognized. The vortices at 20 and 80% span are less distinct as for TEWC-V. Overall, the flow field is homogenized in the span wise direction especially in the hub area. This effect can also be seen for the other operating points shown in Figure B.1 and it can be stated that the downsizing of the inhomogeneous area is mainly impacted by the contouring of the vane.

In MP22, the flow field is much more homogeneous for all configurations because rotor stator interaction does not take place here. Figure 6.2 (respectively Figure B.2) reveal that endwall contouring has a strong impact on the hub area at 20% span.

This change is stronger for TEWC than for TEWC-V, which means that both vane and rotor contouring effect this deviation.

Averaging these flow fields circumferentially (see Figure 6.3 and Figure B.3), supports that TEWC and TEWC-V cause a shift of the incidence to the suction side (SS) in MP12 due to the homogenizing process. Additionally, these plots show that the rotor contouring of the TEWC configurations mainly causes changes close to the casing. The amount of deflection caused by the passage vortex between 5 to 25% span is of the same amount for TEWC and TEWC-V while the peak at 20% span is shifted slightly further towards the channel centre for the TEWC configuration. In MP22 the difference between all airfoil types is smaller than in MP12, however, all described effects occur as well. Especially for OP3 and OP4 in Figure B.3) it can be seen clearly, that the channel vortex is shifted away from the hub compared to the BASE airfoils.

Also the shift of the incidence due to the different loading of each OP can be clearly seen. Therefore, the data is additionally averaged across span shown in Figure 6.4. Here, the resulting yaw angle is plotted for each OP in all three measurement planes. In MP10 the angle is 0 due to the honeycomb structure upstream the first stage that redirects the flow parallel to the machine's axis. The angle level of all OP is lower in MP12 than in MP22 and one can see that TEWC and TEWC-V differ by roughly 5° compared to the BASE configuration. Taking the convention introduced in Figure 3.12 of Section 3.3.3 into consideration, one can also see that OP4 causes negative incidence whereas OP1 and OP2 lead to positive incidence downstream of each measurement plane.

The total pressure distributions in MP12 that are shown in Figure 6.5 and Figure B.4, reveal a pressure drop of 0.35% close to the casing for the TEWC configuration compared to BASE. TEWC-V lies in between, while its overall level within the main channel is the lowest. One can also see that the peak at 90% span is shifted towards the channel centre as it was discussed for the passage vortex above. Furthermore, TEWC and TEWC-V show an increase in pressure close to the hub that cannot be seen for the BASE measurements. An equivalent picture is drawn in MP22.

By looking at the pressure distribution across the vane downstream MP12 that is given in Figure 6.6 as well as Figure B.5 turns out that TEWC does not have an impact on the pressure side (PS) that is represented by the upper curve at a pressure level of $\approx$0.83. This can be explained as the pressure gradient within the flow passage is directed from pressure side (PS) to suction side (SS) as it is shown in Figure 3.4. The impact of the sudden jump therefore mainly influences the suction side (SS). The discrete measurement at 90% span on the left hand side of Figure 6.6 shows that deviations mainly occur at the leading edge of the airfoil located at x/l=0. It is also visible that the deceleration (increasing static pressure) between x/l=0.7 and 0.9 of the BASE configuration is weaker for the TEWC-V and TEWC design.

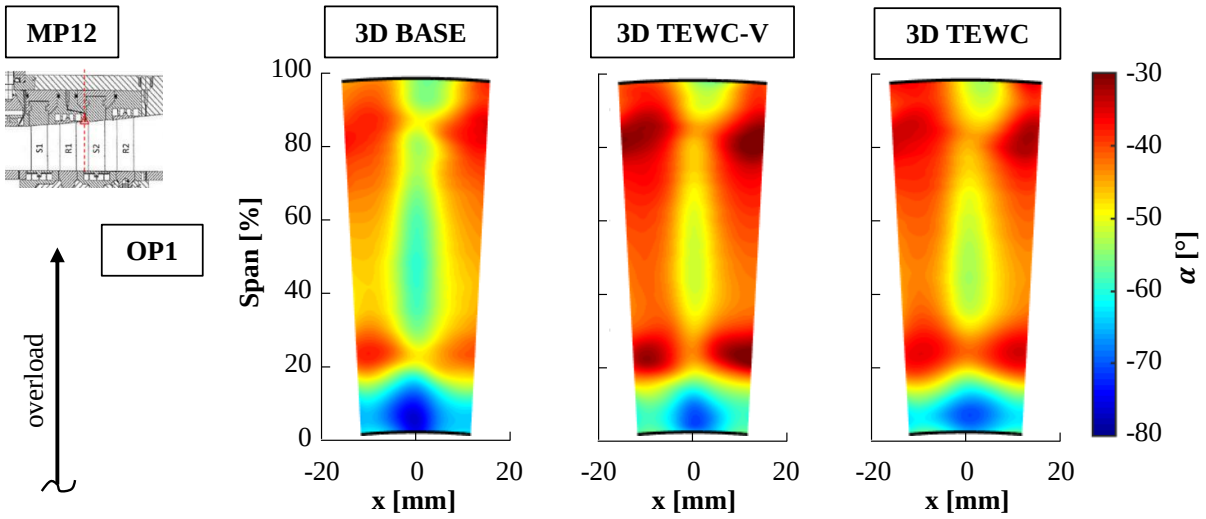

Figure 6.1: Contour plots of yaw angle measured in MP12 and configurations with brush seals

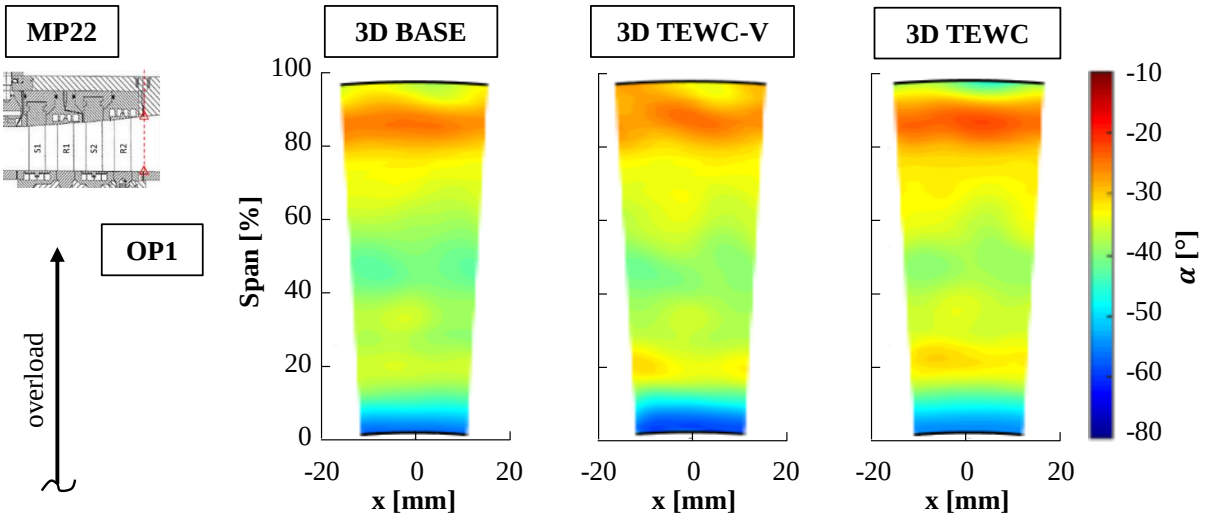

Figure 6.2: Contour plots of yaw angle measured in MP22 and configurations with brush seals

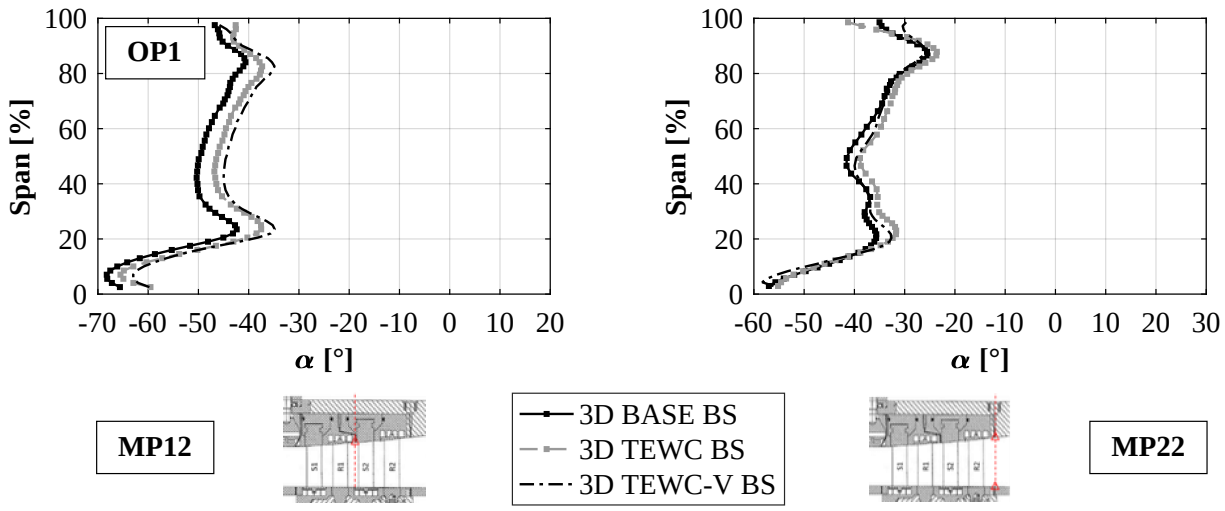

Figure 6.3: Circumferentially averaged distribution of yaw angle measured in MP12 and MP22 and configurations with brush seals

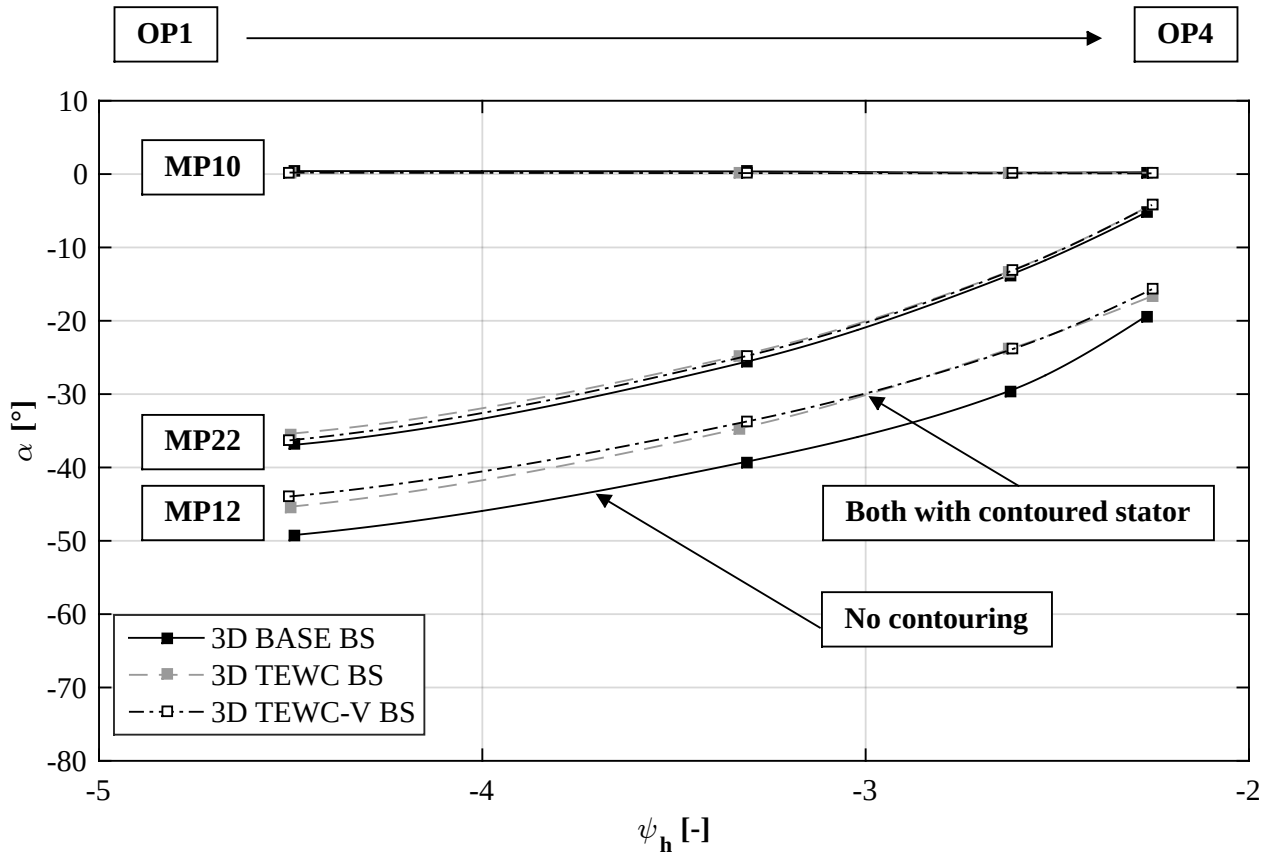

Figure 6.4: Mean averaged yaw angle in MP10, MP12 and MP22 and configurations with brush seals

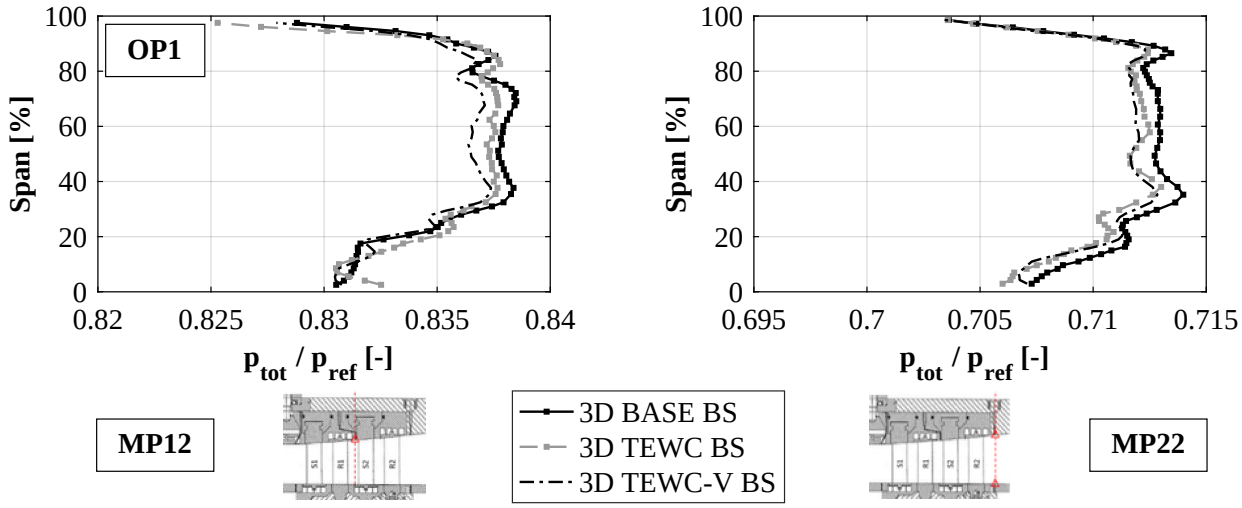

Figure 6.5: Circumferentially averaged distribution of total pressure measured in MP12 and MP22 and configurations with brush seals

Only slight changes can be seen at the channel centre at 50% span. The pressure level of TEWC-V here is the lowest and the fluid also has a higher velocity at x/l=0.9 in relation to the smaller gradient between x/l=0.7 and 0.9.

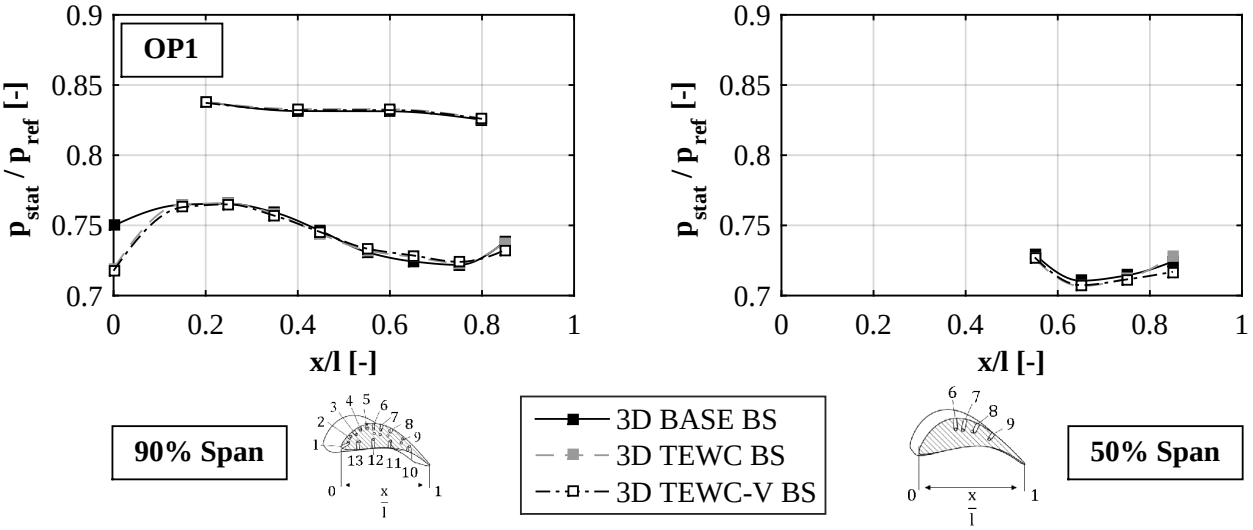

Figure 6.6: Pressure distribution in axial direction across a vane of stator 2 at 90% and 50% span and configurations with brush seals

To visualize losses, the total entropy is plotted in Figure 6.7 and Figure B.6. Ambient conditions are utilized as a reference entropy level thus an increasing entropy level can be interpreted as area of higher losses. In MP12, these images show an improvement for TEWC-V and TEWC in the hub region at 20% span while the application of contouring close to the casing causes losses locally. It is also obvious, that the zone of higher entropy at the casing is slighly higher for TEWC-V compared to BASE. However, this is significantly increased for TEWC leading to the assumption that the contouring on the rotor causes these losses as it was also stated by Restemeier [116] or Dunn et al. [36].

This finding supports the detailed analysis of efficiency shown in Figure 5.7. Another tendency can be seen in MP22 in Figure 6.8 and Figure B.7 where TEWC performs best at the casing area. Again, the phenomena that can be seen for TEWC-V lie in better accordance to the resulting flow field of the BASE configuration than to TEWC. Also the overall level of TEWC in the main channel region is lower corresponding to the highest efficiency of all set ups in stage 2 that was shown in section 5.2.

Averaging the data sets circumferentially shows that the entropy change close to the hub in MP12 is decreasing for TEWC-V and TEWC, which indicates that the passage vortex produces fewer losses compared to the BASE design (see Figure 6.9 and Figure B.8). The vortex shift caused by TEWC towards the channel centre at 90% span is clearly visible in addition to the large deviation at the casing, that was also discussed by means of the contour plots.

In MP22, on the one hand, the entropy levels indicate the performance of each airfoil type. On the other hand, it can be seen that the BASE configuration shows a steady increase close to the hub. In contrary, the entropy is reduced between 0 and 10% span for both, the TEWC-V and TEWC design indicating a local benefit there.

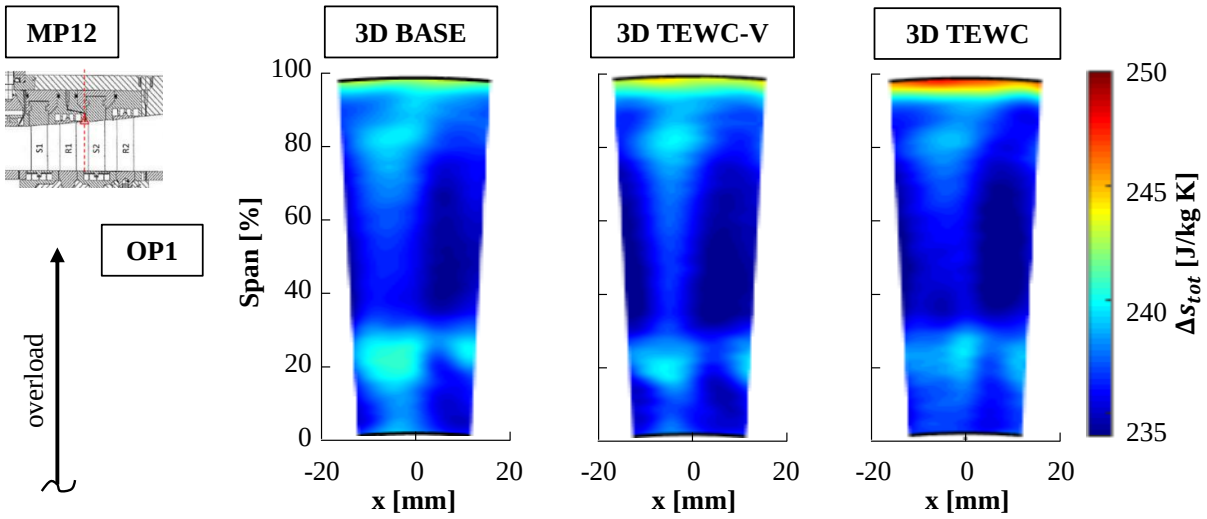

Figure 6.7: Contour plots of total entropy measured in MP12 and configurations with brush seals

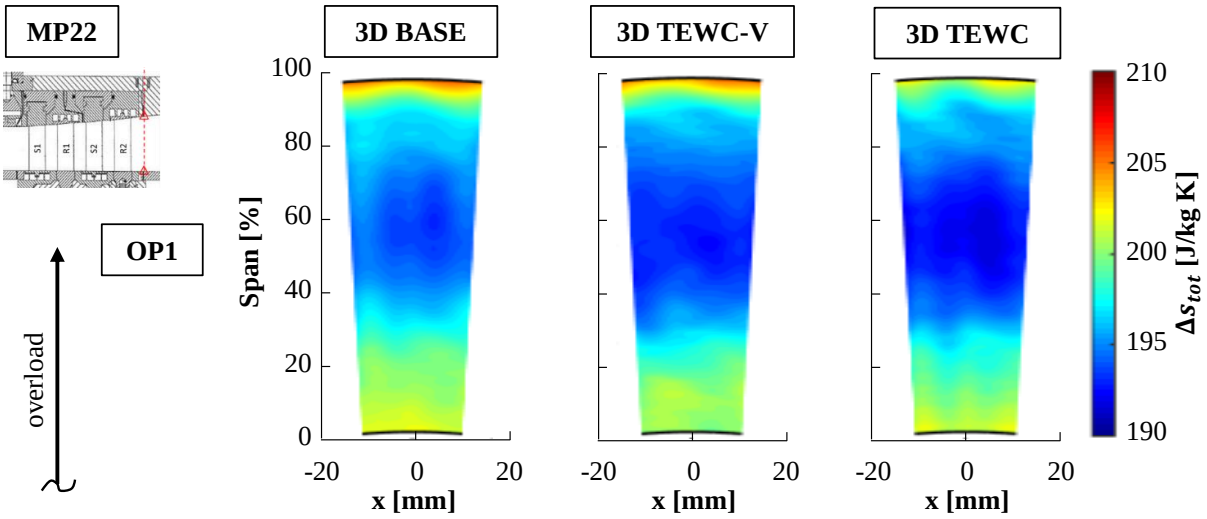

Figure 6.8: Contour plots of total entropy measured in MP22 and configurations with brush seals

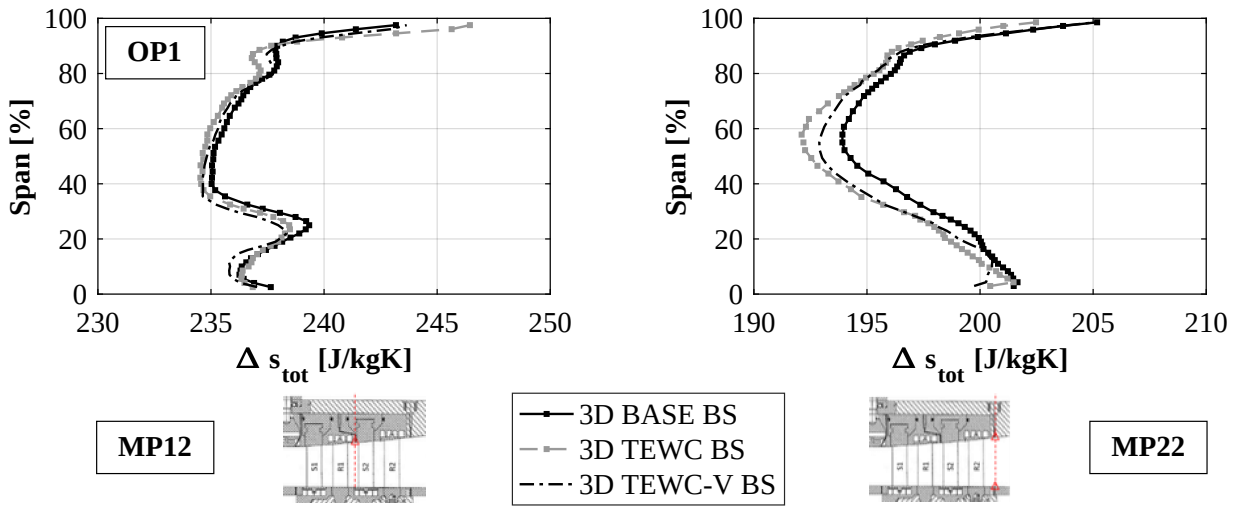

Figure 6.9: Circumferentially averaged distribution of total entropy measured in MP12 and MP22 and configurations with brush seals

Following, the labyrinth seal configurations are investigated to see whether the additional leakage flow impacts the influence of the endwall contouring.

For the angle distribution in MP12 shown in Figure 6.10 and Figure B.9, it can also be seen that the incidence changes across the whole channel height for the BASE design. Again, this area is significantly smaller for the TEWC and TEWC-V designs. Also the trend in change at 20% span is reproduced and it can be seen that the vortex areas at 20% and 80% span are more intense for TEWC-V than for TEWC.

Figure 6.11 and Figure B.10 illustrate the angle distribution in MP22. In the off design condition OP1, a more non uniform flow field can be seen for TEWC-V compared to BASE and TEWC. The increasing change at 20% span from BASE to TEWC is repeated. Furthermore, the flow is deflected close to the casing significantly for the BASE design. This effect decreases for TEWC and TEWC-V as it can be seen best for OP2 in Figure B.10.

By observing the circumferentially averaged yaw angle distribution in Figure 6.12 and Figure B.11, one can see that the incidence changes most for the TEWC-V configuration in MP12 and also in MP22. However, the amount is much smaller. A change of the radial position of the peak at 20% span cannot be seen in MP12 in any OP. In MP22 this phenomenon can be detected.

Figure 6.13 shows the results of additional averaging the distributions of each configuration radially for all OP and in each measurement plane. As already mentioned, the inflow angle to the first stage is set to 0 due to the honeycomb structure. For MP12 it is remarkable to see that the shift between both endwall contoured configurations is less strong as the BASE level lies roughly 3° higher. However, the trend that contouring deflects the flow leading to more negative incidence, has been repeated compared to the brush seal investigations. Also the different outflow angle range of MP22 can be seen. Here, the trend has changed and the contoured versions show an smaller angle for the outflow of the second stage. In general, the overall level of both OP has changed by $+3 - 4^\circ$ in both measurement planes compared to Figure 6.4. This supports the statements that were made in Section 5.2 assuming that endwall contouring is affected by leakage flow interaction.

The total pressure distribution of all configurations is given in Figure 6.14 and Figure B.12. In MP12 the total pressure level of TEWC is the lowest close to the casing followed by TEWC-V and BASE. In the interstage TEWC-V has a lower pressure level than the other configurations between 40% and 90% span. A shift of the casing sided eddy can be recognized for TEWC and TEWC-V. Between 0 and 30% span it is remarkable that the BASE configuration shows a nearly constant increase in Figure B.12 for OP2 to OP4, while both contoured configurations have a peak at 20% span and a decreasing pressure level towards the channel centre.

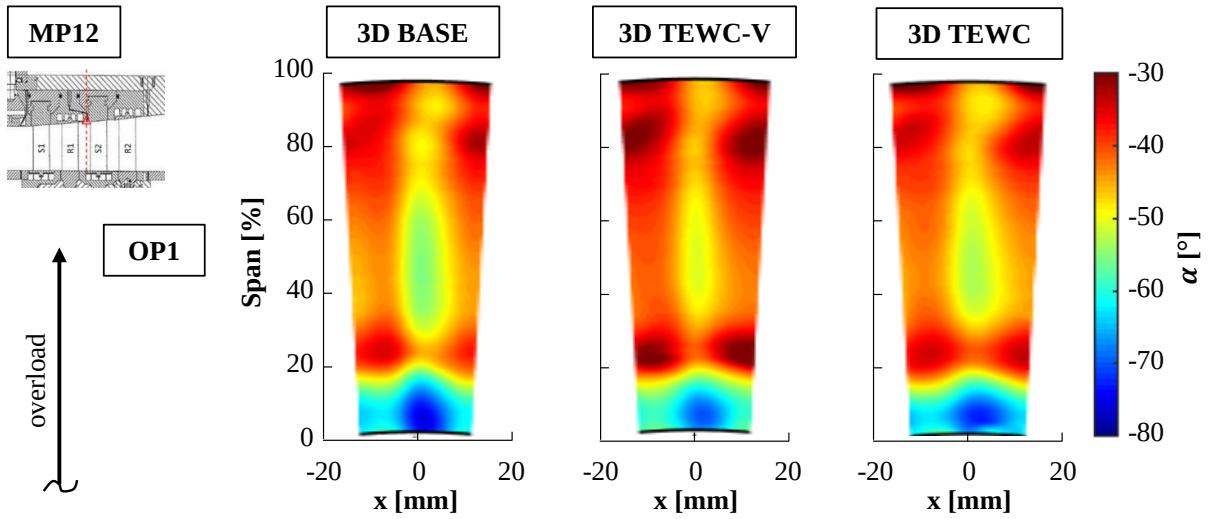

Figure 6.10: Contour plots of yaw angle measured in MP12 and configurations with labyrinth seals

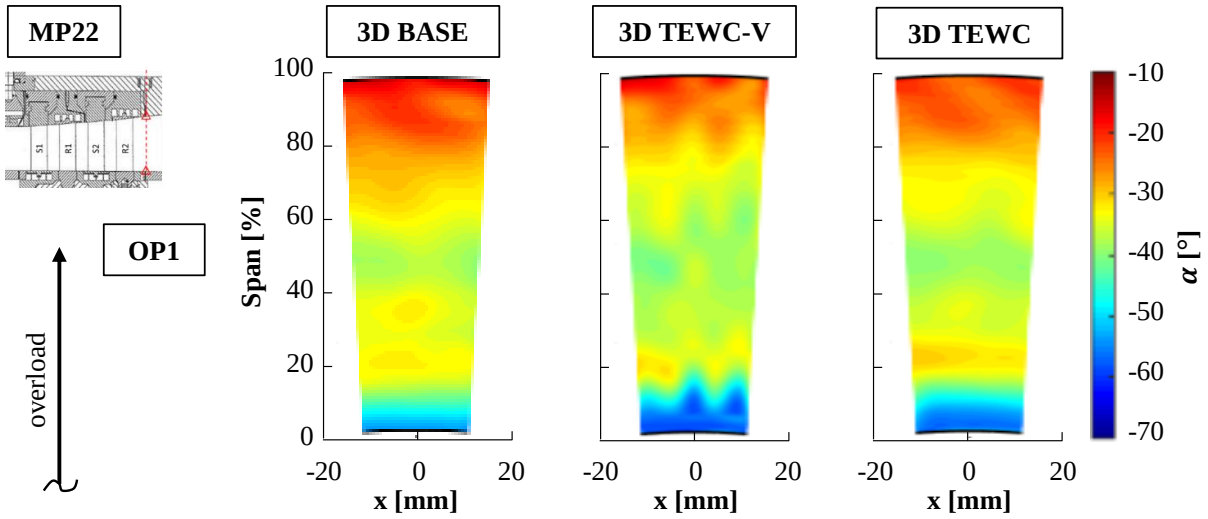

Figure 6.11: Contour plots of yaw angle measured in MP22 and configurations with labyrinth seals

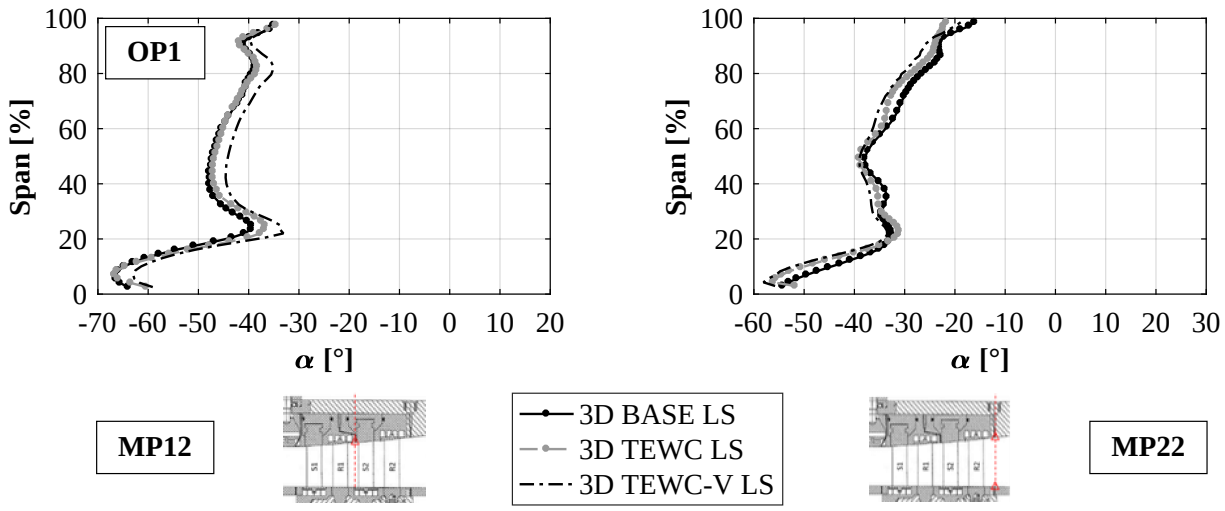

Figure 6.12: Circumferentially averaged distribution of yaw angle measured in MP12 and MP22 and configurations with labyrinth seals

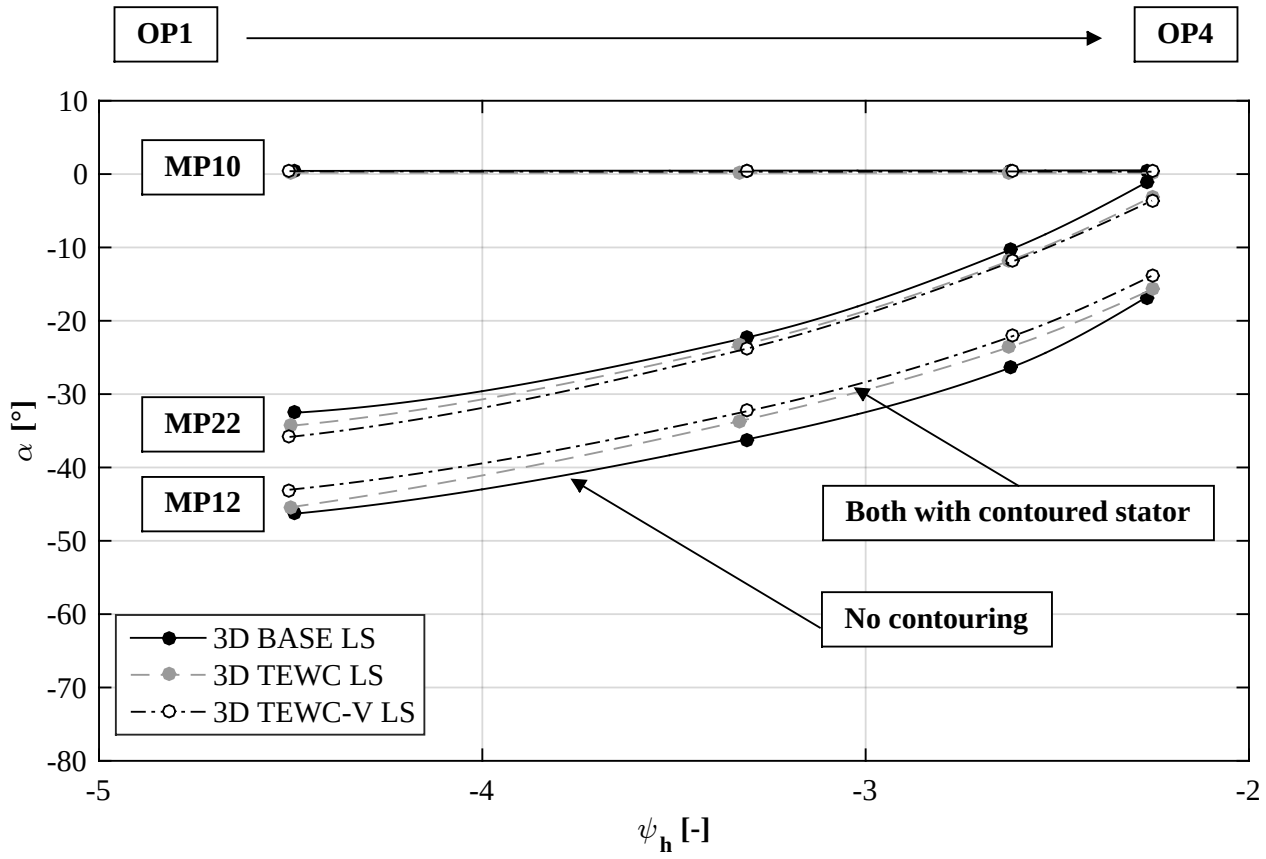

Figure 6.13: Mean averaged yaw angle in MP10, MP12 and MP22 and configurations with labyrinth seals

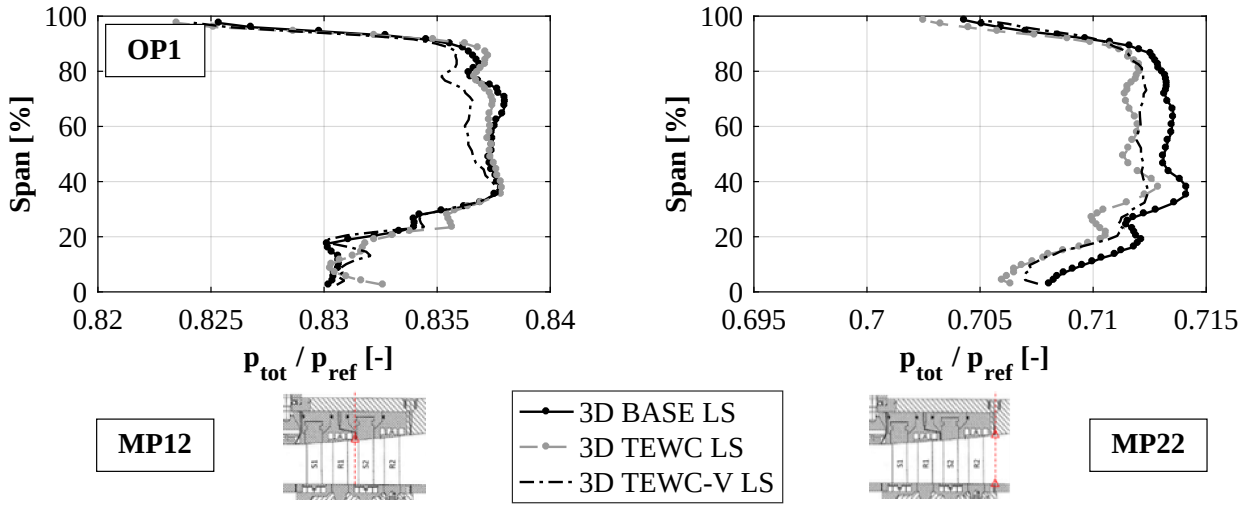

Figure 6.14: Circumferentially averaged distribution of total pressure measured in MP12 and MP22 and configurations with labyrinth seals

In MP22 the phenomena close to the casing are the same as discussed for MP12. The BASE design shows a more vertical distribution between 20 and 80% span while TEWC-V and TEWC have a curved like shape with a lower pressure level in the centre area. Also an increased pressure close to the hub is shown for TEWC and TEWC-V thus it has to be caused by the contouring of the vane.

The pressure distribution across stator 2 at 90% span shows a small impact on the pressure side (PS) in Figure 6.15 as well as in Figure B.13. At the leading edge (x/l=0), the lowest pressure level can be seen for TEWC-V due to the changes in incidence at the second stage. TEWC lies in between. As shown in in Figure B.13, the amount of this deviation decreases from OP1 to OP4 where roughly no change can be seen. Further deviations can be seen at x/l=0.9 where TEWC shows the lowest pressure value followed by TEWC-V and BASE. The nearly constant pressure level of the TEWC curve between measurement points 8 and 9 implies that the velocity on the suction side (SS) is not decreased. In other words it is likely that separation occurs in this area. On the one hand, this effect causes local losses in stator 2, on the other hand, also rotor 2 is not impinged correctly, which results in a further decreased efficiency. This finding supports the massive drop in efficiency of stage 2 that was shown in Figure 5.9 for TEWC in combination with LS. On the suction side (SS) at 50% span TEWC-V shows the lowest pressure level, however, the gradients of BASE and TEWC are nearly equal.

The entropy plots in Figure 6.16 and Figure B.14 show that the entropy level is higher close to the casing for TEWC-V and TEWC down to ≈95% span and therewith twice further towards the channel centre as is was seen for the BS configurations. In contrary to these results, the passage vortex losses around 20% span are increased for TEWC and slightly decreased for TEWC-V. These effects also take place in MP22 and could explain why 3D TEWC LS shows the worst efficiency of all configurations in Figure 5.12. The discrepancy between BASE and TEWC is quite significant in Figure 6.18 and Figure B.16 that illustrate the circumferentially averaged data. Major changes obviously exist close to the hub between 0% and 20% span where TEWC and TEWC-V are on a lower entropy level in MP12 and MP22 compared to the BASE configuration. This deviation cannot be observed in the channel

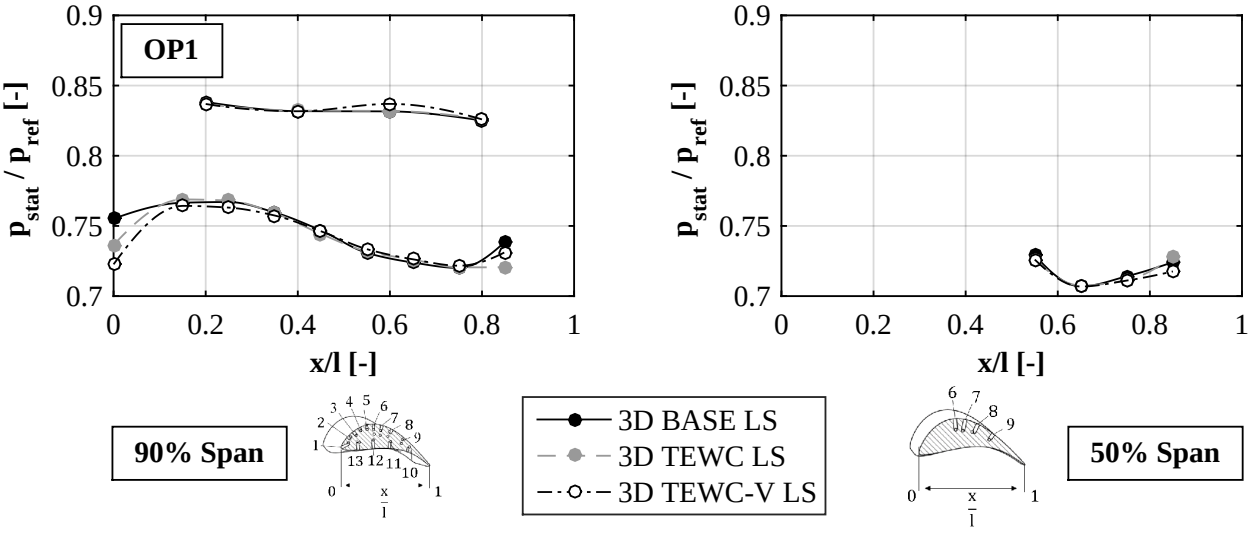

Figure 6.15: Pressure distribution in axial direction across a vane of stator 2 at 90% and 50% span and configurations with labyrinth seals

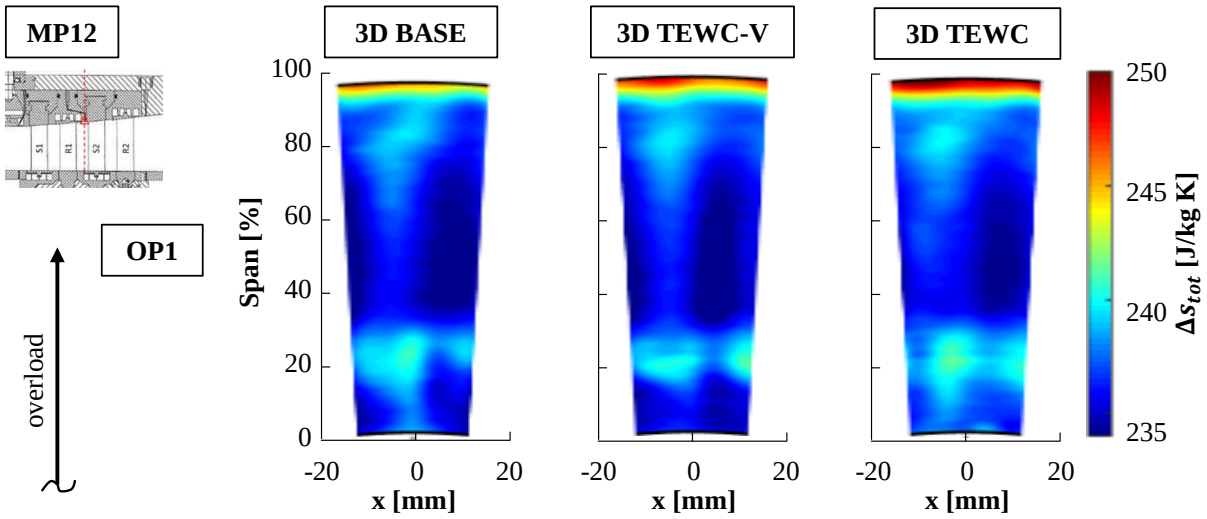

Figure 6.16: Contour plots of total entropy measured in MP12 and configurations with labyrinth seals

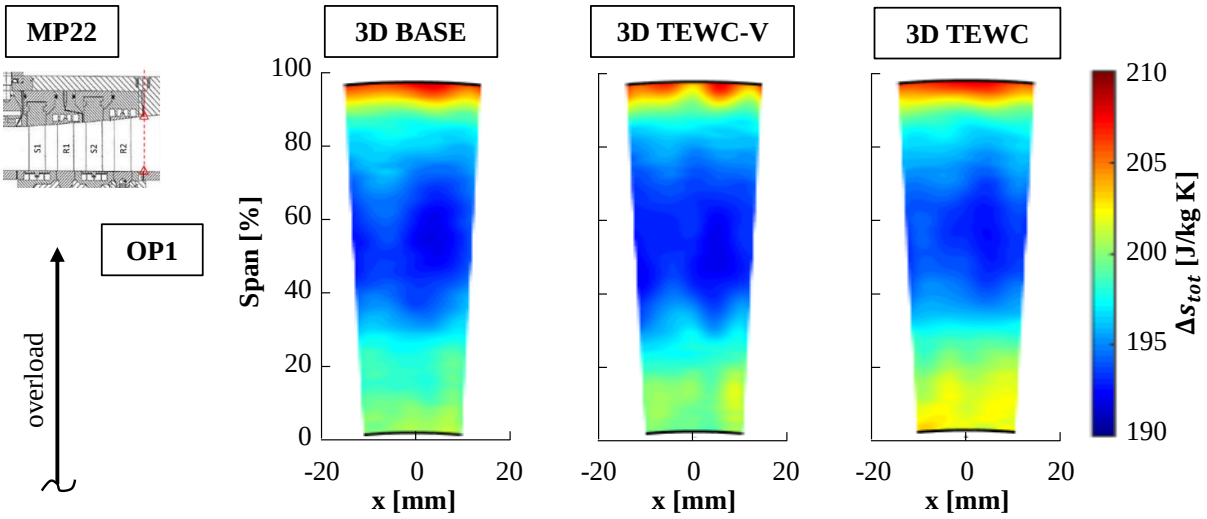

Figure 6.17: Contour plots of total entropy measured in MP22 and configurations with labyrinth seals

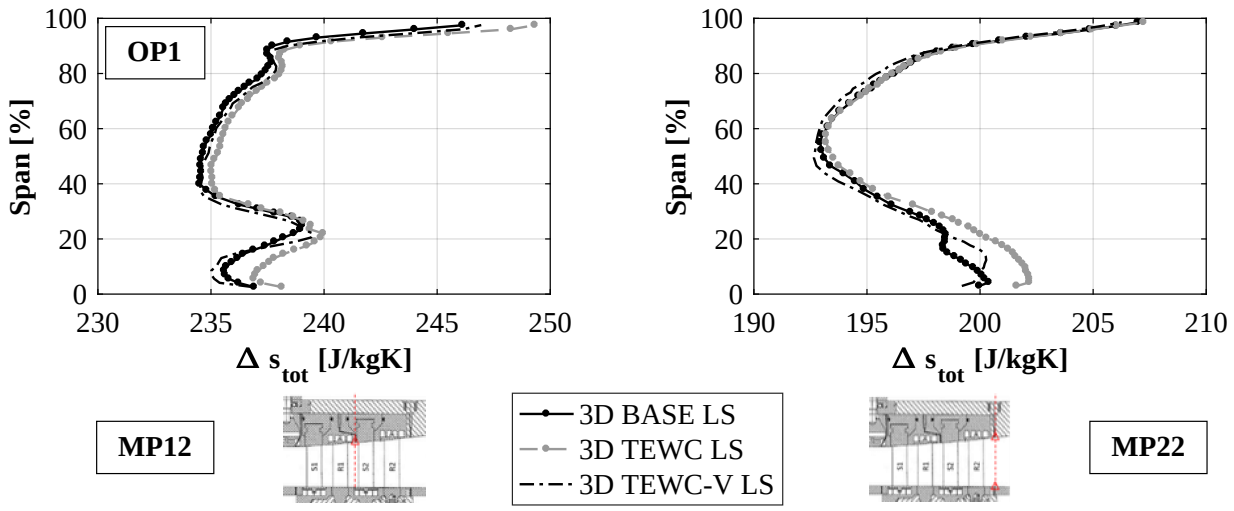

Figure 6.18: Circumferentially averaged distribution of total entropy measured in MP12 and MP22 and configurations with labyrinth seals

centre area between 20% and 80% span. Here, all configurations show nearly the same entropy level, however, TEWC has the highest value of all set ups in both measurement planes.

6.2 Labyrinth seal vs. brush seal

To isolate the impact of leakage flow interaction, the measured data of each airfoil type is compared separately with both sealing configurations LS and BS. Please note that the markers for the BS configuration have been left out for the circumferentially averaged data plots for purpose of illustration. Furthermore only the plots of the BASE configuration are shown in this section. The complete set of figures for all airfoil types and all OP is given in Figure B.17 to Figure B.34.

An analysis of the yaw angle in MP12 (see Figure 6.19 and Figure B.17) shows that the BS configurations turn the trend to negative angles close to the casing. As one can see in the contour plot, this is mainly caused by the droplet shaped area between 90% and 100% span. This effect can also be observed for TEWC-V (Figure B.18) and TEWC (Figure B.19) thus it is not rather caused by the endwall contouring than by the re-entering of the leakage flow.

This effect is also visible in Figure 6.20 (respective in Figure B.20) that shows the contour plots and circumferentially averaged flow fields in MP22. In contrary the incidence changes on a certain radial position across the whole pitch and it does not show the droplet shape as it was discussed in MP12. The same trends can be seen for TEWC-V in Figure B.21 and for TEWC in Figure B.22. All airfoil types have in common, that the amount of change in incidence decreases from OP1 to OP4 close to the casing.

Figure 6.21 summarizes the global changes in incidence caused by the different sealing set ups for all measurement planes. It can be seen that the incidence is shifted by $\approx$-5° for all OP due to the higher leakage flow rate that is present for the LS configurations. This trend can also be observed in both measurement planes for TEWC-V in Figure B.24, however, the deviation is reduced down to $\approx$-2°. That is also the case in MP22 for TEWC, shown in Figure B.25 whereas alsmost no change occurs in MP12.

This finding is remarkable as one has to consider that main mass flow of TEWC almost does not change, and that the change was the highest for BASE with about 90g/s (see Figure 5.11). TEWC-V lies in between, thus the change in incidence appears to be related to the change in main mass flow. This statement further leads to the assumption that the previously discussed impact of the endwall contouring could also just be related to the changes in main mass flow that is $\approx$100g/s higher for TEWC-V and $\approx$200g/s for TEWC in BS configuration (compare Figure 5.5). By looking at the mean averaged yaw angles for all configurations and BS in Figure 6.4, again, it turns out that all configura-

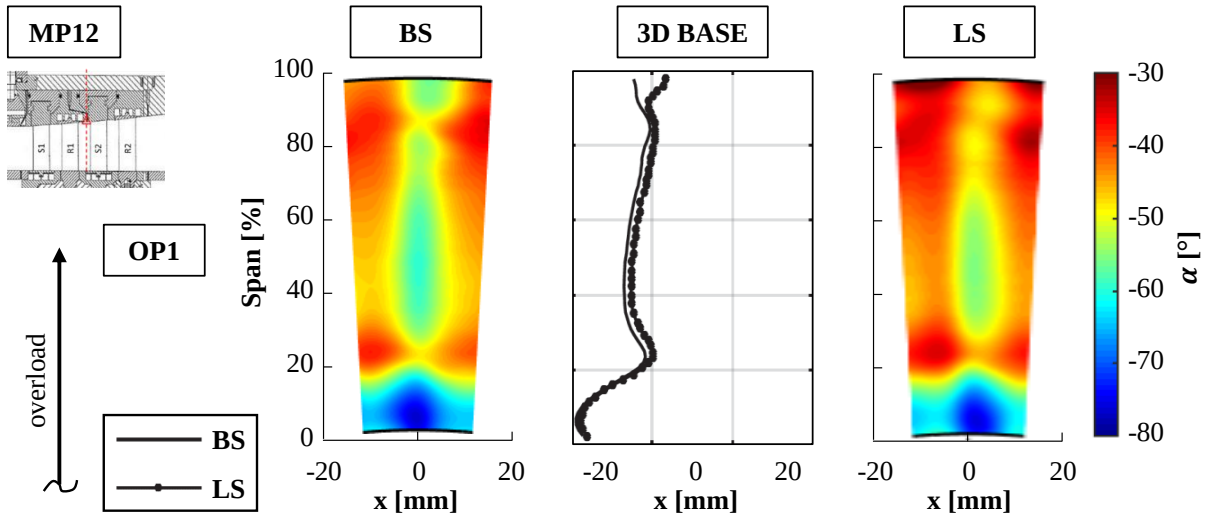

Figure 6.19: Contour plots of yaw angle measured in MP12 and BASE airfoils with LS and BS

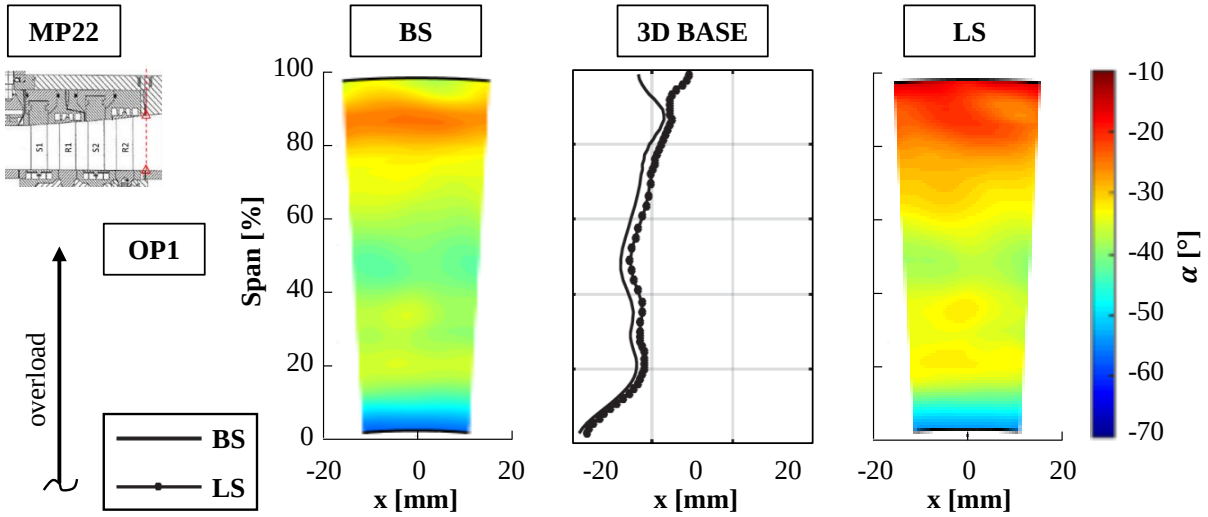

Figure 6.20: Contour plots of yaw angle measured in MP22 and BASE airfoils with LS and BS

tions show nearly the same exit flow angle in MP22. Thus it can be stated that all discussed changes in flow field are a result of the endwall contouring.

By comparing the pressure distribution of vane 2, it turns out that the different sealing designs only show a small impact at the leading edge at 90% span for BASE in OP1. All other OP remain constant (compare Figure 6.22 and Figure B.26). For TEWC-V a small increase in pressure level can be found for the LS configuration on the pressure side (PS) for OP1 and OP2 shown in Figure B.27. On the suction side (SS), the flow is slightly decelerated for the BS set up at x/l=0.2 for all OP. This cannot be seen for TEWC that has an equal distribution for both sealing in OP3 and OP4 (see Figure B.28). A first change can be seen for OP2 at the leading edge, where the pressure level of LS is higher. The largest impact can be found in OP1. The pressure level at the leading edge is also higher for LS and further downstream at x/l=0.75, separation occurs at 50% span BASE. Also, TEWC do not show

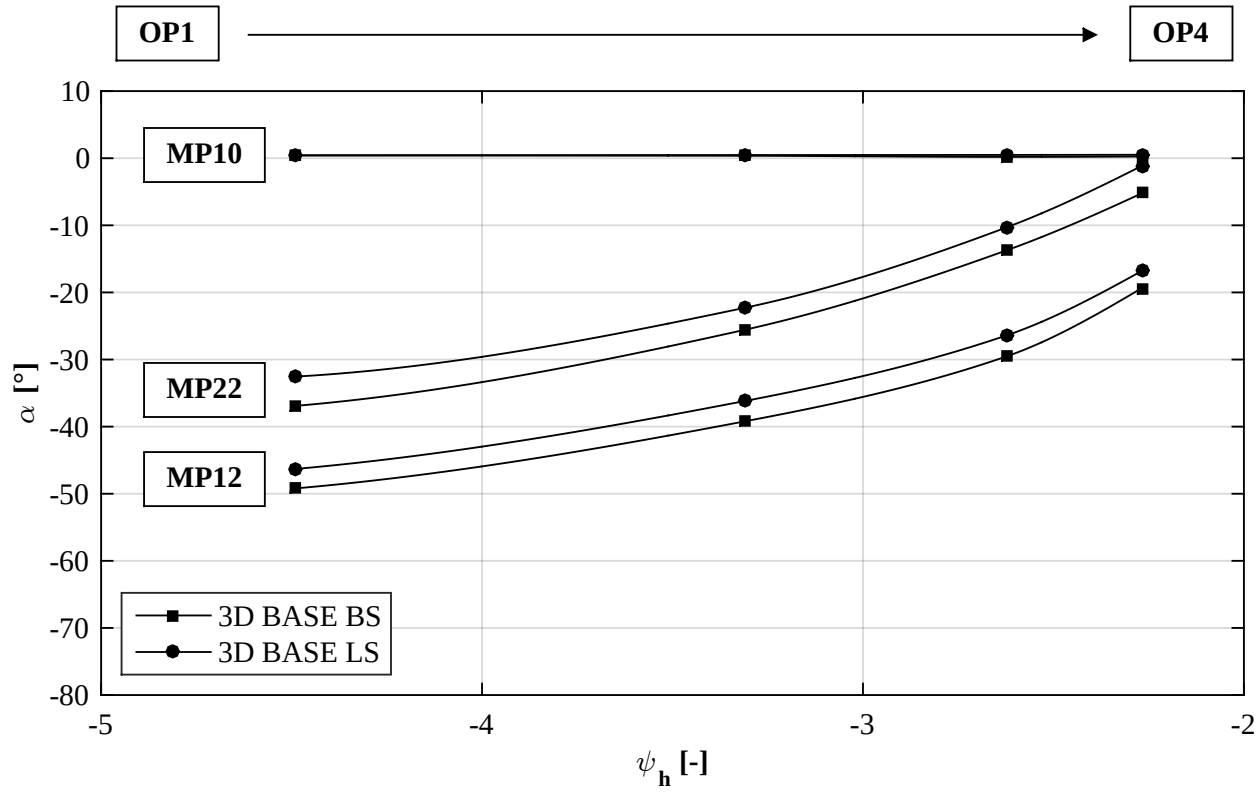

Figure 6.21: Mean averaged yaw angle in MP10, MP12 and BASE airfoils with LS and BS

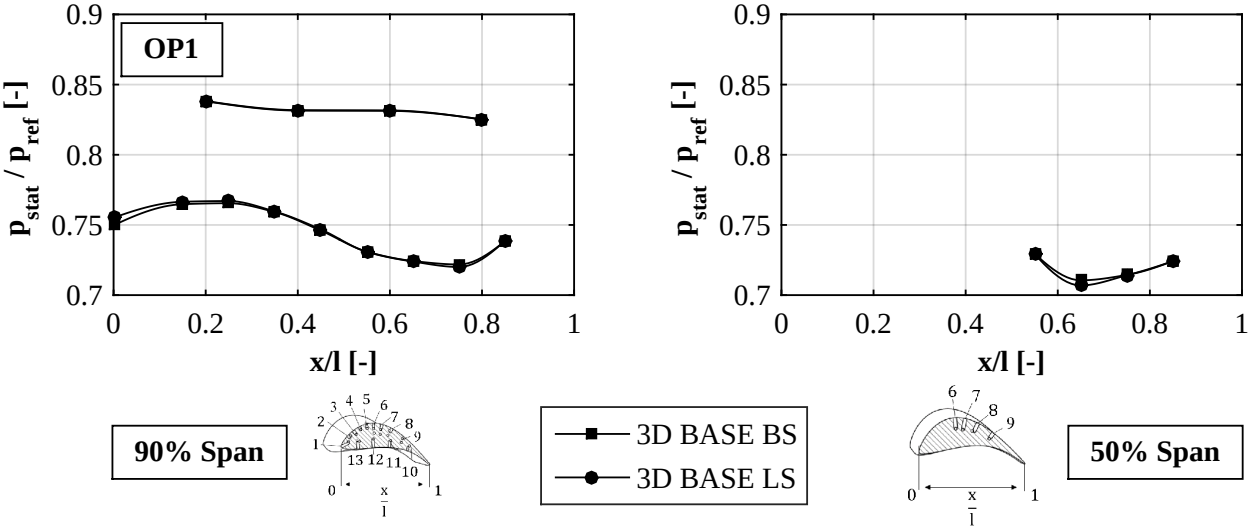

Figure 6.22: Pressure distribution in axial direction across a vane of stator 2 at 90% and 50% span and BASE airfoils with LS and BS

changes where as the pressure level of TEWC-V measured with LS drops constantly from OP1 to OP4 at x/l=0.85 compared to BS. Thus, it also seems that the flow is not able to follow the intended path.

The entropy plots in MP12 in Figure 6.23 and Figure B.29 illustrate that the re-entering leakage

flow influences the main flow field between 95 - 100% span. This amount corresponds to the results of TEWC-V and TEWC that are shown in Figure B.30 and Figure B.31. Considering the worse performance of the LS configurations for TEWC-V and TEWC it is assumed that this re-entering leakage flow thickens the boundary layer and causes flow separation close to the casing wall. Therefore, the flow does not moisture the contouring as it was assumed during the design process of the endwall contouring and causes a malfunction.

The entropy level for BASE is depicted in Figure 6.24 and Figure B.32. For this case, BS performs better close to the casing between 80% and 100% span and gets slightly worse in the hub direction compared to LS. The improvement close to the casing is also present for TEWC-V shown in Figure B.33. The entropy level is then equal across the remaining span for LS and BS. This trend

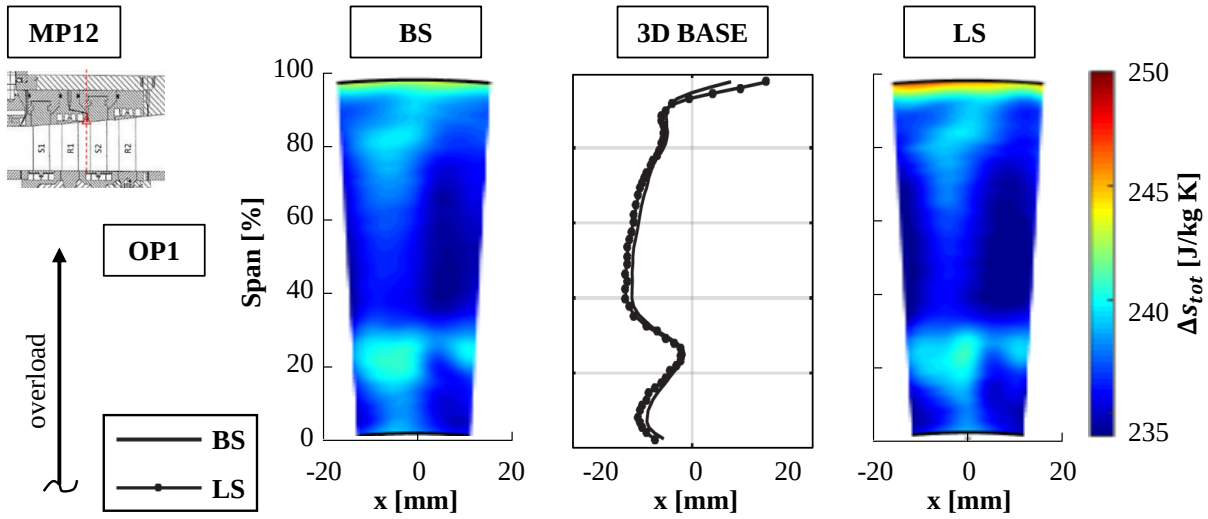

Figure 6.23: Contour plots of total entropy measured in MP12 and BASE airfoils with LS and BS

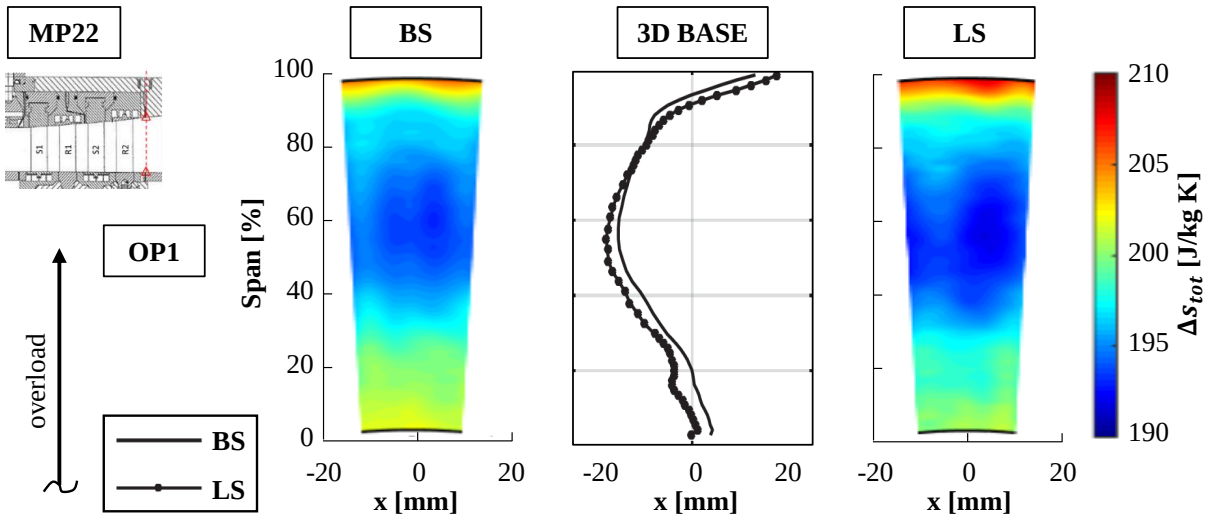

Figure 6.24: Contour plots of total entropy measured in MP22 and BASE airfoils with LS and BS

continues thus for TEWC (see Figure B.34) because the overall level of BS is below LS as it would be expected regarding the efficiency discussion in Figure 5.12. Here, an improvement close to the casing can also be found.

6.3 Summary

The findings of this chapter showed that endwall contouring is sensitive to leakage flow interaction. By taking into consideration that leakages are hard to avoid in commercial turbo machinery, altering the position of endwall contouring within the flow channel could be an appropriate response. By this means the beneficial tendencies, which were accounted for in stage 2, could be kept and the negative impact of a re-entering leakage flow could be avoided. Additionally, the manufacturing costs could be reduced by about 50% as only the casing side has to be modified at the rotor and the hub for the stator, respectively. Nevertheless, the leakage flow of a turbine has to be properly known in advance of the decision to perform a retrofit with TEWC. However, this is mainly required if optimized compound lean airfoils are applied.

The results of Schwab [125] and Zimmermann [161], [163] have shown that TEWC is beneficial in combination with constant section airfoils for both sealing designs and repective higher ratios of leakage flow.

7 Conclusion

The focus of this thesis lies in the investigation of how tangential endwall contouring is a proper method to increase the efficiency of turbomachines with advanced compound lean blading (3D). The speciality of the investigated contouring lies in the requirement to be applied along with a retrofit measure of an existing turbine. Therefore, it is designed to be milled into the casing or rotor sided material.

The motivation is based on the thesis of Schwab [125] who focussed on a constant section blading and a test set up that uses labyrinth sealing within the cavities at shroud and hub. Two configurations have been investigated in baseline (2D BASE LS) and in endwall contoured configuration (2D TEWC LS). Schwab stated an increased efficiency of up to 0.55% for the design point.

To allow the measurement of even smaller deviations that were expected for a 3D airfoil design, the same 2-stage axial turbine test rig has been upgraded with a newly developed probe adjusting device and improved measurement technology. Also the measurement procedure has been changed to ensure redundant results and systematic errors are avoided. A study of the measurement grid has been conducted to ensure a proper measurement of all occuring phenomena. By these means, the measurement resolution has been improved by 400% while the measurement time has been reduced down to 25% of the previous set up. The results of this study have been published by Zimmermann et al. [162]

Furthermore, a second sealing design at the casing side has been utilized that contains a brush seal instead of a centred labyrinth seal fin. The resulting leakage mass flow could be reduced by the factor of eight down to 0.12% of the corresponding leakage flow in each operating point. This measure was motivated to separate the influence of the endwall contouring and leakage flow interaction. Zimmermann et al. [161] have shown for two operating points of the 2D TEWC design that the leakage flow interaction has an significant impact on the performance.

Following, 2D and 3D airfoils were investigated with improved measurement methodology in baseline and endwall contoured design and the minimized leakage flow of the brush seal configuration (2D BASE BS, 2D TEWC BS, 3D BASE BS, 3D TEWC BS). On the one hand, the results by Schwab were confirmed for the 2D airfoils, on the other hand it was shown that for 3D airfoils the trends were equivalent to the 2D configuration. The first stage efficiency suffered due to the application of TEWC, however, the second stage showed beneficial tendencies. This study was presented by Zimmermann et al. [163] and served to compare both airfoil types as the present thesis focusses on 3D airfoils exclusively

Therefore, the previous investigations have been extended for the present thesis to understand how endwall contouring is affecting the flow and to also determine the impact of leakage flow on the performance of the contouring. A configuration with an exclusive vane contouring is investigated additionally to see, whether rotor or vane or both have to be contoured in order to improve the turbine's efficiency. For this purpose the discussion of the results is split into three parts:

At first, only the brush seal configurations are compared. The results show that TEWC-V performs best in stage 1 while TEWC loses in efficiency for the design point and in part load compared to BASE. This trend is flipped in stage 2 as TEWC performs best and TEWC-V loses significantly down to 2%.

The second focus is put on the interaction of endwall contouring and leakage flow. Here, all labyrinth seal configurations are compared and it turned out that neither TEWC-V nor TEWC showed an increased efficiency at any operating point. The trends within the first stage are similar to the brush seal results. In the second stage both contouring designs perform worse than BASE leading to the assumption, that the change in efficiency is mainly caused by the re-entering leakage mass flow upstream and not by the flow that is sucked into the cavities in front of the rotor contouring.

Thirdly, each airfoil type is investigated in isolation regarding it's performance corresponding to the leakage flow. It is shown that in stage 1, all labyrinth seal configurations loose in efficiency by the same amount, due to less flow that participates the energy conversion. For stage two, the BASE design shows no difference by comparing the labyrinth with the brush seal configuration TEWC-V LS performs slightly better in OP1 and OP2, while OP3 and OP4 don't show a change. Despite these findings TEWC-LS is worse than TEWC-BS.

All discussed phenomena lead to the assumption that the present design methodology of endwall contouring has the potential to increase the efficiency of a compound lean blading that already shows a good aerodynamic performance. However, the leakage to main flow ratio of a turbine has to be evaluated in advance to decide whether a retrofit measure is applied as the performance is decreased for ratios $\geq$0.1.

Furthermore, future investigations have to clarify if the beneficial impact of TEWC-BS within the second stage is repeated in following stages. Also a study of the performance behaviour for leakage flow ratios between 0.01 (BS) and 0.1 (LS) would be useful to quantify the exact amount of leakage that is allowed to achieve a benefit due to a retrofit of an engine by means of TEWC. It also has to be studied, whether the contouring design itself can be improved and if a selective contouring on rotor shroud and stator hub for example reduces the losses that are caused by the leakage flow interaction.

List of Figures

List of Tables

A Probe calibration

Calibration is a process that is used to determine the deviation of the measured data to the exact value. The temperature and pressure probes that have been used for the present investigations have been previously calibrated in the open jet wind tunnel of the Institute of Jet Propulsion and Turbomachinery, RWTH Aachen University.

Before calibration, the probes are adjusted in the centre of the outflow nozzle facing the flow perpendicularly. The calibration is performed within an angle range of $\pm 20^{\circ}$ in yaw and pitch direction in steps of 4° for several Ma-numbers (0.1, 0.15 and 0.2) that have been chosen according to the occuring flow within the turbine.

A.1 Pressure probe calibration

The pressure probe calibration is explained exemplary for the 5HP as the methodology is the same for the 3HP.

As one can see in Figure A.1 the pressure at each bore within the probe head is measured separately ($p_0, .., p_4$). After the probes have been installed perpendicular to the nozzle, the pressure differences of bore 1 and 3 are compared and the probe is rotated slightly to realize an aerodynamic zero position of the yaw angle α. The resulting deviation has to be considered for the post processing as it results from the manufacturing process. The same procedure is performed for the pitch angle γ (bore 2 and 4) in advance to the calibration process.

The pressures $p_0, ..., p_4$ are a function of the total state of the flow, α, γ and the Ma-number. Therefore, the measured pressures clearly depend on α, γ and Ma thus dimensionless factors can be derived to formulate their mathematical relation:

$$K_{\alpha} = \frac{p_3 - p_1}{\Delta p} \quad , \quad K_{\gamma} = \frac{p_4 - p_2}{\Delta p} \quad , \quad K_{Mach} = \frac{\Delta p}{p_0} \quad , \quad K_{Stat} = \frac{p_{Stat} - p}{\Delta p} \quad , \quad K_{Tot} = \frac{p_{Tot} - p_0}{\Delta p}$$

$$with$$

$$\Delta p = p_0 - \frac{p_1 + p_3}{2}$$

These so called K-factors separate the influence to only one of the given parameters and therefore allow to recalculate the required flow condition by awareness of all K-factors. To correct the geometry of the probe head, the method by Vinnemeier et al. [146] is applied during the post processing. For the present test rig, the software implementation of the mathematical approach has been published by Schwab [125] and is therefore not further elaborated.

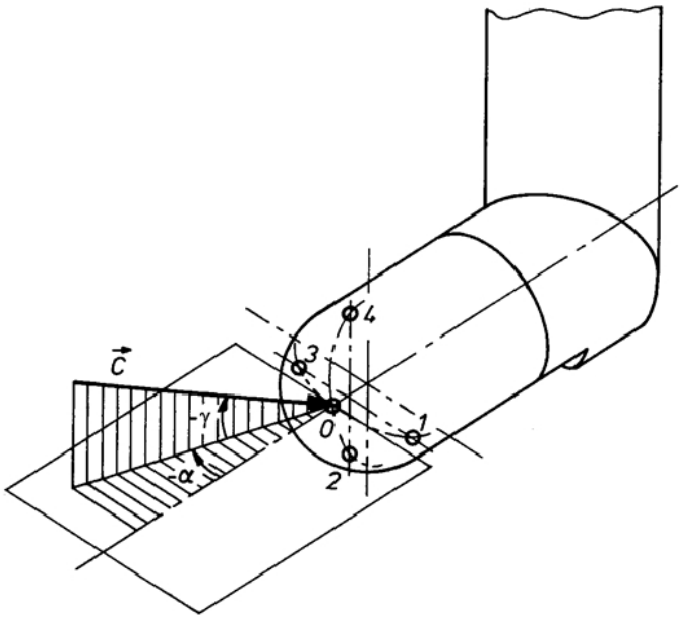

Figure A.1: 5-hole probe with semi-sphere shaped head according to Bohn et al. [14])

A.2 Temperature probe calibration

According to Burns et al. [19] the TP have been calibrated in an oil bath in advance to the wind tunnel calibration. Furthermore, the wind tunnel calibration has been performed using the same MAS, connector cables and cold junction compensation as it is used for the measurement within the turbine. This calibration is performed to determine the recovery factor RF of each single probe [11]. For this purpose, the probe temperature (T_{Probe}) is recorded for each angle position and Ma-number by simultaneously measuring the total temperature (T_{Tot}) within the upstream located equalising tank. By this means, the RF is calculated using Equation A.1

$$RF = \frac{\frac{T_{Probe}}{T_{Tot}} \cdot \left(1 + \frac{\kappa-1}{2} \cdot Ma^2\right) - 1}{\frac{\kappa-1}{2} \cdot Ma^2} \tag{A.1}$$

During the tests, the total temperature as well as the static temperature can be determined via multiple parameter approximation and in combination with the pressure probe data that serves to determine the flow angle as well as the Ma number [14].

B Detail analysis of the flow field

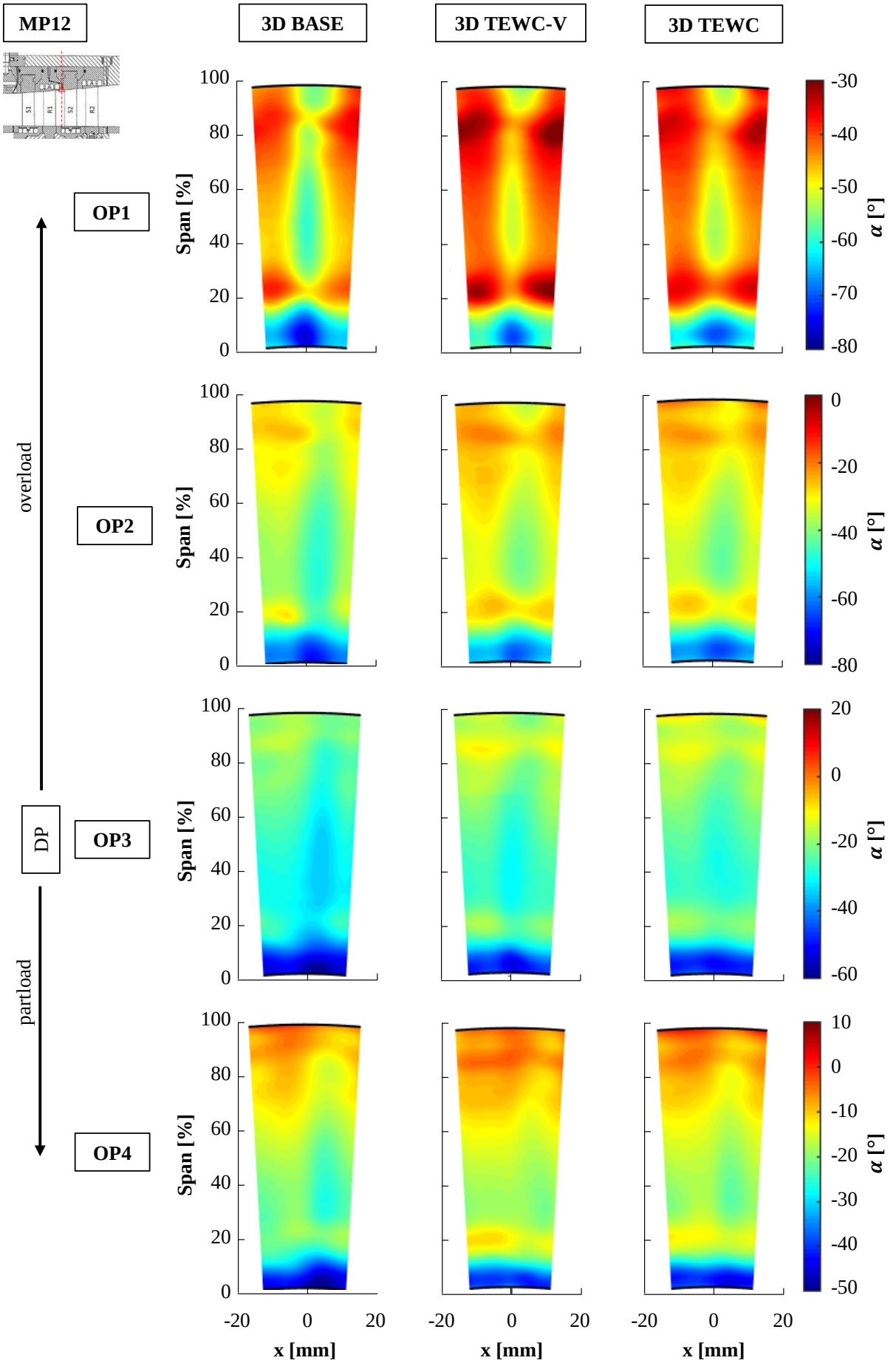

Figure B.1: Contour plots of yaw angle measured in MP12 and configurations with brush seals

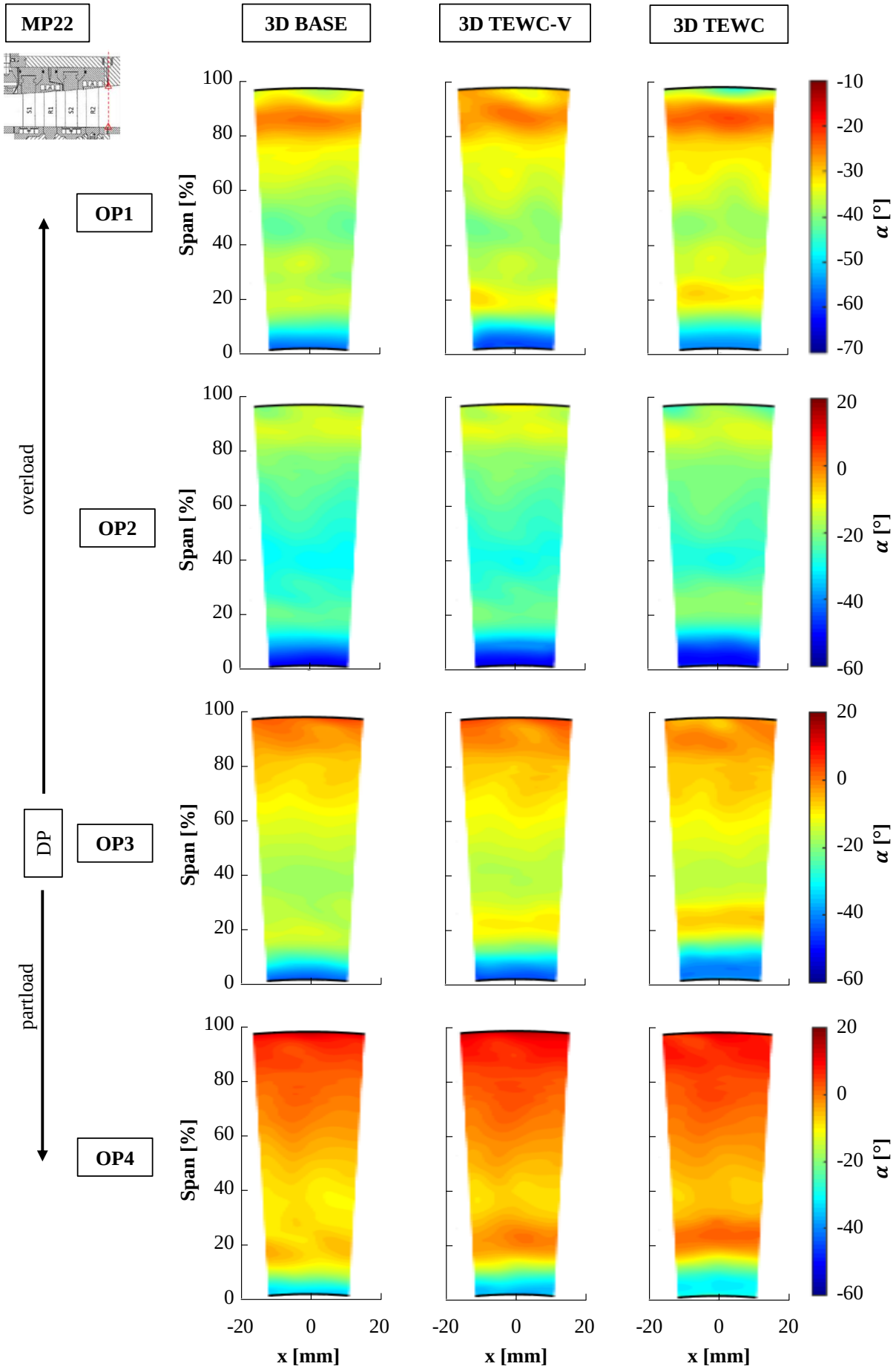

Figure B.2: Contour plots of yaw angle measured in MP22 and configurations with brush seals

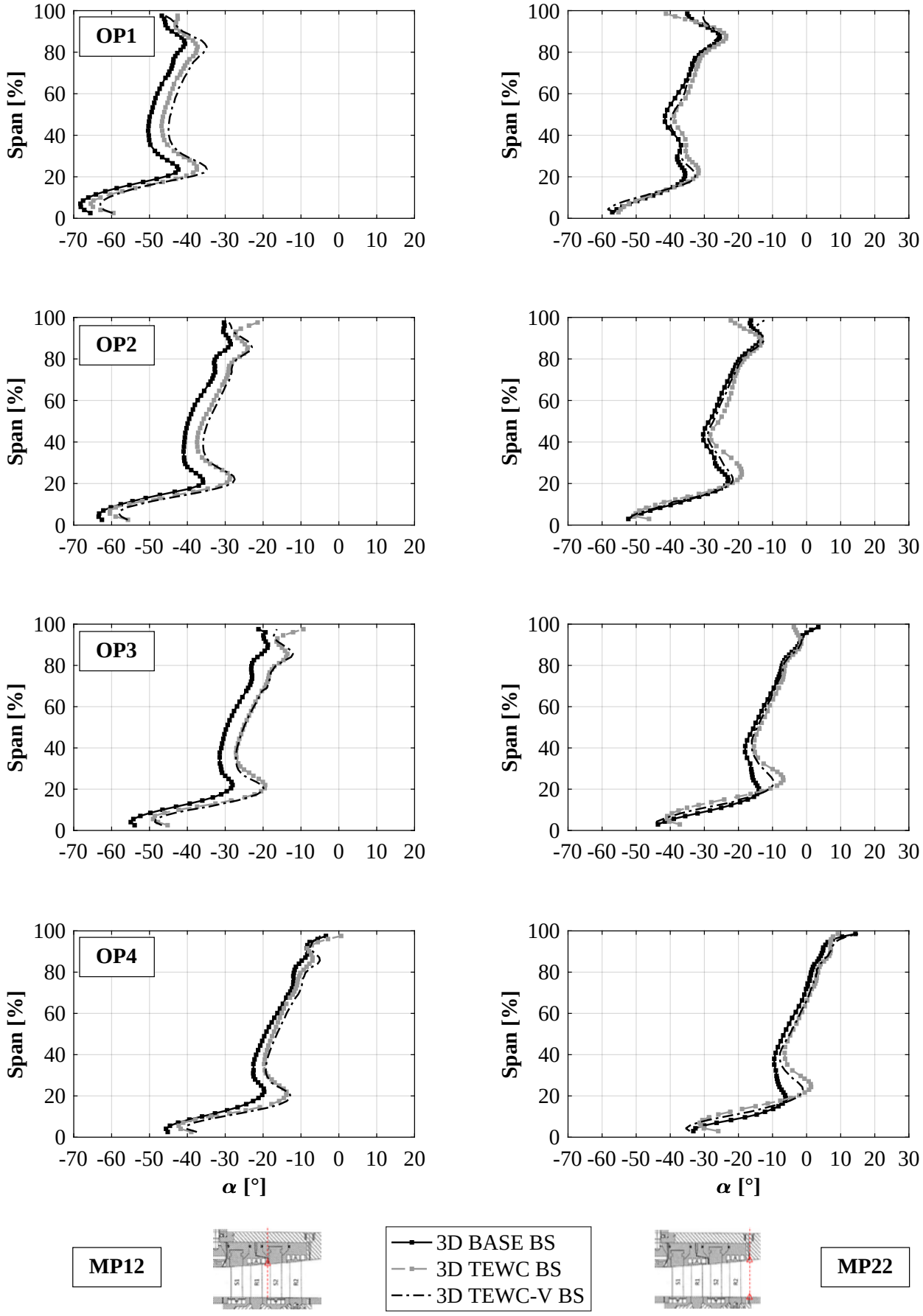

Figure B.3: Circumferentially averaged distribution of yaw angle measured in MP12 and MP22 and configurations with brush seals

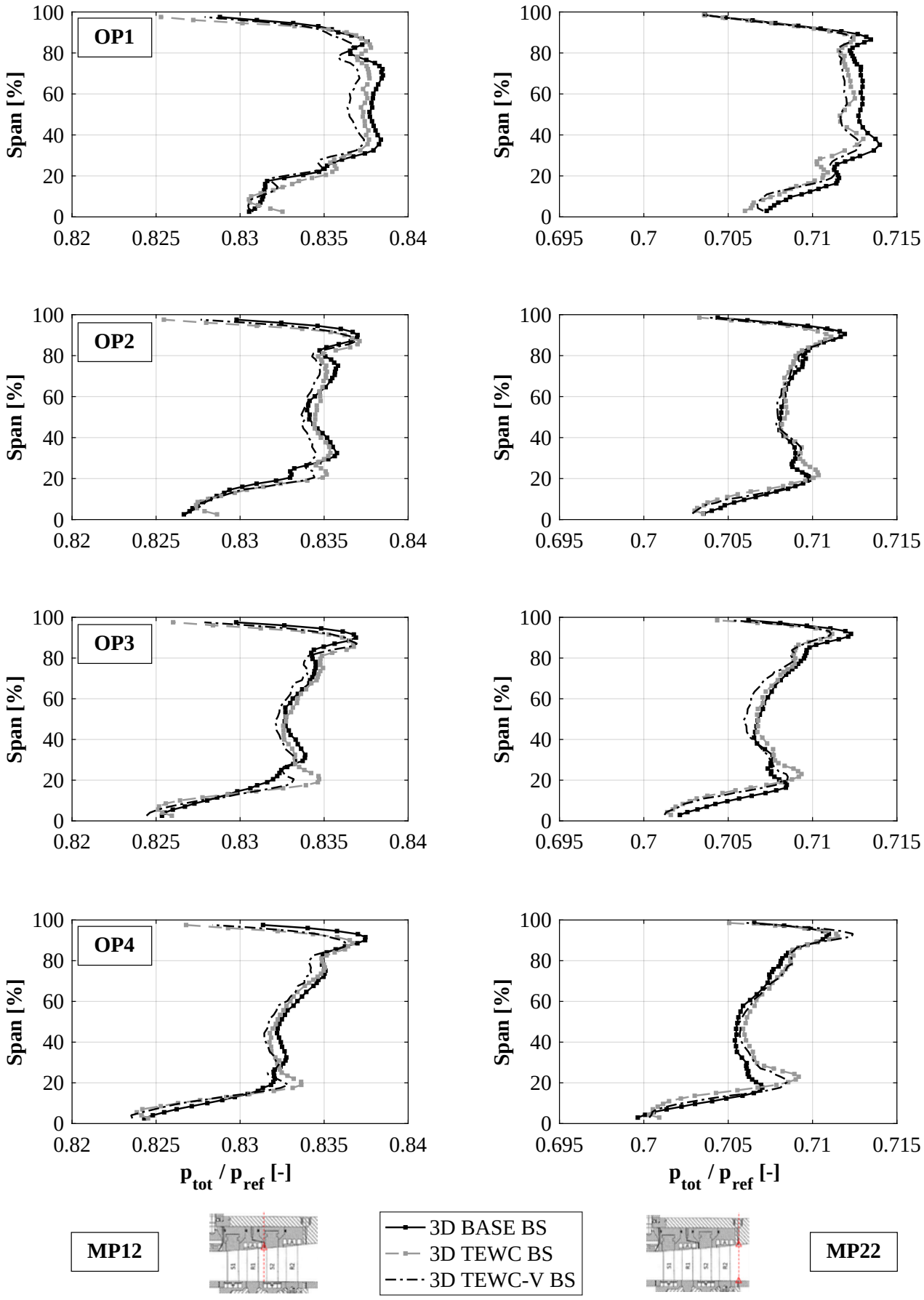

Figure B.4: Circumferentially averaged distribution of total pressure measured in MP12 and MP22 and configurations with brush seals

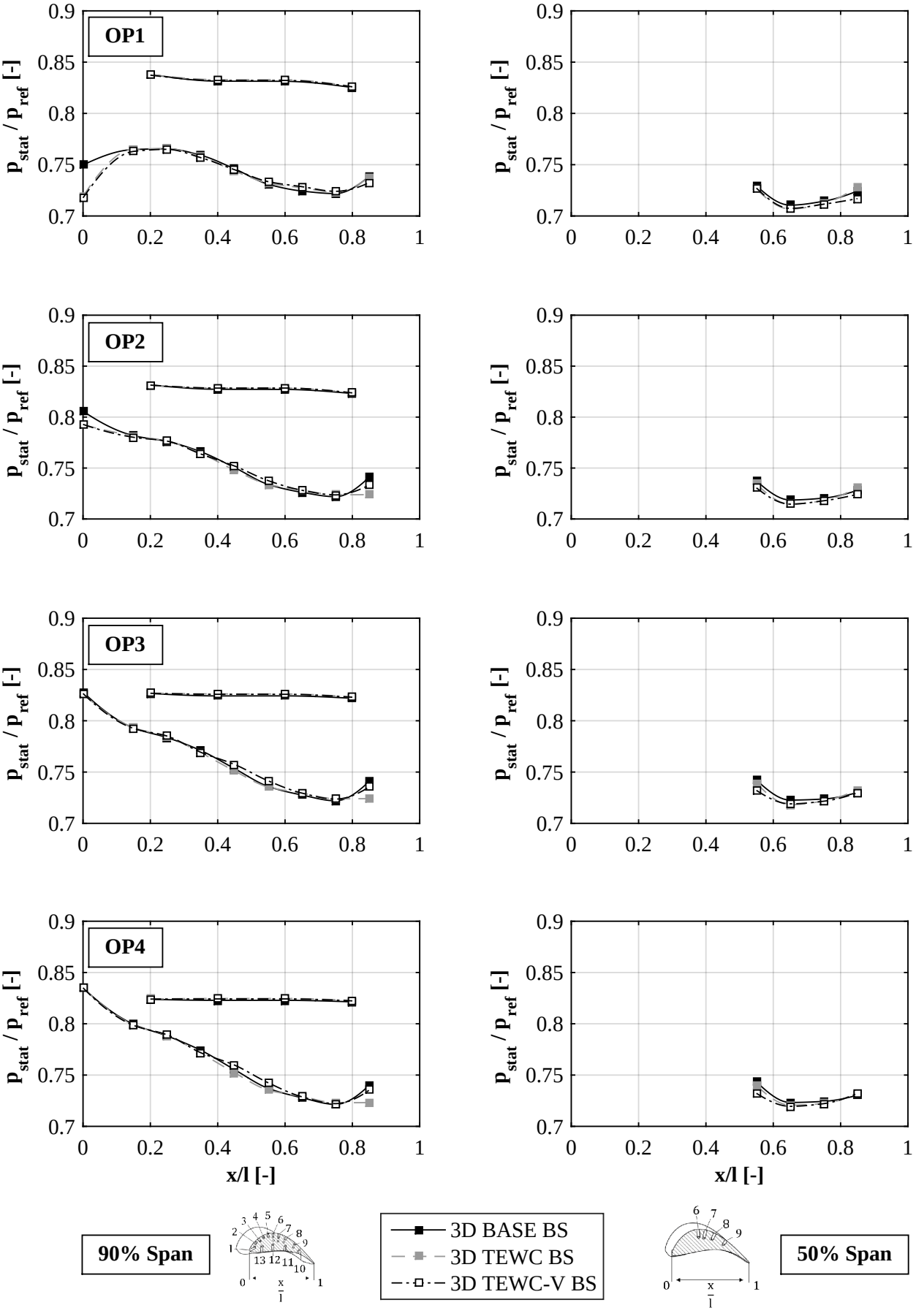

Figure B.5: Pressure distribution in axial direction across a vane of stator 2 at 90% and 50% span and configurations with brush seals

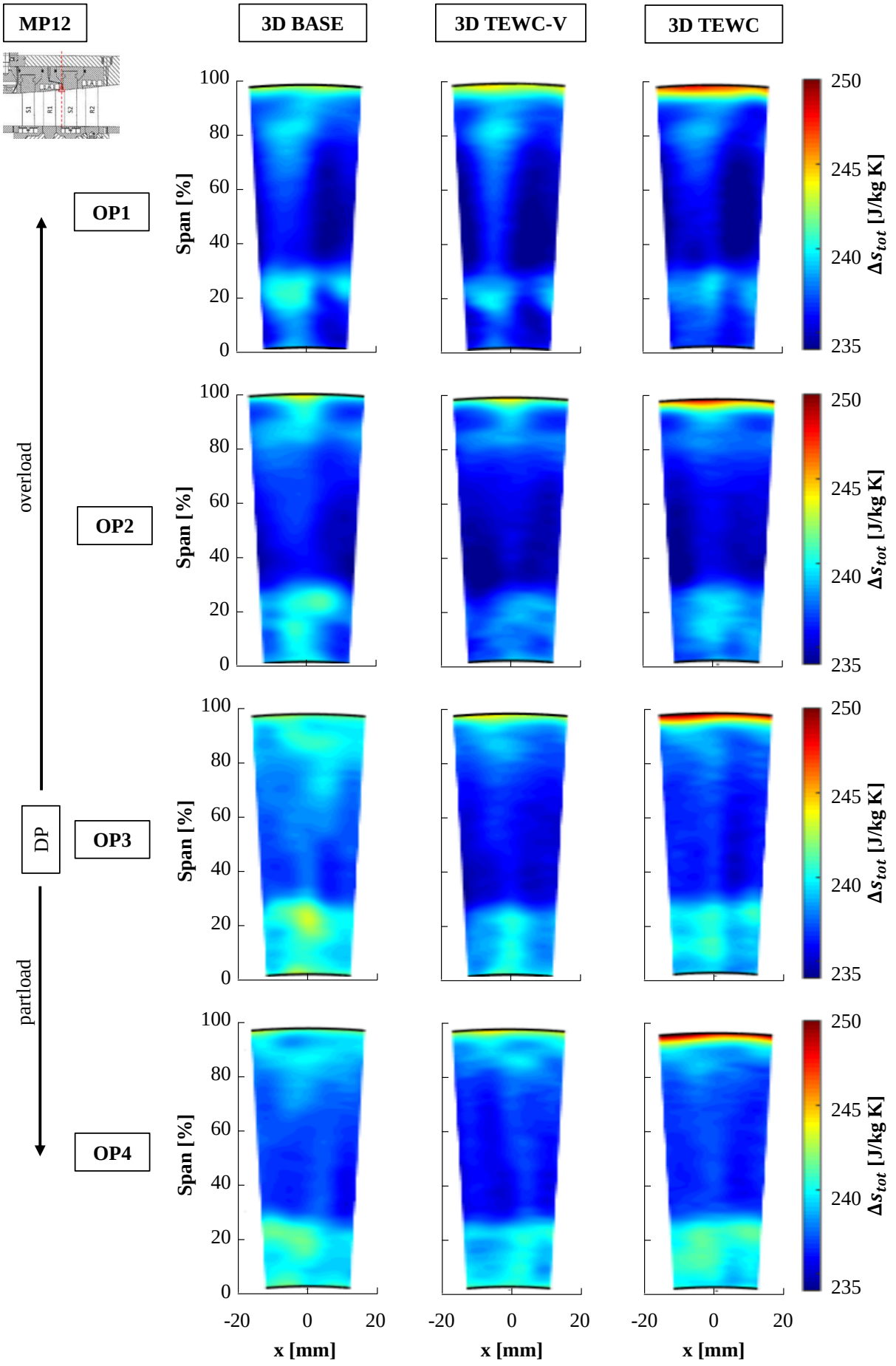

Figure B.6: Contour plots of total entropy measured in MP12 and configurations with brush seals

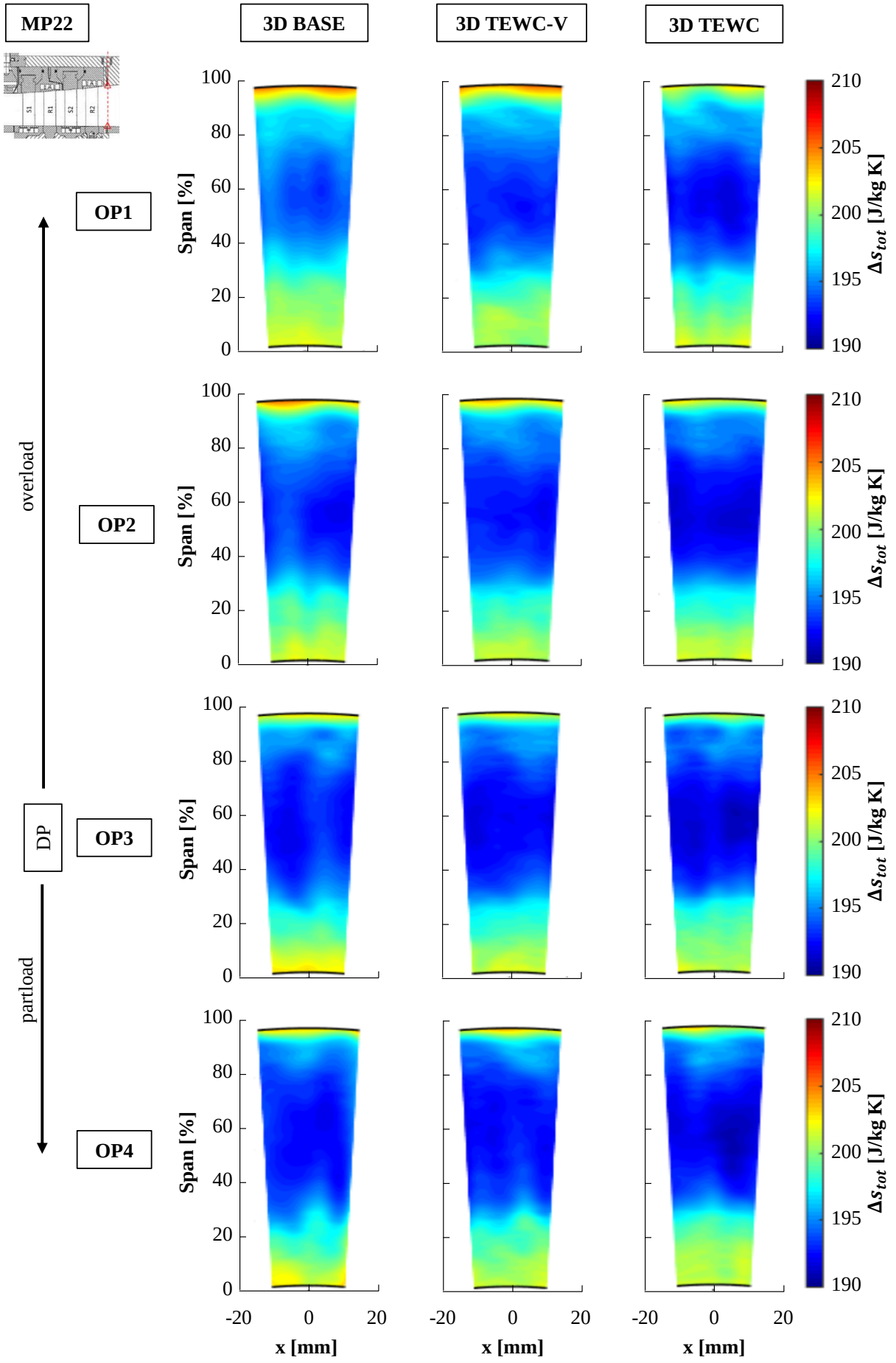

Figure B.7: Contour plots of total entropy measured in MP22 and configurations with brush seals

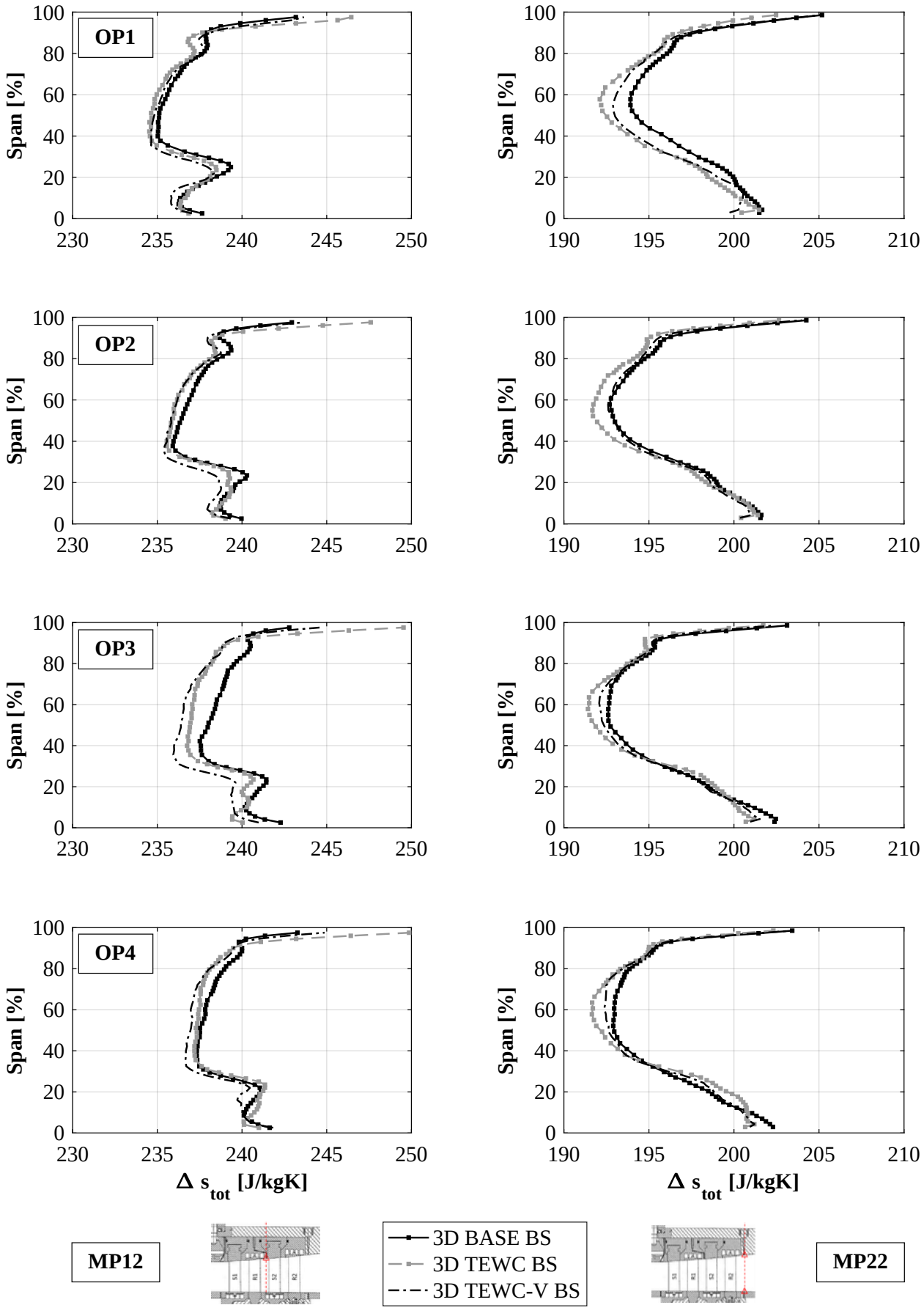

Figure B.8: Circumferentially averaged distribution of total entropy measured in MP12 and MP22 and configurations with brush seals

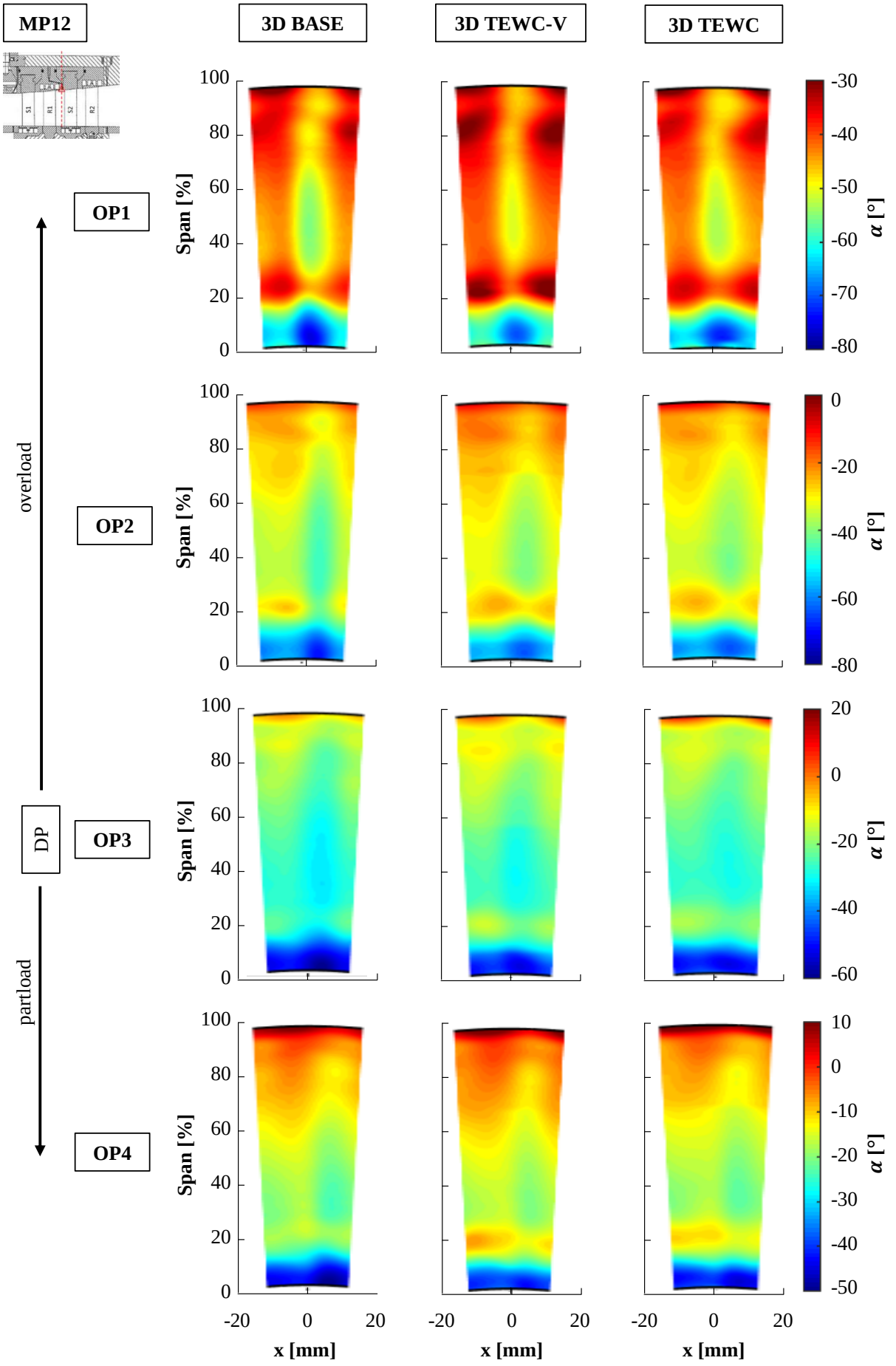

Figure B.9: Contour plots of yaw angle measured in MP12 and configurations with labyrinth seals

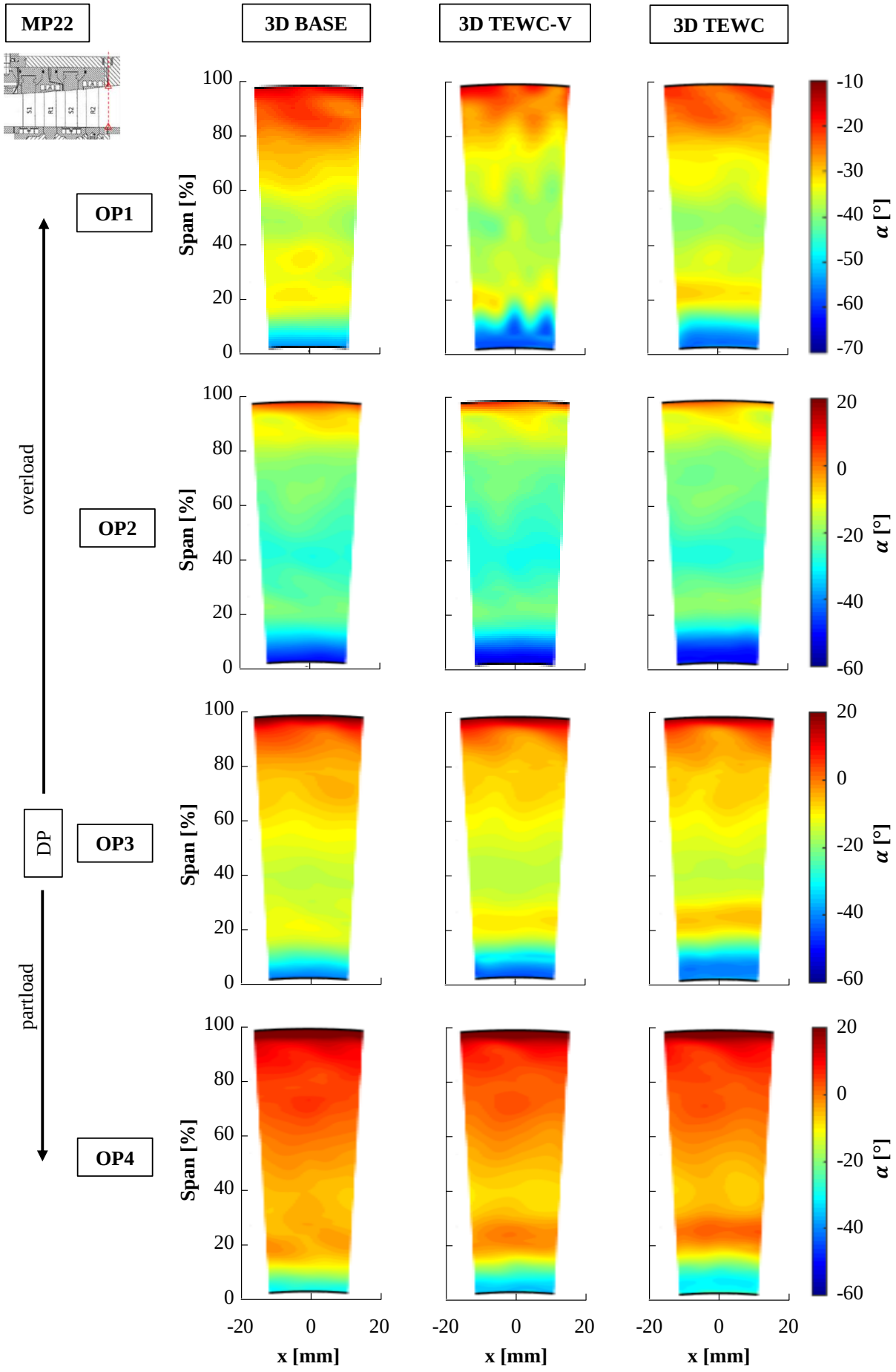

Figure B.10: Contour plots of yaw angle measured in MP22 and configurations with labyrinth seals

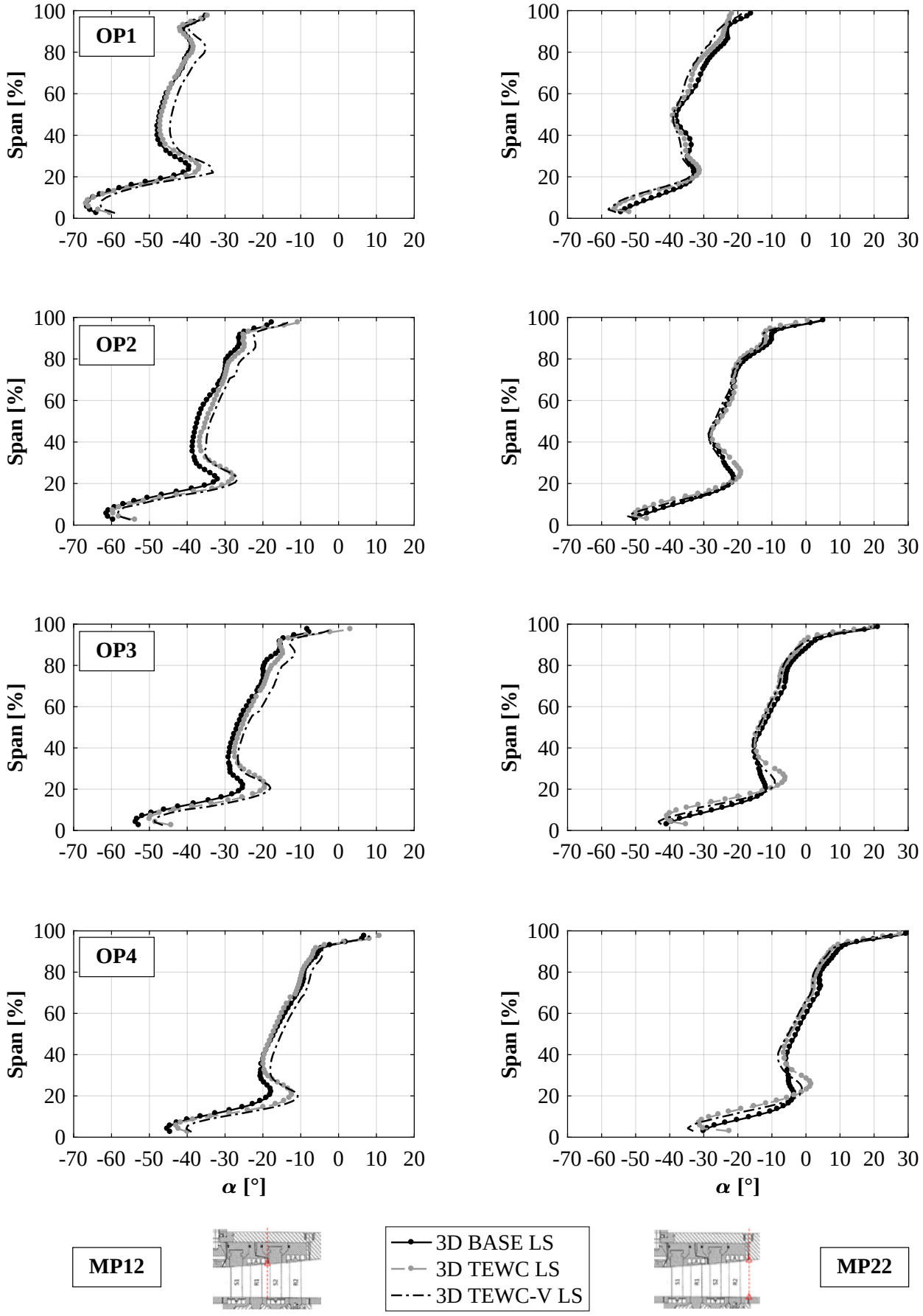

Figure B.11: Circumferentially averaged distribution of yaw angle measured in MP12 and MP22 and configurations with labyrinth seals

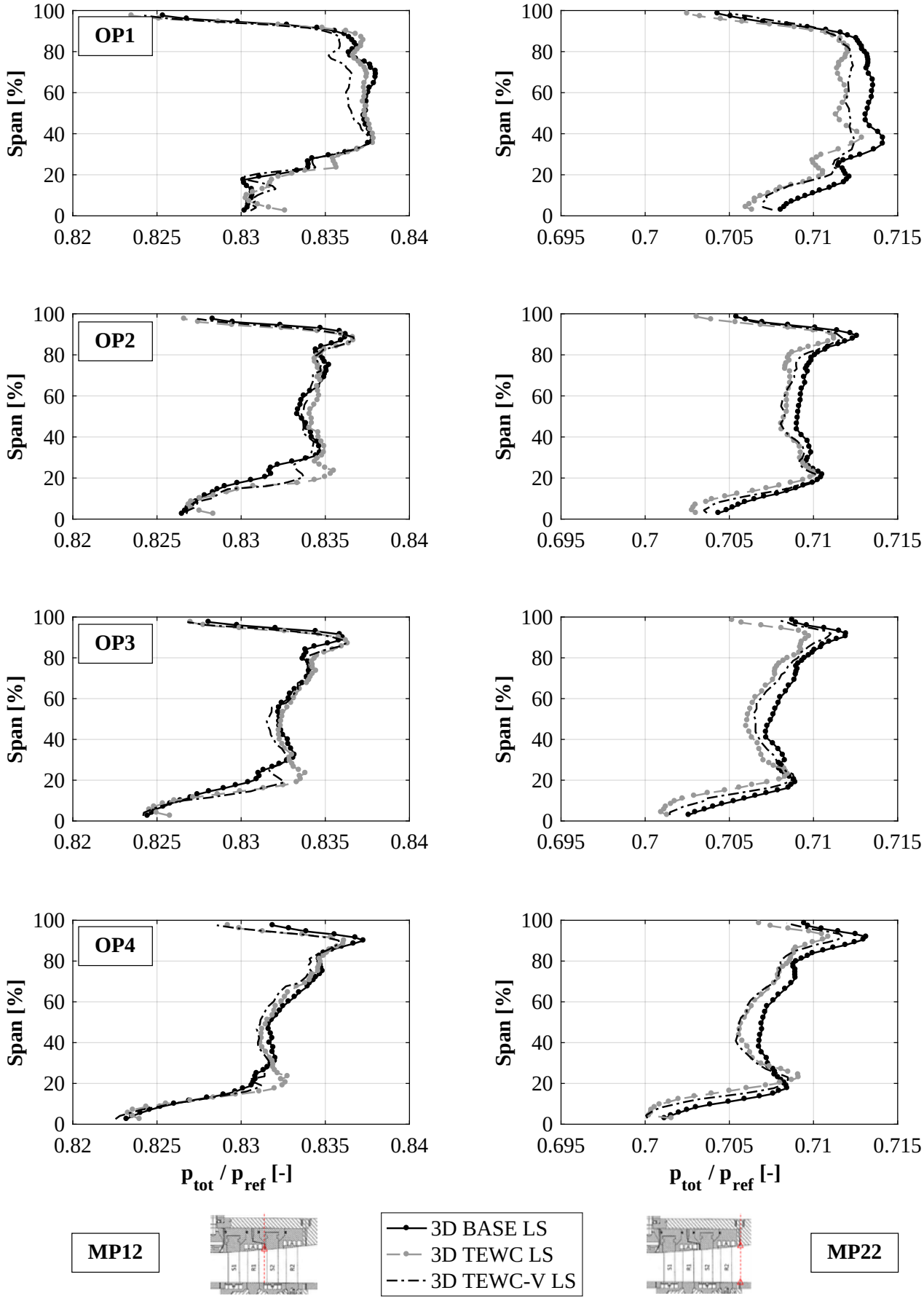

Figure B.12: Circumferentially averaged distribution of total pressure measured in MP12 and MP22 and configurations with labyrinth seals

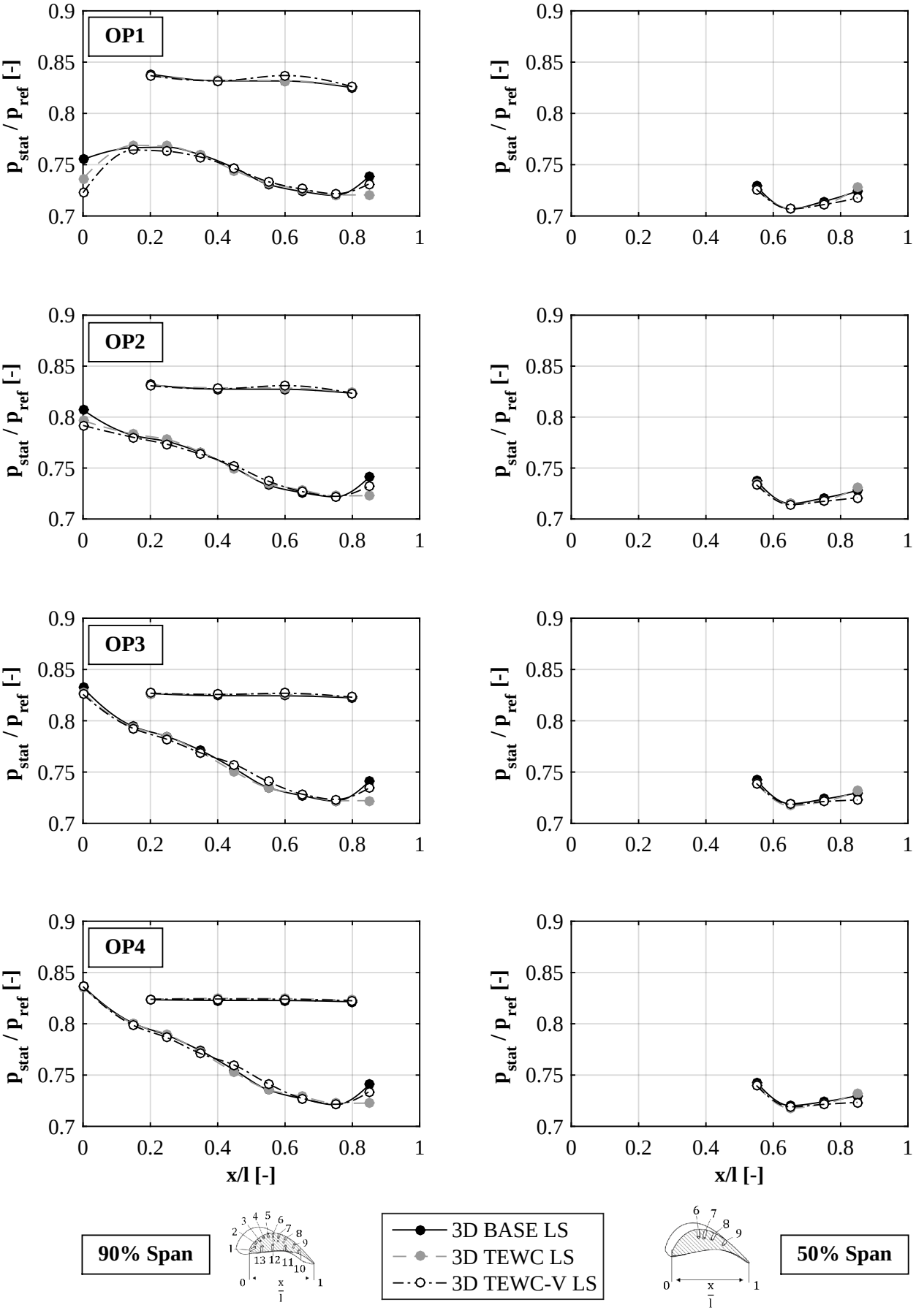

Figure B.13: Pressure distribution in axial direction across a vane of stator 2 at 90% and 50% span and configurations with labyrinth seals

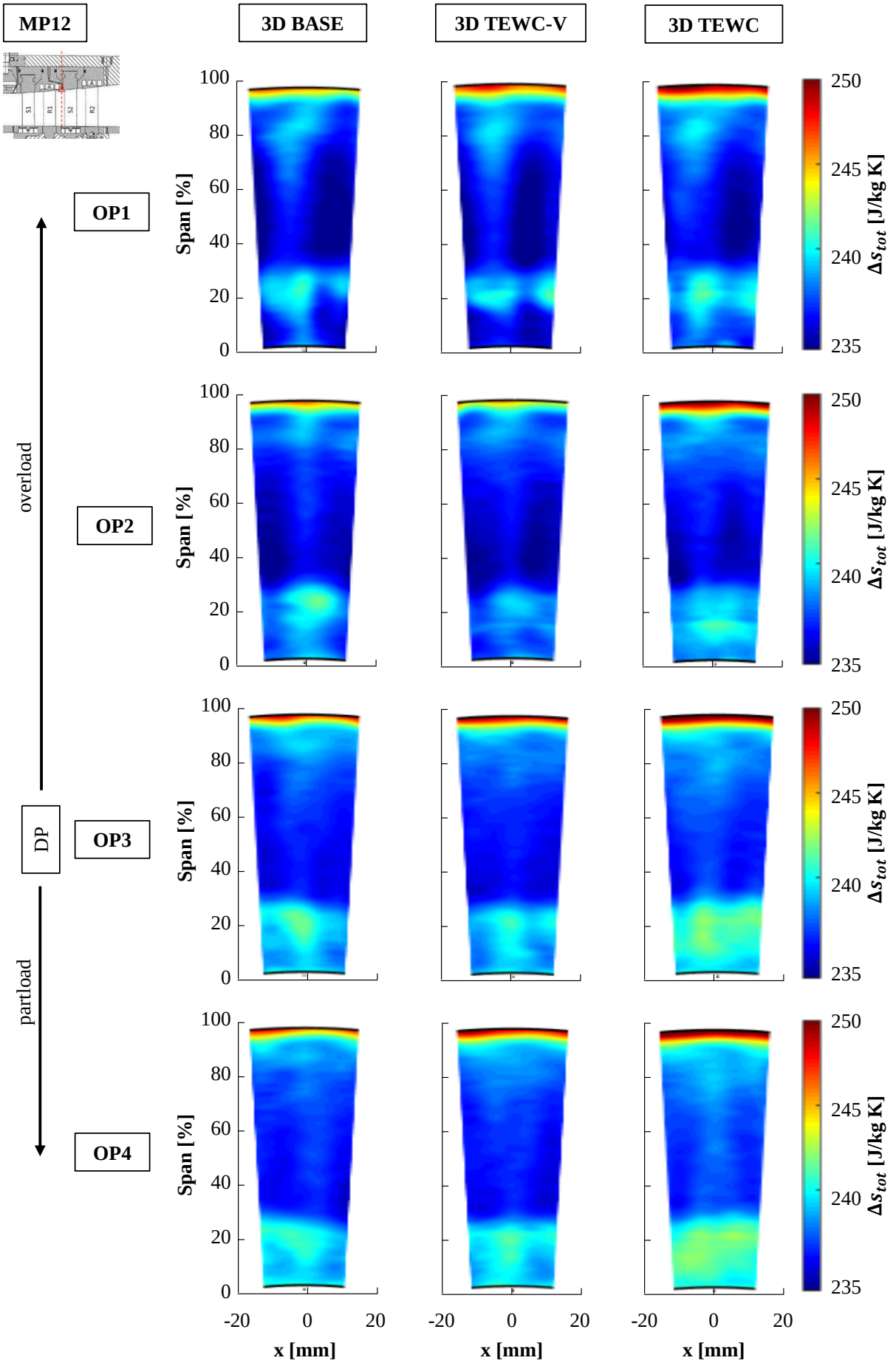

Figure B.14: Contour plots of total entropy measured in MP12 and configurations with labyrinth seals

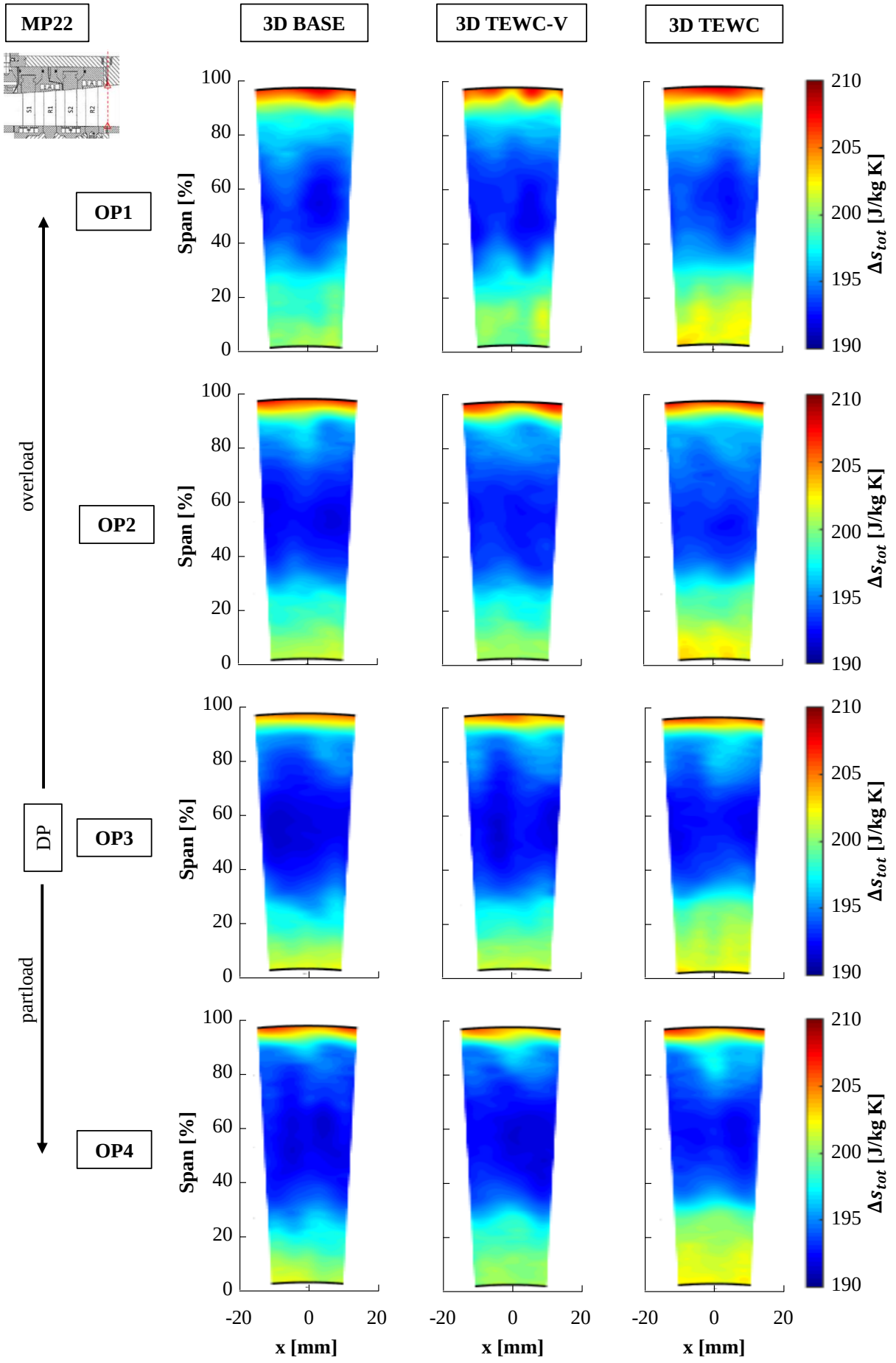

Figure B.15: Contour plots of total entropy measured in MP22 and configurations with labyrinth seals

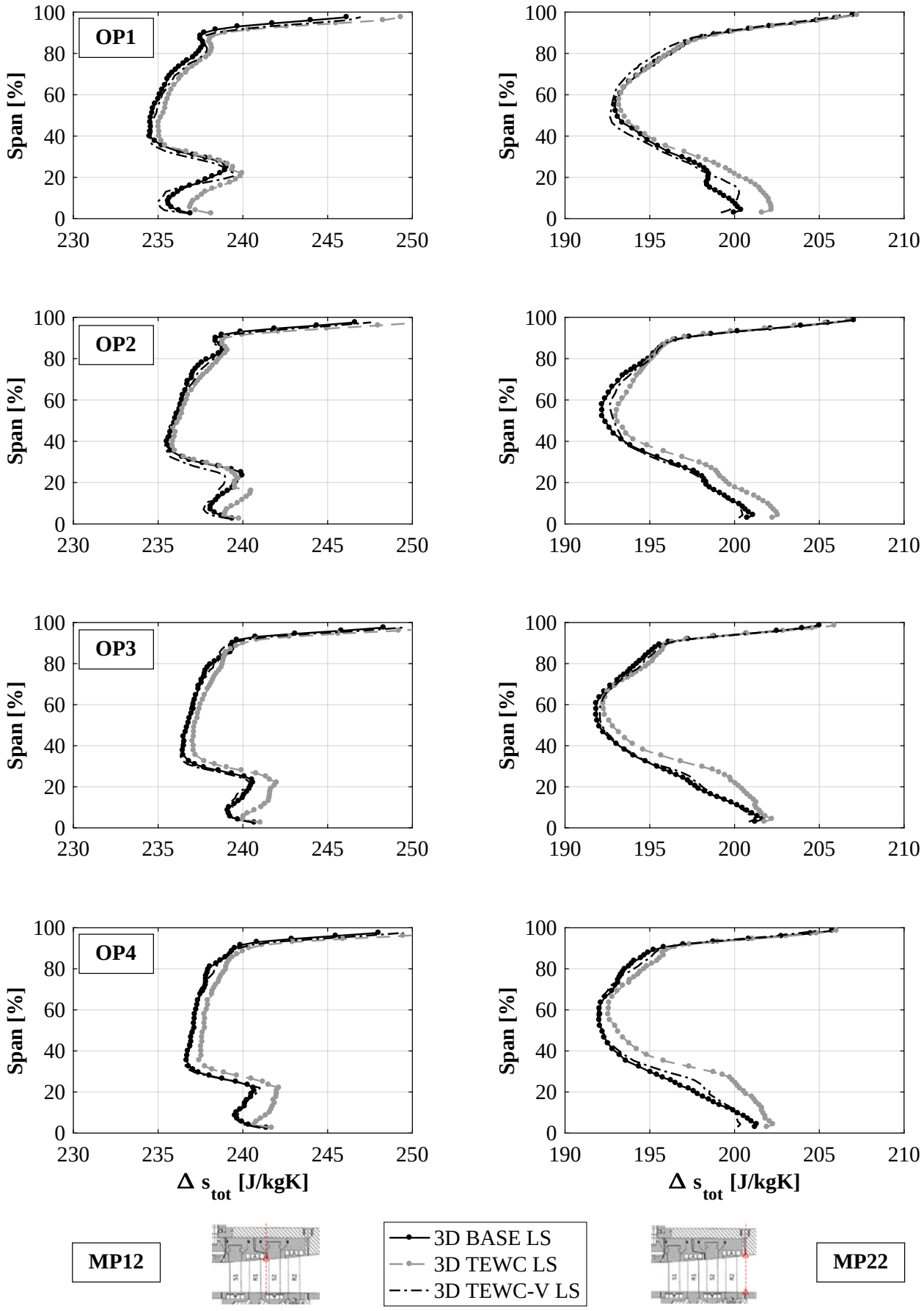

Figure B.16: Circumferentially averaged distribution of total entropy measured in MP12 and MP22 and configurations with labyrinth seals

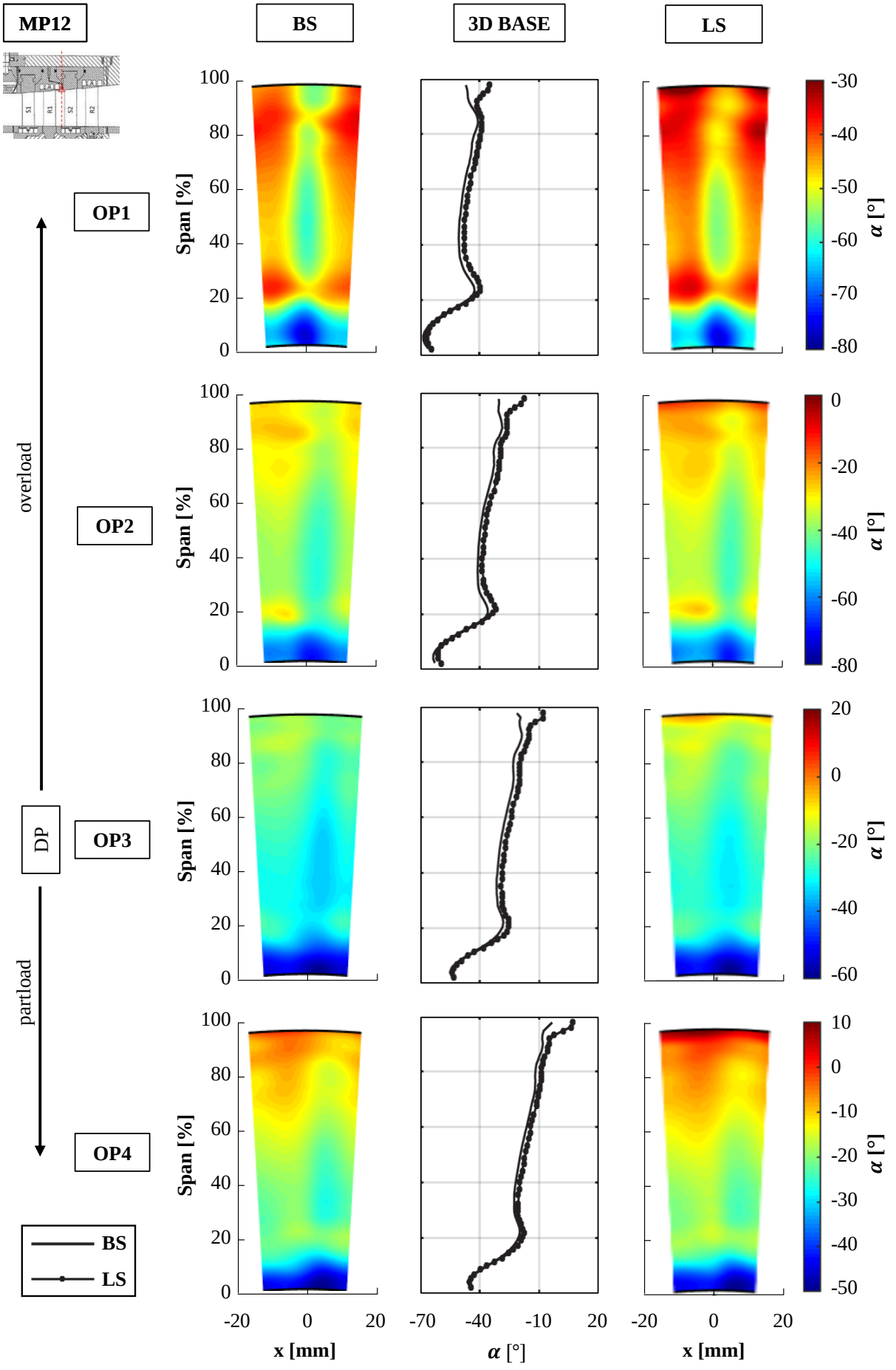

Figure B.17: Contour plots of yaw angle measured in MP12 and BASE airfoils with LS and BS

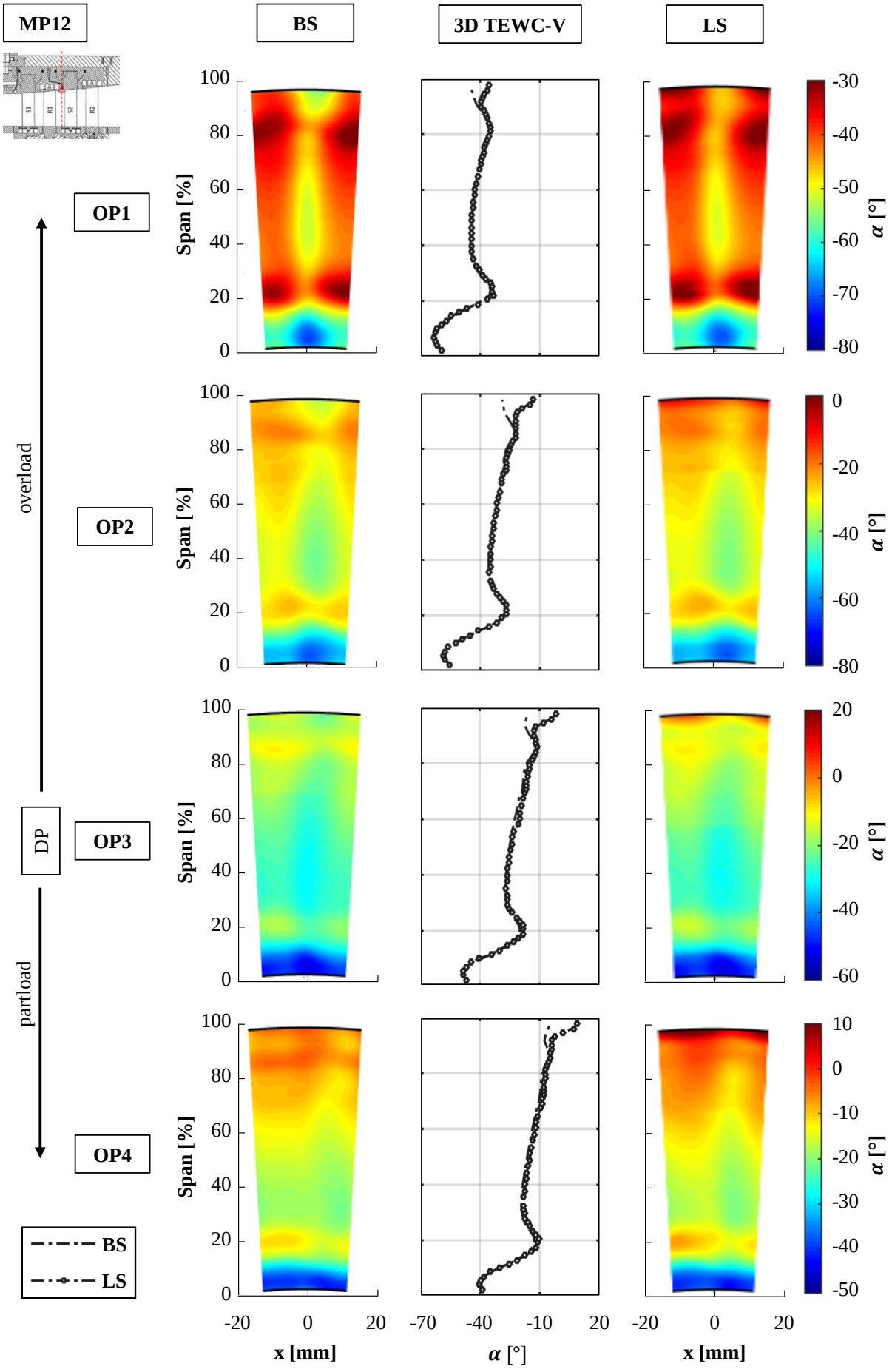

Figure B.18: Contour plots of yaw angle measured in MP12 and TEWC-V airfoils with LS and BS

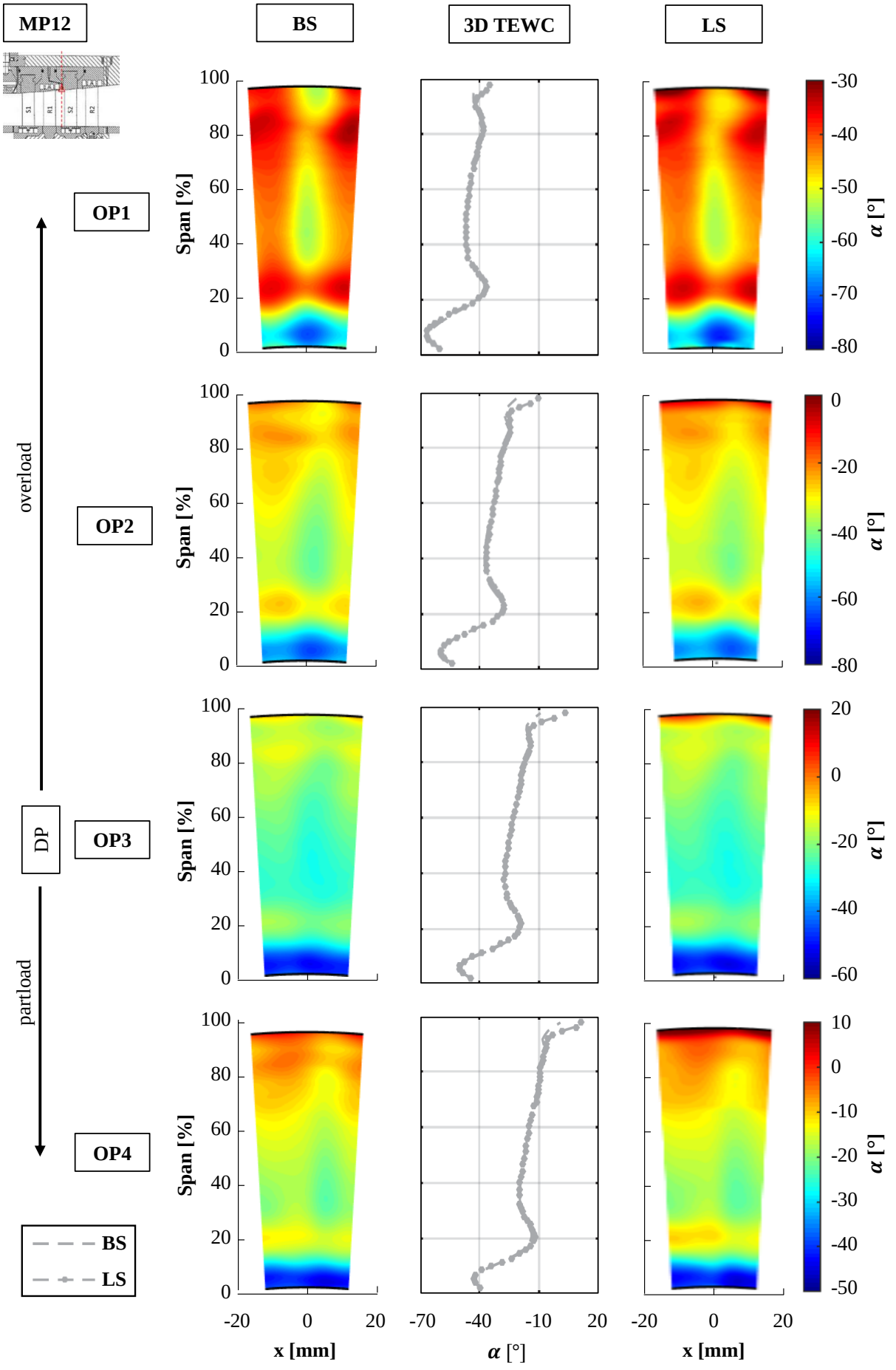

Figure B.19: Contour plots of yaw angle measured in MP12 and TEWC airfoils with LS and BS

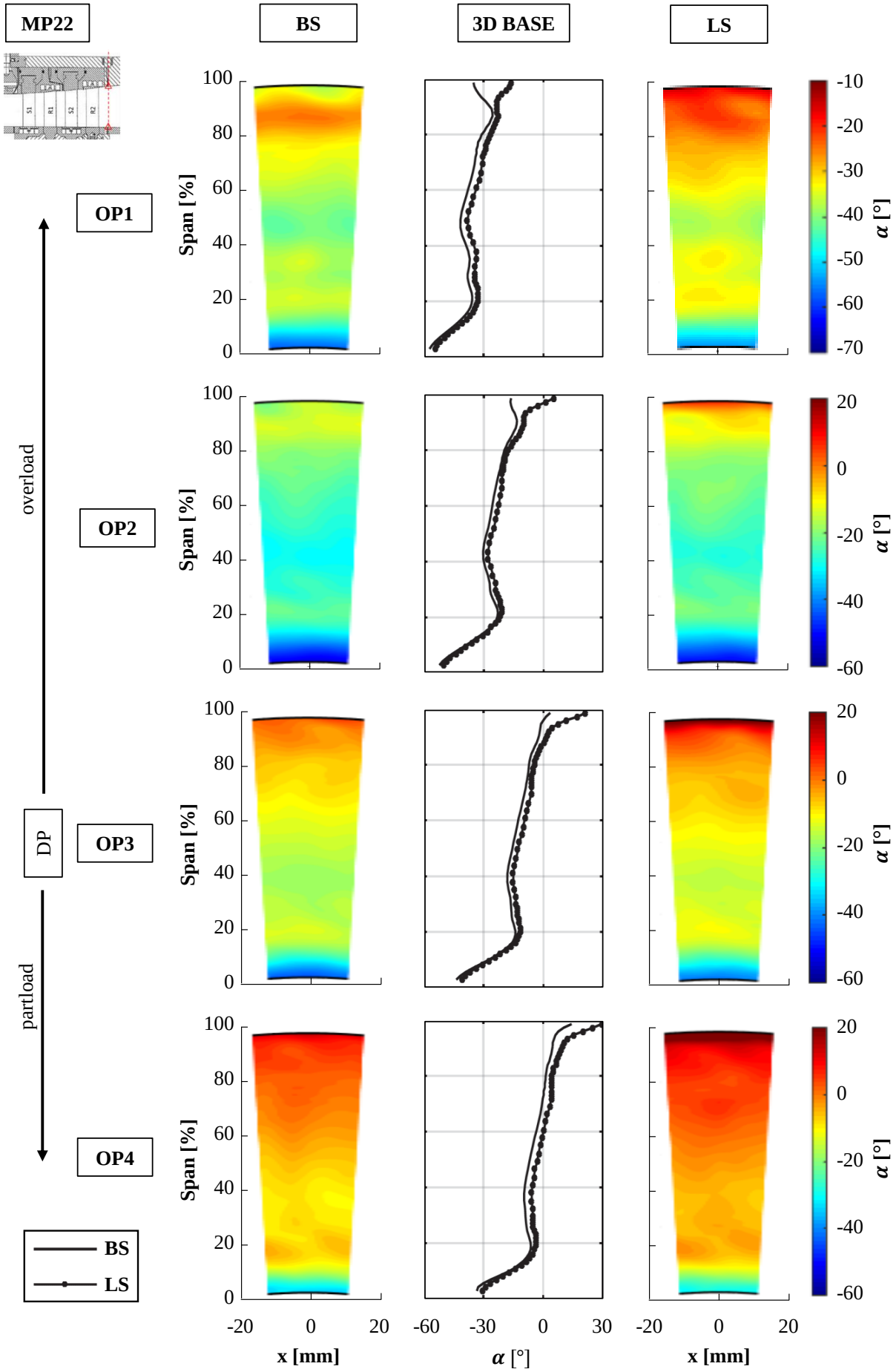

Figure B.20: Contour plots of yaw angle measured in MP22 and BASE airfoils with LS and BS

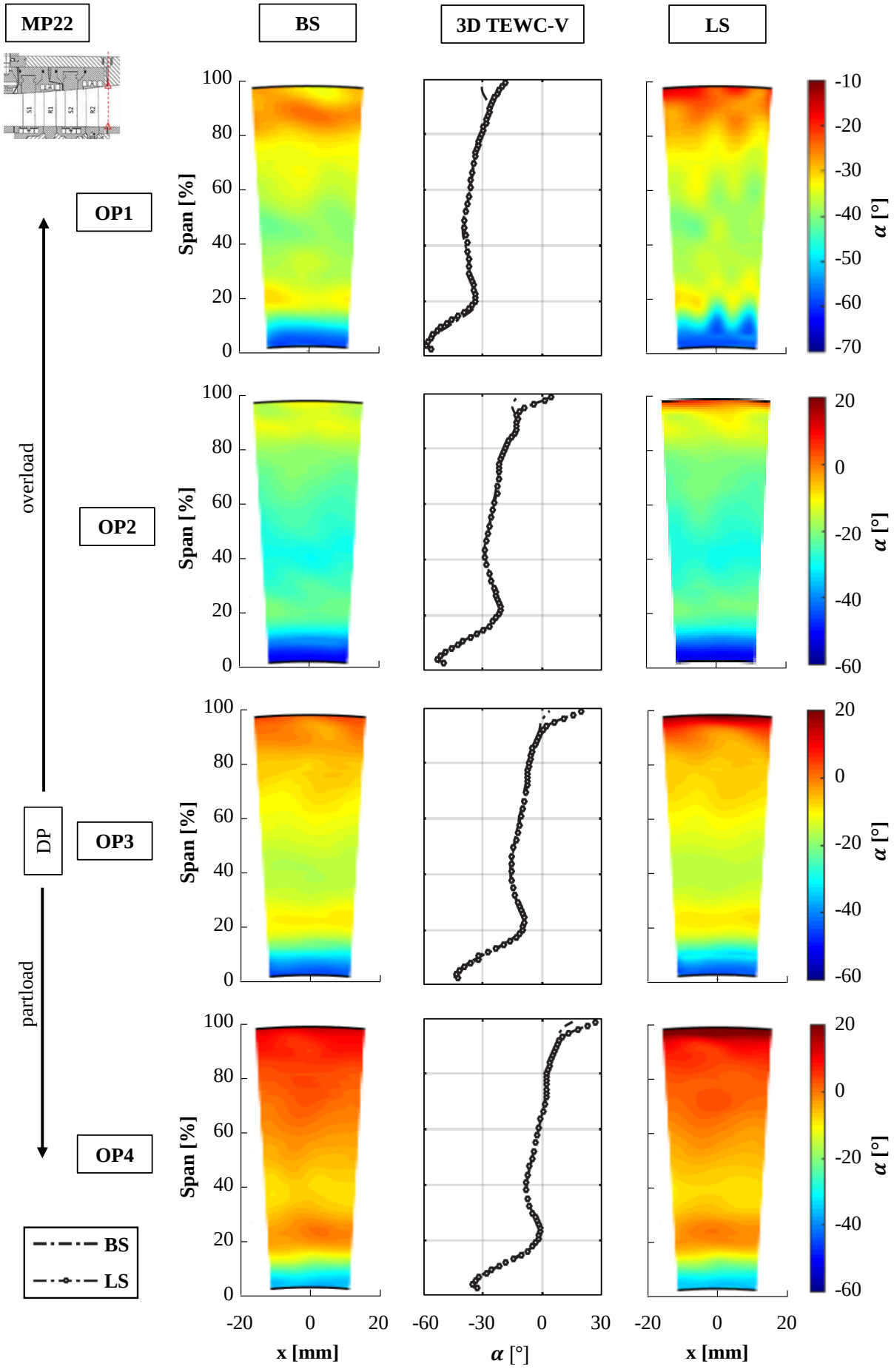

Figure B.21: Contour plots of yaw angle measured in MP22 and TEWC-V airfoils with LS and BS

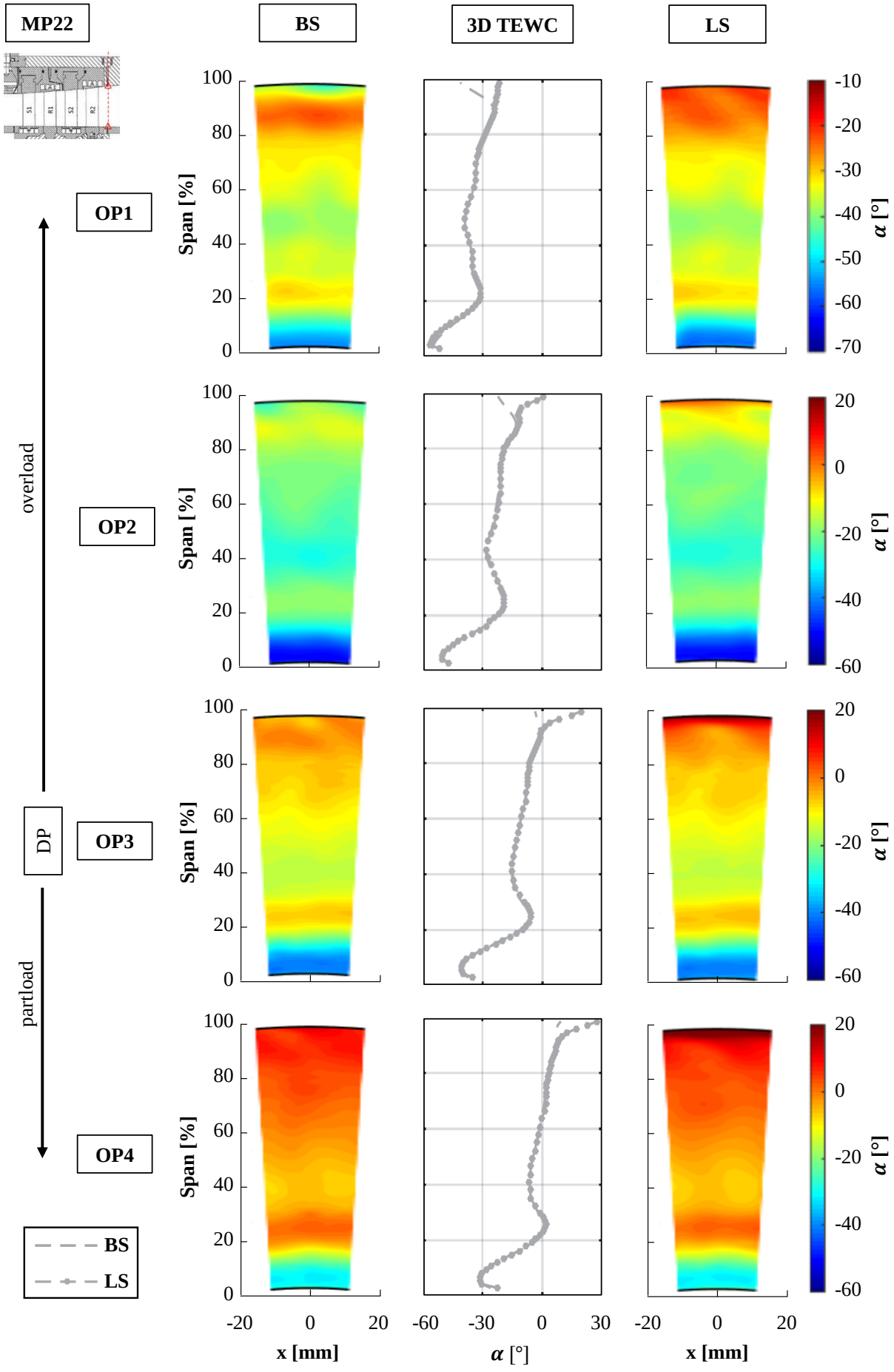

Figure B.22: Contour plots of yaw angle measured in MP22 and TEWC airfoils with LS and BS

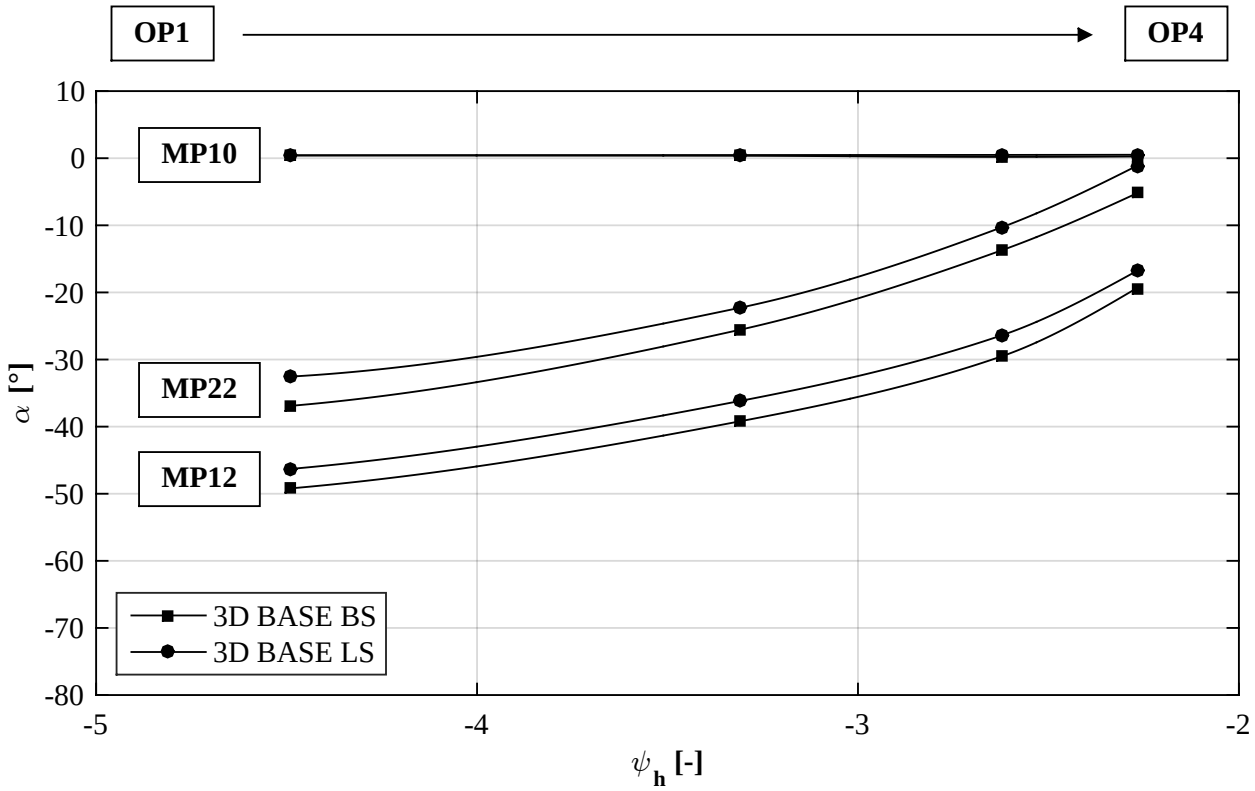

Figure B.23: Mean averaged yaw angle in MP10, MP12 and BASE airfoils with LS and BS

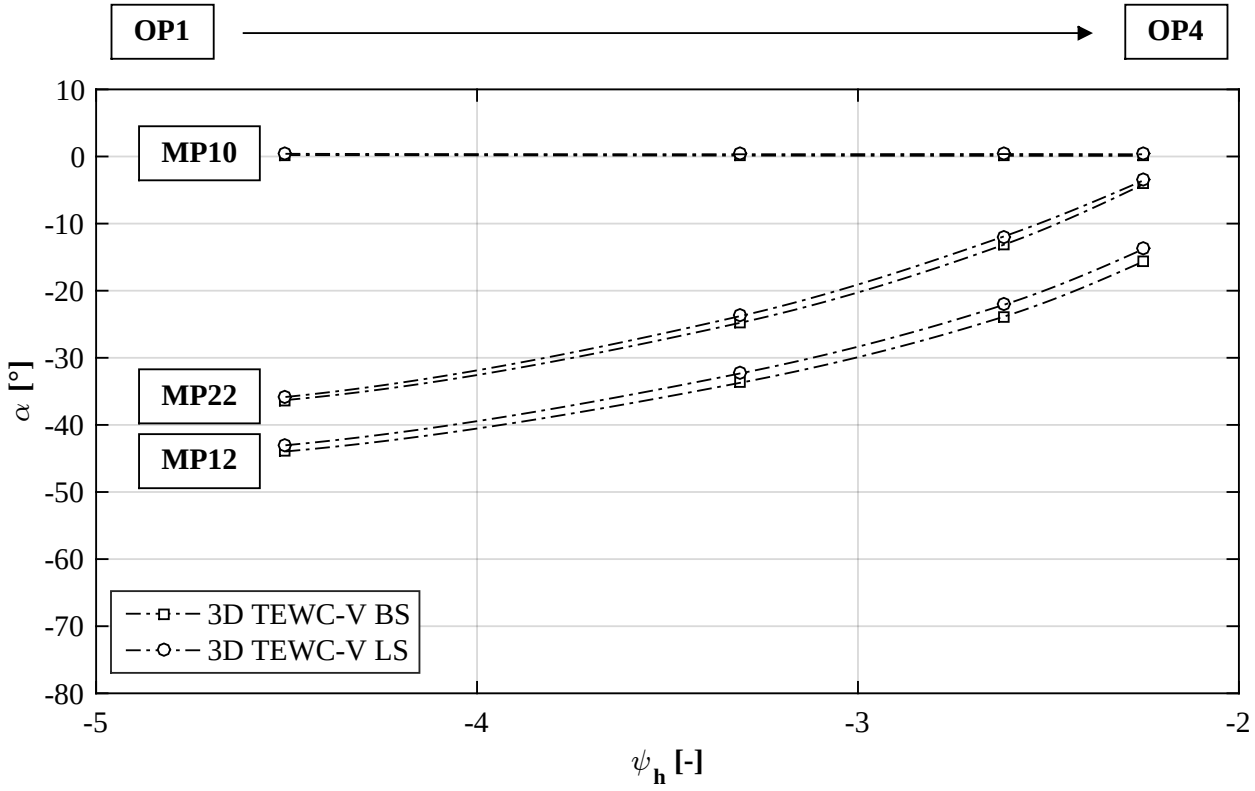

Figure B.24: Mean averaged yaw angle in MP10, MP12 and TEWC-V airfoils with LS and BS

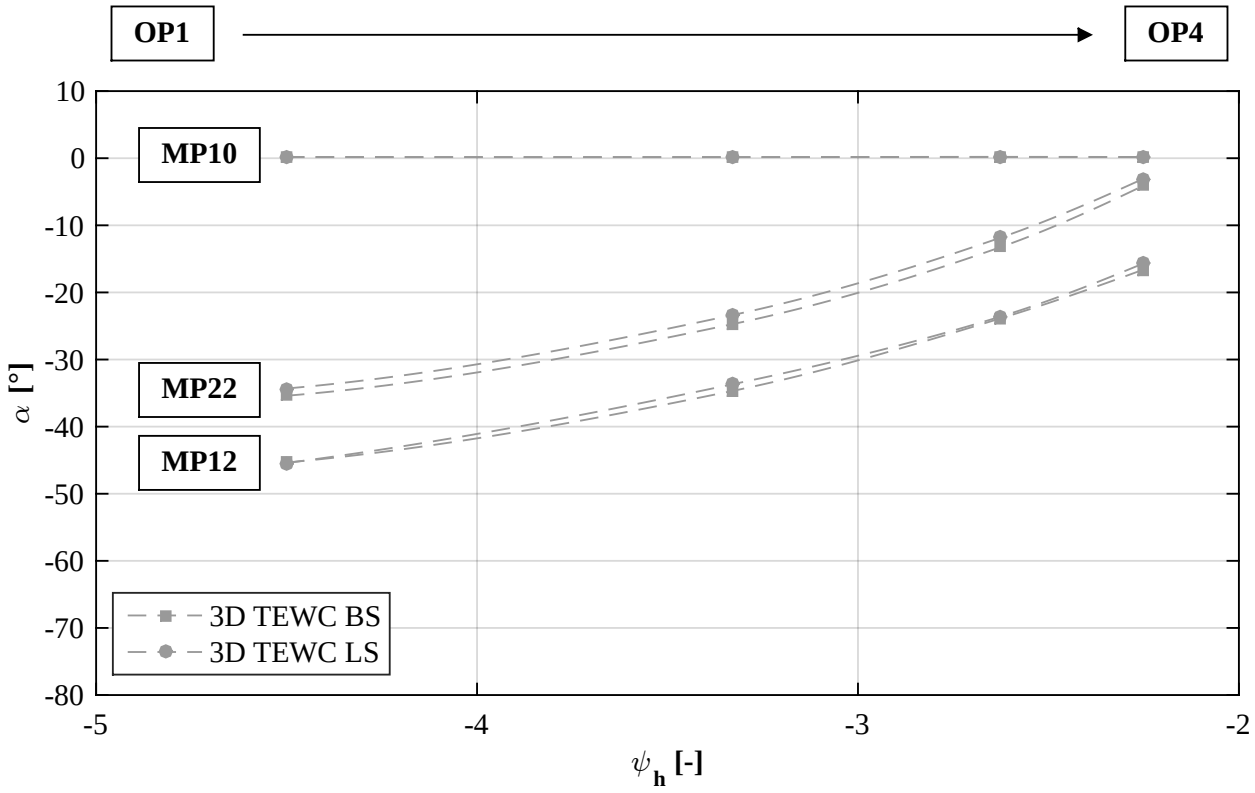

Figure B.25: Mean averaged yaw angle in MP10, MP12 and TEWC airfoils with LS and BS

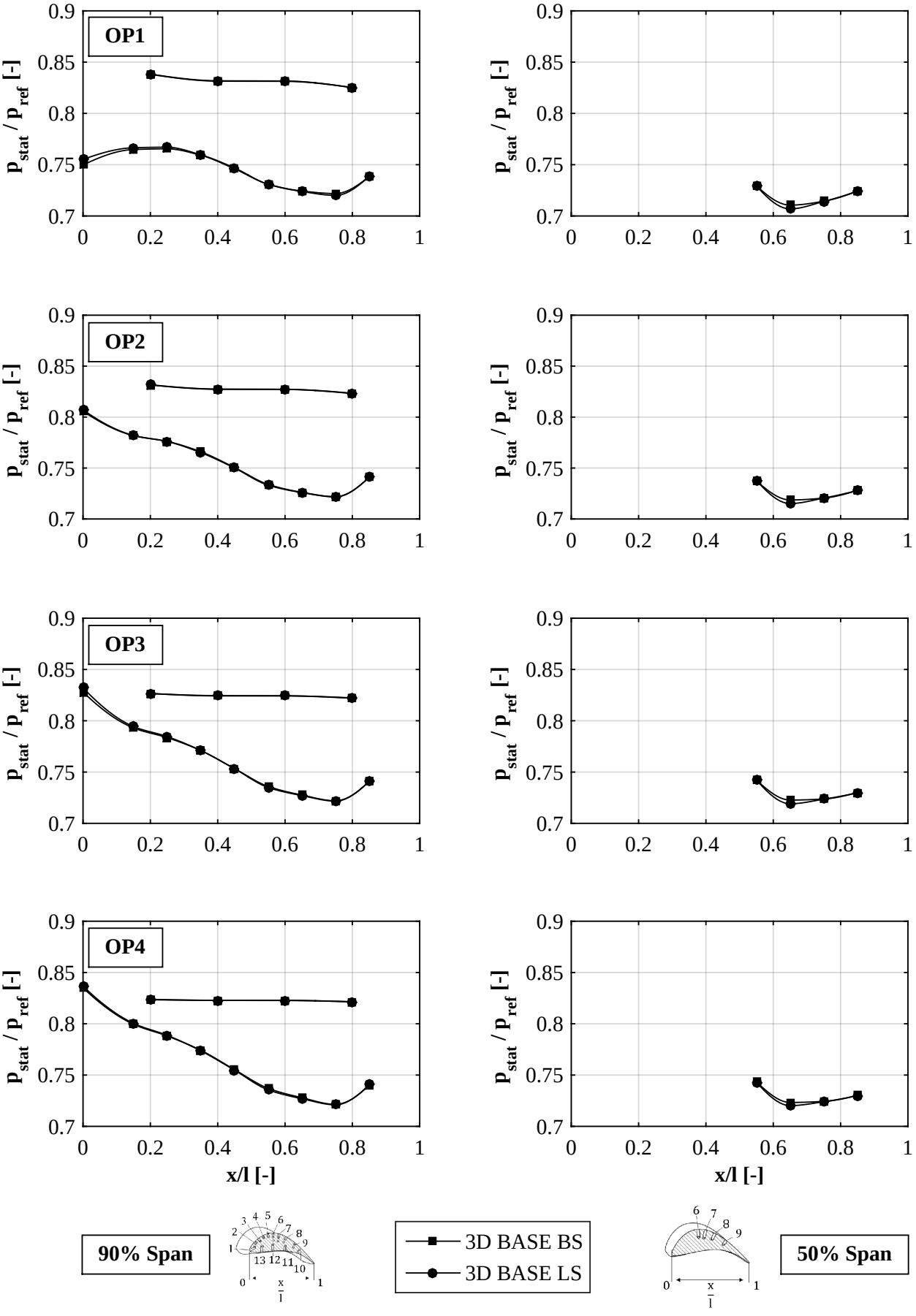

Figure B.26: Pressure distribution in axial direction across a vane of stator 2 at 90% and 50% span and BASE airfoils with LS and BS

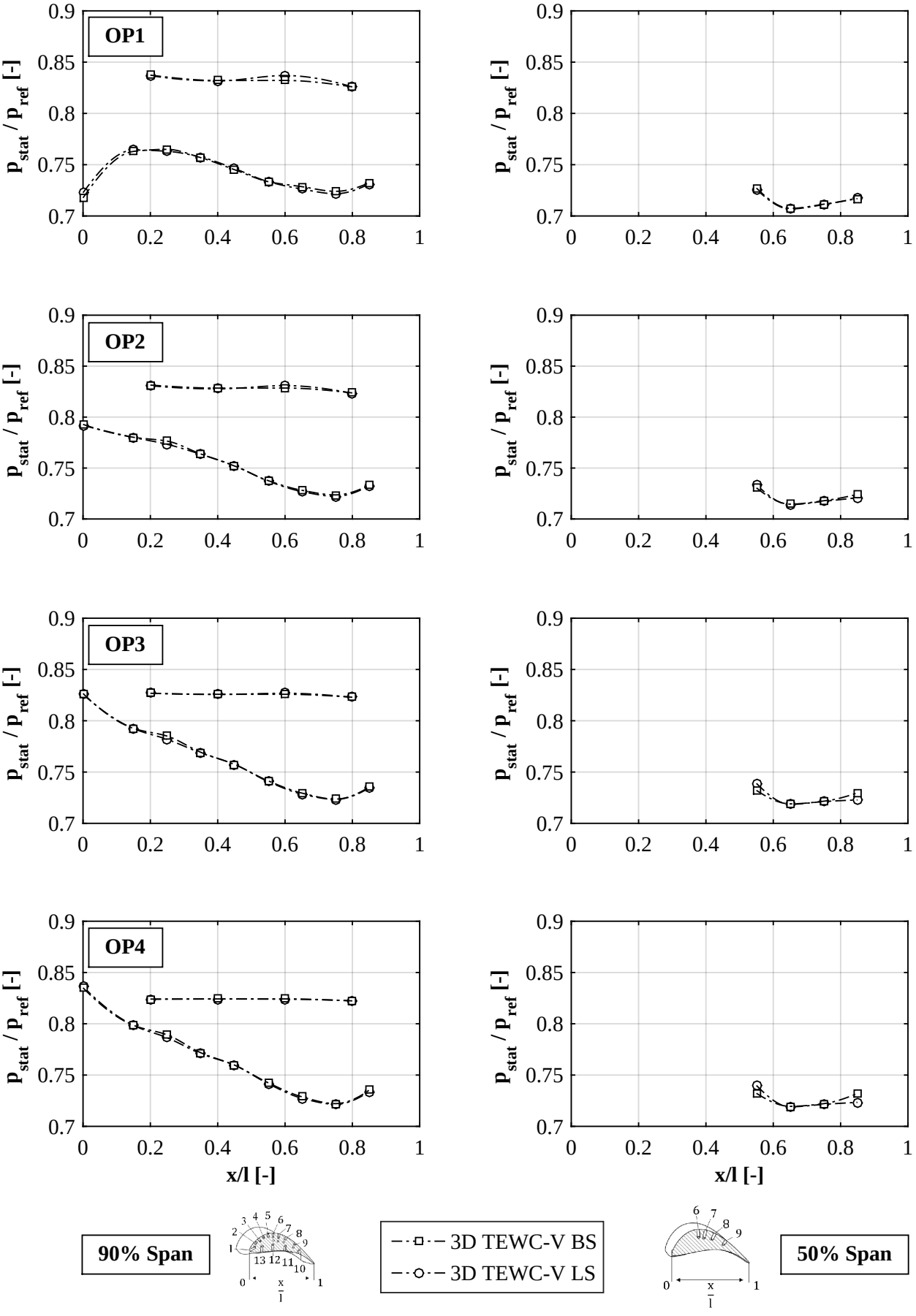

Figure B.27: Pressure distribution in axial direction across a vane of stator 2 at 90% and 50% span and TEWC-V airfoils with LS and BS

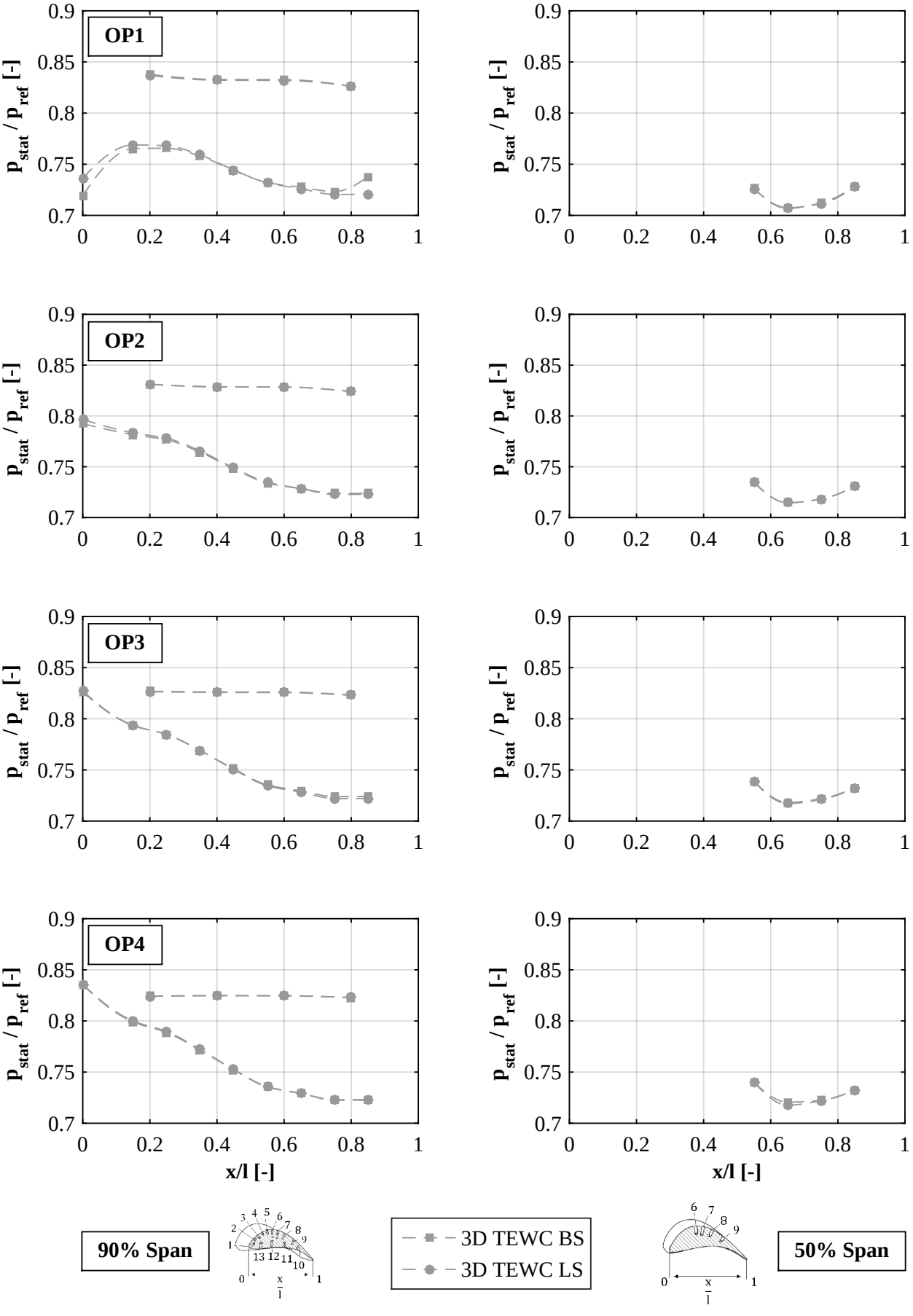

Figure B.28: Pressure distribution in axial direction across a vane of stator 2 at 90% and 50% span and TEWC airfoils with LS and BS

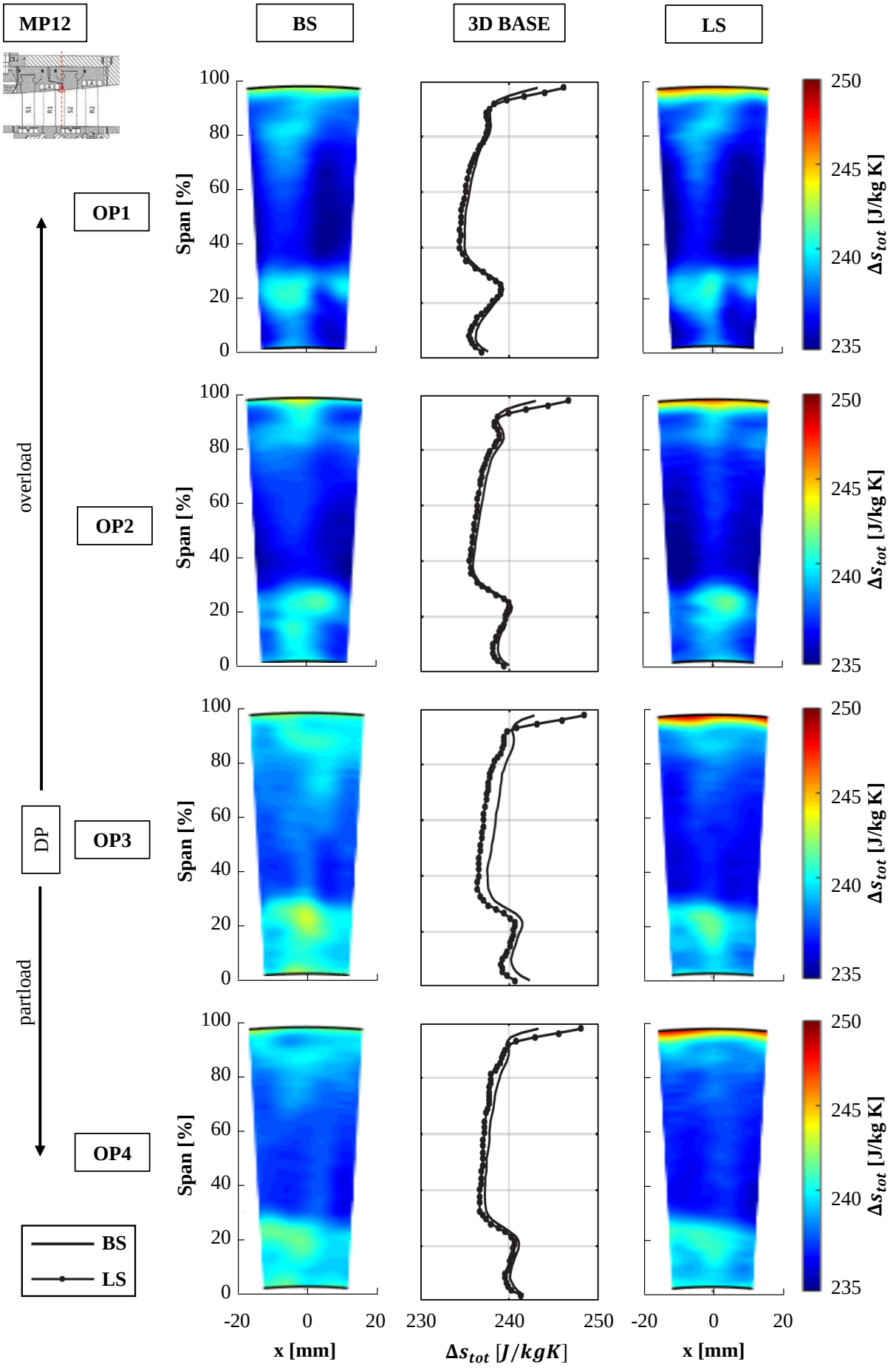

Figure B.29: Contour plots of total entropy measured in MP12 and BASE airfoils with LS and BS

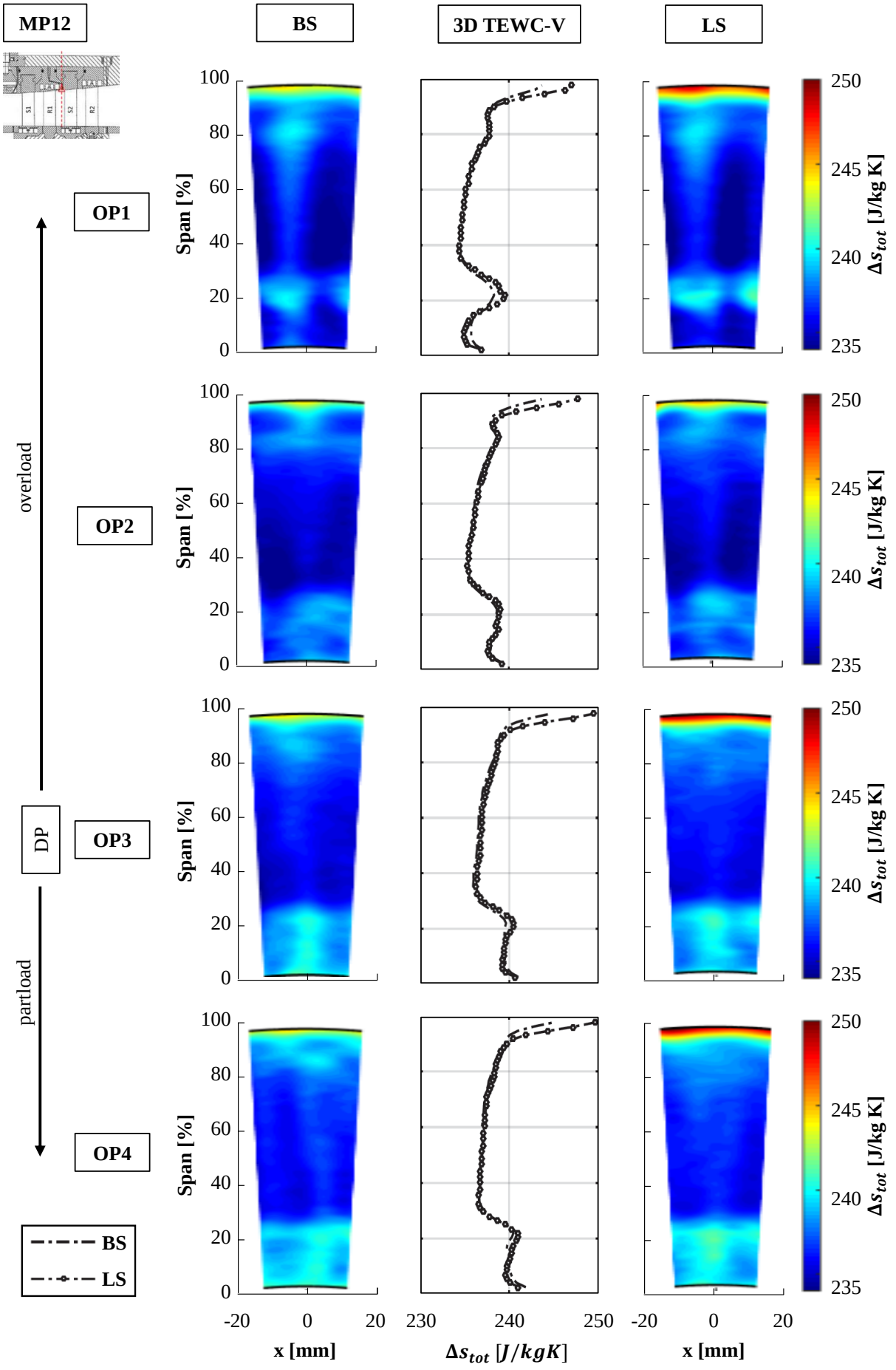

Figure B.30: Contour plots of total entropy measured in MP12 and TEWC-V airfoils with LS and BS

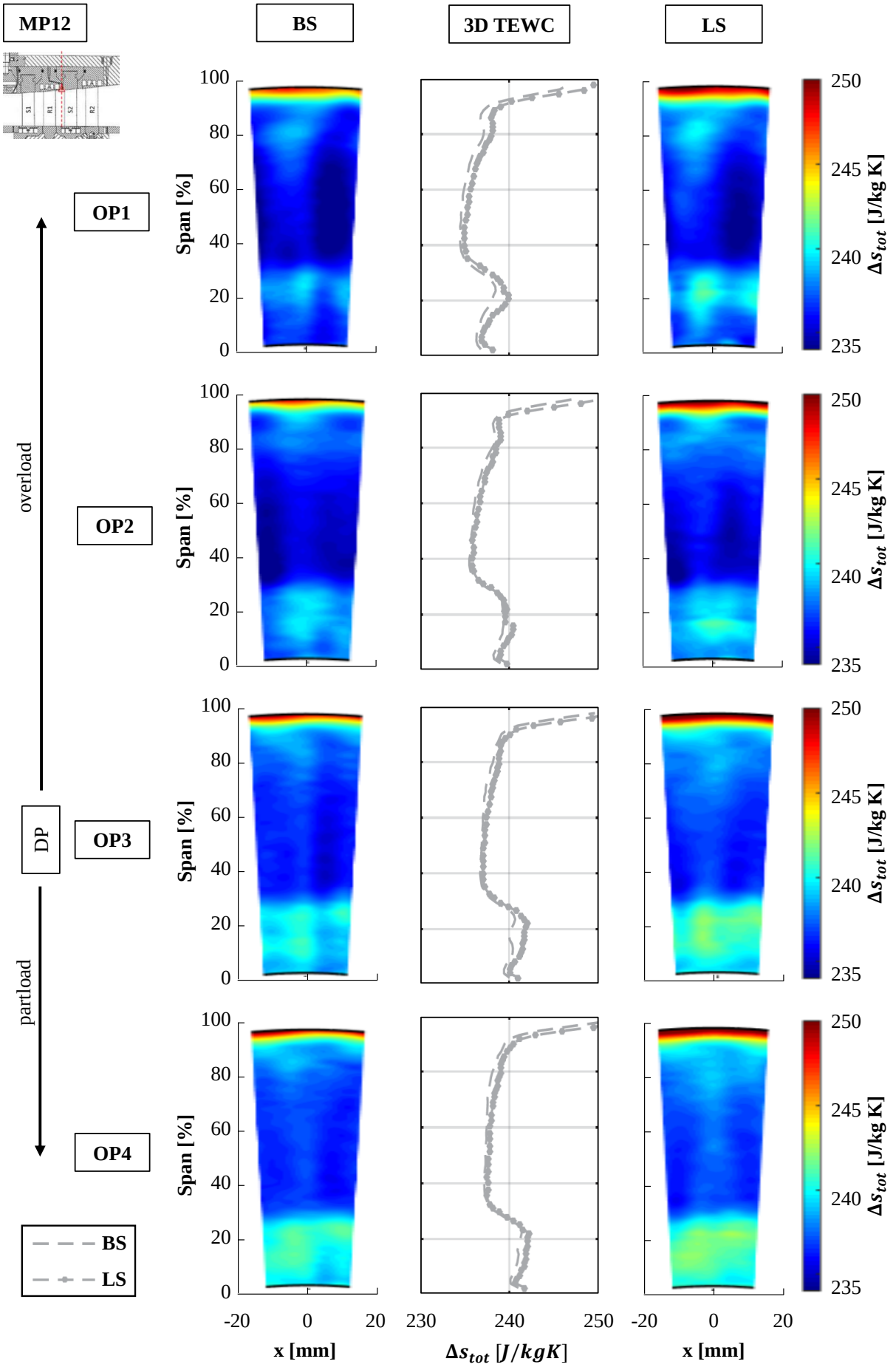

Figure B.31: Contour plots of total entropy measured in MP12 and TEWC airfoils with LS and BS

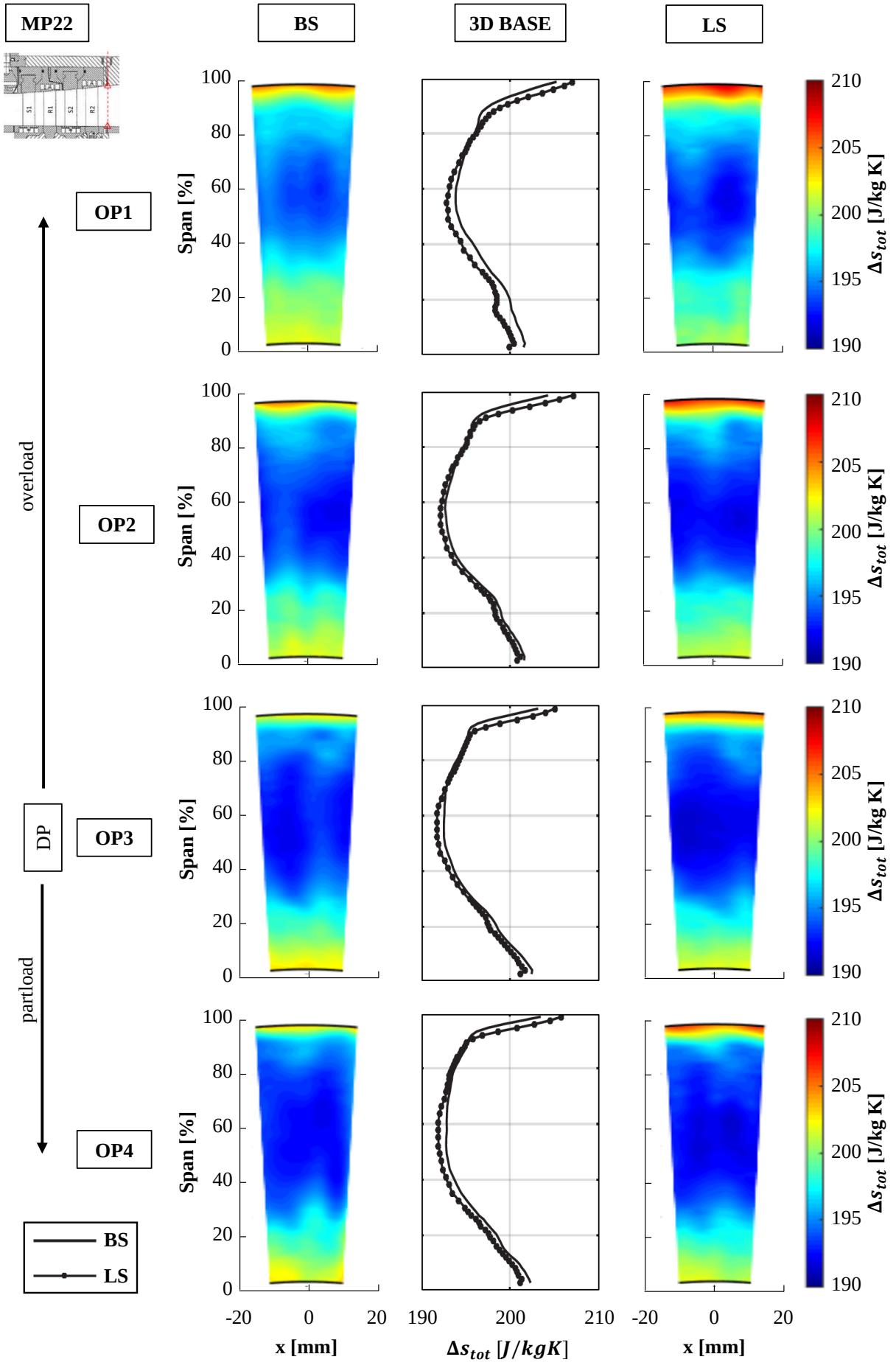

Figure B.32: Contour plots of total entropy measured in MP22 and BASE airfoils with LS and BS

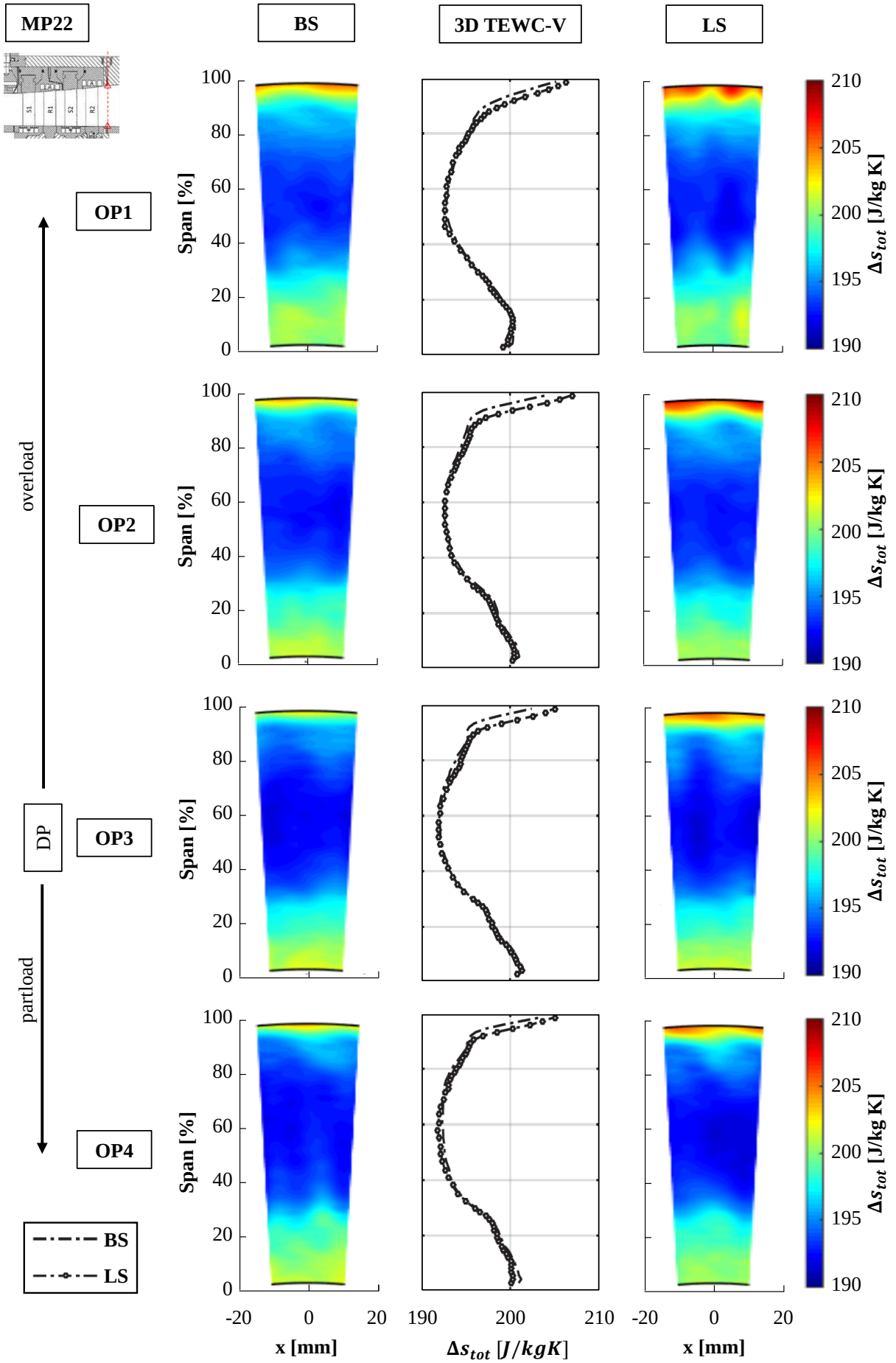

Figure B.33: Contour plots of total entropy measured in MP22 and TEWC-V airfoils with LS and BS

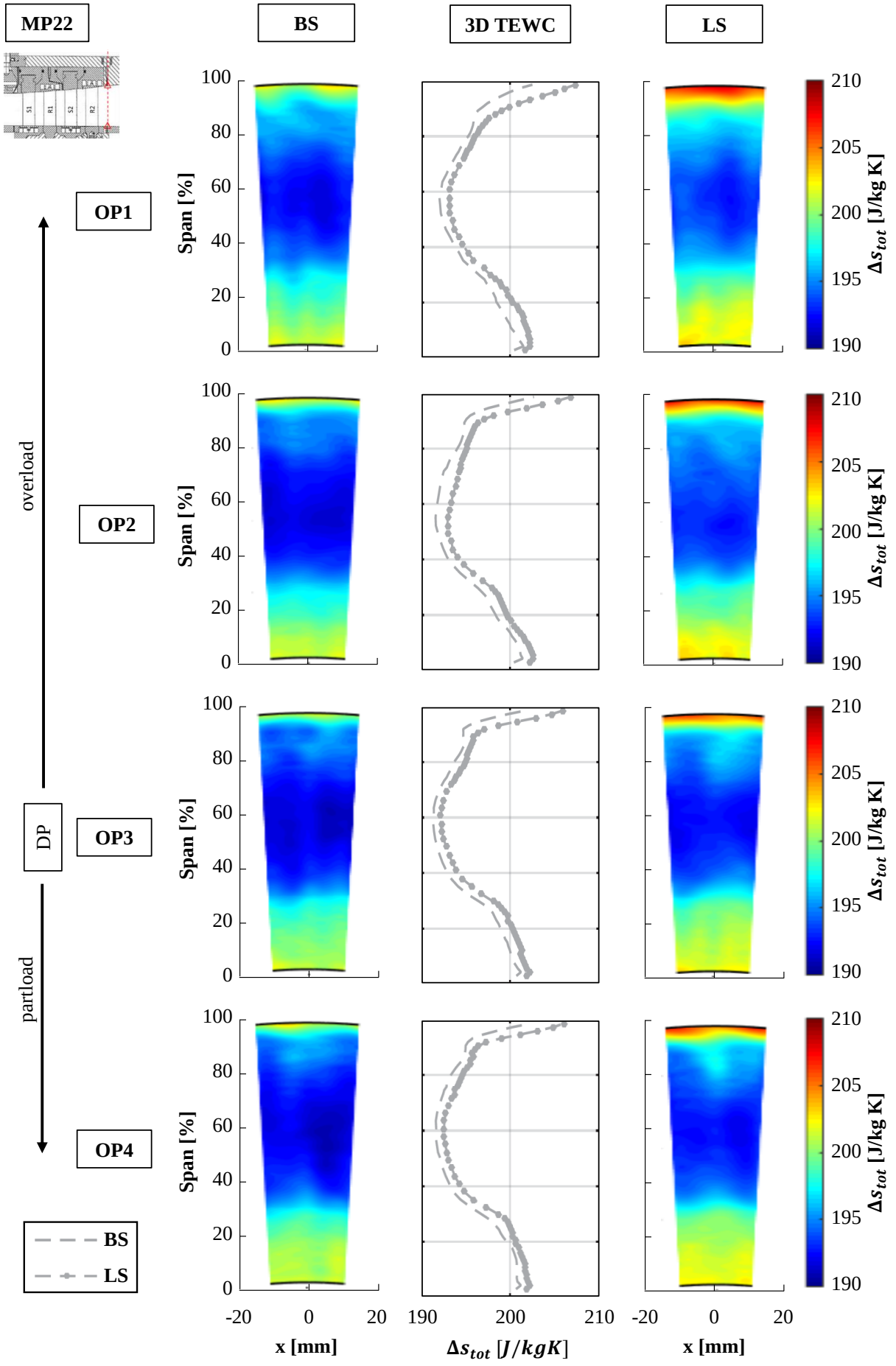

Figure B.34: Contour plots of total entropy measured in MP22 and TEWC airfoils with LS and BS

List of References

[1] Abdulla-Altaii, A. K. and Raj, R. S. Secondary Flow Development Downstream of a Blade Endwall Corner. In *ASME 1994 International Gas Turbine and Aeroengine Congress and Exposition*, Paper No. 94.GT.459, 1994.

[2] Abraham, S., Panchal, K., Ekkad, S. V., Ng, W., Lohaus, A. S., and Malandra, A. Effect of Endwall Contouring on a Transonic Turbine Blade Passage: Part 1—Aerodynamic Performance. In *ASME Turbo Expo 2012: Turbine Technical Conference and Exposition*, Paper No. GT2012-68425, 2012.

[3] Adamczyk, J. J. Model Equation for Simulating Flows in Multistage Turbomachinery. In *ASME Turbo Expo 1985*, Paper No. 85-GT-226, 1985.

[4] Anker, J. E. and Mayer, J. F. Simulation of the Interaction of Labyrinth Seal Leakage Flow and Main Flow in an Axial Turbine. In *ASME Turbo Expo 2002: Power for Land, Sea, and Air*, Paper No. GT2002-30348, 2002.

[5] Atkins, M. J. Secondary losses and end-wall profiling in a turbine cascade. *IMechE Paper C255*, 87, 1987.

[6] Bagshaw, D. A., Ingram, G. L., Gregory-Smith, D. G., and Stokes, M. R. An experimental study of reverse compound lean in a linear turbine cascade. *Proceedings of the Institution of Mechanical Engineers, Part A: Journal of Power and Energy*, 219(6):443–449, 2005.

[7] Bagshaw, D. A., Ingram, G. L., Gregory-Smith, D. G., and Stokes, M. R. An experimental study of three-dimensional turbine blades combined with profiled endwalls. *Proceedings of the Institution of Mechanical Engineers, Part A: Journal of Power and Energy*, 222(1):103–110, 2008.

[8] Bagshaw, D. A., Ingram, G. L., Gregory-Smith, D. G., Stokes, M. R., and Harvey, N. W. The design of three-dimensional turbine blades combined with profiled endwalls. *Proceedings of the Institution of Mechanical Engineers, Part A: Journal of Power and Energy*, 222(1):93–102, 2008.

[9] Beer, W. *Optimisation of a Compound Lean Turbine Blade in a Linear Cascade*. Dissertation, Technischen Universität Wien, 2008.

[10] Bergh, J., Snedden, G., and Meyer, C. Optimization of Non-Axisymmetric End Wall Contours for the Rotor of a Low Speed, 1 1/2 Stage Research Turbine With Unshrouded Blades. In *ASME Turbo Expo 2012: Turbine Technical Conference and Exposition*, Paper No. GT2012-68569, 2012.

[11] Bernhard, F., *Technische Temperaturmessung: Physikalische und meßtechnische Grundlagen, Sensoren und Meßverfahren, Meßfehler und Kalibrierung ; Handbuch für Forschung und Entwicklung, Anwendungenspraxis und Studium ; mit 297 Tabellen und 202 Berechnungsbeispielen*. Springer, Berlin, 2004.

[12] Biester, M. H.-O., Mueller, L., Seume, J. R., and Guendogdu, Y. Time-Resolved Numerical Investigation of the Interaction of Labyrinth Seal Leakage and Main-Flow in a 1.5-Stage LP Turbine. In *ASME 2011 Turbo Expo: Turbine Technical Conference and Exposition*, Paper No. GT2011-45883, 2011.

[13] Bischoff, H. Patentschrift DE 3202855 C1, 1983.

[14] Bohn, D. and Simon, H. Mehrparametrige Approximation der Eichräume und Eichflächen von Unterschall- bzw. Überschall-5-Loch-Sonden. *tm - Technisches Messen*, 468-479(JG), 1975.

[15] Boletis, E. Effects of Tip Endwall Contouring on the Three-Dimensional Flow Field in an Annular Turbine Nozzle Guide Vane: Part 1—Experimental Investigation. *Journal of Engineering for Gas Turbines and Power*, 107(4):983–990, 1985.

[16] Brennan, G., Harvey, N. W., Rose, M. G., Fomison, N., and Taylor, M. D. Improving the Efficiency of the Trent 500-HP Turbine Using Nonaxisymmetric End Walls—Part I: Turbine Design. *Journal of Turbomachinery*, 125(3):497-504, 2003.

[17] Bubeck, H. *Entwicklung einer Keilsonde zur dreidimensionalen instationären Strömungsfeldmessung und deren Anwendung in Axialverdichtern*. Dissertation, Universität Stuttgart, 1987.

[18] Bubolz, T. *Untersuchungen von randzonenkorrigierten Axialverdichterbeschaufelungen mit Strömungs-Meßsonden: Univ., Diss.–Hannover*. Cuvillier, Göttingen, 1. edition, 2005.

[19] Burns, G. W. and Scroger, M. G. *The Calibration of thermocouples and thermocouple materials*. National Institute of Standards and Technology, Gaithersburg, MD, 1989.

[20] Büscher, S. *Untersuchung von mehrstufigen Bürstendichtungen für Dampfturbinen*. Dissertation, TU Braunschweig, 2010.

[21] Chupp, R. E., Ghasripoor, F., Turnquist, N. A., Demiroglu, M., and Aksit, M. F. Advanced Seals for Industrial Turbine Applications: Dynamic Seal Development. *Journal of Propulsion and Power*, 18(6):1260–1266, 2002.

[22] Curkovic, O., Zimmermann, T. W., and Wirsum, M. Brush Seal Modeling for a 2-stage Axial Turbine: A Parametric Study with CFD. In *Proceedings of International Gas Turbine Congress*:755–776, 2015.

[23] Deckner, M. *Eigenschaften kombinierter Labyrinth-Bürstendichtungen für Turbomaschinen: Techn. Univ., Diss.–München*. Energietechnik. Verl. Dr. Hut, München, 1. edition, 2011.

[24] Dejč, M. E. and Trojanovskij, B. M. *Untersuchung und Berechnung axialer Turbinenstufen*. Verlag Technik, 1973.

[25] Denton, J. D. The 1993 IGTI Scholar Lecture: Loss Mechanisms in Turbomachines. *Journal of Turbomachinery*, 115(4):621-656, 1993.

[26] Denton, J. D. and Johnson, C. G. An Experimental Study of the Tip Leakage Flow Around Shrouded Turbine Blades. *CEGB Research Report*, (CEGB-R/M/N848), 1976.

[27] Denton, J. D. and Xu, L. The exploitation of three-dimensional flow in turbomachinery design. *Proceedings of the Institution of Mechanical Engineers, Part C: Journal of Mechanical Engineering Science*, 213(2):125–137, 1998.

[28] DIN 1319. *Grundlagen der Meßtechnik*. Beuth Verlag, Berlin, 1995.

[29] DIN 2481. *Wärmekraftanlagen – Graphische Symbole*. Beuth Verlag, Berlin and Cologne, 1979.

[30] DIN 5167-1. *Durchflussmessung von Fluiden mit Drosselgeräten in voll durchströmten Leitungen mit Kreisquerschnitt - Teil 1: Allgemeine Grundlagen und Anforderungen: Deutsche Fassung EN ISO 5167-1:2003*. 2003.

[31] DIN 5167-2. *Durchflussmessung von Fluiden mit Drosselgeräten in voll durchströmten Leitungen mit Kreisquerschnitt - Teil 2: Blenden: Deutsche Fassung EN ISO 5167-2:2003*. 2003.

[32] Doligalski, T. L., Smith, C. R., and Walker, J. D. A. Vortex Interactions with Walls. *Annual Review of Fluid Mechanics*, 26(1):573–616, 1994.

[33] Dominy, R. G. and Hodson, H. P. An Investigation of Factors Influencing the Calibration of Five-Hole Probes for Three-Dimensional Flow Measurements. *Journal of Turbomachinery*, 115(3):513-519, 1993.

[34] Duden, A. *Strömungsbeeinflussung zur Reduzierung der Sekundärströmungen in Turbinengittern: Diss. UniBw München*. Dr. Hut, München, 1. edition, 1999.

[35] Dunn, D., Snedden, G., Backström, T. v., and Mdluli, M. P. Unsteady Effects of a Generic Non-Axisymmetric Endwall Contour on the Rotor of a $1\frac{1}{2}$ Stage Low Speed Turbine Test Rig. In *ASME Turbo Expo 2013: Turbine Technical Conference and Exposition*, Paper No. GT2013-94961, 2013.

[36] Dunn, D., Snedden, G., and Backström, T. v. Unsteady Effects of a Generic Non-Axisymmetric Rotor Endwall Contour on a $1\frac{1}{2}$ Stage Turbine Test Rig at Off Design Conditions. In *ASME Turbo Expo 2014: Turbine Technical Conference and Exposition*, Paper No. GT2014-25524, 2014.

[37] Eckert, E. Temperature recording in high-speed gases. In *NACA Technical Memorandum 983, Washington, 1941*.

[38] Edwards, J., Schwartz, T., and Hart, R. Measuring turbine engine inlet total temperature problems and solutions. In *20th Joint Propulsion Conference*, 1984.

[39] Egli, A. The leakage of steam through labyrinth seals. *Transactions of the ASME FSP-57-5*:115-122, 1935.

[40] European Commission. World energy, technology and climate policy outlook 2030, 2003.

[41] European Commission. Vision 2020: Energie sparen!, 2007.

[42] Eymann, S., Reinmöller, U., Niehuis, R., Förster, W., Beversdorff, M., and Gier, J. Improving 3D Flow Characteristics in a Multistage LP Turbine by Means of Endwall Contouring and Airfoil Design Modification: Part 1 — Design and Experimental Investigation. In *ASME Turbo Expo 2002: Power for Land, Sea, and Air*, Paper No. GT2002-30352, 2002.

[43] Favre, A. Équation des gaz turbulents compressible: 1.) Formes générales. *Journal de Mécanique*, 4:361–390, 1965.

[44] Favre, A. Équation des gaz turbulents compressible: 2.) Méthode des vitesses moyennes; méthode des vitesses macroscopiques pondérées par la masse volumique. *Journal de Mécanique*, 4: 391–421, 1965.

[45] Gail, A. and Beichl, S. MTU brush seal - Main features of an alternative design. In *36th AIAA/ASME/SAE/ASEE Joint Propulsion Conference and Exhibit*, 2000.

[46] Germain, T., Nagel, M., Raab, I., Schuepbach, P., Abhari, R. S., and Rose, M. Improving Efficiency of a High Work Turbine Using Non-Axisymmetric Endwalls: Part I—Endwall Design and Performance. In *ASME Turbo Expo 2008: Power for Land, Sea, and Air*, Paper No. GT2008-50469, 2008.

[47] Gier, J., Stubert, B., Brouillet, B., and Vito, L. d. Interaction of Shroud Leakage Flow and Main Flow in a Three-Stage LP Turbine. *Journal of Turbomachinery*, 127(4):649, 2005.

[48] Girgis, S., Vlasic, E., Lavoie, J.-P., and Moustapha, S. H. The Effect of Secondary Air Injection on the Performance of a Transonic Turbine Stage. In *ASME Turbo Expo 2002: Power for Land, Sea, and Air*, Paper No. GT2002-30340, 2002.

[49] Goldstein, R. J., Wang, H. P., and Jabbari, M. Y. The Influence of Secondary Flows Near the Endwall and Boundary Layer Disturbance on Convective Transport From a Turbine Blade. In *ASME 1994 International Gas Turbine and Aeroengine Congress and Exposition*, Paper No. 94-GT-165, 1994.

[50] Gotthardt, H. *Theoretische und experimentelle Untersuchungen an ebenen Turbinengittern mit Pfeilung und V-Stellung*. Dissertation, TU Braunschweig, 1983.

[51] Grant, J., Borthwick, D. Fully three-dimensional inviscid flow calculations for the final stage of a large low-pressure steam turbine. *IMechE Paper C281*, 87, 1987.

[52] Gregory-Smith, D. G., Ingram, G., Jayaraman, P., Harvey, N. W., and Rose, M. G. Non-axisymmetric turbine end wall profiling. *Proceedings of the Institution of Mechanical Engineers, Part A: Journal of Power and Energy*, 215(6):721–734, 2001.

[53] Gregory-Smith, D., Bagshaw, D., Ingram, G., and Stokes, M. Using Profiled Endwalls, Blade Lean and Leading Edge Extensions to Minimize Secondary Flow. In *ASME Turbo Expo 2008: Power for Land, Sea, and Air*, Paper No. GT2008-50811, 2008.

[54] Gustafson, R., Mahmood, G., and Acharya, S. Aerodynamic Measurements in a Linear Turbine Blade Passage With Three-Dimensional Endwall Contouring. In *ASME Turbo Expo 2007: Power for Land, Sea, and Air*, Paper No. GT2007-28073, 2007.

[55] Haas, J. E. Analytical and Experimental Investigation of Stator Endwall Contouring in a Small Axial-Flow Turbine. 1-Stator Performance. In *AVRADCOM Technical Report*, Paper No. 82-C-4, 1982

[56] Harrison, S. The Influence of Blade Lean on Turbine Losses. *Journal of Turbomachinery*, 114 (1):184-190, 1992.

[57] Hartland, J. C., Gregory-Smith, D. G., Harvey, N. W., and Rose, M. G. Nonaxisymmetric Turbine End Wall Design: Part II—Experimental Validation. *Journal of Turbomachinery*, 122 (2):286–293, 1999.

[58] Harvey, N. W., Brennan, G., Newman, D. A., and Rose, M. G. Improving Turbine Efficiency Using Non-Axisymmetric End Walls: Validation in the Multi-Row Environment and With Low Aspect Ratio Blading. In *ASME Turbo Expo 2002: Power for Land, Sea, and Air*, Paper No. GT2002-30337, 2002.

[59] Harvey, N. W., Rose, M. G., Taylor, M. D., Shahpar, S., Hartland, J., and Gregory-Smith, D. G. Nonaxisymmetric Turbine End Wall Design: Part I— Three-Dimensional Linear Design System. *Journal of Turbomachinery*, 122(2):278–285, 1999.

[60] Havakechian, S. and Greim, R. Aerodynamic design of 50 per cent reaction steam turbines. *Proceedings of the Institution of Mechanical Engineers, Part C: Journal of Mechanical Engineering Science*, 213(1):1–25, 1999.

[61] Hawthorne, W. R. and Novak, R. A. The Aerodynamics of Turbo-Machinery. *Annual Review of Fluid Mechanics*, 1(1):341–366, 1969.

[62] Herbst, F. *Modellierung des Einflusses von Ausblasungen auf die Grenzschichttransition in hochbelasteten Niederdruckturbinen*. Dissertation, Leibniz Universität Hannover, 2013.

[63] Hodson, H. P. and Dominy, R. G. The Off-Design Performance of a Low-Pressure Turbine Cascade. *Journal of Turbomachinery*, 109(2):201-209, 1987.

[64] Holle, G. F. Generalizing Circular Brush Seal Leakage Through a Randomly Distributed Bristle Bed. *Journal of Turbomachinery*, 118(1):153-161, 1996.

[65] Horlock, J. H. and Lakshminarayana, B. Secondary Flows: Theory, Experiment, and Application in Turbomachinery Aerodynamics. *Annual Review of Fluid Mechanics*, 5(1):247–280, 1973.

[66] Hottel, H. C. and Kaltinsky, A. Temperature Measurements in High-Velocity Air Streams. In *Journal of Applied Mechanics*, 94-GT-165:A25-A32, 1945.

[67] Hourmouziadis, J. and Hübner, N. 3-D Design of Turbine Airfoils. In *ASME 1985 International Gas Turbine Conference and Exhibit*, Paper No. 85-GT-188, 1985.

[68] Hunter, S. D. and Manwaring, S. R. Endwall Cavity Flow Effects on Gaspath Aerodynamics in an Axial Flow Turbine: Part I — Experimental and Numerical Investigation. In *ASME Turbo Expo 2000: Power for Land, Sea, and Air*, Paper No. 2000-GT-0651, 2000.

[69] Hunter, S. D. and Orkwis, P. O. Endwall Cavity Flow Effects on Gaspath Aerodynamics in an Axial Flow Turbine: Part II — Source Term Model Development. In *ASME Turbo Expo 2000: Power for Land, Sea, and Air*, Paper No. 2000-GT-0513, 2000.

[70] Ingram, G. L. *Endwall Profiling for the Reduction of Secondary Flow in Turbines*. Dissertation, University of Durham, 2003.

[71] Ingram, G., Gregory-Smith, D., Rose, M., Harvey, N., and Brennan, G. The Effect of End-Wall Profiling on Secondary Flow and Loss Development in a Turbine Cascade. In *ASME Turbo Expo 2002: Power for Land, Sea, and Air*, Paper No. GT2002-30339, 2002.

[72] Ingram, G., Gregory-Smith, D., and Harvey, N. Investigation of a novel secondary flow feature in a turbine cascade with end wall profiling. *Journal of Turbomachinery*, 127(1):209–214, 2005.

[73] ISO. *Guide to the Expression of Uncertainty in Measurements*. International Organisation for Standardisation (Geneva, Switzerland), 1993.

[74] Jabbari, M. Y., Goldstein, R. J., Marston, K. C., and Eckert, E. R. G. Three dimensional flow at the junction between a turbine blade and end-wall. *Wärme - und Stoffübertragung*, 27(1): 51–59, 1992.

[75] Jansen, M. and Ulm, W. Modern blade design for improving steam turbine efficiency. *VDI BERICHTE*, 1185:277, 1995.

[76] Jenny, P., Abhari, R. S., Rose, M. G., Brettschneider, M., and Gier, J. A Low Pressure Turbine With Profiled End Walls and Purge Flow Operating With a Pressure Side Bubble. In *ASME 2011 Turbo Expo: Turbine Technical Conference and Exposition*, Paper No. GT2011-46309, 2011.

[77] Kauke, G. Übertragbarkeit der Kalibrierung von Sonden für verschiedene Reynoldszahlen in Unter- und Überschallströmungen. *Inst. für Strahlantriebe und Turboarbeitsmaschinen, RWTH*, 1981(81), 1981.

[78] Kawai, T., Shinoki, S., and Adachi, T. Secondary Flow Control and Loss Reduction in a Turbine Cascade. *JSME International Journal II 32*, 1989(3):375–387, 1989.

[79] Klein, A. Untersuchungen über den Einfluß der Zuströmgrenzschicht auf die Sekundärströmungen in den Beschaufelungen von Axialturbinen. *Forschung im Ingenieurwesen*, 32(6): 175–188, 1966.

[80] Knezevici, D. C., Sjolander, S. A., Praisner, T. J., Allen-Bradley, E., and Grover, E. A. Measurements of Secondary Losses in a Turbine Cascade With the Implementation of Non-Axisymmetric Endwall Contouring. In *ASME Turbo Expo 2008: Power for Land, Sea, and Air*, Paper No. GT2008-51311, 2008.

[81] Kopper, F. C., Milanot, R., and Vancot, M. Experimental investigation of endwall profiling in a turbine vane cascade. *AIAA Journal*, 19(8):1033–1040, 1981.

[82] Korschunov, B. A. and Döhler, S. W. Einfluß von Leckageströmungen an der Laufradspitze auf die Aerodynamischen Charakteristiken des Folgenden Leitgitters. *BWK*, (46):49–55, 1996.

[83] Kreitmeier F. Integralbehandlung inhomogener Strömungsfelder – Teilbericht 1: Theorie. *ABB Baden, Schweiz*, 1977, .

[84] Kreitmeier F. Space-averaging 3D flows in turbomachinery using strictly formulated balance equations. In *IGT I -Vol. 7: 397-408,*, 1992. .

[85] Kretzschmar, H. J., Stoecker, I., Jaehne, I., Knobloch, K., Hellriegel, T., Kleemann, L., and Seibt, D. *Property Software for Humid Air Calculated as Ideal Mixture of Real Fluids*. Faculyty of Mechanical Engineering, Department of Technical Thermodynamics, Zittau/Görlitz University of Applied Sciences, 2010.

[86] Langston, L. S. Secondary Flows in Axial Turbines-A Review. *Annals of the New York Academy of Sciences*, 934(1):11–26, 2001.

[87] Langston, L. S., Nice, M. L., and Hooper, R. M. Three-Dimensional Flow Within a Turbine Cascade Passage. *Journal of Engineering for Power*, 99(1):21-28, 1977.

[88] Lemmon, E. W. and Jacobsen, R. T. Viscosity and Thermal Conductivity Equations for Nitrogen, Oxygen, Argon, and Air. *International Journal of Thermophysics*, 25(1):21–69, 2004.

[89] Lemmon, E. W. Thermodynamic Properties of Air and Mixtures of Nitrogen, Argon, and Oxygen From 60 to 2000 K at Pressures to 2000 MPa. *Journal of Physical and Chemical Reference Data*, 29(3):331-385, 2000.

[90] Livesey, J. L. and Hugh, T. 'Suitable mean values' in one–dimensional gas dynamics. *ARCHIVE: Journal of Mechanical Engineering Science 1959-1982 (vols 1-23)*, 8(4):374–383, 1966.

[91] Lynch, S. P., Thole, K. A., Kohli, A., Lehane, C., and Praisner, T. Aerodynamic Loss for a Turbine Blade With Endwall Leakage Features and Contouring. In *ASME Turbo Expo 2013: Turbine Technical Conference and Exposition*, Paper No. GT2013-94943, 2013.

[92] Mahle, I. Improving the Interaction Between Leakage Flows and Main Flow in a Low Pressure Turbine. In *ASME Turbo Expo 2010*, Paper No. GT2010-22448, 2010

[93] Matthias, A. *Das Durchflussverhalten von Labyrinthdichtungen bei unterschiedlichen Betriebsbedingungen.* Dissertation, Technische Universität Wien, 2007.

[94] McLean, C., Camci, C., and Glezer, B. Mainstream Aerodynamic Effects Due to Wheelspace Coolant Injection in a High-Pressure Turbine Stage: Part I—Aerodynamic Measurements in the Stationary Frame. *Journal of Turbomachinery*, 123(4):687-696, 2001.

[95] McLean, C., Camci, C., and Glezer, B. Mainstream Aerodynamic Effects Due to Wheelspace Coolant Injection in a High-Pressure Turbine Stage: Part II—Aerodynamic Measurements in the Rotational Frame. *Journal of Turbomachinery*, 123(4):697-703, 2001.

[96] Miyoshi, I., Higuchi, S., and Kishibe, T. Improving the Performance of a High Pressure Gas Turbine Stage Using a Profiled Endwall. In *ASME Turbo Expo 2013*, Paper No. GT2013-95148, 2013

[97] Morris, A. W. H. and Hoare, R. G. Secondary loss measurements in a cascade of turbine blades with meridional wall profiling. In *ASME Winter Annual Meeting 1975*.

[98] Müller, H. K. and Nau, B. S. *Fluid sealing technology: Principles and applications*, volume 117 of *Mechanical engineering*. M. Dekker, New York, NY, 1998.

[99] Nagel, M. G. *Numerische Optimierung dreidimensional parametrisierter Turbinenschaufeln mit umfangsunsymmetrischen Plattformen – Entwicklung, Anwendung und Validierung*. Dissertation, Universität der Bundeswehr, 01.01.2004.

[100] Niehuis, R., Luecking, P., and Stubert, B. Experimental and Numerical Study on Basic Phenomena of Secondary Flows in Turbines. In *AGARD CP-469,Neuilly-sur-Seine*, 1990.

[101] Niewoehner, J., Poehler, T., Jeschke, P., and Guendogdu, Y. Investigation of Non-Axisymmetric Endwall Contouring and 3D Airfoil Design in a 1.5 Stage Axial Turbine: Part II — Experimental Validation. In *ASME Turbo Expo 2014*, Paper No. GT2014-26785, 2014.

[102] Nitsche, W. and Brunn, A. *Strömungsmesstechnik*. VDI-Buch. Springer-Verlag Berlin Heidelberg, Berlin, Heidelberg, 2., aktualisierte und bearbeitete auflage edition, 2006.

[103] Pastrana, R., Wolfe, C., Turnquist, A., Burnett, M. Improved Steam Turbine Leakage Control with a Brush Seal Design. In *GE Energy Services, 2001*. 2001.

[104] Peters, P., Breisig, V., Giboni, A., Lerner, C., and Pfost, H. The Influence of the Clearance of Shrouded Rotor Blades on the Development of the Flowfield and Losses in the Subsequent Stator. In *ASME Turbo Expo 2000: Power for Land, Sea, and Air*, Paper No. 2000-GT-478, 2000.

[105] Pfau, A., Treiber, M., Sell, M., and Gyarmathy, G. Flow Interaction From the Exit Cavity of an Axial Turbine Blade Row Labyrinth Seal. *Journal of Turbomachinery*, 123(2):342-352, 2001.

[106] Pfau, A., Schlienger, J., Rusch, D., Kalfas, A. I., and Abhari, R. S. Unsteady Flow Interactions Within the Inlet Cavity of a Turbine Rotor Tip Labyrinth Seal. *Journal of Turbomachinery*, 127(4):679, 2005.

[107] Pfau, A., Kalfas, A. I., and Abhari, R. S. Making Use of Labyrinth Interaction Flow. In *ASME Turbo Expo 2004: Power for Land, Sea, and Air*, Paper No. GT2004-53797, 2004.

[108] Pfau, A. *Loss Mechanisms in Labyrinth Seals of Shrouded Axial Turbines*. Dissertation, ETH Zürich, 2003.

[109] Pioske, C. *3D-Turbinenbeschaufelung: Vorhaben Nr. 653, Optimierung der Turbinenseitenwandgestaltung im Gitterbereich im Hinblick auf die Einflüsse der Sekundärströmung: Abschlußbericht*, volume Bd. 2. FVV, 1999.

[110] Pioske, C., Vogt, H.-F. 3D-Turbinenbeschaufelung I – Optimierung von Turbinenbeschaufelungen im Hinblick auf die Einflüsse der Sekundärströmung. In *FVV Abschlussbericht, Vorhaben Nr. 571, RWTH Aachen, 1995*.

[111] Poehler, T., Niewoehner, J., Jeschke, P., and Guendogdu, Y. Investigation of Non-Axisymmetric Endwall Contouring and 3D Airfoil Design in a 1.5 Stage Axial Turbine: Part I — Design and Novel Numerical Analysis Method. In *ASME Turbo Expo 2014: Turbine Technical Conference and Exposition*, Paper No. GT2014-26784, 2014.

[112] Povinelli, L. A. Assessment of Three-Dimensional Inviscid Codes and Loss Calculations for Turbine Aerodynamic Computations. *Journal of Engineering for Gas Turbines and Power*, 107(2):265-275, 1985.

[113] Praisner, T. J., Allen-Bradley, E., Grover, E. A., Knezevici, D. C., and Sjolander, S. A. Application of Non-Axisymmetric Endwall Contouring to Conventional and High-Lift Turbine Airfoils. In *ASME Turbo Expo 2007: Power for Land, Sea, and Air*, Paper No. GT2007-27579, 2007.

[114] Pullan, G., Denton, J., and Dunkley, M. An Experimental and Computational Study of the Formation of a Streamwise Shed Vortex in a Turbine Stage. *Journal of Turbomachinery*, 125 (2):291-297, 2003.

[115] Regina, K. *High-Pressure Turbines with Novel Airfoils and End Walls Operating under Engine Representative Aero-Thermodynamic Effects*. Dissertation, ETH Zürich, 2015.

[116] Restemeier, M. S. *Einfluss des Schaufelreihenabstands auf Strömung und Wirkungsgrade in einer subsonischen Axialturbine: Techn. Univ., Diss.–Aachen, 2012*. Dr. Hut, München, 1. aufl. edition, 2012.

[117] Reynolds, O. On the Dynamical Theory of Incompressible Viscous Fluids and the Determination of the Criterion. *Philosophical Transactions of the Royal Society A: Mathematical, Physical and Engineering Sciences*, 186(0):123–164, 1895.

[118] Rose, M. G., Harvey, N. W., Seaman, P., Newman, D. A., and McManus, D. Improving the Efficiency of the Trent 500 HP Turbine Using Non-Axisymmetric End Walls: Part II — Experimental Validation. In *ASME Turbo Expo 2001: Power for Land, Sea, and Air*, Paper No. 2001-GT-0505, 2001.

[119] Saravanamuttoo, H. I. H., editor. *Recommended practices for measurement of gas path pressures and temperatures for performance assessment of aircraft turbine engines and components: Report of the Propulsion and Energetics Panel Working Group 19 = Les méthodes recommandées pour la mesure de la pression et de la température de la veine gazeuse en vue*

de l'evaluation des performances des turbines aéronautiques et de leurs composants, volume 245 of *AGARD advisory report*. AGARD, Neuilly-sur-Seine, 1990.

[120] Sauer, H., Müller, R., and Vogeler, K. Reduction of Secondary Flow Losses in Turbine Cascades by Leading Edge Modifications at the Endwall. *Journal of Turbomachinery*, 123(2): 207-213, 2001.

[121] Schlienger, J., Kalfas, A. I., and Abhari, R. S. Vortex-Wake-Blade Interaction in a Shrouded Axial Turbine. *Journal of Turbomachinery*, 127(4):699-707, 2005.

[122] Scholz, N. Über die Durchführung systematischer Messungen an ebenen Schaufelgittern. *Zeitschrift für Flugwissenschaften*, 4(10):313–334, 1956.

[123] Schuepbach, P., Abhari, R. S., Rose, M. G., Germain, T., Raab, I., and Gier, J. Improving Efficiency of a High Work Turbine Using Non-Axisymmetric Endwalls: Part II—Time-Resolved Flow Physics. In *ASME Turbo Expo 2008: Power for Land, Sea, and Air*, Paper No. GT2008-50470, 2008.

[124] Schuepbach, P., Abhari, R. S., Rose, M. G., and Gier, J. Influence of Rim Seal Purge Flow on the Performance of an Endwall-Profiled Axial Turbine. *Journal of Turbomachinery*, 133(2): 21011-01-21011-10, 2011.

[125] Schwab, S. *Experimentelle Untersuchung von umfangsunsymmetrischen Dampfturbinenbeschaufelungen und von Temperatur- ausgleichsphänomenen an einer 2-stufigen Versuchsturbine*. Dissertation, RWTH Aachen, 01.01.2014.

[126] Schwab, S., Wendland, D., and Wirsum, M. Numerical and Experimental Investigation of Tangential Endwall Contoured Blades in a 2-Stage Turbine. In *ASME Turbo Expo 2013: Turbine Technical Conference and Exposition*, Paper No. GT2013-94169, 2013.

[127] Schwarz, H., Friedrichs, J., and Flegler, J. Design Parameters of Brush Seals and Their Impact on Seal Performance. In *ASME Turbo Expo 2012: Turbine Technical Conference and Exposition*, Paper No. GT2012-68956, 2012.

[128] Schwarz, H., Friedrichs, J., and Flegler, J. Axial Inclination of the Bristle Pack, a New Design Parameter of Brush Seals for Improved Operational Behavior in Steam Turbines. In *ASME Turbo Expo 2014: Turbine Technical Conference and Exposition*, Paper No. GT2014-26330, 2014.

[129] Shaw, R. The influence of hole dimensions on static pressure measurements. *Journal of Fluid Mechanics*, 7(04):550, 1960.

[130] Shreeve, R. P. On the use of fine wire thermocouple probes in heated high speed flows. In *7th Aerodynamic Testing Conference*, 1972.

[131] Sieverding, C. H. Recent Progress in the Understanding of Basic Aspects of Secondary Flows in Turbine Blade Passages. *Journal of Engineering for Gas Turbines and Power*, 107(2):248-257, 1985.

[132] Sieverding, C. H. and van den Bosche, P. The use of coloured smoke to visualize secondary flows in a turbine-blade cascade. *Journal of Fluid Mechanics*, 134(-1):85-90, 1983.

[133] Snedden, G., Dunn, D., Ingram, G., and Gregory-Smith, D. The Application of Non-Axisymmetric Endwall Contouring in a Single Stage, Rotating Turbine. In *ASME Turbo Expo 2009: Power for Land, Sea, and Air*, Paper No. GT2009-59169, 2009.

[134] Snedden, G., Dunn, D., Ingram, G., and Gregory-Smith, D. The Performance of a Generic Non-Axisymmetric End Wall in a Single Stage, Rotating Turbine at On and Off-Design Conditions. In *ASME Turbo Expo 2010: Power for Land, Sea, and Air*, Paper No. GT2010-22006, 2010.

[135] Spurk, J. and Aksel, N. *Strömungslehre: Einführung in die Theorie der Strömungen*. Springer-Lehrbuch. Springer-Verlag Berlin Heidelberg, Berlin, Heidelberg, 8. aufl. edition, 2010.

[136] Stewart, W. L. Analysis of two-dimensional compressibleflow loss characteristics downstream of turbomachine blade rows in terms of basic boundary-layer characteristics. In *NACA TN 3515, 1955*.

[137] Stodola, A. *Dampf- und Gasturbinen*. Springer Berlin Heidelberg, Berlin, Heidelberg, 1924.

[138] Taremi, F., Sjolander, S. A., and Praisner, T. J. Application of Endwall Contouring to Transonic Turbine Cascades: Experimental Measurements at Design Conditions. In *ASME 2011 Turbo Expo: Turbine Technical Conference and Exposition*, Paper No. GT2011-46511, 2011.

[139] Thomas, H.-J. *Thermische Kraftanlagen*. Hochschultext. Springer, Berlin, Heidelberg, 1975.

[140] Tietze, W., editor. *Handbuch Dichtungspraxis*. Vulkan-Verl., Essen, 3. aufl. edition, 2003.

[141] Tollmien, W., Schlichting, H., and Görtler, H. *Ludwig Prandtl Gesammelte Abhandlungen: Zur angewandten Mechanik, Hydro- und Aerodynamik*. Springer Berlin Heidelberg, Berlin, Heidelberg, s.l., 1961.

[142] Traupel, W. *Thermische Turbomaschinen: Thermodynamisch-strömungstechnische Berechnung*. Klassiker der Technik. Springer, Berlin, Heidelberg, 4. auflage edition, 2001.

[143] Truckenbrodt, E. *Fluidmechanik*. Springer, Berlin, 4., ergänzte aufl. 1996, nachdr. 2008 in veränderter ausstattung edition, 2008.

[144] Trutnovsky, K. and Komotori, K. *Berührungsfreie Dichtungen*. VDI-Verl., Düsseldorf, 4., überarb. und erw. aufl. edition, 1981.

[145] VDI 4675. *Bilanzgerechte Mittelung inhomogener Strömungsfelder*. 2012.

[146] Vinnemeier, F., Simon, L., and Koschel, W. Korrektur des Kopfgeometrieeinflusses einer Fünfloch- Drucksonde auf die Meßergebnisse / Correction method for the head geometry influence of a five-hole pressure probe on the measurement results. *tm - Technisches Messen*, 57 (JG), 1990.

[147] Völker, L. *Neue Aspekte der aerodynamischen Gestaltung von Niederdruck-Endstufen-Beschaufelungen*. Dissertation, Universität Stuttgart, 2006.

[148] Walker, P. J. *Blade lean in axial Turbines: Model Turbine Measurements and Simulation by a novel numerical method*. Dissertation, University of Cambridge, 1987.

[149] Wallén, G. *Experimentelle Untersuchung des Einflusses von Reynoldszahl und von Schaft- und Gradienteneffekten bei Strömungsmessungen mit kegelförmigen Fünfloch-Sonden: Univ., Diss.–Espoo, 1980*, volume 475 of *Dissertation from Helsinki University of Technology*. , 1981.

[150] Wallis, A. M., Denton, J. D., and Demargne, A. A. J. The Control of Shroud Leakage Flows to Reduce Aerodynamic Losses in a Low Aspect Ratio, Shrouded Axial Flow Turbine. In *ASME Turbo Expo 2000: Power for Land, Sea, and Air*, Paper No. 2000-GT-475, 2000.

[151] Wang, H. P., Olson, S. J., Goldstein, R. J., and Eckert, E. R. G. Flow Visualization in a Linear Turbine Cascade of High Performance Turbine Blades. *Journal of Turbomachinery*, 119(1): 1-8, 1997.

[152] Wang, Z. and Han, W. The Influence of Blade Negative Curving on the Endwall and Blade Surface Flows. In *ASME 1995 International Gas Turbine and Aeroengine Congress and Exposition*, Paper No. 95-GT441:1-7, 1995.

[153] Wanjin, H., Zhongqi, W., Chunqing, T., Hong, S., and Mochun, Z. Effects of Leaning and Curving of Blades With High Turning Angles on the Aerodynamic Characteristics of Turbine Rectangular Cascades. *Journal of Turbomachinery*, 116(3):417-424, 1994.

[154] Waterman, W. F. and Tall, W. A. Measurement and Prediction of 3-D Viscous Flows in Low-Aspect-Ratio Turbine Nozzles. In *ASME Turbo Expo 1976*, Paper No. 76-GT-73, 1976

[155] Willinger, R. *Einfluss der Reynoldszahl auf die Kalibrierkurven von pneumatischen Strömungssonden*. Dissertation, TU Wien, 2007.

[156] Wingelhofer, F. *Neue Kriterien zur Auslegung dreidimensionaler Beschaufelungen von Axialturbinen*. Dissertation, TU Wien, 2003.

[157] Wuest, W. *Strömungsmeßtechnik*. Vieweg+Teubner Verlag, Wiesbaden, 1969.

[158] Yamamoto, A. and Nouse, H. Effects of Incidence on Three-Dimensional Flows in a Linear Turbine Cascade. *Journal of Turbomachinery*, 110(4):486-496, 1988.

[159] Zebner, H. M. *Experimentelle und theoretische Untersuchung der Sekundärströmung durch Turbinengitter mit besonderer Berücksichtigung der durch die Interaktion zwischen Profil und Seitenwandgrenzschichten entstehende Verluste*. Dissertation, RWTH Aachen, 1991.

[160] Zeisberger A. Total temperature probes for turbine and combustor applications. In *18th, International symposium on air breathing engines ISABE 2007, Paper No. 1108* . 2007.

[161] Zimmermann, T. W., Curkovic, O., and Wirsum, M. Influence of tip seal configurations on flow and efficiency for shrouded turbine blades. *International Journal of Gas Turbine, Propulsion and Power Systems*, 8(2):9–17, 2016.

[162] Zimmermann, T. W., Curkovic, O., Wirsum, M., and Fowler, A. Influence of adjusting control accuracy on pressure probe measurements in turbo machines. *Journal of Energy and Power Engineering*, 10(9):522–533, 2016.

[163] Zimmermann, T. W., Curkovic, O., Wirsum, M., Fowler, A., and Patel, K. Comparison of Two-Dimensional and Three-Dimensional Turbine Airfoils in Combination With Nonaxisymmetric Endwall Contouring. *Journal of Turbomachinery*, 139(6):061007-061007-13, 2017.